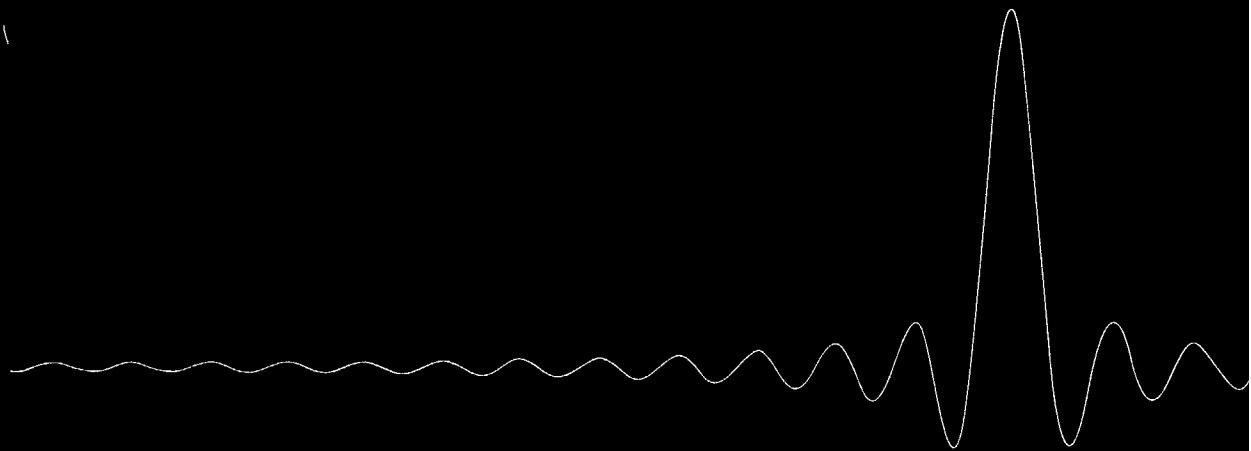
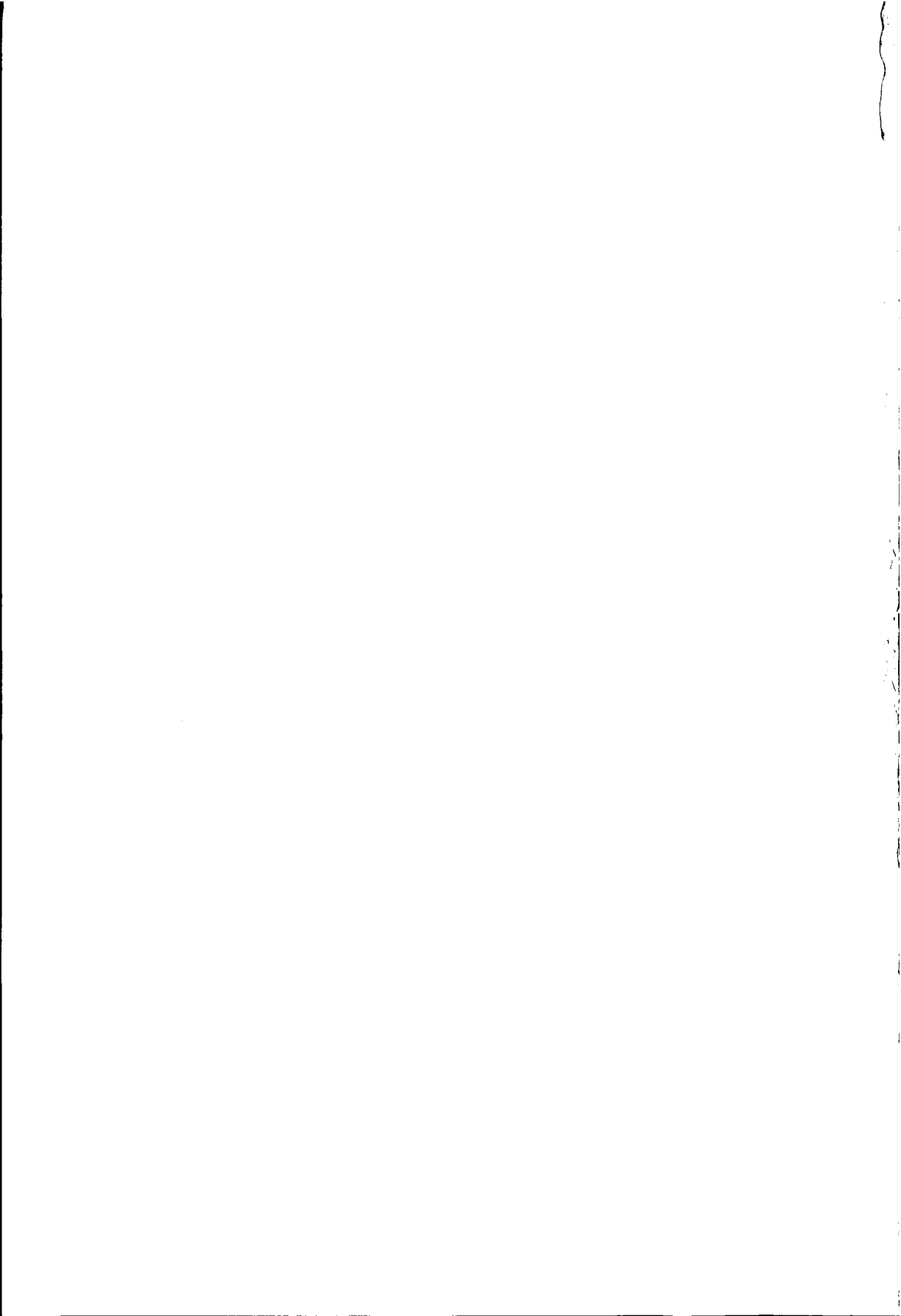


**MODELLING AND INVERSION
OF
PULSED EDDY CURRENT DATA**



Simon van den Berg



TR 4158 S

Stellingen

behorend bij het proefschrift

Modelling and Inversion of Pulsed Eddy Current Data

door

Simon van den Berg

Delft, 10 december 2003

1. PEC (Perfectly Electrically Conducting) randvoorwaarden zijn niet geschikt om de PEC (Pulsed Eddy Current) techniek te modelleren.
2. Als een discreet signaal, gedefinieerd op de punten $\{k\Delta x; k = 0, \dots, 2^N - 1\}$, na het toepassen van een FFT slechts op de discrete subset van punten $\{2^p k\Delta x; p \in \{0, \dots, N\}; k = 0, \dots, 2^{N-p} - 1\}$ benodigd is, verdient het de aanbeveling gridreductie toe te passen.
3. Tijd domein of multifrequentie inversie, gekoppeld aan een geparametriseerd defectmodel, zal gebruikt moeten worden om defecten te reconstrueren met behulp van "Pulsed Eddy Current" data.
4. Het expanderende "smoke ring" model van Nabighian voor diffuse velden moet vervangen worden door een niet-expanderend model voor velden in metaal (Nabighian, M.N., *Quasi-static transient response of a conducting half-space - An approximate representation*).
5. Bij het oplossen van de gekoppelde integraalvergelijkingen voor het elektrisch en magnetisch veld zijn ontwikkelingsfuncties voor de vectorpotentiaal nodig die in iedere richting tenminste stuksgewijs lineair zijn.
6. Bij gelijktijdige inversie van conductiviteit en permeabiliteit is er minder afhankelijkheid tussen de gereconstrueerde parameters dan tussen conductiviteit en permittiviteit in een vergelijkbare configuratie.
7. Een fundamenteel voordeel van een elektromagnetische inspectiemethode ten opzichte van een akoestische inspectiemethode is dat bij de eerste geen materiële contact nodig is tussen de sensor en het te onderzoeken object.
8. In het huidige financieringsklimaat voor universiteiten staat korte-termijn utiliteit gelijk aan maatschappelijke relevantie. Hierbij wordt voorbij gegaan aan de lange-termijn utiliteit van wetenschappelijk relevant onderzoek.
9. Gemiddeld genomen is het gemak waarmee men een bericht kan versturen omgekeerd evenredig met het belang van de inhoud.
10. Het nut van computers in het onderwijs wordt overschat en de schade onderschat.

Deze stellingen worden verdedigbaar geacht en zijn als zodanig goedgekeurd door de promotor:

Prof.dr.ir. H. Blok

1. PEC (Perfectly Electrically Conducting) boundary conditions are not suitable for modelling the PEC (Pulsed Eddy Current) technique.
2. Grid reduction should be used when a discrete signal, defined on the points $\{k\Delta x; k = 0, \dots, 2^N - 1\}$, is needed only on the discrete subset of points $\{2^p k\Delta x; p \in \{0, \dots, N\}; k = 0, \dots, 2^{N-p} - 1\}$ after application of an FFT.
3. Time domain or multifrequency inversion, together with a parametric defect model, should be used to reconstruct defect parameters from "Pulsed Eddy Current" data.
4. Nabighians expanding "smoke ring" model for diffusive fields has to be replaced by a non-expanding model for fields in metals (Nabighian, M.N., *Quasi-static transient response of a conducting half-space - An approximate representation*).
5. Expansion functions for the vector potentials that are at least piecewise linear in each spatial direction are necessary to solve the coupled integral equations for the electric and magnetic fields.
6. There is less dependence between the reconstructed parameters in simultaneous inversion of conductivity and permeability than for conductivity and permittivity in a comparable configuration.
7. A fundamental advantage of electromagnetic inspection techniques over acoustic inspection techniques is that the former are non-contact methods.
8. In the present financial climate for universities, short term usefulness is taken to be equal to social relevance. In this way, the long-term usefulness of scientifically relevant work is neglected.
9. On average, the ease with which one can send a message is inversely proportional to the importance of the contents of that message.
10. The usefulness of computers in education is overrated, while the negative effects are underrated.

These propositions are considered defensible and as such have been approved by the supervisor:

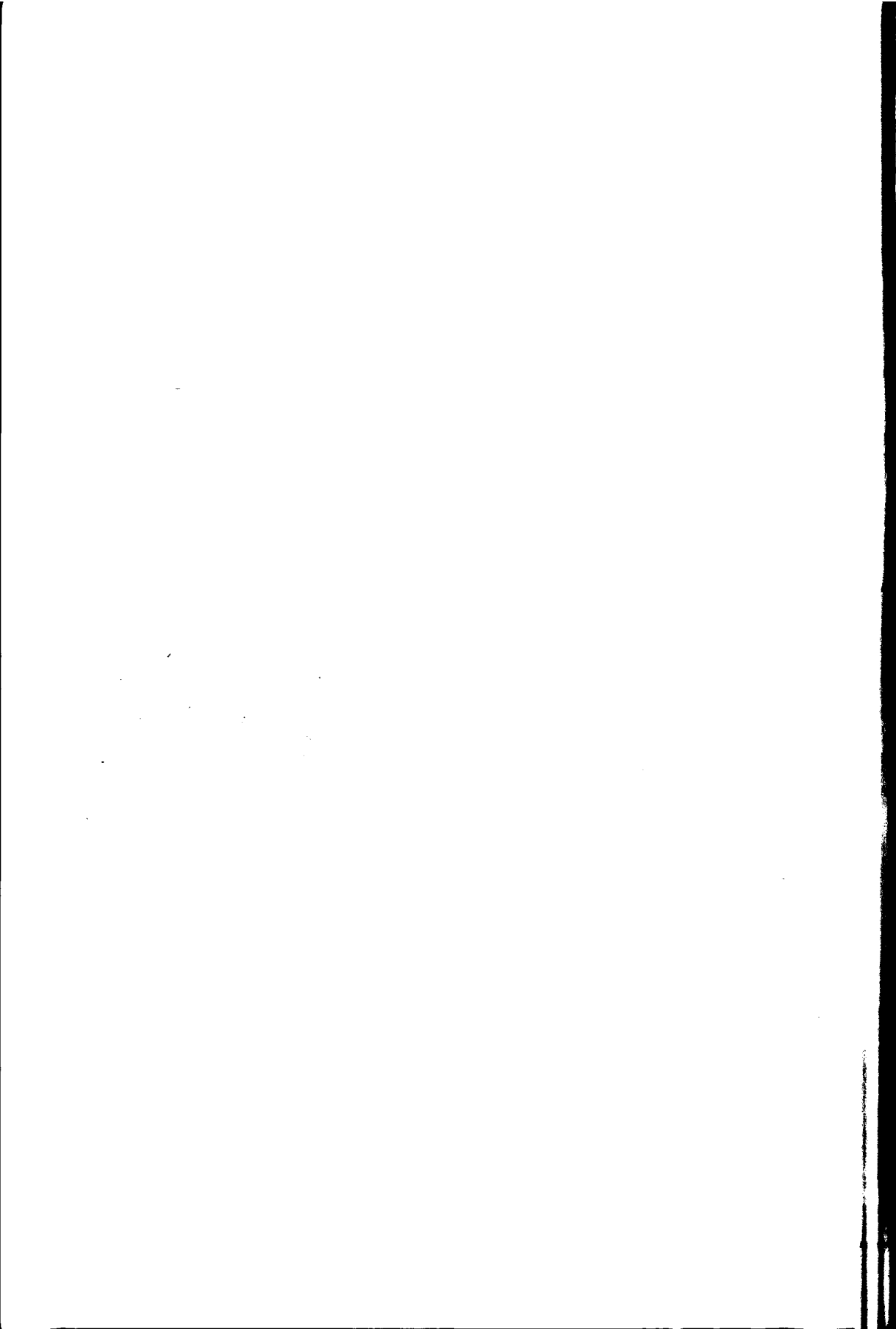
Prof.dr.ir. H. Blok



000 811
4150
2010050

**MODELLING AND INVERSION
OF
PULSED EDDY CURRENT DATA**

TR 4150



6.5.1

MODELLING AND INVERSION OF PULSED EDDY CURRENT DATA

Proefschrift

ter verkrijging van de graad van doctor
aan de Technische Universiteit Delft,
op gezag van de Rector Magnificus prof.dr.ir. J.T. Fokkema,
voorzitter van het College van Promoties,
in het openbaar te verdedigen

op woensdag 10 december 2003 om 10:30 uur

door

Simon Martijn van den BERG

elektrotechnisch ingenieur

geboren te Brielle.



Dit proefschrift is goedgekeurd door de promotor:
Prof.dr.ir. H. Blok

Toegevoegd promotor: Dr.ir. B.J. Kooij

Samenstelling promotiecommissie:

Rector Magnificus	voorzitter,
Prof.dr.ir. H. Blok	Technische Universiteit Delft, promotor
Dr.ir. B.J. Kooij	Technische Universiteit Delft, toegevoegd promotor
Prof.dr.Eng. J.A. Ferreira	Technische Universiteit Delft
Prof.dr.ir. F. Olyslager	Universiteit Gent
Prof.dr. A.G. Tjhuis	Technische Universiteit Eindhoven
Dr.ir. A. Abubakar	Schlumberger Doll Research
Ir. M.T. Looijer	Shell Research and Technology Centre Amsterdam

Prof.dr.ir. P.M. van den Berg Technische Universiteit Delft, reservelid

Published and distributed by: DUP Science

DUP Science is an imprint of
Delft University Press
P.O. Box 98
2600 MG Delft
The Netherlands
Telephone: +31 15 27 85 678
Telefax: +31 15 27 85 706
E-mail: info@library.tudelft.nl

ISBN 90-407-2461-X

Keywords: Pulsed Eddy Current, forward modelling, inversion

Copyright ©2003 by S.M. van den Berg

All rights reserved. No part of the material protected by this copyright notice may be reproduced or utilized in any form or by any means, electronic or mechanical, including photocopying, recording or by any information storage and retrieval system, without written permission from the publisher:

Delft University Press

Printed in The Netherlands

Aan mijn ouders
Aan Gemke

Financial support

The research reported in this thesis was financed by Shell Research and Technology Centre, Amsterdam. This support is gratefully acknowledged.

Contents

1	Introduction	1
1.1	Non-Destructive evaluation	1
1.1.1	NDE Techniques for corrosion detection	2
1.1.2	Defect types	3
1.2	Eddy current nondestructive evaluation	5
1.2.1	Frequency domain Eddy Current NDE	5
1.2.2	Time domain Eddy Current NDE	5
1.3	Eddy current Non-Destructive Evaluation in the petrochemical industry	6
1.4	Description of the problem	8
1.4.1	The configuration	8
1.4.2	The forward problem	9
1.4.3	The inverse problem	9
1.5	Review of literature	10
1.6	Outline of the thesis	13
2	Basic Equations	17
2.1	Maxwell's equations	18
2.2	Magnetic hysteresis losses	19
2.3	Boundary conditions	20
2.4	Frequency domain equations	20
2.5	Spatial Fourier transformation	21
2.6	The frequency domain reciprocity theorem	22

3	The PEC tool and the measurement setup	25
3.1	PEC tool	25
3.1.1	Operating principles of the PEC tool	27
3.1.2	The probe	28
3.1.3	Data processing unit	29
3.1.4	Operation of the tool	30
3.2	PEC signals	31
3.2.1	Effects of medium and configuration parameters	33
3.2.2	Influence of test wall parameters on the PEC signal	33
	Influence of wall thickness on the PEC signal	34
	Influence of permeability on the PEC signal	34
	Influence of conductivity on the PEC signal	37
3.2.3	Influence of probe parameters on the PEC signal	38
3.3	Lumped circuit model	38
3.3.1	Expressions for the resistance and inductance coefficients	41
3.3.2	Eigenvalues and eigenvectors of the system matrix	42
4	The Forward Problem	45
4.1	Review of computational techniques	45
4.1.1	The FDTD method	46
4.1.2	Integral equations	46
4.2	2D Stratified configuration	47
4.2.1	Scattering formulation	49
4.2.2	Sensitivity	50
4.3	3D Configuration with a homogeneous background	52
4.3.1	Discretization of the computational domain	55
4.3.2	Weighting procedure	56
4.3.3	Weighted forms of $\hat{A}'_{k;m,n,p}$ and $\hat{F}'_{j;m,n,p}$	58
4.3.4	Weighted forms of $\hat{A}''_{k;m,n,p}$ and $\hat{F}''_{j;m,n,p}$	60

4.3.5	Weighted forms of $\hat{A}_{k;m,n,p}$ and $\hat{F}_{j;m,n,p}$	61
4.4	Operator formulation	63
4.4.1	Inner product and norm	64
4.5	Conjugate Gradient scheme	64
4.5.1	Update directions	65
4.5.2	Weighting parameters	67
4.5.3	The object operator and adjoint object operator	67
4.5.4	The data operator and the adjoint data operator	69
	Adjoint data operator	71
	Discretized data operator	72
	Discretized adjoint data operator	73
4.6	Preconditioning operator	73
	Preconditioned gradients	74
	Extended Born approximation	74
4.7	Marching-on-in-frequency	76
4.8	Calculation of the incident fields	77
4.8.1	Incident field of a magnetic dipole	78
4.9	3D Stratified configuration	78
4.9.1	Discretized operators and adjoint operators	80
4.9.2	Calculation of the PEC signals	83
5	Numerical Results for the Forward Problem	85
5.1	2D Configuration	85
5.2	3D Configuration with a homogeneous background	90
5.2.1	Conducting cube	90
5.2.2	Scattering by a conducting and permeable sphere	91
5.2.3	Numerical results for the preconditioning operator	92
5.3	3D Stratified configuration	93
6	The Inverse Problem	99
6.1	3D Inversion for a homogeneous background	100

6.1.1	Updating the contrast sources	102
6.1.2	Updating the contrasts	103
	Non-CG update of the contrasts	104
	CG update of the contrasts	104
6.1.3	Starting values	107
6.2	3D Inversion for a stratified configuration	108
6.3	Binary inversion	110
6.4	Total variation regularization	113
7	Numerical Results for the Inverse Problem	117
7.1	Inversion for a homogeneous background	117
7.1.1	Single scatterer with contrast in μ and σ	118
7.1.2	Separate scatterers	119
7.1.3	Binary inversion	120
7.1.4	One-sided illumination	120
7.1.5	Negative contrasts	121
7.2	Inversion for a stratified configuration	130
7.2.1	Sensitivity	130
7.2.2	Geophysical configuration	132
7.2.3	PEC configuration	134
8	Discussion and Conclusions	141
A	Scalar Green's Functions	145
A.1	Single layer configuration	145
A.2	Three-layer configuration	148
A.3	Branch points and poles	150
B	Dyadic Green's Functions	153
B.1	The Green's function for a stratified medium	154
B.1.1	Maxwell's equations in the Fourier transform domain	155
B.1.2	Electromagnetic fields in a homogeneous subdomain	157

B.1.3	Scattering formalism at an interface	158
B.1.4	Scattering formalism at the source interface	159
B.2	The Green's function for a 3-media configuration	161
B.2.1	Sources located within the layer	161
B.2.2	Sources located above the layer	164
B.2.3	Calculating the field quantities	166
B.3	Symmetry properties of the Green's function	167
B.4	Numerical implementation of the Green's functions	169
B.4.1	Branch points and poles	169
B.4.2	Using the FFT for the inverse transformation	170
	Accuracy of the FFT	170
C	Grid reduction for FFTs	173
C.1	Using periodicity to reduce the number of grid points	173
C.2	Application to the FFT algorithm	175
	Bibliography	179
	Samenvatting	187
	Curriculum Vitae	191
	Acknowledgements	193

Chapter 1

Introduction

This thesis deals with the Non-Destructive Evaluation (NDE) of materials, specifically the Pulsed Eddy Current (PEC) technique for detecting corrosion in metals. In this chapter, we provide some background information and a general overview of NDE techniques. We define the problems that are discussed in this thesis and introduce the general concepts of forward and inverse problems. An outline of the thesis can be found in Section 1.6 of this chapter.

1.1 Non-Destructive evaluation

In this section we aim to give a short, general overview of Non-Destructive Evaluation (NDE) or Non-Destructive Testing (NDT), as it is also called. Non-Destructive Evaluation enables one to see inside an object or inside a domain, specifically to locate and size defects without damaging said object. In a broad sense, one could even call the use of radar a form of NDE, since it enables us to see into the air around us (the domain) and locate moving objects (the defects). However, NDE techniques do not necessarily involve the location of defects. For example, the thickness of a paint layer on a metal surface can be measured using NDE techniques, as can stress in materials. Since this thesis deals with corrosion detection, we will confine ourselves to the testing of objects and materials for defects. For this application, one could say that Non-Destructive Evaluation is akin to an MRI scan of the human body. This analogy is where the 'Non-Destructive' part of NDE is especially clear: the MRI scan does not harm the patient who is undergoing it, similarly, after NDE testing, the object that was tested is still intact.

If we consider nondestructive evaluation for detecting defects, we can distinguish between qualitative and quantitative NDE. In qualitative NDE, we are only concerned with detecting the defect and no information is recovered concerning its location or size. With quantitative NDE, on the other hand, more parameters are recovered, such as the location, size or medium parameters of the defect. Which NDE technique should be applied depends on the configuration, the type of defect that one aims to find and the required accuracy.

1.1.1 NDE Techniques for corrosion detection

We will now focus on NDE techniques for corrosion detection. Presently, a large number of NDE techniques are available for this application, depending on the configuration and the object that has to be inspected. Generally, an NDE technique works by applying energy (for example a wavefield) to the object via some probe, after which the reflected signal is examined. One should be aware that some techniques are more suitable for the detection and/or sizing of certain types of defects than others. The type of energy, be it acoustic, electromagnetic or elastodynamic, and the manner of application must be such that the presence of a defect has a significant influence on the reflected signal. The following list, which is by no means complete, gives some common NDE techniques and their application

- **Ultrasonic**

The ultrasonic inspection technique consists of a transducer which induces high-frequency sound waves in the test object. The round-way travel time of the sound waves provides information on the thickness of the test object. This technique is widely used, and an example of a common application is testing welds for integrity.

- **X Ray**

This is analogous to the use of X rays in hospitals. It gives high resolution, but is cumbersome and expensive. An example of its use is checking castings for voids or inclusions.

- **Magnetic Flux Leakage**

The magnetic flux leakage technique magnetizes the test object using a static magnetic field, after which a Hall-sensor is used to detect the stray field which results from defects in the test object. This is an electromagnetic technique which is used to check the integrity of pipes and vessels.

- **Acoustic (Seismic) Subsurface Survey**

An acoustic or elastodynamic wavefield is generated in the ground and the reflected signals are then recorded. One can look at the direct reflections or run complete inversion schemes on the data. This technique is used to find new oil fields or mineral deposits.

- **Ground Penetrating Radar (GPR)**

A radar antenna is placed close to the ground in order to generate an electromagnetic wavefield in the ground. The reflected signals are picked up and processed. Using GPR one can form a high-resolution image of the ground to a depth of several meters.

- **Eddy Current**

The frequency domain eddy current technique entails the generation of induction currents in the test object by means of a coil with a sinusoidally varying driving current. The electromagnetic field generated by the eddy currents is picked up and information on the test object is recovered from the amplitude and the phase of the received signals.

On the other hand, time domain eddy current uses a pulsed current in the transmitting coil, after which the secondary fields generated by the induced eddy currents is picked up. The time dependence of the received signals contains information on the object under test. This is a relatively new technique, and it forms the subject of this thesis.

1.1.2 Defect types

The number of different defect types that can be encountered is, if anything, even larger than the number of inspection techniques. We will confine ourselves to the defect types which involve some loss of material (one could also think of a defect as an area where locally the material has slightly different medium parameters). Therefore, with the rest of the thesis in mind, we will give this summary of defect types (see also Figure 1.1).

1. **Pit defect**

A defect where a relatively large (in the order of the thickness of the pipe, or larger) piece of material has disappeared. This type of defect is frequently found in pipelines.

2. **Inclusion defect/delamination**

This type of defect is located within the test object. An example of this is delamination, where a gap or inclusion occurs within the metal. This can be caused by material imperfections, and occurs frequently in composites as well.

3. **Erosion defect**

A type of defect found on the inside of pipelines, often in bends and corners. The product which flows through the pipeline has eroded the metal of the pipe wall.

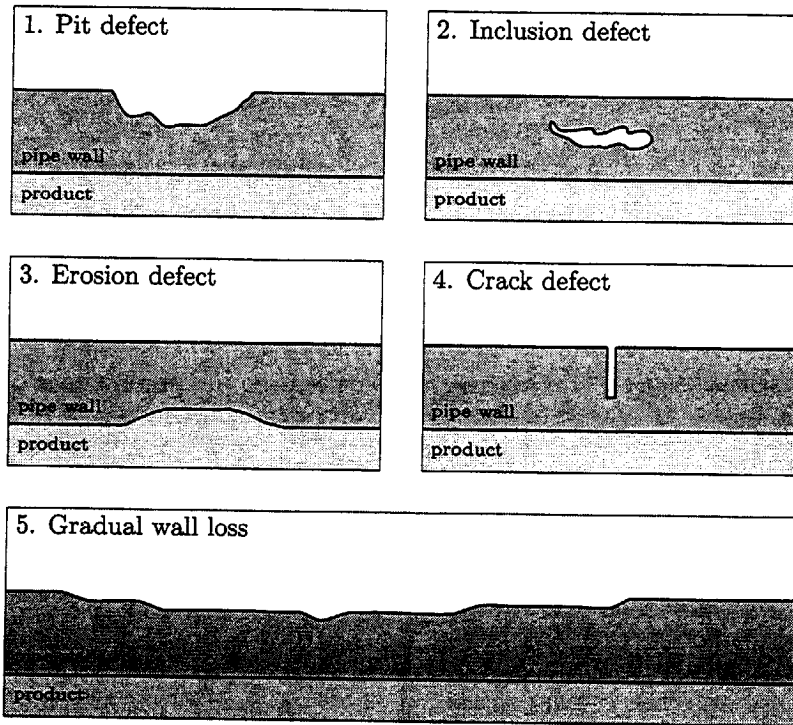


Figure 1.1: Schematic overview of different defect types.

4. Crack defect

A small defect (an order or more smaller in size than the wall thickness), which can occur because of repeated stressing of the material. This type of defect occurs frequently near welds.

5. Gradual wall loss

Very large defect (in the order of several times the wall thickness), where there is a small, gradual decrease in wall thickness. This type of defect can be easily detected using the PEC technique.

The type of defect will vary with the type and use of the object, for example, aircraft will exhibit crack-type defects, while larger corrosion spots will mostly occur in pipelines. In this thesis we will focus mainly on the pit-type corrosion defects.

1.2 Eddy current nondestructive evaluation

Since the topic of this thesis is the Pulsed Eddy Current NDE technique (hereafter referred to as the PEC technique), we will now describe this technique in more detail. In doing this, we will distinguish between frequency domain and time domain (pulsed) eddy current NDE.

1.2.1 Frequency domain Eddy Current NDE

In frequency domain eddy current testing, the simplest setup is one with two coils: a transmitting coil and a receiving coil. A sinusoidally varying current with a constant frequency in the transmitting coil generates eddy currents in the test object. These eddy currents generate a secondary electromagnetic field and the combination of the driving (primary) field from the transmitting coil and this secondary field induces a voltage on the receiving coil. Often the impedance of the receiving coil is used as a measure of the object under test. When a defect is present, it will disrupt the eddy current flow, and thus produce a change in the secondary field. This change in the field can be measured at the receiving coil, where both phase and amplitude of the received signal can be used to get an indication of the size of the defect.

Frequency domain eddy current testing has widespread applications, ranging from large-scale geophysical measurements to measurements of delaminations in composite structures. It came of age in the aviation industry, where it is still widely used to detect hairline cracks caused by metal fatigue.

1.2.2 Time domain Eddy Current NDE

The general setup for time domain Eddy Current NDE is the same as its frequency domain counterpart: a transmitting coil which induces the eddy currents in the object and a receiving coil to pick up the secondary electromagnetic field. However, it is the manner in which the eddy currents are induced that is different. The current in the transmitting coil does not have a constant frequency, but instead it is pulsed. This pulsed driving current induces eddy currents in the object that decay over time, which causes the secondary electromagnetic field to decay over time as well. It is that decay over time that provides the information on the object under test. The measured voltage is plotted as a function of time, and from this graph observations concerning the test object can be made.

Since Pulsed Eddy Current NDE is a relatively new technique, its applications are not as widespread as those of frequency domain EC. It was originally developed to detect corrosion under insulation (CUI), but is currently used in a much more diverse manner. Applications for PEC include corrosion monitoring, inspection of support structures for spheres and columns and underwater inspection of risers. Its ability to handle large lift-off and high temperatures, as well as good repeatability

give it an advantage over other NDE techniques. For a detailed explanation of the workings of the PEC technique and the PEC tool, the reader is referred to Chapter 3.

1.3 Eddy current Non-Destructive Evaluation in the petrochemical industry

The petrochemical industry has an abundance of pipelines, vessels, and other metal objects, which must be inspected regularly. A refinery plant is shut down periodically, and in this period all replacement and maintenance must take place which cannot be carried out in-service. It is obviously a great advantage if the components that need replacement are known in advance. Furthermore, continuous monitoring of certain critical pipes and vessels can give an indication of the rate of wear of these components, and hence of the need for shorter or longer maintenance intervals. Therefore, the need for regular inspection of these pipes and vessels by some NDE technique is clear. However, this is not as trivial as it may seem. The objects which need to be tested are often insulated for energy conservation and personnel protection reasons. This insulation usually consists of a rockwool blanket wrapped around the object, covered by an aluminium layer to prevent weather damage (see Figure 1.2). This poses a problem, in that most inspection techniques cannot penetrate this insulation effectively. The insulation also gives rise to another problem: the aluminium weather protection which has aged is not watertight and this will accelerate the corrosion process, making an adequate inspection technique all the more desirable.

Frequency domain eddy current techniques have been used extensively in the petrochemical industry in recent years, especially for the inspection of heat exchanger pipes and the detection of small cracks in larger pipelines. To this end, the eddy current tools are mounted on so-called 'pigs', which are then pushed through the pipe by the flow of the product inside. A 'pig' is more or less a cylindrical plug, which fits narrowly in the pipe. Pigging has its drawbacks: dedicated sections must be present in the pipeline for inserting and removing the pigs, and the frequency domain eddy current tools on the pig are not suitable for detecting large defects on the outside of the pipe.

Since it is very difficult to penetrate the insulation using frequency domain eddy current and ultrasonic measurement techniques, and since the removal of the insulation is a time-consuming and costly affair, one would like a measurement technique which is capable of direct measurement of the thickness of an object through the insulation that covers it. This is where the PEC NDE technique comes into play, since it is capable of taking wall thickness measurements through the insulation. This property of being able to take non-contact measurements at large lift-off and through plating makes the technique suitable for measurements on high-temperature objects as well (Ultrasonic techniques do not work well for this type of application, since

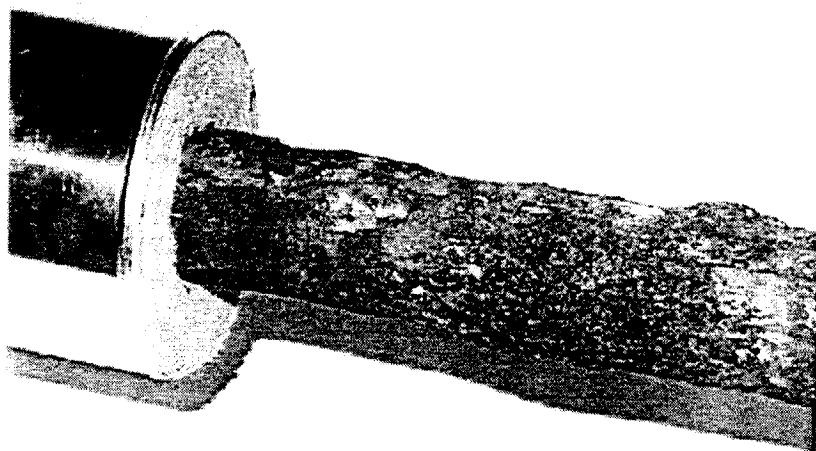


Figure 1.2: Corroded pipe with insulation and weather jacket.

the contact paste needed to improve energy transfer between the transducer and the object vaporizes at high temperatures).

The PEC technique has been implemented by Shell Global Solutions at the Shell Research and Technology Centre Amsterdam (SRTCA), who have produced a tool capable of measuring the wall thickness of a pipe through insulation. The tool can also be used to detect the presence of defects and is able to determine size and location of these defects, depending on size and defect type. The PEC project for the detection of corrosion under insulation started in 1993 and the author has been involved since 1997, first as part of an MSc project and for the last 4 years on a PhD project, which resulted in this thesis. Since 1995, 4 students have been involved in this project, leading to close cooperation between Delft University of Technology and SRTCA. The research reported on in this thesis was financially supported by Shell Research and Technology Centre, Amsterdam.

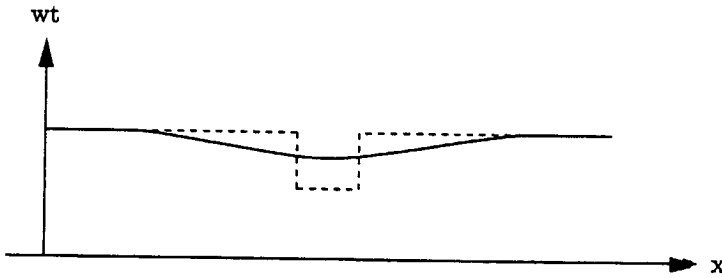


Figure 1.3: Schematic plot of the measured (solid) and actual (dotted) wall thickness (wt) for a scan over a defect using the PEC tool.

1.4 Description of the problem

The development of the PEC tool has now reached a stage where corrosion can be reliably detected under a variety of circumstances. However, when a corrosion spot has been detected, it would be advantageous to be able to recover the defect dimensions (especially the remaining wall thickness, i.e., nominal pipe thickness minus defect depth) from the measurements. This would be particularly useful for applications where the pipe is under pressure and where removal of the corrosion products can be dangerous. By using the PEC tool we make a volume measurement of the metal directly underneath the sensor, which can lead to difficulties for the determination of the defect depth using only the measured wall thickness (see Figure 1.3). However, if the influence of the defect on the measured PEC signal is known, it may be possible to determine the actual defect depth. We would therefore like to investigate the influence of defects on the measured PEC signals in detail by constructing a mathematical model (the so-called forward problem). By using such a model we are able to isolate the influence of a defect on the measured signal and we can calculate these effects for various configurations. Furthermore, we would like to use this model to investigate the possibility of recovering the defect parameters (width and depth) from the measured data (which is called the inverse problem). The configuration that we use for the model, the forward problem and the inverse problem are now briefly discussed.

1.4.1 The configuration

The configuration that we will model in the thesis consists of 2 transmitting coils and 2 receiving coils located some distance above a flat metal layer, which can contain a defect. In applications where the PEC tool is used on a pipe there is also the question of the curvature of the pipe, but experiments have shown that the approximation

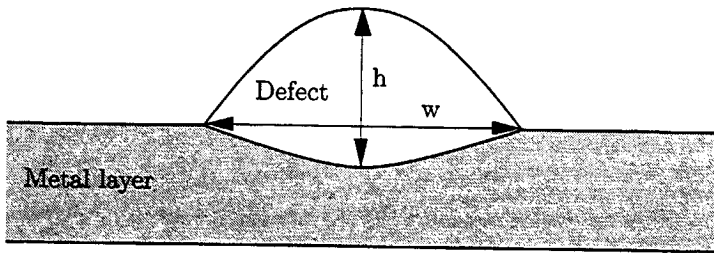


Figure 1.4: Parametrization of a defect using ellipses.

using a flat layer works well for most applications. For the exact setup of the coil system, the reader is referred to Chapter 3, which deals with the PEC tool itself.

1.4.2 The forward problem

The forward problem entails the calculation of the electromagnetic field quantities at the receiver location and within the defect, when the sources and the defect are known. The pipe wall is modelled as an infinitely large flat plate, which means that the curvature of the pipe is neglected; this is an approximation that has shown to be valid in most practical cases. Using the forward model, we can calculate the influence of the defect on the signals that are received using the PEC tool.

1.4.3 The inverse problem

The inverse problem consists of recovering the dimensions and the medium parameters (conductivity and permeability) of the defect from a set of measurements. Since the conductivity and permeability of the defect are assumed to be known, we can use a binary inversion scheme, whereby only the width and depth of the defect are reconstructed. Furthermore, often the geometry of the defect is such that we can use a parametrization of the defect. In this approximation, the defect is modelled by using a number of ellipses (see Figure 1.4), which enables us to characterize the dimensions of the defect with only a few parameters. This drastically reduces the number of unknowns in the inversion scheme, increasing computational speed.

Because of the physical nature of the test setup, where measurements are taken only on the outside of the pipe, full-angle coverage cannot be obtained. This restriction on the data set that can be obtained has consequences for the inverse problem, and is discussed in Chapters 7 and 8.

1.5 Review of literature

For the purpose of this review, we distinguish between frequency domain eddy current testing and pulsed (time domain) eddy current testing. Frequency domain eddy current testing has been around a long time and much research has been done in this area. Early work (before any significant computing power was available) started with analytical solutions for the probe impedance near halfspaces and layered structures. Dodd and Deeds [28] gave solutions to the problem of a coil located above a two-conductor plane and a coil surrounding an infinitely long conducting rod coated with another conductor. Further important contributions were the paper by Wait and Hill [88] and the paper by Cheng *et al.* [21]. Bowler [12] used halfspace and dyadic Green's functions to calculate coil responses for coils located above a conducting halfspace.

The modelling of defects received a major contribution by the work of Burrows [19] in 1964. His results were later verified by Dodd and Deeds [28]. They measured impedance changes from artificial defects in aluminium plates and tubes and compared these results with their numerical calculations. It was found that when the defect was small compared to the skin depth but large enough to have a measurable influence on the impedance, the accuracy of the model was good. However, this meant that their work was limited to very small defects.

The Born approximation has been used with some success in the reconstruction of defects and conductivity profiles (Sabbagh [70] and [71]). The field inside the scatterer is taken to be the incident field, which amounts to saying that the scatterer is weak. By doing this, the integral equation for the field is linearized and can then be solved. Later on, more accurate 3D models were made, enabling larger defects to be modelled, including surface-breaking defects, see for example Bowler *et al.* [16]. Looijer [51] used the Born approximation to calculate the effect of coaxial cylindrical defects on the PEC signal.

Reconstruction (imaging) of defects

The reconstruction (imaging) of defects entails the determination of the dimensions (lateral extent and depth) of the defect. Especially for corrosion applications on pressurized objects, the depth of the defect is an important parameter. For the case of corrosion of a metal layer, Luong and Santosa [53] developed a method to determine the material loss with eddy current impedance measurements. They derived a linearized relation between the observed impedance change and the loss profile, which resulted in a 2D convolution problem. The linearized inverse problem was then proven to have a unique loss profile provided that impedance data is obtained for all observation locations. They present numerical results for which a least-squares algorithm with either positivity constraints or total variation regularization was used to obtain estimates of the material loss depth.

Reconstruction of medium parameters

Reconstruction of the medium parameters is the full inverse problem, where both the size of the defect and the medium parameters are resolved. This can be done by linearizing the problem by applying, for example, the Born approximation. Nair and Rose [57] used this in combination with a combined Fourier-Laplace transformation to reconstruct the conductivity and thickness of a conducting coating on a conducting halfspace. Sabbagh and Lautzenheiser [70] use gradient techniques to solve both the electric field and the conductivity from the integral equation. They conclude that Fletcher-Reeves and Polak-Ribière algorithms are superior to the steepest descent algorithm and the choice of initial value for the field and contrast are important for the convergence of the scheme. Upda and Upda [80] give an overview of techniques used in the solution of inverse problems in eddy current NDE. Jenkins [39] used dyadic Green's functions and integral equations for 3D modelling of small cracks and slots in conducting halfspaces and slabs.

For high-frequency eddy current NDE of cracks in metals, one usually only takes the contrast in conductivity into account. When the defect size increases and/or the metal has a relative permeability greater than one, it is necessary to take the additional contrast in permeability into account. For geophysical applications, Zhang and Oldenburg, [94] and [95], have reconstructed one-dimensional conductivity and permeability from measurements obtained using a horizontal loop antenna. They use model objective functions for the conductive and permeable contrast separately, which are then simultaneously minimized by a least-squares algorithm. The scheme is also used on 3D electromagnetic data, which shows that the addition of a permeability contrast serves to enhance the solution of the conductivity contrast. For the imaging of 3D objects with magnetic susceptibility, Sepulveda *et al.* [73] describe a technique where they use matrix inversion with singular value decomposition (SVD) to obtain a least-squares solution. For the method to work, the source and measurement locations must be such that the matrix containing the Green's function is well-conditioned. Finally, we mention the work of Dos Reis *et al.* [29], who reconstruct defects in a thin metal layer using an exponential mapping with the contrast source inversion algorithm. They use a dyadic Green's function to solve the electric field integral equation where the conductivity of the contrast and the contrast source are the unknown quantities. The magnetic permeability of the configuration is taken to be equal to μ_0 throughout and a frequency of either 150 kHz or 300 kHz is used.

Numerical techniques for modelling eddy current NDE

The use of a local method such as the FDTD method for eddy current NDE of metal objects has its problems in that the contrasts are usually very high for these configurations. This can either be solved by very fine sampling, which is not realistic, or solving an additional integral equation for the fields along the boundary of the scatterer (see Oristaglio and Hohmann [59]). Badics *et al.* [6] presented a 3D finite

element scheme for computing electromagnetic field distortions due to defects. A simplification to the scheme for small, crack-like defects leads to reduced computational costs, however, this limits the type of defect that can be handled. Kriezis *et al.* [45] give a comprehensive overview of analytical and numerical methods for solving eddy current problems, including BEM and FEM methods. However, integral equations are most widely used, see for example Sabbagh [71] and Luong and Santosa [53].

Idemen and Akduman [42] consider the 2D inverse scattering problem for a configuration where dielectric and/or conductive cylinders are located within a dielectric slab. Taking the slab and the halfspaces to be non-conductive and non-magnetic, they then use integral equations and the Born approximation to determine the conductivity and permittivity of the object within the layer. Cui [25] and [26] uses a CG-FFT method and steepest descent path integration to evaluate the Sommerfeld integrals which result from the problem of a buried object. He then uses the method of moments (MoM) to solve the resulting matrix equations.

Time domain (pulsed) eddy current

Compared to the frequency domain eddy current techniques, time domain (pulsed) eddy current NDE is relatively new, and consequently, not as much has been published in this area. However, in the last decade, more and more research has been done, since the technique has several advantages, such as an inherent large data content and the ability to detect defects in structures with large dimensions.

Early work was done by Beissner and Fisher [9]. They considered different pulse shapes and concluded that a step-like (hyperbolic tangent) pulse gave the best results. For geophysical applications, more work has been done on time domain pulsed sources. We mention here the work of Wait and Hill [88], Cheesman [20], and Lee and Lewis [48]. Preda *et al.* [66] presented a FEM-BEM method for the reconstruction of cracks using pulsed eddy currents, while Rose and Uzal [68] used pulsed eddy currents to detect wall loss due to corrosion. They modelled a ferrite-cored probe located above a layered aluminium structure and then considered the transient voltage difference due to a step-function current. Instead of more commonly used Fourier transformation, Bowler and Johnson [18] used a Laplace transformation with respect to time and considered a configuration where the inverse Laplace transformation is reducible to a standard form which can be evaluated exactly using contour integration. They reported a good agreement between the model and experimental measurements acquired using a Hall sensor. Ludwig and Dai [52] describe a 2D weighted-residual-based finite element model for the calculation of eddy current distributions in a conducting halfspace and compare the results to analytical models which use an inverse Laplace transformation.

It should be noted that most publications in this area only consider contrasts in conductivity and/or permittivity, setting the permeability to μ_0 . For further information on time domain inversion, which is beyond the scope of this thesis,

the reader is referred to Farquharson and Oldenburg [31], Wang *et al.* [89] and Bloemenkamp [10].

In the context of the PEC project for the detection of corrosion under insulation, Looijer [51] has calculated the sensitivity of the received voltage with respect to plate thickness and defect size for defects that are coaxial with the transmitting coil and which are cylindrically symmetric. He also derived the Green's function for the case of an axially symmetric configuration of a loop source above a metal layer, which can be found in this thesis in Appendix A. For the design of the transmitting coils, Morsink [55] used FFTs to calculate the electromagnetic fields within a metal layer for a transmitting coil that is composed of wire segments.

Probe design

Attention has been paid to the design of the probe to maximize effectiveness and Signal-to-Noise Ratio (SNR). Sabbagh and Vernon [72] gave a model, numerical and experimental results for a coil with a ferrite core, showing good agreement between the model and the experiments. Later, Sabbagh [69] presented a more complete model of a coil with a ferrite core in the presence of a conducting halfspace. He used the method of moments (MoM) to solve the integral equation for the field in the ferrite core. This was extended to 3D models of ferrite-core probes by Bowler *et al.* [16]. Placko and Dufour [65] present a fully shielded probe design, where the coil is completely enclosed within a ferrite structure, leading to enhanced directivity and gain.

General information on Non-Destructive Evaluation

For more general material on NDE techniques, the reader is referred to the Nondestructive Testing Handbook, especially to Volume 4 [54], which deals with electromagnetic testing methods.

1.6 Outline of the thesis

In this chapter, we have given a short introduction to Non-Destructive Evaluation techniques, with a focus on Eddy Current and Pulsed Eddy Current NDE. Section 1.5 deals with the literature on electromagnetic methods in Non-Destructive Evaluation to give an overview of the work that has already been done in this field. We described the background of the project and discussed the motivations for this thesis.

In Chapter 2 we will discuss Maxwell's equations for the electromagnetic field quantities and the associated constitutive relations, as well as the boundary conditions for the electric and magnetic field components. We also introduce the necessary integral transformations which we need to calculate the electromagnetic fields in our configuration.

Chapter 3 deals with the actual PEC tool and the measurement setup. We start by describing the working principles of the tool, followed by a discussion of the two main components of the tool: the probe and the data processing unit. The configuration of the transmitting and receiving coils within the probe is briefly discussed, and we give a short description of the various components of the data processing unit, as well as a few examples of the actual operation of the tool. We then use the computational model, which is described in Chapter 4, to calculate the influence of various configuration and medium parameters on the PEC signals. In the last part of Chapter 3, we present a simple physical model for the PEC technique. This model describes the physics behind the PEC technique in terms of a mutually coupled system of current filaments. By calculating the eigenvalues and eigenvectors of the resulting system matrix, we can explain the electromagnetic diffusion of the eddy currents in terms of modes that are excited in the test object.

To obtain a mathematical model for the PEC technique, and specifically for the configuration where a defect is present, we use Maxwell's equations to derive expressions for the electromagnetic field quantities for a loop source located above a metal layer. We start Chapter 4 with a 2D configuration where no defect is present. In that case, we can use the symmetry properties of the configuration to obtain expressions for a scalar Green's function (derived in Appendix A), which we then use to calculate the electromagnetic field quantities at the receiver positions. For the configuration where a defect is present, we are no longer able to use this symmetry and hence we need to calculate the dyadic Green's function for a layered configuration. We start with the case of a homogeneous 3D configuration, for which we derive the integral equations for the electromagnetic field quantities in terms of the vector potentials. By using linear expansion functions, we end up with the finite difference approximation for the differential operators working on the vector potentials. We then use a Conjugate Gradient scheme to calculate both the electric and magnetic field quantities. Subsequently, the effect of the layer is taken into account by introducing the reflected part of the Green's functions. These are calculated in the spatial Fourier-transform domain, after which we use FFTs to calculate the Green's function in the spatial domain. Combined with the solution for the homogeneous configuration, this leads to a model for a defect that is located within a (metal) layer. The derivation of the reflected part of the Green's function is discussed in Appendix B, while in Appendix C we discuss a method whereby the number of grid points for the FFT can be considerably reduced. The numerical results pertaining to the forward problem are presented in Chapter 5.

Having completed the forward model, we now turn our attention to the inverse problem in Chapter 6. We extend the Contrast Source Inversion method described by Van den Berg and Kleinman [82] to reconstruct both electrical and magnetic contrasts and derive a formulation for binary inversion for homogeneous objects, where the contrast values are known and only the supporting domains of the objects have to be determined. In that case we use a non-linear mapping function for the contrasts, which gives improved reconstruction results, or we can use a regularization method such as TV-regularization. The numerical results obtained with the

algorithms that are presented in this chapter are given in Chapter 7.

We end this thesis with a discussion of the methods that were used and the corresponding results, which can be found in Chapter 8, where we also discuss our conclusions and offer suggestions for further research.

Chapter 2

Basic Equations

In this chapter we will discuss the basic equations pertaining to the electromagnetic field. We will consider electromagnetic fields in a 3-dimensional space defined by a right-handed Cartesian reference frame with origin \mathcal{O} . The reference frame is defined by three mutually independent base-vectors $\{\mathbf{i}_1, \mathbf{i}_2, \mathbf{i}_3\}$ of unit length, where the \mathbf{i}_3 -axis is oriented downward. The position vector is specified by $\mathbf{x} = x_1\mathbf{i}_1 + x_2\mathbf{i}_2 + x_3\mathbf{i}_3$. Partial differentiation with respect to time is denoted by ∂_t , while partial differentiation with respect to a spatial coordinate is denoted by ∂_j , where $j \in \{1, 2, 3\}$. Latin subscripts range over the values $\{1, 2, 3\}$, while Greek subscripts range over the values $\{1, 2\}$.

Both subscript and vector notations are used, therefore we introduce the symmetrical unit tensor of rank 2 (Kronecker delta) as

$$\delta_{m,n} = \begin{cases} 1 & , \text{ if } m \neq n \\ 0 & , \text{ if } m = n \end{cases} \quad (2.1)$$

Further, we define

$$\epsilon_{k,n,p} = \begin{cases} 1 & , \text{ if } \{k, n, p\} \text{ is an even permutation of } \{1, 2, 3\}, \\ 0 & , \text{ if not all subscripts are different,} \\ -1 & , \text{ if } \{k, n, p\} \text{ is an odd permutation of } \{1, 2, 3\}, \end{cases} \quad (2.2)$$

which is the Levi-Civita tensor of rank 3. Using these definitions, the vector outer product and inner product become

$$\epsilon_{k,n,r} A_n B_r = \mathbf{A} \times \mathbf{B}, \quad (2.3)$$

and

$$A_n B_n = \mathbf{A} \cdot \mathbf{B}, \quad (2.4)$$

respectively.

2.1 Maxwell's equations

The electromagnetic field quantities in the previously defined coordinate frame are described by Maxwell's equations, which are given by

$$-\epsilon_{k,m,p} \partial_m H_p + J_k + \partial_t D_k = -J_k^{ext}, \quad (2.5)$$

$$\epsilon_{j,m,r} \partial_m E_r + \partial_t B_j = -K_j^{ext}, \quad (2.6)$$

or, in vector notation

$$-\nabla \times \mathbf{H} + \mathbf{J} + \partial_t \mathbf{D} = -\mathbf{J}^{ext}, \quad (2.7)$$

$$\nabla \times \mathbf{E} + \partial_t \mathbf{B} = -\mathbf{K}^{ext}. \quad (2.8)$$

The quantities in Eqs. (2.5) – (2.8) are

E_r, \mathbf{E}	=	electric field strength (V/m),
H_p, \mathbf{H}	=	magnetic field strength (A/m),
J_k, \mathbf{J}	=	volume density of electric current (A/m ²),
D_k, \mathbf{D}	=	electric flux density (C/m ²),
B_j, \mathbf{B}	=	magnetic flux density (T),
$J_k^{ext}, \mathbf{J}^{ext}$	=	volume source density of electric current (A/m ²),
$K_j^{ext}, \mathbf{K}^{ext}$	=	volume source density of magnetic current (V/m ²).

The relationship between the electric and magnetic field strengths $\{E_r, H_j\}$ and the quantities $\{J_k, D_k, B_j\}$ is given by the constitutive relations, which describe the influence of the electromagnetic properties of the media that are present. In this thesis we will restrict ourselves to linear, isotropic, locally and instantaneously reacting and time-invariant media, which leads to

$$J_k(\mathbf{x}, t) = \sigma(\mathbf{x}) E_k(\mathbf{x}, t), \quad (2.9)$$

$$D_k(\mathbf{x}, t) = \epsilon(\mathbf{x}) E_k(\mathbf{x}, t), \quad (2.10)$$

$$B_j(\mathbf{x}, t) = \mu(\mathbf{x}) H_j(\mathbf{x}, t), \quad (2.11)$$

where

$$\sigma(\mathbf{x}) = \text{conductivity (S/m),}$$

$$\epsilon(\mathbf{x}) = \text{permittivity (F/m),}$$

$$\mu(\mathbf{x}) = \text{permeability (H/m).}$$

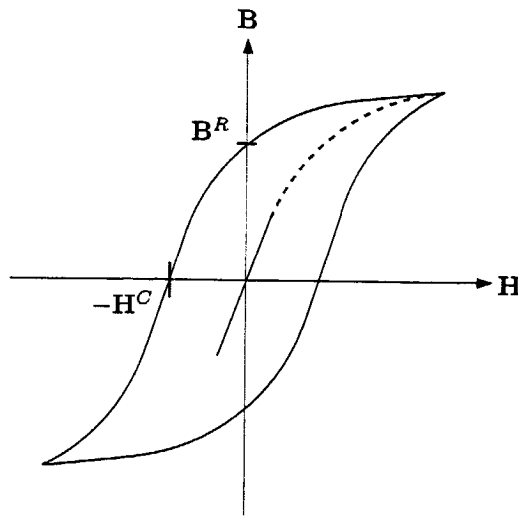


Figure 2.1: Hysteresis curve.

Note that we use both vector and subscript notation throughout this thesis. This is done because it is easier to implement formulae in computer code when written in subscript notation. However, since subscript notation is not as widespread as vector notation, we will also use vector notation.

2.2 Magnetic hysteresis losses

The relative permeability of an object determines to which extent the object can be magnetized. At microscopic level, the medium can be viewed as a set of domains, in each of which the magnetic moments of the atoms are aligned. At macroscopic level and in the magnetized state, the magnetic moments of the domains are randomly aligned and the resulting net magnetization is zero. When an external magnetic field is applied, the magnetic moments of the domains will be aligned and the material will be magnetized.

Generally, the magnetic flux density depends nonlinearly on the applied magnetic field, as can be seen in Figure 2.1. Starting from the demagnetized state and for small values of the magnetic field strength, the magnetic flux density depends approximately linearly on the magnetic field strength. However, at high magnetic field strengths the relation becomes strongly nonlinear. This corresponds to the situation that at high magnetic field strengths no more domains can be aligned, and therefore the slope of the curve in Figure 2.1 will become μ_0 for field strengths higher

than the saturation field strength \mathbf{H}^S . For field strengths much smaller than \mathbf{H}^S , the slope of the B-H curve is approximately $\mu_r\mu_0$.

The hysteresis curve is not a single-valued function, as can be seen in Figure 2.1. This is because when the applied magnetic field \mathbf{H} is $\mathbf{0}$, the object can have a remanent flux density \mathbf{B}^R , or in other words, the object is still magnetized even though there is no external magnetic field. In order to totally demagnetize the object, a coercive magnetic field \mathbf{H}^C is needed. When an object is alternatively magnetized and demagnetized, losses occur and these hysteresis losses are given by the area spanned by the B-H curve in Figure 2.1. In this thesis, we will assume that the fields that we encounter are of such a magnitude that we can take a linear relation between the magnetic flux density and the magnetic field strength, i.e., magnetic hysteresis losses are not taken into account.

2.3 Boundary conditions

Across an interface where one or more medium properties show a jump discontinuity the electromagnetic field quantities may exhibit discontinuous behavior. Therefore, Maxwell's equations have to be supplemented by boundary conditions at the interface. Let \mathcal{S} denote an interface between domains \mathcal{D}_1 and \mathcal{D}_2 . The interface \mathcal{S} is assumed to have a unique tangent plane everywhere. Next, let ν_m denote the unit vector oriented along the normal to \mathcal{S} such that upon traversing \mathcal{S} in the direction of ν_m , we pass from domain \mathcal{D}_1 to domain \mathcal{D}_2 (see Figure 2.2). We require the tangential components of $\{E_r, H_p\}$ to be continuous, which leads to the following boundary conditions for a source free interface

$$\epsilon_{j,m,r}\nu_m E_r \quad \text{is continuous across } \mathcal{S}, \quad (2.12)$$

$$\epsilon_{k,m,p}\nu_m H_p \quad \text{is continuous across } \mathcal{S}. \quad (2.13)$$

2.4 Frequency domain equations

We employ a Fourier transformation with respect to time, given by

$$\hat{f}(\mathbf{x}, \omega) = \int_{t \in \mathbf{R}} \exp(i\omega t) f(\mathbf{x}, t) dt. \quad (2.14)$$

The inverse transformation is defined as

$$f(\mathbf{x}, t) = \frac{1}{2\pi} \int_{\omega \in \mathbf{R}} \exp(-i\omega t) \hat{f}(\mathbf{x}, \omega) d\omega. \quad (2.15)$$

Here, we have assumed excitations sinusoidally varying with a time factor $\exp(-i\omega t)$. Applying the rule that ∂_t transforms to $-i\omega$, we obtain the following expressions for

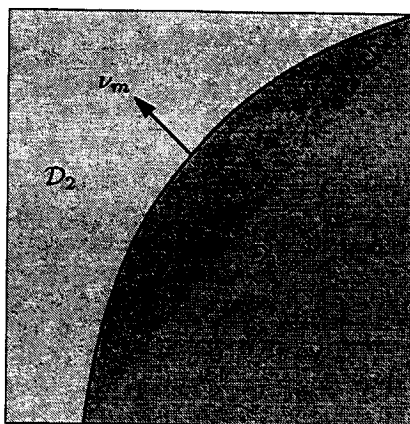


Figure 2.2: Interface S between two domains D_1 and D_2 with different electromagnetic properties.

Maxwell's equations in the frequency domain

$$-\epsilon_{k,m,p} \partial_m \hat{H}_p + (\sigma - i\omega\epsilon) \hat{E}_k = -\hat{j}_k^{ext}, \quad (2.16)$$

$$\epsilon_{j,m,r} \partial_m \hat{E}_r - i\omega\mu \hat{H}_j = -\hat{K}_j^{ext}, \quad (2.17)$$

or, in vector notation

$$-\nabla \times \hat{\mathbf{H}} + (\sigma - i\omega\epsilon) \hat{\mathbf{E}} = -\hat{\mathbf{j}}^{ext}, \quad (2.18)$$

$$\nabla \times \hat{\mathbf{E}} - i\omega\mu \hat{\mathbf{H}} = -\hat{\mathbf{K}}^{ext}. \quad (2.19)$$

2.5 Spatial Fourier transformation

In Chapter 4 we will consider stratified configurations, where the interfaces between the layers are oriented in the i_1 - and i_2 -directions. Therefore we introduce a two-dimensional spatial Fourier transformation to take advantage of the invariance of this configuration in the i_1 - and i_2 -directions. The spatial Fourier transformation acting on a frequency domain quantity $\hat{\mathbf{f}}(\mathbf{x}, \omega)$ is given by

$$\tilde{\mathbf{f}}(k_\nu, x_3, \omega) = \int_{x_1 \in \mathbf{R}} \int_{x_2 \in \mathbf{R}} \exp(jk_\nu x_\nu) \hat{\mathbf{f}}(\mathbf{x}, \omega) dx_2 dx_1, \quad (2.20)$$

where it is understood that Greek subscripts run through $\{1, 2\}$ only. The inverse spatial Fourier transformation is defined as

$$\hat{f}(\mathbf{x}, \omega) = \left(\frac{1}{2\pi}\right)^2 \int_{k_1 \in \mathbb{R}} \int_{k_2 \in \mathbb{R}} \exp(-jk_\nu x_\nu) \tilde{f}(k_\nu, x_3, \omega) dk_2 dk_1. \quad (2.21)$$

The application of this transformation to Maxwell's equations is given in Appendix B. We will also consider a configuration of a loop source above a layered configuration that is symmetric with respect to the axis of the loop. In that case it is advantageous to use cylindrical coordinates, given by

$$x_1 = r \cos(\phi), \quad (2.22)$$

$$x_2 = r \sin(\phi), \quad (2.23)$$

$$x_3 = x_3. \quad (2.24)$$

Using this coordinate transformation and the symmetry properties of the configuration, we end up with a two-dimensional problem. To take advantage of the invariance in the r -direction, we introduce the one-dimensional spatial Fourier transformation in cylindrical coordinates (also known as the Hankel transformation) as

$$\tilde{f}(k_r, x_3, \omega) = \int_{r=0}^{\infty} f(r, x_3, \omega) J_1(k_r r) r dr, \quad (2.25)$$

while the inverse Hankel transformation is given by

$$\hat{f}(r, x_3, \omega) = \int_{k_r=0}^{\infty} \tilde{f}(k_r, x_3, \omega) J_1(k_r r) k_r dk_r, \quad (2.26)$$

where J_1 is the Bessel function of the first kind and order one and k_r is the Hankel transform parameter. The application of this transformation to Maxwell's equations is given in Section 4.2 Appendix A.

2.6 The frequency domain reciprocity theorem

The Lorenz reciprocity theorem interrelates in a specific manner the field quantities of two non-identical physical states that can occur in one and the same time-invariant, bounded domain. We will use this theorem to derive the integral relations for the field quantities in the forward problem. The domain is denoted by \mathcal{D} with an enclosing surface $\partial\mathcal{D}$. The unit vector along the normal to $\partial\mathcal{D}$ is denoted by ν_m (or ν in vector notation), and is pointing outward from \mathcal{D} . We will distinguish between the two states that can occur by using the superscripts A and B. Neither the media nor the sources present in the two states need be the same (Figure 2.3). Let state A be characterized by the following field quantities, constitutive parameters and

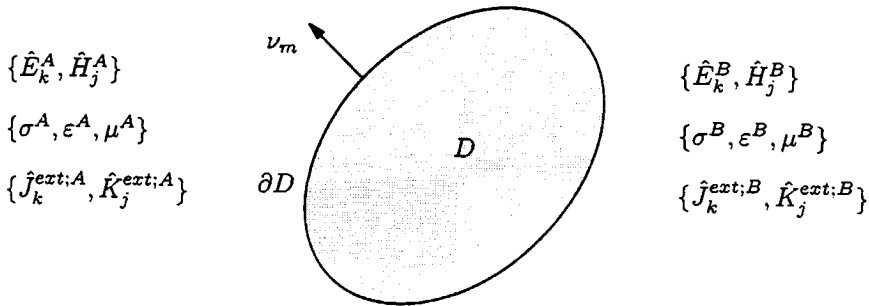


Figure 2.3: Configuration for the application of the reciprocity theorem.

volume source quantities

$$\{\hat{E}_k, \hat{H}_j\}(\mathbf{x}, \omega) = \{\hat{E}_k^A, \hat{H}_j^A\}(\mathbf{x}, \omega), \quad (2.27)$$

$$\{\sigma, \varepsilon, \mu\}(\mathbf{x}) = \{\sigma^A, \varepsilon^A, \mu^A\}(\mathbf{x}), \quad (2.28)$$

$$\{\hat{j}_k^{ext}, \hat{K}_j^{ext}\}(\mathbf{x}, \omega) = \{\hat{j}_k^{ext;A}, \hat{K}_j^{ext;A}\}(\mathbf{x}, \omega). \quad (2.29)$$

Maxwell's equations relevant to state A are then given by

$$-\varepsilon_{k,m,p} \partial_m \hat{H}_p^A + (\sigma^A - i\omega \varepsilon^A) \hat{E}_k^A = -\hat{j}_k^{ext;A}, \quad (2.30)$$

$$\varepsilon_{j,m,r} \partial_m \hat{E}_r^A - i\omega \mu^A \hat{H}_j^A = -\hat{K}_j^{ext;A}, \quad (2.31)$$

Similarly, state B is characterized by the field quantities, constitutive parameters and volume source quantities that are defined as

$$\{\hat{E}_k, \hat{H}_j\}(\mathbf{x}, \omega) = \{\hat{E}_k^B, \hat{H}_j^B\}(\mathbf{x}, \omega), \quad (2.32)$$

$$\{\sigma, \varepsilon, \mu\}(\mathbf{x}) = \{\sigma^B, \varepsilon^B, \mu^B\}(\mathbf{x}), \quad (2.33)$$

$$\{\hat{j}_k^{ext}, \hat{K}_j^{ext}\}(\mathbf{x}, \omega) = \{\hat{j}_k^{ext;B}, \hat{K}_j^{ext;B}\}(\mathbf{x}, \omega). \quad (2.34)$$

Then, Maxwell's equations relevant to state B are given by

$$-\varepsilon_{k,m,p} \partial_m \hat{H}_p^B + (\sigma^B - i\omega \varepsilon^B) \hat{E}_k^B = -\hat{j}_k^{ext;B}, \quad (2.35)$$

$$\varepsilon_{j,m,r} \partial_m \hat{E}_r^B - i\omega \mu^B \hat{H}_j^B = -\hat{K}_j^{ext;B}, \quad (2.36)$$

The fundamental interaction quantity between the two states is $\epsilon_{m,k,j} \partial_m (\hat{E}_k^A \hat{H}_j^B - \hat{E}_k^B \hat{H}_j^A)$, or $\nabla \cdot (\hat{\mathbf{E}}^A \times \hat{\mathbf{H}}^B - \hat{\mathbf{E}}^B \times \hat{\mathbf{H}}^A)$ in vector notation, which can be rewritten as

$$\begin{aligned} \epsilon_{m,k,j} \partial_m (\hat{E}_k^A \hat{H}_j^B - \hat{E}_k^B \hat{H}_j^A) = & \quad (2.37) \\ & -i\omega(\mu^A - \mu^B) \hat{H}_j^B \hat{H}_j^A + i\omega(\epsilon^A - \epsilon^B) \hat{E}_k^B \hat{E}_k^A - (\sigma^A - \sigma^B) \hat{E}_k^B \hat{E}_k^A \\ & + \hat{E}_k^A \hat{j}_k^{ext;B} - \hat{E}_k^B \hat{j}_k^{ext;A} - \hat{H}_j^A \hat{K}_j^{ext;B} + \hat{H}_j^B \hat{K}_j^{ext;A}, \end{aligned}$$

which is the local form of the Lorenz reciprocity theorem. The global form of the reciprocity theorem is obtained by integrating Eq. (2.37) over the domain \mathcal{D} and applying Gauss' theorem, which results in

$$\begin{aligned} \int_{\mathbf{x} \in \partial \mathcal{D}} \epsilon_{m,k,j} (\hat{E}_k^A \hat{H}_j^B - \hat{E}_k^B \hat{H}_j^A) dA_m = & \quad (2.38) \\ \int_{\mathbf{x} \in \mathcal{D}} \left[-i\omega(\mu^A - \mu^B) \hat{H}_j^B \hat{H}_j^A + i\omega(\epsilon^A - \epsilon^B) \hat{E}_k^B \hat{E}_k^A - (\sigma^A - \sigma^B) \hat{E}_k^B \hat{E}_k^A \right] dV \\ + \int_{\mathbf{x} \in \mathcal{D}} \left[\hat{E}_k^A \hat{j}_k^{ext;B} - \hat{E}_k^B \hat{j}_k^{ext;A} - \hat{H}_j^A \hat{K}_j^{ext;B} + \hat{H}_j^B \hat{K}_j^{ext;A} \right] dV, \end{aligned}$$

or, in vector notation

$$\begin{aligned} \int_{\mathbf{x} \in \partial \mathcal{D}} \boldsymbol{\nu} \cdot (\hat{\mathbf{E}}^A \times \hat{\mathbf{H}}^B - \hat{\mathbf{E}}^B \times \hat{\mathbf{H}}^A) dA = & \quad (2.39) \\ \int_{\mathbf{x} \in \mathcal{D}} \left[-i\omega(\mu^A - \mu^B) \hat{\mathbf{H}}^B \cdot \hat{\mathbf{H}}^A + (i\omega(\epsilon^A - \epsilon^B) - (\sigma^A - \sigma^B)) \hat{\mathbf{E}}^B \cdot \hat{\mathbf{E}}^A \right. \\ \left. + \int_{\mathbf{x} \in \mathcal{D}} \left[\hat{\mathbf{E}}^A \cdot \hat{\mathbf{j}}^{ext;B} - \hat{\mathbf{E}}^B \cdot \hat{\mathbf{j}}^{ext;A} - \hat{\mathbf{H}}^A \cdot \hat{\mathbf{K}}^{ext;B} + \hat{\mathbf{H}}^B \cdot \hat{\mathbf{K}}^{ext;A} \right] dV. \right. \end{aligned}$$

When the medium parameters in states A and B are chosen to be identical, the first three terms on the right-hand side of Eq. (2.37) and the first integrals on the right-hand sides of Eqs. (2.38) and (2.39) vanish. Under these conditions, the interaction between the two states is solely related to the source distributions in each state.

Chapter 3

The PEC tool and the measurement setup

The Pulsed Eddy Current (PEC) tool will be described in this chapter, as well as the effect of various medium and configuration parameters on the received signals. An intuitive description of the operation of the PEC tool is given, which serves to help to understand the behavior of the electromagnetic fields in the test object (i.e., the metal layer). We start by giving a description of the tool and the measurement setup, with some examples of applications from actual field use. Next, we will give an intuitive circuit-based model for the electromagnetic fields and received signals, followed by an overview of the effect of the medium and configuration parameters on the signals.

3.1 PEC tool

Shell Global Solutions have developed a man-portable inspection tool based on the PEC technique. The PEC tool consists of two elements (see Figure 3.1) :

- The probe, which contains the transmitting and receiving coils.
- The data processing unit, which contains an on-board computer and memory for data processing and storage.

The tool is designed to be used by a single operator who carries the data processing unit (DPU) on a carrying-band. The probe containing the transmitting and receiving coils is hand-held. When the unit is triggered, the data processing unit gives an immediate reading of the wall thickness, while the data is stored in the onboard

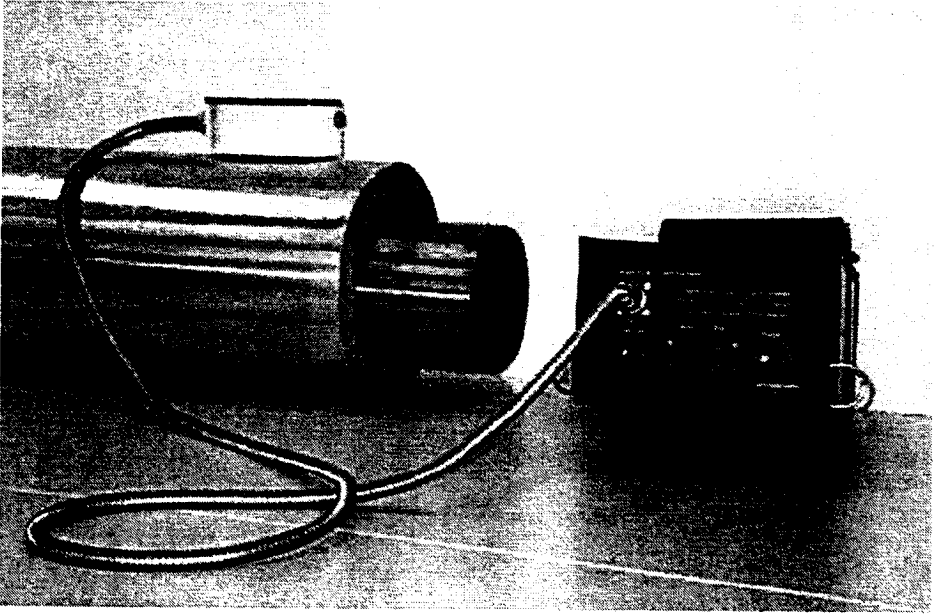


Figure 3.1: The Pulsed Eddy Current tool.

memory for off-line processing. For this purpose, the DPU has a serial interface by which the data can be transferred to a PC. The general measurement configuration is given in Figure 3.2, with on the left-hand side the actual configuration and on the right-hand side the model configuration. The model configuration will be further elaborated in Chapter 4 and is given here to show the relation to the actual physical configuration with curved pipe walls (see also Figure 1.2). The numbers in Figure 3.2 denote the following

1. Transmitting coil.
2. Receiving coil.
3. Weather jacket (Usually aluminum).
4. Thermal insulation (e.g., rockwool).
5. Metal layer or object under test (Pipe wall, vessel, etc).

The lift-off of the probe from the object under test is the distance between the coil system in the probe and the metal layer. The insulation layer is usually rockwool or a similar material, which has the electromagnetic properties of air. The weather jacket, however, which is the aluminium layer that protects the insulation, has a very distinct effect on the PEC signal, but only at the start of the signal (the first 1 to 5 ms). In this thesis we will confine ourselves to a configuration where only a

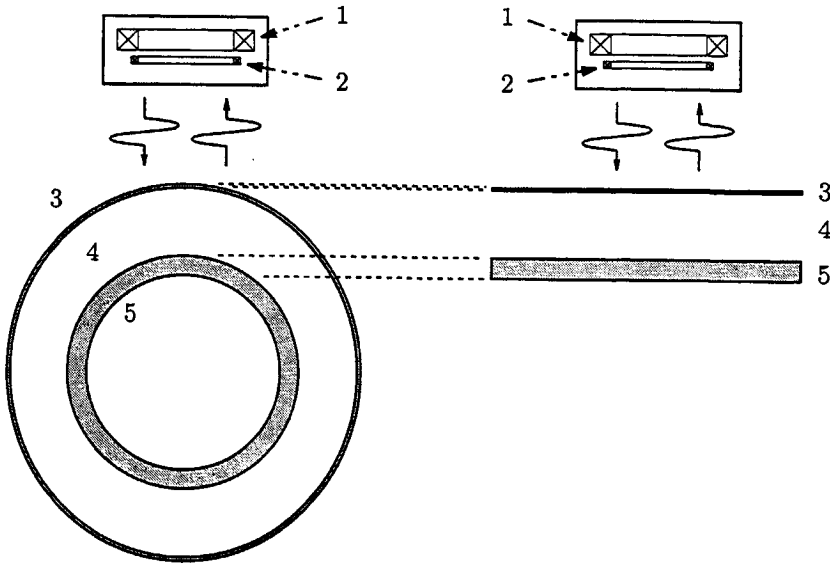


Figure 3.2: Measurement configuration and planar approximation, with transmitting coil (1), receiving coil (2), weather jacket (3), insulation (4) and pipe wall (5).

single metal layer is present (no weather jacket), since we are primarily interested in the effects of a defect in the metal layer and the influence of the medium parameters and thickness of that layer.

3.1.1 Operating principles of the PEC tool

The tool derives its name, Pulsed Eddy Current tool, from its operating principles. First, a block-pulse current is generated in the transmitting coil. After some time, the initial switch-on effects of the block pulse current are no longer present and the field generated by the transmitting coil can then be considered to be a quasi-static magnetic field. When the switch-off part of the block pulse current occurs, eddy currents are again induced in the test object. These eddy currents generate a secondary electromagnetic field (the quasi-static magnetic field generated by the transmitting coils being the primary field). This secondary field induces a time-varying voltage on the terminals of the receiving coils, and this signal contains information on medium parameters and wall thickness. As the term 'Pulsed' in the name of the tool implies, the information is extracted from a time domain signal.

Separate transmitting and receiving coils are necessary because there are different requirements for each type of coil : the transmitting coils must be able to handle a large current capable of generating a strong static magnetic field, while the receiving coils must have a large number of windings to be able to pick up the weak secondary field generated by the eddy currents. Furthermore, the receiving coils must ideally be as small as the footprint of the eddy currents in the layer to maximize sensitivity.

The use of the tool in NDT lies in the fact that information on the thickness of the object under test (often pipes, vessels or metal plating) is present in the measured signal. Decreasing wall thickness can be evidence of corrosion or erosion, but can also be caused by varying medium parameters and/or configuration parameters. In the following sections we will discuss the effect of these parameters on the measured signal, keeping in mind that the wall thickness is the parameter of interest.

3.1.2 The probe

The probe section of the tool houses the transmitting and receiving coils. It consists of a plastic housing in which the coils are located. There are two transmitting coils side by side with the current in each of the coils flowing in opposite direction. This has the effect that at the location where the two coils touch, the current density, and hence the field, is approximately twice as high as would have been the case had there only been a single transmitting coil. Consequently, this results in a focussing effect and a higher amplitude of the electromagnetic fields (and thus the eddy currents) induced in the test object (see Section 5.1). A schematic drawing of the probe configuration is given in Figure 3.3. The pair of receiving coils is located just under the transmitting coils, symmetrically around the point where the transmitting coils touch. Two receiving coils are used for greater sensitivity and higher received voltage.

The signals picked up by the receiver coils are sent along a cable to the data processing unit. This cable also houses the power feed for the transmitting coils. Different probes with varying transmitting coil radii have been produced for various applications. For example, for measuring wall thickness at large lift-off, the radius of the transmitting coil should be increased to maintain depth resolution, while for taking precise measurements at low lift-off one should use a probe with small-radius transmitting coils. For use underwater the coils are embedded in plastic in order to be able to withstand the water pressure.

Research has been done on the shape of the transmitting coil to maximize the focussing effect (see Morsink [55]). It was found that the configuration with two circular transmitting coils was the best compromise between focussing capability and ease of manufacture, therefore this type of coil has been used throughout the project.

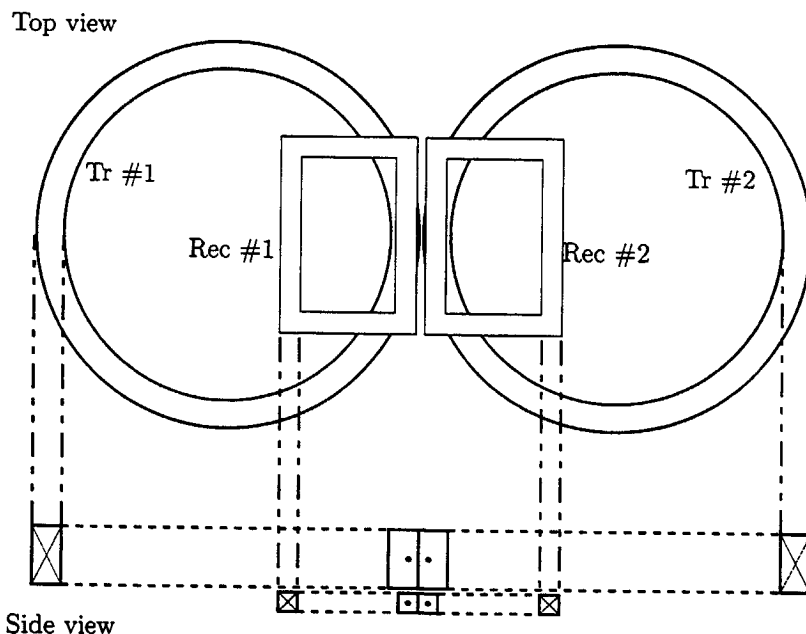


Figure 3.3: Schematic PEC probe layout with two transmitting coils and two receiving coils.

3.1.3 Data processing unit

The data processing unit (DPU) processes and stores the signals, giving an indication of the wall thickness to the operator. The unit is small enough to be carried on a shoulder strap, enabling the operator to move around freely. Schematically, the DPU consists of the following subunits (see Figure 3.4)

1. Signal amplifier, amplifies the received signal.
2. Processing unit (CPU), performs the wall thickness calculation and controls the operation of the tool.
3. Memory, a removable flash memory card on which the measurements can be stored.
4. Display/control section, user interface to display wall thickness and control the tool.
5. Serial interface which enables the data to be downloaded to a PC for further processing.
6. Battery pack.

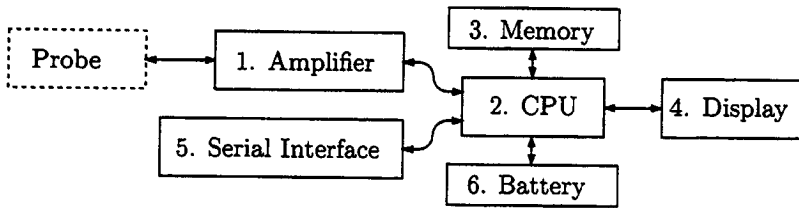


Figure 3.4: Schematic layout of the Data Processing Unit.

The operator controls the tool by means of buttons next to the display. In the field, the tool only gives a basic wall thickness reading, but the data can be stored and downloaded to a personal computer for more detailed analysis.

3.1.4 Operation of the tool

The operator carries the Data Processing Unit on a sling across his shoulder, while holding the probe in hand. The tool is then operated by placing the probe against the object under test and pressing the button on the probe which starts the measurement. The tool then takes a number of measurements, the results of which will be averaged to obtain a reliable result. The probe should not be moved during the time it takes for the measurement to be completed, since this would give an inaccurate reading of the wall thickness. The reason for this is that the electromagnetic diffusion of the eddy currents in the object takes a finite amount of time (between 10 and 150 ms, depending on the thickness of the metal), during which the receiver coils must not be moved. The measurement is more or less a volume measurement, the area of the 'footprint' or 'hot spot' of the eddy current distribution and the size and location of the receiving coils determine the size of the volume where the wall thickness is measured. Depending on the orientation of the probe, crack defects much smaller than the footprint can be detected. Note that this footprint depends on the lift-off of the probe above the test object.

The tool has been used for a number of applications within the oil industry, including corrosion detection in pipelines and vessels, corrosion monitoring and underwater inspection of risers. It has been used to measure the wall thickness of high-temperature vessels, something that cannot easily be done using ultrasonic techniques because the contact paste necessary for ultrasonic measurements is not capable of withstanding these high temperatures. Since the PEC technique is a non-contact measurement this does not pose a problem. Because of the small size of the tool it can be used in locations where space and weight are at a premium (see Figure 3.5a).

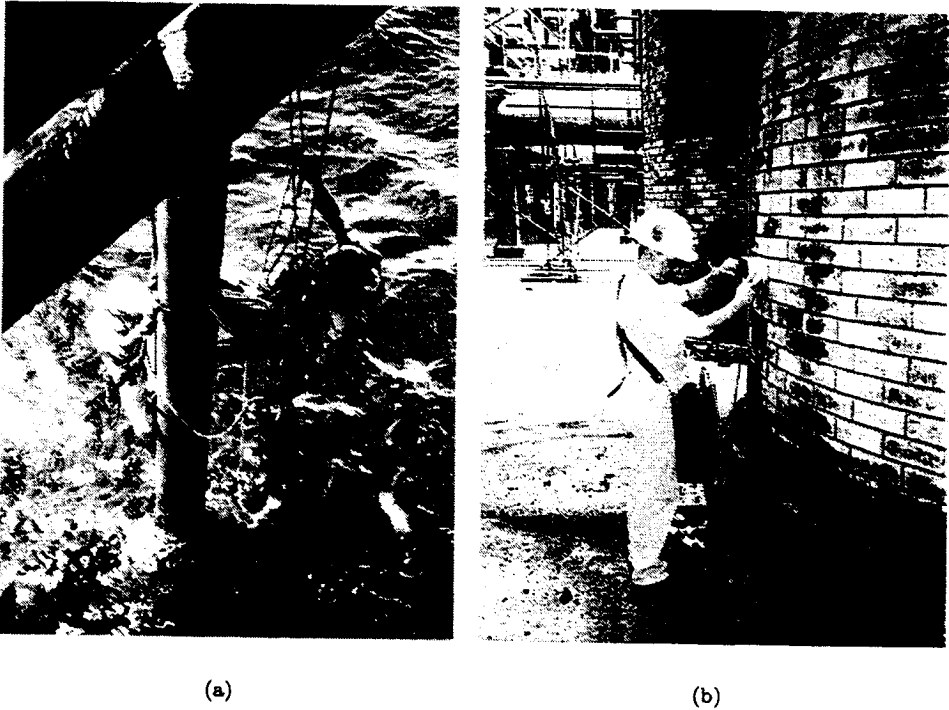


Figure 3.5: PEC inspection of a high-pressure gas riser on an offshore platform in Brunei (a) and a column skirt at an LNG plant in Malaysia (b)

Special fixtures have been made to keep the probe at a constant lift-off to ensure good repeatability and to ease operation. A version has been produced for use with remotely operated underwater vehicles for inspection of offshore-platform legs and underwater pipelines. For this application the DPU was located in a pressure vessel, while the probe was modified to withstand the water pressure. The measured data was stored in the DPU and was processed when the tool returned from its underwater journey.

3.2 PEC signals

This section covers the PEC measurement signals. The secondary electromagnetic field generated by the eddy currents in the metal gives rise to a time-varying voltage on the receiver coils. This signal is recorded by the data processing unit and can then be transferred to a PC for detailed analysis. The effects of the diffusion of the

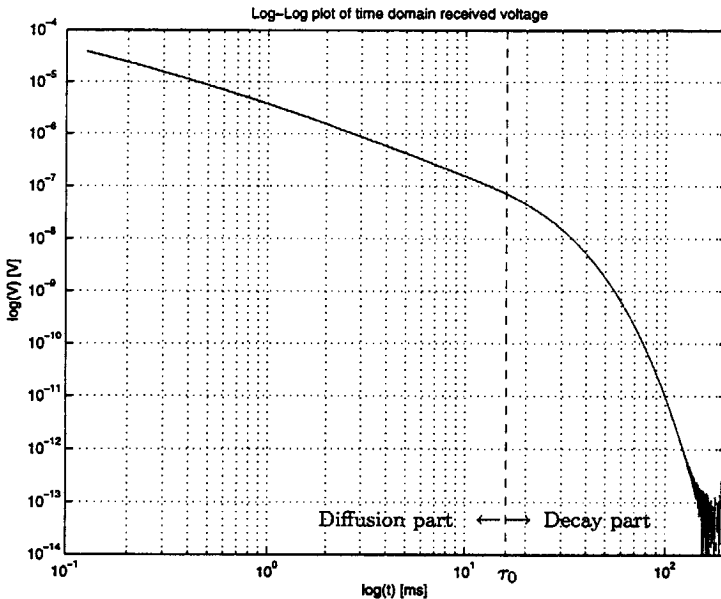


Figure 3.6: Generic PEC signal corresponding to the reference parameters in Table 3.1.

electromagnetic field within the layer can be seen best when the signal is plotted in a log-log plot, as is done for a generic PEC signal in Figure 3.6. We can discern two distinct parts in the signal. The first part until $t = \tau_0 \approx 16$ ms, where the curve is approximately straight (in the log-log plot), is the diffusive part. For times larger than 16 ms the signal exhibits exponential decay. These two parts of the signal correspond to different behavior of the electromagnetic fields in the layer :

Diffusion part: There is electromagnetic diffusion of the fields within the layer, the amplitude of the signal is proportional to t^{-n} , where $n \approx 1.5$.

Decay part: The electromagnetic diffusion of the fields has stopped, the signal only exhibits an exponential amplitude decay.

The point in time where the two parts of the signal meet is denoted τ_0 ($\tau_0 \approx 16$ ms for the reference signal shown in Figure 3.6). This parameter varies as function of the wall thickness of the metal layer: for thick layers τ_0 has a higher value than for thin layers. In the data analysis, the parameter τ_0 is extracted from the measured data and compared to the value of $\tau_{0,ref}$ of a reference measurement. It is then possible to determine the thickness of the layer with respect to the thickness at the

reference point. Note that it is not possible to make an absolute measurement of the wall thickness using the PEC tool. The presence of corrosion means that some metal is converted into rust, resulting in a thinner metal layer and consequently a change in the parameter τ_0 . However, other configuration parameters, such as lift-off and medium parameters of the metal, also have an influence on τ_0 . Therefore we will now discuss the influence of various configuration parameters on the PEC signals, with respect to a reference configuration.

3.2.1 Effects of medium and configuration parameters

In this section, we will discuss the influence of medium and configuration parameters (such as wall thickness and lift-off) on the PEC signals. From the plot of the generic PEC signal in Figure 3.6, we can distinguish the three basic parameters that describe the PEC signal

τ_0 - Time at which the diffusion phase ends.

n - Slope of the PEC signal (in log-log scale) during the diffusion phase.

A - Initial amplitude of the signal.

The decay rate of the signal for $t > \tau_0$ is not taken into account, since this information is difficult to extract from the data due to noise and the very low amplitude of the signal for these values of t . In the following sections we will discuss the influence of each of the configuration parameters on these signal parameters. In order to investigate the influence of a certain parameter on the PEC signal, we will take a reference configuration and change one parameter while holding the others constant. This enables us to isolate the effect that the variation of the parameter under investigation has on the signal. In doing so, we assume that the parameters are mutually independent and that the effects of the different parameters can be linearly added. The reference configuration is specified in Table 3.1. The plots of the received voltage as function of time in the following sections are obtained by the 2D forward model described in Section 4.2.

3.2.2 Influence of test wall parameters on the PEC signal

In this section we will discuss the influence of the test wall parameters (thickness, permeability and conductivity) on the PEC signal. Note that throughout this thesis we take the permittivity equal to that of free space, i.e., $\epsilon = \epsilon_0$. While discussing the influence of the medium parameters on the PEC signals, we refer to a lumped circuit model, which is described in the next section.

Table 3.1: Configuration parameters, with the corresponding values for the reference configuration.

<i>Test wall parameters</i>		
Wall thickness (d_{wall})	10	[mm]
Permeability (μ_{wall})	$200\mu_0$	[H/m]
Conductivity (σ_{wall})	$6.7e6$	[S/m]
<i>Probe parameters</i>		
Coil radius (r_{tr})	25	[mm]
Lift-off (l)	50	[mm]

Influence of wall thickness on the PEC signal

We consider a reference configuration where no weather jacket (cladding) is present and vary the wall thickness d_{wall} between 2 mm and 20 mm, in steps of 2 mm, which gives the signals plotted in Figure 3.7. We can see from Figure 3.7 that an increase in wall thickness causes an increase in τ_0 , while the slope n and the initial amplitude A stay the same. Furthermore, we observe from Figure 3.8 that the relation between the wall thickness and τ_0 is quadratic, i.e., $\tau_0 \sim d_{wall}^2$. This means that information about the thickness of the test wall can be directly obtained from the parameter τ_0 .

Influence of permeability on the PEC signal

Keeping the rest of the parameters again at their reference values, we now vary the relative permeability of the test wall over the range $\mu_r \in \{1, 50, 100, 150, 200, 250, 300\}$. The effect of this variation on the PEC signal is given in Figure 3.9. Variation of the relative permeability of the test wall has the following effects

- An increase in the parameter τ_0 , which indicates that the electromagnetic diffusion process takes longer. The parameter τ_0 varies linearly as function of the relative permeability. In terms of the lumped circuit model presented in the next section, an increase in the relative permeability of the test wall has the effect that the coupling between adjacent current filaments in the lumped circuit model are stronger (see Section 3.3).
- A decrease in the initial amplitude of the signal when the relative permeability of the test wall increases. This is due to the fact that for higher relative permeability, the electromagnetic fields are more confined within the layer. In the frequency domain, this is readily apparent from the expressions for the reflection and transmission coefficients.

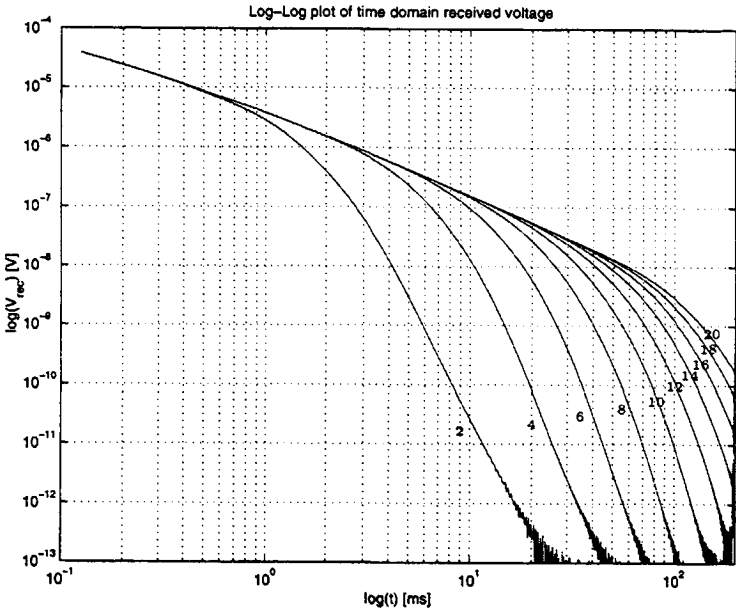


Figure 3.7: Influence of wall thickness variation on the PEC signal, wall thickness values are indicated in mm.

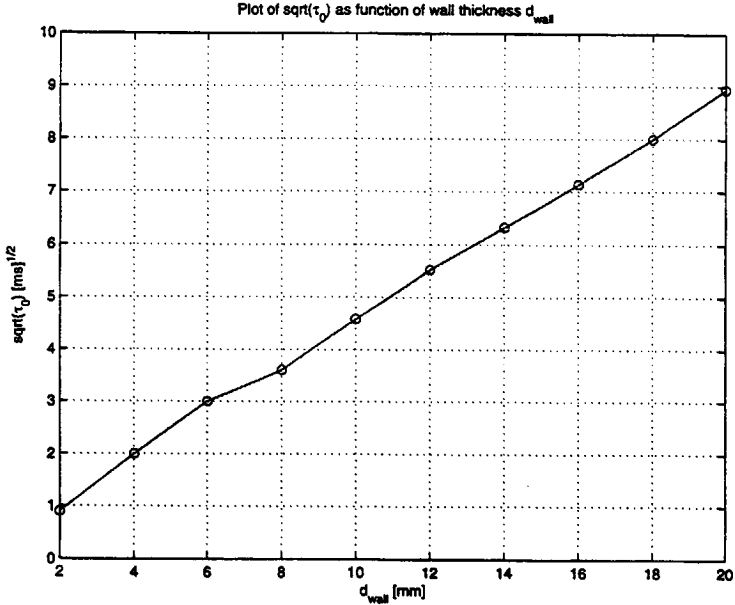


Figure 3.8: Relation between τ_0 and wall thickness d_{wall} .

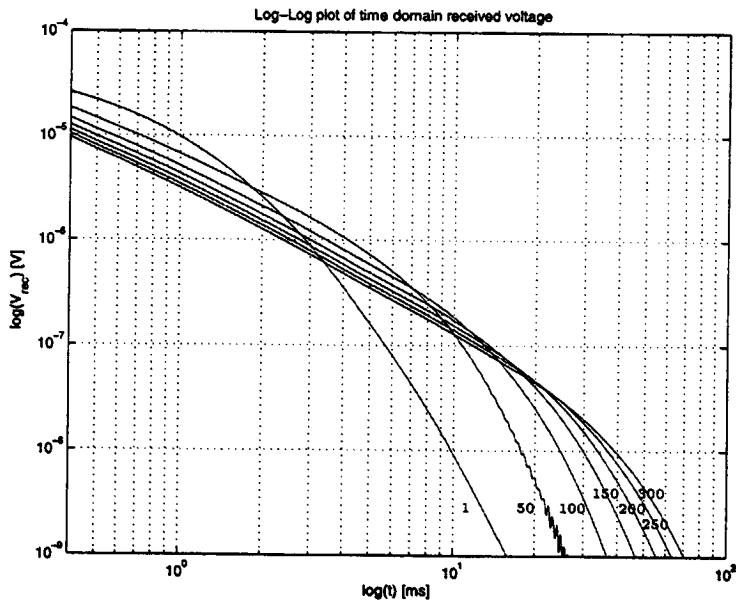


Figure 3.9: Influence of relative permeability variation on the PEC signal, values of μ_r as indicated.

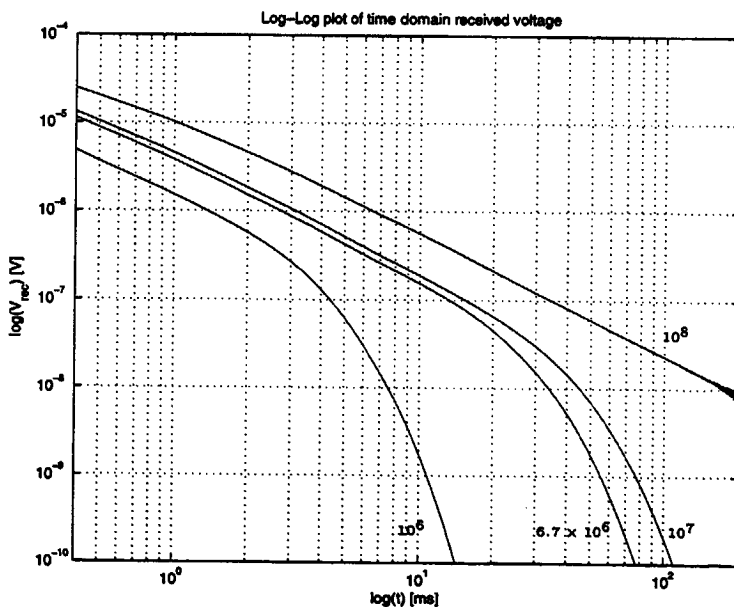


Figure 3.10: Influence of conductivity variations on the PEC signal, values of σ in S/m as indicated.

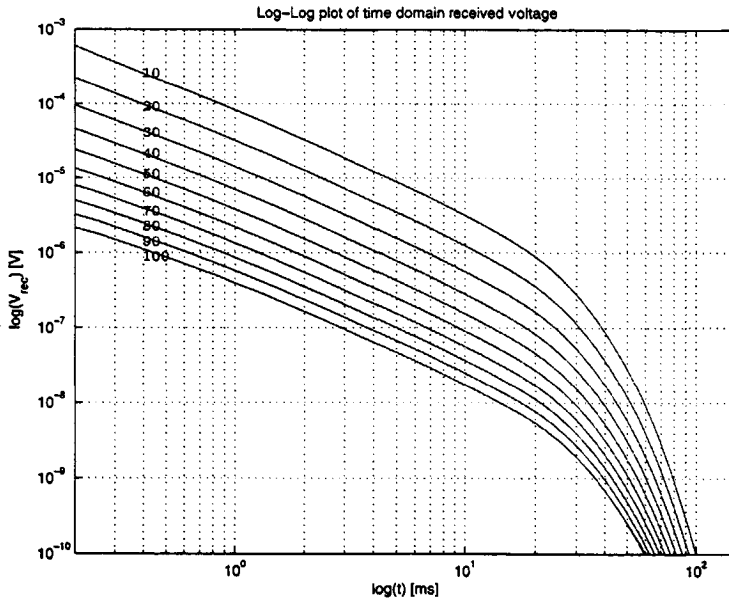


Figure 3.11: Influence of lift-off variation on the PEC signal, values of lift-off in mm as indicated.

Influence of conductivity on the PEC signal

Variation of the conductivity of the test wall over the range $\sigma \in \{10^6, 6.7 \times 10^6, 10^7, 10^8\}$ S/m gives the signals plotted in Figure 3.10. We can see that the effects are similar to the effects obtained by varying the relative permeability of the test wall, which gives the following influence of the conductivity variation

- As with the variation of the relative permeability, we see that the parameter τ_0 depends linearly on the conductivity of the test wall. In terms of the lumped circuit model (see Section 3.3), an increase in the conductivity of the test wall has the effect that the resistance of a current filament drops, which results in the maximum of the current distribution taking longer to reach the center of the layer.
- For increased conductivity of the test wall, the initial amplitude of the PEC signal increases as well, contrary to the effect seen for variation of the relative permeability.

3.2.3 Influence of probe parameters on the PEC signal

In Figure 3.11, we vary the lift-off of the probe above the test wall from $l = 10$ mm to $l = 100$ mm in steps of 10 mm. From the PEC signals, we see that the influence of the variation of the lift-off parameter has the following effects

- A slight decrease in the parameter τ_0 . This means that it is necessary to either measure the lift-off at each measurement point, or to keep the lift-off constant for all measurements.
- The initial amplitude of the PEC signal decreases for increasing lift-off because the distance between the transmitters/receivers (the probe) and the test wall increases.

3.3 Lumped circuit model

In this section, we will derive a simple model based on a single transmitting (primary) coil to give insight into the physical processes that take place in the layer during the diffusion and decay phases of the signal. To this end, we make the observation that the eddy currents induced in the metal layer approximately flow in coaxial paths, which can be considered as secondary current filaments. These current filaments constitute multiple (secondary) circuits, each with a self-inductance and a finite resistance (see Figure 3.12). Note that we assume all current filaments to have the same radius. Nabighian [56] showed that for the case of a half space the radius of the current filaments increases with depth. However, from the numerical results for the current distribution within a layer (see Section 5.1) we see that the radius of the current filaments can be taken constant. This discrepancy is probably due to the difference in configuration, since Nabighian considered a half-space problem with an air-earth interface having dimensions in the order of meters, while here we have a slab-configuration with significantly higher values for the medium parameters and dimensions in the order of centimeters.

To derive the lumped circuit model we consider the medium parameters of the (sourcefree) layer, which are given by $\sigma = 6.7 \times 10^6$ S/m, $\mu = 200\mu_0$ and $\varepsilon = \varepsilon_0$, while the thickness of the layer is assumed to be 10 mm. Given these values, we can calculate the characteristic times for the electroquasistatic, magnetoquasistatic and wave solutions to Maxwell's equations. These characteristic times are defined as $\tau_e = \varepsilon/\sigma$, $\tau_m = \mu\sigma l^2$ and $\tau_{em} = l\sqrt{\varepsilon\mu}$, respectively, where l is the characteristic dimension of the problem (in this case the layer thickness). Calculation of the characteristic times shows that $\tau_e \ll \tau_{em} \ll \tau_m$ and therefore we can use the magnetoquasistatic approximation, i.e., we can neglect the displacement currents. We now consider a single current filament as current path (Figure 3.13). Using the fact that

$$\nabla \cdot \mathbf{B} = 0, \quad (3.1)$$

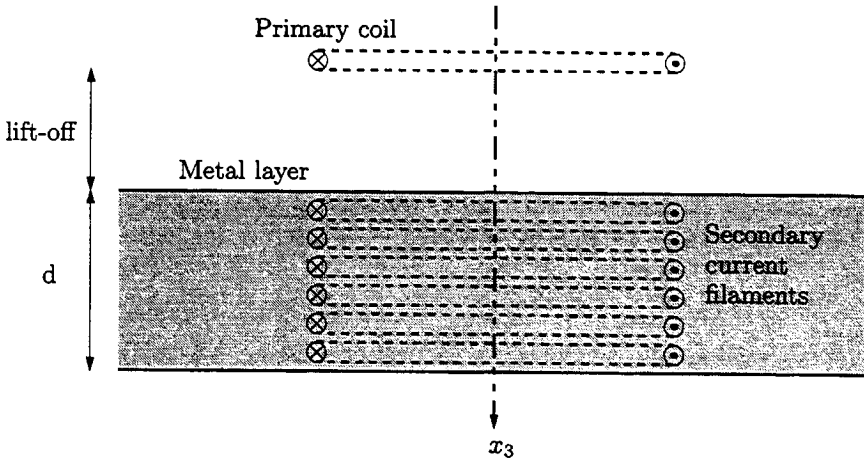


Figure 3.12: Secondary current filaments inside metal layer induced by primary coil located above layer.

where $\mathbf{B} = \mu\mathbf{H}$, we write \mathbf{B} in terms of the electric vector potential \mathbf{A} as

$$\mathbf{B} = \nabla \times \mathbf{A}. \quad (3.2)$$

Using Faraday's law, i.e., $\nabla \times \mathbf{E} + \mu\partial_t\mathbf{H} = 0$, we now write

$$\nabla \times (\mathbf{E} + \partial_t\mathbf{A}) = 0, \quad (3.3)$$

from which we can see that the electric field can be written in terms of a scalar electric potential Φ and an electric vector potential \mathbf{A} , resulting in

$$\mathbf{E} = -\nabla\Phi - \partial_t\mathbf{A}. \quad (3.4)$$

To obtain the Kirchoff voltage law for the current filament, we integrate Eq. (3.4) over the contour C in the current filament, which gives

$$\oint_C \mathbf{E} \cdot d\mathbf{l} = -\oint_C (\nabla\Phi) \cdot d\mathbf{l} - \partial_t \oint_C \mathbf{A} \cdot d\mathbf{l}, \quad (3.5)$$

The first integral on the right-hand side of Eq. (3.5) is zero by definition, while we can rewrite the other integrals as

$$\oint_C \mathbf{E} \cdot d\mathbf{l} = \frac{1}{\sigma} \oint_C \mathbf{J} \cdot d\mathbf{l} = RI, \quad (3.6)$$

and

$$\partial_t \oint_C \mathbf{A} \cdot d\mathbf{l} = \partial_t \iint_S \mathbf{B} \cdot d\mathbf{S} = \partial_t \psi_m, \quad (3.7)$$

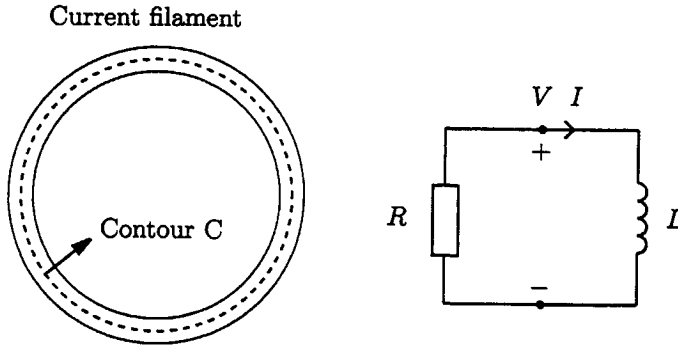


Figure 3.13: Current filament and corresponding lumped circuit model.

respectively. In Eq. (3.6), σ is the conductivity corresponding to the current filament, the quantity ψ_m in Eq. (3.7) is the magnetic flux, which can be written in terms of the self-inductance of the filament L and the current I as

$$\psi_m = LI. \quad (3.8)$$

Combining these equations, we obtain the lumped circuit expression for the current in the filament as

$$L\partial_t I + RI = 0. \quad (3.9)$$

Since the current flowing in filament i induces currents in all the other current filaments, we introduce a coefficient of mutual induction M_{ij} , and for N filaments with mutual induction we get the following expression for the current in filament j

$$R_j I_j + \partial_t \left(L_j I_j + \sum_{\substack{k=1 \\ k \neq j}}^N M_{jk} I_k \right) = 0, \quad j, k = 1, \dots, N \quad (3.10)$$

which can be written in matrix notation as

$$\mathbf{M}\partial_t \mathbf{I} + \mathbf{R}\mathbf{I} = 0, \quad (3.11)$$

where $\mathbf{R} = \text{diag}(R_1, \dots, R_N)$ and $\text{diag}(\mathbf{M}) = L_1, \dots, L_N$. The off-diagonal elements of \mathbf{M} are the coefficients of mutual induction. It can easily be seen that the matrix \mathbf{M} must be symmetric. The differential equation for the current vector \mathbf{I} is then

$$\partial_t \mathbf{I} = -(\mathbf{M}^{-1}\mathbf{R})\mathbf{I}. \quad (3.12)$$

This system of equations can be solved by taking a Laplace-transformation with respect to t , but we chosen to use a simple finite difference approximation. However, we must first find expressions for the resistance and inductance coefficients, which we will do in the next section. When we have found those expressions, it is instructive to take a look at the eigenvalues and eigenvectors of the system matrix $\mathbf{M}^{-1}\mathbf{R}$.

3.3.1 Expressions for the resistance and inductance coefficients

For the resistance of each current filament we take the following expression

$$R_j = \frac{\sigma^{-1}l_{ec}}{A_{ec}} = \frac{\sigma^{-1}2\pi r_{ec}}{w_{ec}h_{ec}}, \quad (3.13)$$

in which l_{ec} is the length of the path along which the eddy currents flow in the filaments, A_{ec} is the cross-sectional area of the eddy currents. This can be expressed in more convenient variables, where r_{ec} is the radius of the eddy current path, w_{ec} is the width (with a typical, numerically determined value of 6×10^{-3} m for the reference configuration given in Table 3.1) and h_{ec} is the height of the eddy current path. This is defined as

$$h_{ec} = \frac{d_{wall}}{N}, \quad (3.14)$$

where d_{wall} is the layer thickness and N is the number of filaments. The width w_{ec} is determined by means of numerical experiments. An approximate (empirical) expression for the radius of the eddy current path which takes into account the effect of transmitting coil lift-off is given by

$$r_{ec} = r_{tr} + \tan\left(\frac{\pi}{6}\right)l, \quad (3.15)$$

in which r_{tr} is the radius of the transmitting coil and l is the transmitting coil lift-off.

For the self-inductance of a current filament with circular cross-section in free space we can write (see Johnk [40])

$$L = L_{int} + L_{ext}, \quad (3.16)$$

where L_{int} is the internal self-inductance and L_{ext} is the external self-inductance. For the internal self-inductance, we have

$$L_{int} = \frac{\mu_0 r_{ec}}{4} l, \quad (3.17)$$

in which l is the length of the current filament. This expression represents the internal self-inductance for the DC case, however we will use it as an approximation in our configuration. For the external self-inductance we write

$$L_{ext} = \mu_0 \sqrt{r_{ec}\left(r_{ec} - \frac{w_{ec}}{2}\right)} \left[\left(\frac{2}{k} - k\right) K(k) - \frac{2}{k} E(k) \right], \quad (3.18)$$

where k is given by

$$k = \sqrt{\frac{4r_{ec}(r_{ec} - w_{ec}/2)}{(2r_{ec} - w_{ec}/2)^2}}, \quad (3.19)$$

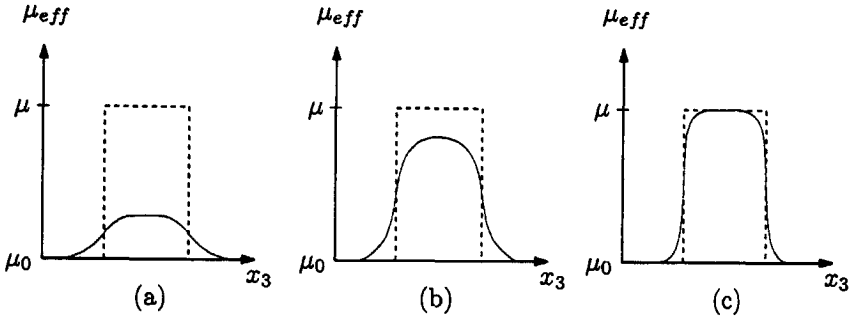


Figure 3.14: Effective permeability for the cases where a) $w/r_{ec} \ll 1$, b) $w/r_{ec} \approx 1$ and c) $w/r_{ec} \gg 1$.

and $K(k)$ and $E(k)$ are the complete elliptic integrals of the first and second kinds, respectively.

Since the filaments with index 1 and N are located near the edges of the layer, it would not be correct to use the permeability of the layer itself in Eq. (3.18). Instead, we should use some effective permeability, the distribution of which over the thickness of the layer is governed by the location of the filament and the thickness of the layer. We choose to use a parabolic distribution for the permeability, where the maximum and minima are a fraction of the normal permeability (see Figure 3.14). The dotted lines indicate the actual permeability of the test wall. The coupling between filaments i and j is modelled by means of a mutual induction coefficient

$$M_{ij} = k\sqrt{L_i L_j}. \quad (3.20)$$

The coefficient k is defined by the geometry of the filaments, and is given empirically by

$$k = \left(\frac{|z_i - z_j|w}{hr_{ec}} + 1 \right)^{-2}, \quad (3.21)$$

in which z_i and z_j are the coordinates of filaments i and j , respectively. We solve the system of differential equations for the currents in Eq. (3.11) numerically using a backward difference approximation, which is given by

$$\mathbf{I}[t + \Delta t] = -(\mathbf{M} + \Delta t \mathbf{R})^{-1} \mathbf{M} \mathbf{I}[t], \quad (3.22)$$

where Δt is the discrete time step.

3.3.2 Eigenvalues and eigenvectors of the system matrix

Given the expressions for the resistance and inductance coefficients, we can calculate the eigenvalues and eigenvectors of the system matrix for a certain set of values

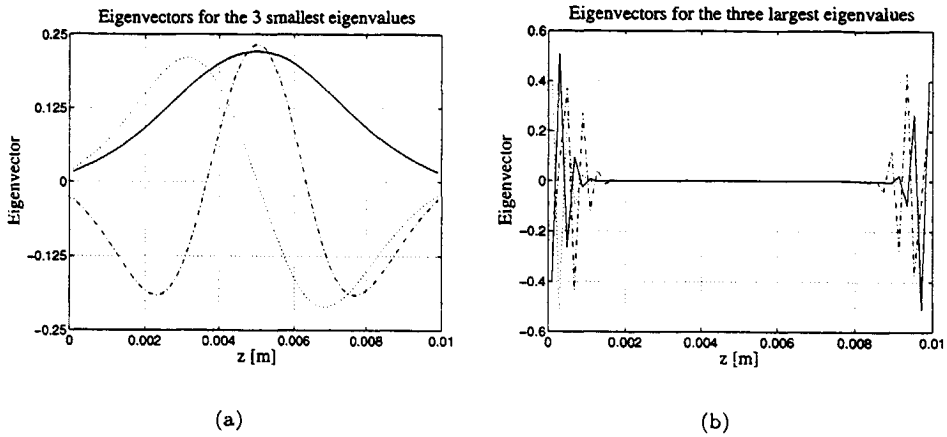


Figure 3.15: Eigenvectors corresponding to the three smallest (a) and the three largest (b) eigenvalues (in absolute sense) of the system matrix.

for the coefficients. The eigenvectors are the set of fundamental solutions to the differential equation for the current distribution in the layer. In Figure 3.15a we plot the eigenvectors corresponding to the three smallest (in absolute value) eigenvalues, in Figure 3.15b the eigenvectors corresponding to the three largest eigenvalues.

Since the system matrix is symmetric, the eigenvalues will be real-valued. If we write the solution to the system of first order differential equations for the current distribution in terms of time-dependent exponential functions, we see that the eigenvectors are the current distributions corresponding to an exponential function, the amplitude of which decreases rapidly or slowly in time depending on the magnitude of the corresponding eigenvalue. Consequently, we would expect that the current distribution corresponding to the eigenvalue with the smallest absolute value is the current distribution that is present in the layer for late times. For early times, the eigenvectors corresponding to large (in absolute value) eigenvalues dominate the current distribution. These eigenvectors have mostly zero amplitude at the center of the layer, but large amplitudes near the edges (see Figure 3.15b). However, since the absolute values of the corresponding eigenvalues are large, these modes decay much faster in time than the modes of which the eigenvalues have a small absolute value. This has the effect that the maximum of the current distribution moves from the edge of the layer to the center, which is equivalent to saying that the electromagnetic fields exhibit diffusive behavior over time. Comparing Figures 3.15a and 3.15b, we see that the eigenvectors corresponding to eigenvalues with large absolute values have a larger amplitude than the eigenvectors corresponding to eigenvalues with small absolute values. For early times therefore, the effect of the modes cor-

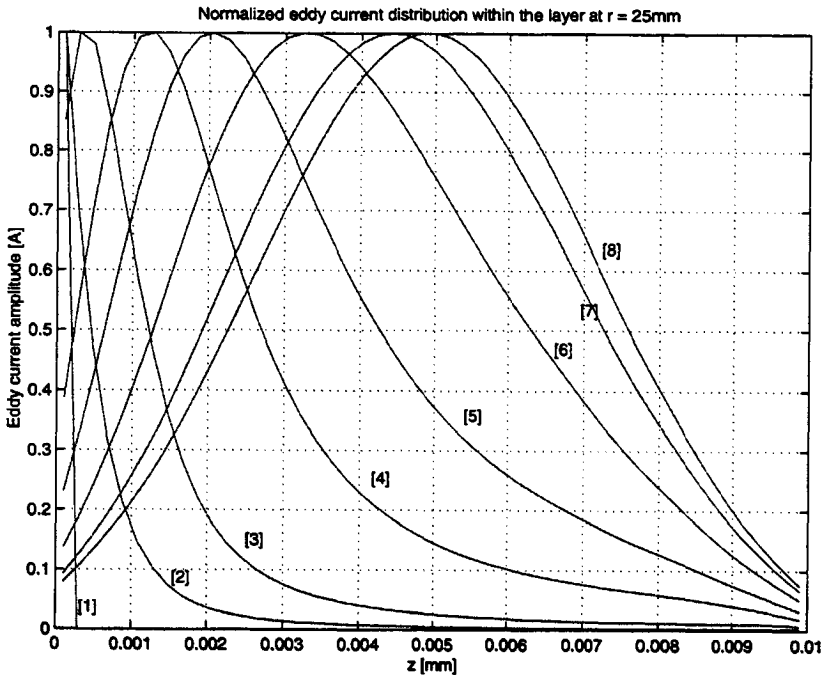


Figure 3.16: Normalized eddy current distribution within the layer, $t = 0.1$ ms (1), $t = 0.2$ ms (2), $t = 0.3$ ms (3), $t = 0.6$ ms (4), $t = 1$ ms (5), $t = 1.8$ ms (6), $t = 3.2$ ms (7), $t = 5.6$ ms (8).

responding to eigenvalues with large absolute values will be dominant, leading to an eddy current distribution with a maximum near the edge of the layer. For later times, those modes decay faster than the modes corresponding to the eigenvalues with small absolute values, which causes the maximum of the eddy current distribution to shift to the center of the layer (in effect giving rise to electromagnetic diffusion), as can be seen in Figure 3.16.

If we compare the eddy current distributions within the layer calculated using the current filament based model (Figure 3.16) to those calculated using the 2D model described in Section 4.2 (see Figure 5.1), we see that the eddy current distribution exhibits behavior similar to what the current filament based model predicts. Thus, the maximum of the eddy current distribution is located at the center of the layer for late times, while for early times, the maximum of the eddy current distribution is located near the edge of the layer. The effects of the electromagnetic diffusion can therefore be explained in terms of the different decay-rate of the fundamental modes that are excited within the layer by the switch-off current in the transmitting coil.

Chapter 4

The Forward Problem

As stated in Chapter 1, the forward problem entails the calculation of the field quantities when the sources and the medium parameters in the configuration are known (i.e., the PEC tool in the presence of a defect where the configuration of the defect is known and where we need to calculate the received signals). For modelling the PEC tool in the presence of a defect, we introduce a layered configuration, where the sources and receivers are located above the layer. We then solve the electromagnetic field equations to obtain the PEC signals.

This chapter is split into four parts. We start by giving an overview of the computational methods that we used to solve the forward problem. Next, we discuss the configuration where we have a circular loop source above a layer in which no defect is present, in which case we can use the symmetry of the configuration to obtain 2D scalar expressions for the field quantities. Finally we discuss the full vectorial 3D problem, where we have a layer in which a defect can be present. To solve this problem, we first discuss the solution to the field equations for a configuration with a homogeneous background, after which we take into account the presence of the layer.

4.1 Review of computational techniques

We start with a brief review of the computational techniques that can be used to calculate the forward problem. We distinguish between local methods, where Maxwell's equations are solved in local form, and global methods, where Maxwell's

equations are solved in integral form. For the forward problem of the PEC tool, we considered both local (FDTD) and global (integral equations) methods.

4.1.1 The FDTD method

In the Finite Difference Time Domain method we start from the local Maxwell equations. The domain is discretized in a rectangular grid, where we take the medium parameters to be piecewise constant. Next, the differential operators occurring in Maxwell's equations are replaced by finite differences according to a certain stencil which determines the accuracy. Unfortunately, it is difficult to handle large contrasts without a prohibitively large increase of the number of grid points. For 2D planar structures, Oristaglio and Hohmann [59] and Goldman *et al.* [34] have derived an analytical boundary condition, but this method cannot be used for non-planar boundaries, as would be the case when a corrosion defect is present in the configuration.

Using a local method such as the FDTD method has some advantages: the electromagnetic fields are calculated directly in the time domain and the field values are known everywhere within the computational domain, which would enable us to visualize the current flow around the defect. On the other hand, the method also has some distinct disadvantages: as previously mentioned, large contrasts cannot readily be handled and since the fields are calculated directly in the time domain, we would need a time domain Green's function for a layered medium to calculate the fields at the receiver positions outside the layer. Because of these difficulties we have chosen to use integral equations to model the problem, as described in the rest of this chapter.

4.1.2 Integral equations

Since we only need the values of the field quantities within the defect to be able to calculate the fields at the receiving coils, it would be advantageous to use a global technique such as integral equations. Using this technique, we limit our computational domain to the defect, which gives a large reduction in computer storage. The disadvantage is that it is difficult to solve the integral equations directly in the time domain. In order to get the time domain voltage on the receiver coil terminals we must calculate the frequency domain voltage for a number of frequencies, after which a temporal Fourier transformation gives the desired voltage in the time domain.

For the integral equation method, the computational domain is again discretized into a rectangular grid, on which expansion functions are defined. We then follow the method described by Kooij and Van den Berg [44], to discretize the integral equations. **Since we have both a contrast in conductivity and permeability, we have chosen to solve the full Maxwell's equations for both the electric and magnetic field quantities.** It is possible to rewrite Maxwell's equations such that we end up with a

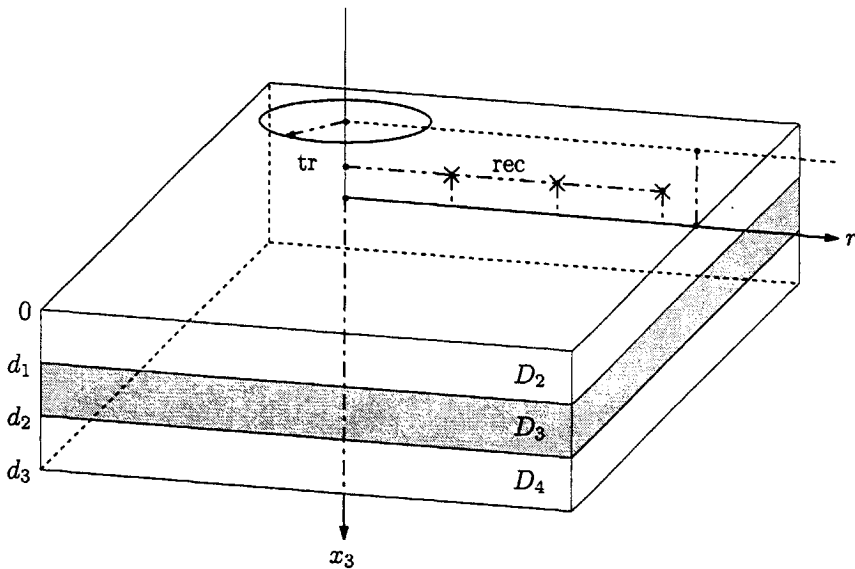


Figure 4.1: Configuration for the 2D layered configuration.

single field quantity, but this would involve more complicated expansion functions for the vector potentials.

For the PEC configuration of a source above a metal layer, the problem is split into two parts: first we need to solve the integral equations for a source radiating in a homogeneous medium, after which we introduce the Green's functions for a layered medium to calculate the field quantities within a scatterer located within the layer. Using the Green's functions, we then calculate the scattered field quantities at the receiver locations which are located outside the layer.

Note that for a circularly symmetric defect that is coaxial with the transmitting coil axis, we would have been able to solve the problem in two dimensions (see Looijer [51]). However, this severely limits the type and location of the defect with respect to the probe, hence we have chosen not to use this configuration.

4.2 2D Stratified configuration

First we will discuss the 2D stratified configuration, where a coil is located some distance above the layer (see Figure 4.1). This layer is then divided into three sub-layers, each of which can have different medium parameters. In the derivation of the expressions for the field quantities, we have included the permittivity. To obtain

the diffusion approximation it suffices to let $\varepsilon_0 \rightarrow 0$. Since the configuration is rotationally symmetric around the coil axis, the problem reduces to a 2D problem in the $r - x_3$ plane. We write Maxwell's equations in cylindrical coordinates (see Chapter 2), which gives

$$\partial_3 H_r - \partial_r H_3 - (\sigma + \varepsilon_0 \partial_t) E_\phi = J_\phi^{ext}, \quad (4.1)$$

$$-\partial_3 E_\phi + \mu \partial_t H_r = 0, \quad (4.2)$$

$$\frac{1}{r} \partial_r (r E_\phi) + \mu \partial_t H_3 = 0. \quad (4.3)$$

In the frequency domain, with time excitation $\exp(-i\omega t)$, this becomes

$$\partial_3 \hat{H}_r - \partial_r \hat{H}_3 - (\sigma - i\omega \varepsilon_0) \hat{E}_\phi = \hat{J}_\phi^{ext}, \quad (4.4)$$

$$-\partial_3 \hat{E}_\phi - i\omega \mu \hat{H}_r = 0, \quad (4.5)$$

$$\frac{1}{r} \partial_r (r \hat{E}_\phi) - i\omega \mu \hat{H}_3 = 0. \quad (4.6)$$

In order to measure the fields generated by the eddy currents in the layers, receiving coils are used. The time-dependence of the voltage on the terminals of these coils gives information on how the fields in the layers change, and consequently contains information about the material parameters and thickness of the layers. The voltage on the terminals of a receiving coil is given by either

$$\hat{V}_{rec} = i\omega \mu \int_{A_{rec}} \hat{H}_3(r, x_3) dA, \quad (4.7)$$

or

$$\hat{V}_{rec} = \int_{C_{rec}} \hat{\mathbf{E}}(r, x_3) \cdot d\mathbf{l}, \quad (4.8)$$

where A_{rec} is the area of the receiving coil and C_{rec} its contour. In our analysis we take \hat{E}_ϕ as the primary unknown field value. The partial differential equation for the electric field \hat{E}_ϕ within a layer is given by

$$\partial_3^2 \hat{E}_\phi + \partial_r \left[\frac{1}{r} \partial_r (r \hat{E}_\phi) \right] + (\sigma_n - i\omega \varepsilon_0) i\omega \mu_n \hat{E}_\phi = -i\omega \mu_n \hat{J}_\phi^{ext}, \quad (4.9)$$

where the index n denotes the layer. We introduce the Green's function as the solution to Eq. (4.9) when \hat{J}_ϕ is a loop source, i.e.,

$$\partial_3^2 \hat{G} + \partial_r \left[\frac{1}{r} \partial_r (r \hat{G}) \right] + (\sigma_n - i\omega \varepsilon_0) i\omega \mu_n \hat{G} = -\frac{i\omega \mu_n}{2\pi r} \delta(r - r', x_3 - x'_3). \quad (4.10)$$

where the primed coordinates denote the source position. Using the Hankel transformation with respect to r , the Green's function can be written as (see Appendix A)

$$\hat{G}(r, x_3; r', x'_3) = \int_{k_r=0}^{\infty} \tilde{G}(k_r, x_3; r', x'_3) J_1(k_r r) k_r dk_r, \quad (4.11)$$

in which J_1 is a Bessel function of the first kind and of order one. The Green's functions for the 2D configuration are given in Appendix A. We will neglect the direct contribution from the transmitting coil to the receiving coils, since this part of the field does not contain any information on the properties of the layer. In the actual measurement configuration, the direct contribution and the contribution from the layer are separated in time. The electric field is now given by

$$\hat{E}_\phi(r, x_3) = \int_{D^e} \hat{G}(r, x_3; r', z') \hat{j}_\phi^{ext}(r', x'_3) dA, \quad (4.12)$$

in which D^e is the source domain, i.e., the domain occupied by the transmitting coil when the transmitting coil has finite thickness and width. When \hat{j}_ϕ^{ext} reduces to an infinitely thin loop source we obtain

$$\hat{E}_\phi(r, x_3) = \hat{G}(r, x_3; r', x'_3). \quad (4.13)$$

Using the properties of the Bessel function, we can write the following expressions for the components of the magnetic field (again for the case where \hat{j}_ϕ^{ext} is a loop source)

$$\hat{H}_r(r, x_3) = -\frac{1}{i\omega\mu} \int_{k_r=0}^{\infty} \left(\partial_3 \tilde{G}(k_r, x_3; r', x'_3) \right) J_1(k_r r) k_r dk_r, \quad (4.14)$$

$$\hat{H}_3(r, x_3) = \frac{1}{i\omega\mu} \int_{k_r=0}^{\infty} \tilde{G}(k_r, x_3; r', x'_3) J_0(k_r r) k_r^2 dk_r, \quad (4.15)$$

where J_0 is the Bessel function of the first kind and of order zero.

4.2.1 Scattering formulation

We now consider scattering by a layer with a contrast in conductivity and/or permeability and define the background configuration as the configuration where all the layers have medium parameters $\{\sigma_b, \mu_b, \varepsilon_0\}$. When a scatterer is present, i.e., when one of the layers has one or more medium parameters $\{\sigma_s, \mu_s\}$ differing from those of the background, we write the electric field as

$$\hat{E}_\phi = \hat{E}_\phi^{inc} + \hat{E}_\phi^{sct}. \quad (4.16)$$

Note that we assume that there are no contrasts in permittivity present. The incident field \hat{E}_ϕ^{inc} corresponds to the background configuration, where all layers have medium parameters $\{\sigma_b, \mu_b, \varepsilon_0\}$. We now assume that the layer with the contrasting medium parameters is D_3 , see Figure 4.1. Furthermore, we assume that the sources in our configuration are loop sources, and consequently the incident field \hat{E}_ϕ^{inc} in Eq. (4.16) is given by Eq. (4.13). The scattered field \hat{E}_ϕ^{sct} is given by

$$\hat{E}_\phi^{sct}(r, x_3) = 2\pi \int_{D_s} \hat{G}(r, x_3; r', x'_3) \chi(r', x'_3) \hat{E}_\phi(r', x'_3) dA, \quad (4.17)$$

where D^S is the scattering domain (which, in this case, is the layer D_3). The equivalent electric contrast χ is given by

$$\chi = \Delta\sigma + (\sigma_s - i\omega\varepsilon_0) \frac{\Delta\mu}{\mu_b}, \quad (4.18)$$

in which

$$\Delta\sigma = \sigma_s - \sigma_b, \quad (4.19)$$

$$\Delta\mu = \mu_s - \mu_b. \quad (4.20)$$

For $\mathbf{x} \in D^S$, Eq. (4.17) represents an integral equation for the total electric field within the scatterer. Because the scatterer is unbounded in the r -direction, we can simply calculate the total electric field using the Green's function defined in Appendix A and perform inversion in the Fourier-transform domain. If the scatterer had been bounded in the r -direction, Eq. (4.17) would have to be solved using (for example) the method of moments.

4.2.2 Sensitivity

We will now consider the sensitivity of the field quantities using the configuration given in Figure 4.1. Calculating the sensitivity functions for the 2D configuration gives us an indication for the 3D case, while enabling us to use the Green's functions for the 2D stratified configuration as defined in Appendix A. To derive the sensitivity functions, we follow the method of Oristaglio and Habashy [60]. We start by defining the medium parameters as

$$\sigma(\mathbf{x}) = \sum_{n=1}^5 \sigma_n \phi_n(x_3), \quad (4.21)$$

$$\mu(\mathbf{x}) = \sum_{n=1}^5 \mu_n \phi_n(x_3), \quad (4.22)$$

where the expansion function $\phi_n(x_3)$ is given by

$$\phi_n(x_3) = \begin{cases} 1, & x_3 \in D_n, \\ 0, & \text{otherwise.} \end{cases} \quad (4.23)$$

The permittivity is set to $\varepsilon = \varepsilon_0$ for the entire configuration. To derive the sensitivity functions with respect to the medium parameter of a layer, we now need to calculate the derivatives $\partial_{\sigma_n} \hat{\mathbf{E}}$ and $\partial_{\mu_n} \hat{\mathbf{E}}$, where we have considered the electric field only (partial derivatives of the magnetic field are calculated in the same manner). Taking the partial derivatives of the source-free Maxwell equations with respect to σ_n and μ_n leads to

$$\begin{aligned} -\nabla \times (\partial_{\sigma_n} \hat{\mathbf{H}}) + (\sigma - i\omega\varepsilon_0) (\partial_{\sigma_n} \hat{\mathbf{E}}) &= -\phi_n(x_3) \hat{\mathbf{E}}, \\ \nabla \times (\partial_{\sigma_n} \hat{\mathbf{E}}) - i\omega\mu (\partial_{\sigma_n} \hat{\mathbf{H}}) &= \mathbf{0}, \end{aligned} \quad (4.24)$$

Table 4.1: States of the reciprocity theorem for the sensitivity with respect to conductivity (State A1) and permeability (State A2).

State A1	State A2	State B
$\hat{\mathbf{E}}^{A1} = \partial_{\sigma_n} \hat{\mathbf{E}}$	$\hat{\mathbf{E}}^{A2} = \partial_{\mu_n} \hat{\mathbf{E}}$	$\hat{\mathbf{E}}^B = \hat{\mathbf{E}}$
$\hat{\mathbf{H}}^{A1} = \partial_{\sigma_n} \hat{\mathbf{H}}$	$\hat{\mathbf{H}}^{A2} = \partial_{\mu_n} \hat{\mathbf{H}}$	$\hat{\mathbf{H}}^B = \hat{\mathbf{H}}$
$\sigma^{A1} = \sigma(\mathbf{x})$	$\sigma^{A2} = \sigma(\mathbf{x})$	$\sigma^B = \sigma(\mathbf{x})$
$\mu^{A1} = \mu(\mathbf{x})$	$\mu^{A2} = \mu(\mathbf{x})$	$\mu^B = \mu(\mathbf{x})$
$\varepsilon^{A1} = \varepsilon_0$	$\varepsilon^{A2} = \varepsilon_0$	$\varepsilon^B = \varepsilon_0$
$\hat{\mathbf{J}}^{A1} = \phi_n(x_3) \hat{\mathbf{E}}$	$\hat{\mathbf{J}}^{A2} = \mathbf{0}$	$\hat{\mathbf{J}}^B = \hat{\mathbf{J}}$
$\hat{\mathbf{K}}^{A1} = \mathbf{0}$	$\hat{\mathbf{K}}^{A2} = -i\omega\phi_n(x_3) \hat{\mathbf{H}}$	$\hat{\mathbf{K}}^B = \hat{\mathbf{K}}$

and

$$\begin{aligned} -\nabla \times (\partial_{\mu_n} \hat{\mathbf{H}}) + (\sigma - i\omega\varepsilon_0) (\partial_{\mu_n} \hat{\mathbf{E}}) &= \mathbf{0}, \\ \nabla \times (\partial_{\mu_n} \hat{\mathbf{E}}) - i\omega\mu (\partial_{\mu_n} \hat{\mathbf{H}}) &= \phi_n(x_3) \hat{\mathbf{H}}, \end{aligned} \quad (4.25)$$

respectively. We can see that Eqs. (4.24) - (4.25) represent Maxwell's equations with new source terms and different field quantities. To derive the sensitivity with respect to the conductivity of the layers, we use the states A1 and B as indicated in Table 4.1 in the frequency domain reciprocity theorem Eq. (2.39), which yields

$$\int_{\mathbf{x} \in D_n} [(\partial_{\sigma_n} \hat{\mathbf{E}}) \cdot \hat{\mathbf{J}} - \hat{\mathbf{E}} \cdot \phi(x_3) \hat{\mathbf{E}} - (\partial_{\sigma_n} \hat{\mathbf{H}}) \cdot \hat{\mathbf{K}}] dx = 0, \quad (4.26)$$

where we have used the fact that the medium parameters of both states are equal. We now consider the 2D configuration, where a transmitting coil is located at $\mathbf{x}' = \{r', x'_3\}$ and where we want to calculate the sensitivity of the electric field with respect to the conductivity of layer D_3 . We assume that the receiver is located at $\mathbf{x} = \mathbf{x}'$, which simplifies calculations. Furthermore, we observe that the field quantities in this configuration are given by $\hat{\mathbf{E}} = \hat{E}_\phi \mathbf{i}_\phi$ and $\hat{\mathbf{H}} = \hat{H}_r \mathbf{i}_r + \hat{H}_3 \mathbf{i}_3$. If we now take $\hat{\mathbf{J}} = \delta(\mathbf{x} - \mathbf{x}') \mathbf{i}_\phi$ and $\hat{\mathbf{K}} = \mathbf{0}$ as sources for state B, we obtain the following relation for the sensitivity with respect to σ_3

$$(\partial_{\sigma_3} \hat{\mathbf{E}})(r', x'_3; \omega) = 2\pi \int_{x_3=d_1}^{d_2} \int_{r=0}^{\infty} (\hat{G}(r', x'_3; r, x_3; \omega))^2 r dr dx_3, \quad (4.27)$$

where we have used the fact that $\hat{E}_\phi(\mathbf{x}) = \hat{G}(\mathbf{x}, \mathbf{x}')$ for an infinitely thin loop source located at $\mathbf{x} = \mathbf{x}'$. Note that $\hat{G}(r', x'_3; r, x_3; \omega)$ is the electric field within layer D_3 at $\mathbf{x} = (r, x_3)$, generated by a source at $\mathbf{x}' = (r', x'_3)$.

To calculate the sensitivity relations with respect to permeability, we use

states A2 and B in the reciprocity relation Eq. (2.39), which leads to

$$\int_{\mathbf{x} \in D_n} \left[(\partial_{\mu_n} \hat{\mathbf{E}}) \cdot \hat{\mathbf{J}} - (\partial_{\mu_n} \hat{\mathbf{H}}) \cdot \hat{\mathbf{K}} - i\omega \hat{\mathbf{H}} \cdot \phi(x_3) \hat{\mathbf{H}} \right] d\mathbf{x} = 0. \quad (4.28)$$

Using the same configuration as for the sensitivity with respect to conductivity, we obtain the relation

$$\begin{aligned} (\partial_{\mu_3} \hat{\mathbf{E}})(r', x'_3; \omega) = \\ 2\pi i \omega \int_{x_3=d_1}^{d_2} \int_{r=0}^{\infty} \left(\hat{H}_r^2(r, x_3; \omega) + \hat{H}_3^2(r, x_3; \omega) \right) r dr dx_3. \end{aligned} \quad (4.29)$$

where \hat{H}_r and \hat{H}_3 are given in Eqs. (4.14) and (4.15). We can see that the sensitivity function with respect to permeability is proportional to ω , which suggests that reconstruction of the permeability is very difficult at low frequencies (see also the numerical results in Chapter 7). Numerical results for the sensitivity functions can be found in Section 7.2.1.

4.3 3D Configuration with a homogeneous background

If we have a configuration where a scatterer (defect) is located within a layer and this scatterer is not axially symmetric around the axis of the transmitting coil, then we have to solve the full 3D field problem. In that case the contrast function cannot be written as to include both the electric and magnetic contrasts (as was done in Eq. (4.18)). Instead, we must apply a discrete grid over the scatterer and solve the integral equations for the field quantities within the scatterer itself, after which we can calculate the field quantities at the receiver positions. For a scatterer located within a layer, we distinguish between the direct contribution from the sources and the reflections from the interfaces (see Figure 4.5). In this section we will discuss the direct contribution from the sources (which can be viewed as a problem in a homogeneous background medium, where the medium parameters are those of the layer), the effects of the presence of the interfaces will be discussed in Section 4.9. Again, we take $\varepsilon = \varepsilon_0$ throughout the configuration and consider only contrasts in conductivity and/or permeability. We only consider contrasts in conductivity and/or permeability.

For the homogeneous background configuration, we start from Maxwell's equations in the frequency domain for the total field quantities in the scatterer

$$\left. \begin{aligned} -\nabla \times \hat{\mathbf{H}} + (\sigma - i\omega\varepsilon_0)\hat{\mathbf{E}} &= \mathbf{0}, \\ \nabla \times \hat{\mathbf{E}} - i\omega\mu\hat{\mathbf{H}} &= \mathbf{0}, \end{aligned} \right\} \mathbf{x} \in D^s, \quad (4.30)$$

where D^s denotes the scattering domain. The equations for the incident field are

$$\left. \begin{aligned} -\nabla \times \hat{\mathbf{H}}^i + (\sigma_b - i\omega\epsilon_0)\hat{\mathbf{E}}^i &= \mathbf{0}, \\ \nabla \times \hat{\mathbf{E}}^i - i\omega\mu_b\hat{\mathbf{H}}^i &= \mathbf{0}, \end{aligned} \right\}, \quad \mathbf{x} \in D^s. \quad (4.31)$$

We can now write the equations for the scattered field in which the incident field appears as a distributed source

$$\left. \begin{aligned} -\nabla \times \hat{\mathbf{H}}^s + (\sigma - i\omega\epsilon_0)\hat{\mathbf{E}}^s &= -\Delta\sigma\hat{\mathbf{E}}^i, \\ \nabla \times \hat{\mathbf{E}}^s - i\omega\mu\hat{\mathbf{H}}^s &= i\omega\Delta\mu\hat{\mathbf{H}}^i, \end{aligned} \right\}, \quad \mathbf{x} \in D^s, \quad (4.32)$$

where

$$\Delta\sigma = \sigma - \sigma_b, \quad (4.33)$$

$$\Delta\mu = \mu - \mu_b. \quad (4.34)$$

The medium parameters σ and μ correspond to the scatterer and σ_b and μ_b correspond to the background medium. It is noted that in Eqs. (4.32) the medium parameters are those of the actual scatterer. If we would have manipulated Maxwell's equations such that the total field is present in the source term (see Section 4.9), then the medium parameters occurring in the equations would be those of the background medium. We now use the reciprocity theorem given in Eq. (2.39) to derive integral representations for the field quantities. We choose for state A in the reciprocity theorem the actual state in which the scatterer is present

$$\{\hat{\mathbf{E}}^A, \hat{\mathbf{H}}^A\} = \{\hat{\mathbf{E}}^s, \hat{\mathbf{H}}^s\}, \quad (4.35)$$

$$\{\hat{\mathbf{J}}^A, \hat{\mathbf{K}}^A\} = \{\Delta\sigma\hat{\mathbf{E}}^i, -i\omega\Delta\mu\hat{\mathbf{H}}^i\}, \quad (4.36)$$

$$\{\sigma^A, \mu^A, \epsilon^A\} = \{\sigma, \mu, \epsilon_0\}. \quad (4.37)$$

For state B we choose either

$$\{\hat{\mathbf{E}}^B, \hat{\mathbf{H}}^B\} = \{\hat{\mathbf{G}}^{EE}, \hat{\mathbf{G}}^{HE}\}, \quad (4.38)$$

$$\{\hat{\mathbf{J}}^B, \hat{\mathbf{K}}^B\} = \{\delta(\mathbf{x} - \mathbf{x}')\mathbf{I}, 0\}, \quad (4.39)$$

$$\{\sigma^B, \mu^B, \epsilon^B\} = \{\sigma_b, \mu_b, \epsilon_0\}. \quad (4.40)$$

or

$$\{\hat{\mathbf{E}}^B, \hat{\mathbf{H}}^B\} = \{\hat{\mathbf{G}}^{EH}, \hat{\mathbf{G}}^{HH}\}, \quad (4.41)$$

$$\{\hat{\mathbf{J}}^B, \hat{\mathbf{K}}^B\} = \{0, \delta(\mathbf{x} - \mathbf{x}')\mathbf{I}\}, \quad (4.42)$$

$$\{\sigma^B, \mu^B, \epsilon^B\} = \{\sigma_b, \mu_b, \epsilon_0\}. \quad (4.43)$$

which represents an electric or magnetic point source radiating in a homogeneous background medium, respectively. The \mathbf{I} symbol in the source term denotes a unit vector. Since the background medium is homogeneous, the dyadic Green's functions occurring in Eqs. (4.38) and (4.41) are those of a homogeneous medium.

Using the aforementioned states in the reciprocity relation given in Eq. (2.39), we can write the following expressions for the electric field and magnetic field integral representations

$$\hat{\mathbf{E}}(\mathbf{x}) = \hat{\mathbf{E}}^i(\mathbf{x}) + \int_{\mathbf{x}' \in D^s} \left(\Delta\sigma \hat{\mathbf{G}}^{EE}(\mathbf{x}, \mathbf{x}') \cdot \hat{\mathbf{E}}(\mathbf{x}') - i\omega\Delta\mu \hat{\mathbf{G}}^{EH}(\mathbf{x}, \mathbf{x}') \cdot \hat{\mathbf{H}}(\mathbf{x}') \right) d\mathbf{x}', \quad (4.44)$$

$$\hat{\mathbf{H}}(\mathbf{x}) = \hat{\mathbf{H}}^i(\mathbf{x}) + \int_{\mathbf{x}' \in D^s} \left(\Delta\sigma \hat{\mathbf{G}}^{HE}(\mathbf{x}, \mathbf{x}') \cdot \hat{\mathbf{E}}(\mathbf{x}') - i\omega\Delta\mu \hat{\mathbf{G}}^{HH}(\mathbf{x}, \mathbf{x}') \cdot \hat{\mathbf{H}}(\mathbf{x}') \right) d\mathbf{x}'. \quad (4.45)$$

In deriving Eqs. (4.44) and (4.45), we have used the fact that $\hat{\mathbf{G}}^{EH}(\mathbf{x}, \mathbf{x}') = -\hat{\mathbf{G}}^{HE}(\mathbf{x}', \mathbf{x})$. Since both electric and magnetic contrasts are present, we can either rewrite Eqs. (4.44) and (4.45) to a single integral representation for the electric field or we can use a combined-field method, where we solve for both the electric and magnetic field quantities. We have chosen the latter to avoid introducing more differentiation operators on the vector potentials. Introducing the normalized electric and magnetic contrasts as

$$\chi^E = \frac{\sigma - \sigma_b}{\sigma_b - i\omega\epsilon_0} = \frac{\Delta\sigma}{\sigma_b - i\omega\epsilon_0}, \quad (4.46)$$

$$\chi^H = \frac{\mu - \mu_b}{\mu_b} = \frac{\Delta\mu}{\mu_b}, \quad (4.47)$$

the integral representations are rewritten as

$$\hat{\mathbf{E}}(\mathbf{x}) = \hat{\mathbf{E}}^i(\mathbf{x}) + \int_{\mathbf{x}' \in D^s} \left(\mathcal{G}^{EE}(\mathbf{x}, \mathbf{x}') \cdot \chi^E \hat{\mathbf{E}}(\mathbf{x}') + \mathcal{G}^{EH}(\mathbf{x}, \mathbf{x}') \cdot \chi^H \hat{\mathbf{H}}(\mathbf{x}') \right) d\mathbf{x}', \quad (4.48)$$

$$\hat{\mathbf{H}}(\mathbf{x}) = \hat{\mathbf{H}}^i(\mathbf{x}) + \int_{\mathbf{x}' \in D^s} \left(\mathcal{G}^{HE}(\mathbf{x}, \mathbf{x}') \cdot \chi^E \hat{\mathbf{E}}(\mathbf{x}') + \mathcal{G}^{HH}(\mathbf{x}, \mathbf{x}') \cdot \chi^H \hat{\mathbf{H}}(\mathbf{x}') \right) d\mathbf{x}'. \quad (4.49)$$

When $\mathbf{x} \in D^S$, Eqs. (4.44) – (4.45) and (4.48) – (4.49) constitute a system of coupled integral equations for the electric and magnetic field quantities. In that case we will use the term Integral Equation of the Electric type (IEE) for Eqs. (4.44) and (4.48) and Integral Equation of the Magnetic type (IEM) for Eqs. (4.45) and (4.49). The dyadic Green's functions occurring in these equations are given by

$$\mathcal{G}^{EE}(\mathbf{x}, \mathbf{x}') = (k_b^2 + \nabla\nabla\cdot) \hat{\mathbf{G}}(\mathbf{x} - \mathbf{x}')\mathbf{I}, \quad (4.50)$$

$$\mathcal{G}^{EH}(\mathbf{x}, \mathbf{x}') = i\omega\mu_b \nabla \times \hat{\mathbf{G}}(\mathbf{x} - \mathbf{x}')\mathbf{I}, \quad (4.51)$$

$$\mathcal{G}^{HE}(\mathbf{x}, \mathbf{x}') = (\sigma_b - i\omega\epsilon_0) \nabla \times \hat{\mathbf{G}}(\mathbf{x} - \mathbf{x}')\mathbf{I}, \quad (4.52)$$

$$\mathcal{G}^{HH}(\mathbf{x}, \mathbf{x}') = (k_b^2 + \nabla\nabla\cdot) \hat{\mathbf{G}}(\mathbf{x} - \mathbf{x}')\mathbf{I}, \quad (4.53)$$

where $\hat{\mathbf{G}}(\mathbf{x} - \mathbf{x}')$ is the scalar Green's function, given by

$$\hat{\mathbf{G}}(\mathbf{x} - \mathbf{x}') = \frac{\exp(ik_b|\mathbf{x} - \mathbf{x}'|)}{4\pi|\mathbf{x} - \mathbf{x}'|}, \quad (4.54)$$

in which the wave number k_b is defined as

$$k_b = (\omega^2 \epsilon_0 \mu_b + i\omega \mu_b \sigma_b)^{\frac{1}{2}}, \quad \text{Re}(k_b) > 0. \quad (4.55)$$

Note that the differential operators in the expressions for the dyadic Green's functions work on the unprimed variables. The equations pertaining to the diffusion approximation can be obtained by setting $\epsilon_0 = 0$ in Eqs. (4.46), (4.52) and (4.55). Using subscript notation, we can write the integral equations as

$$\hat{E}_k = \hat{E}_k^i + k_b^2 \hat{A}_k + \partial_k \partial_n \hat{A}_n + i\omega \mu_b \epsilon_{klm} \partial_l \hat{F}_m, \quad (4.56)$$

$$= \hat{E}_k^i + k_b^2 \hat{A}_k + \hat{A}'_k + i\omega \mu_b \hat{F}_k'', \quad (4.57)$$

$$\hat{H}_j = \hat{H}_j^i + k_b^2 \hat{F}_j + \partial_j \partial_k \hat{F}_k + (\sigma_b - i\omega \epsilon_0) \epsilon_{jkl} \partial_k \hat{A}_l, \quad (4.58)$$

$$= \hat{H}_j^i + k_b^2 \hat{F}_j + \hat{F}'_j + (\sigma_b - i\omega \epsilon_0) \hat{A}_j'', \quad (4.59)$$

or, in vector notation,

$$\hat{\mathbf{E}} = \hat{\mathbf{E}}^i + k_b^2 \hat{\mathbf{A}} + \nabla \nabla \cdot \hat{\mathbf{A}} + i\omega \mu_b \nabla \times \hat{\mathbf{F}}, \quad (4.60)$$

$$\hat{\mathbf{H}} = \hat{\mathbf{H}}^i + k_b^2 \hat{\mathbf{F}} + \nabla \nabla \cdot \hat{\mathbf{F}} + (\sigma_b - i\omega \epsilon_0) \nabla \times \hat{\mathbf{A}}, \quad (4.61)$$

where we have introduced the electric and magnetic vector potentials, which are defined as

$$\hat{A}_k(\mathbf{x}) = \int_{\mathbf{x}' \in D^s} \hat{G}(\mathbf{x} - \mathbf{x}') \chi^E(\mathbf{x}') \hat{E}_k(\mathbf{x}') d\mathbf{x}', \quad (4.62)$$

$$\hat{F}_j(\mathbf{x}) = \int_{\mathbf{x}' \in D^s} \hat{G}(\mathbf{x} - \mathbf{x}') \chi^H(\mathbf{x}') \hat{H}_j(\mathbf{x}') d\mathbf{x}'. \quad (4.63)$$

4.3.1 Discretization of the computational domain

To solve the system of integral equations, we discretize the computational domain using a rectangular grid D , where the boundaries of D are located along the Cartesian axis (see Figure 4.2). The domain occupied by the scatterer itself is denoted by D^S , where $D^S \in D$ and D^S and D can have a common boundary. The subdomains are given by

$$D_{m,n,p} = \{(x_1, x_2, x_3 \in \mathbf{R}^3) | x_{1;m} - \frac{1}{2} \Delta x_1 < x_1 < x_{1;m} + \frac{1}{2} \Delta x_1, \quad (4.64)$$

$$x_{2;n} - \frac{1}{2} \Delta x_2 < x_2 < x_{2;n} + \frac{1}{2} \Delta x_2, x_{3;p} - \frac{1}{2} \Delta x_3 < x_3 < x_{3;p} + \frac{1}{2} \Delta x_3\},$$

where the center point of $D_{m,n,p}$ is

$$x_{1;m} = x_{1;1/2} + (m-1) \Delta x_1, \quad m = 1, \dots, M \quad (4.65)$$

$$x_{2;n} = x_{2;1/2} + (n-1) \Delta x_2, \quad n = 1, \dots, N \quad (4.66)$$

$$x_{3;p} = x_{3;1/2} + (p-1) \Delta x_3, \quad p = 1, \dots, P \quad (4.67)$$

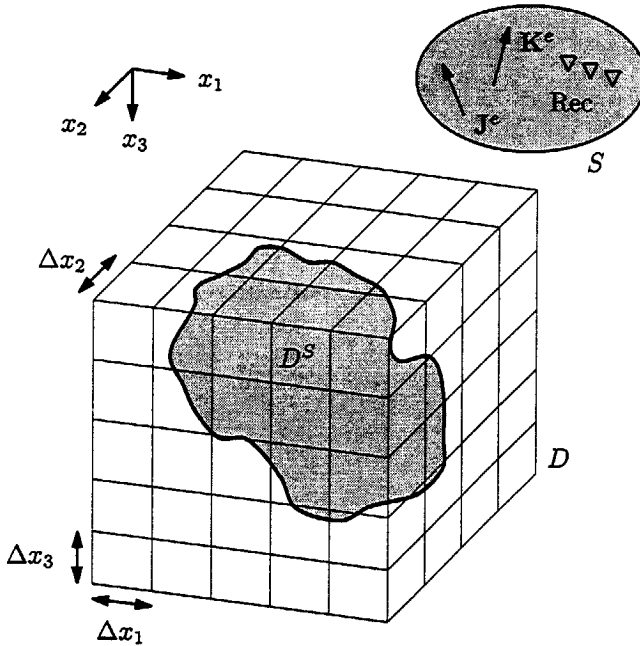


Figure 4.2: Discretization of the computational domain.

or

$$\mathbf{x}_{m,n,p} = x_{k;m,n,p} \mathbf{i}_k = x_{1;m} \mathbf{i}_1 + x_{2;n} \mathbf{i}_2 + x_{3;p} \mathbf{i}_3. \quad (4.68)$$

In each subdomain we will assume both electric and magnetic contrasts to be constant with values $\chi_{m,n,p}^E$ and $\chi_{m,n,p}^H$, respectively.

4.3.2 Weighting procedure

In order to calculate the field quantities at the grid points, we must first obtain a discrete formulation of the domain integral equations defined in the previous section. This is done by performing a weighting procedure on Eqs. (4.56) and (4.58), i.e., by **multiplying with an appropriate weighting function and integrating over the computational domain**. The electric and magnetic vector potentials are then expanded using the same functions as those used for the weighting procedure. We define the

discrete quantities

$$\hat{E}_{k;m,n,p} = \hat{E}_k(x_{1;m}, x_{2;n}, x_{3;p}), \quad (4.69)$$

$$\hat{H}_{j;m,n,p} = \hat{H}_j(x_{1;m}, x_{2;n}, x_{3;p}), \quad (4.70)$$

$$\hat{A}_{k;m,n,p} = \hat{A}_k(x_{1;m}, x_{2;n}, x_{3;p}), \quad (4.71)$$

$$\hat{F}_{k;m,n,p} = \hat{F}_k(x_{1;m}, x_{2;n}, x_{3;p}), \quad (4.72)$$

where $\{m, n, p\}$ are defined as before. The electric and magnetic vector potentials are expanded as

$$\hat{A}_k(\mathbf{x}) = \sum_{m,n,p} \hat{A}_{k;m,n,p} \psi_{m,n,p}(\mathbf{x}), \quad (4.73)$$

$$\hat{F}_j(\mathbf{x}) = \sum_{m,n,p} \hat{F}_{j;m,n,p} \psi_{m,n,p}(\mathbf{x}), \quad (4.74)$$

in which $\psi_{m,n,p}(\mathbf{x})$ are the as yet undefined expansion functions. Using these expressions, the domain integral equations now become

$$\hat{E}_{k;m,n,p} = \hat{E}_{k;m,n,p}^i + k_b^2 \hat{A}_{k;m,n,p} + \hat{A}'_{k;m,n,p} + i\omega\mu_b \hat{F}''_{k;m,n,p}, \quad (4.75)$$

$$\hat{H}_{j;m,n,p} = \hat{H}_{j;m,n,p}^i + k_b^2 \hat{F}_{j;m,n,p} + \hat{F}'_{j;m,n,p} + (\sigma_b - i\omega\epsilon_0) \hat{A}''_{j;m,n,p}. \quad (4.76)$$

The weighted forms of $\hat{A}'_{k;m,n,p}$ and $\hat{F}'_{j;m,n,p}$ are given by

$$\hat{A}'_{k;m,n,p} = \frac{\int_{\mathbf{x} \in D} \psi_{m,n,p}(\mathbf{x}) \partial_k \partial_j \hat{A}_j(\mathbf{x}) d\mathbf{x}}{\int_{\mathbf{x} \in D} \psi_{m,n,p}(\mathbf{x}) d\mathbf{x}}, \quad (4.77)$$

and

$$\hat{F}'_{j;m,n,p} = \frac{\int_{\mathbf{x} \in D} \psi_{m,n,p}(\mathbf{x}) \partial_j \partial_k \hat{F}_k(\mathbf{x}) d\mathbf{x}}{\int_{\mathbf{x} \in D} \psi_{m,n,p}(\mathbf{x}) d\mathbf{x}}, \quad (4.78)$$

while the weighted forms of $\hat{A}''_{j;m,n,p}$ and $\hat{F}''_{k;m,n,p}$ are given by

$$\hat{F}''_{k;m,n,p} = \frac{\int_{\mathbf{x} \in D} \psi_{m,n,p}(\mathbf{x}) \epsilon_{k,n,r} \partial_n \hat{F}_r(\mathbf{x}) d\mathbf{x}}{\int_{\mathbf{x} \in D} \psi_{m,n,p}(\mathbf{x}) d\mathbf{x}}, \quad (4.79)$$

and

$$\hat{A}''_{j;m,n,p} = \frac{\int_{\mathbf{x} \in D} \psi_{m,n,p}(\mathbf{x}) \epsilon_{j,n,r} \partial_n \hat{A}_r(\mathbf{x}) d\mathbf{x}}{\int_{\mathbf{x} \in D} \psi_{m,n,p}(\mathbf{x}) d\mathbf{x}}. \quad (4.80)$$

Note that we have used the same functions for the weighting procedure as those for the expansion of the vector potentials.

The expansion functions $\psi_{m,n,p}(\mathbf{x})$ are chosen such that the differential operators that are present in Eqs. (4.77) - (4.80) and act on the expansion functions do not generate Dirac delta functions. The second order derivatives acting on the vector

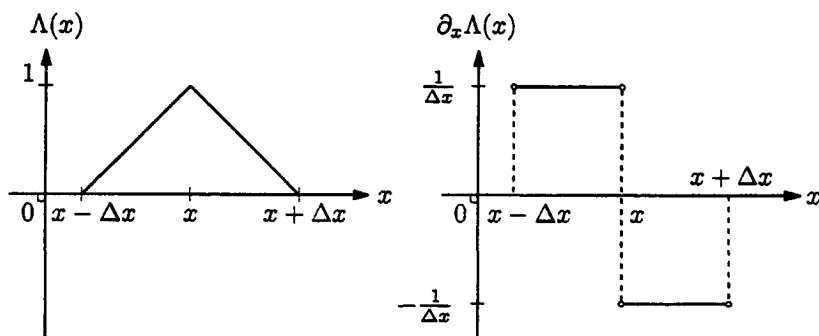


Figure 4.3: The hat expansion function and its derivative.

potentials in Eqs. (4.77) and (4.78) can be reduced by using integration by parts (which is described in the next section), therefore we can see that the expansion functions must be at least continuous in each of the vectorial directions. Because of the presence of the curl operator, we cannot use the expansion functions defined by Kooij [44] and Abubakar [2], who use a combination of pulse and hat expansion functions to solve the electric field integral equation. Consequently, we define on the domain D the expansion functions $\psi_{m,n,p}(\mathbf{x})$, which are continuous in each vectorial direction. To construct these expansion functions we first introduce an auxiliary function, the hat function, as

$$\Lambda(x|2\Delta x) = \begin{cases} (1 + \frac{x}{\Delta x}), & \text{if } -\Delta x < x < 0, \\ (1 - \frac{x}{\Delta x}), & \text{if } 0 \leq x < \Delta x, \\ 0, & \text{elsewhere,} \end{cases} \quad (4.81)$$

which is piecewise linear and continuous with support $2\Delta x$ (see Figure 4.3). Using this function we write

$$\psi_{m,n,p}(\mathbf{x}) = \Lambda(x_1 - x_{1,m}|2\Delta x_1)\Lambda(x_2 - x_{2,n}|2\Delta x_2) \times \Lambda(x_3 - x_{3,p}|2\Delta x_3), \quad (4.82)$$

for $m = 1, \dots, M$, $n = 1, \dots, N$ and $p = 1, \dots, P$. This choice of expansion function satisfies the condition that it must be at least one time differentiable in each vectorial direction. In the next section we use this expansion function to obtain weighted forms for the gradient-divergence and curl operators acting on the vector potentials.

4.3.3 Weighted forms of $\hat{A}'_{k;m,n,p}$ and $\hat{F}'_{j;m,n,p}$

In this section we will discuss the weak formulation of the gradient-divergence operator acting on the electric and magnetic vector potentials. We start by rewriting

the nominator of Eq. (4.77) as

$$\begin{aligned} \int_{\mathbf{x} \in D} \psi_{m,n,p} \partial_k [\partial_1 \hat{A}_1 + \partial_2 \hat{A}_2 + \partial_3 \hat{A}_3] d\mathbf{x} = & \quad (4.83) \\ \int_{\mathbf{x} \in D} \partial_k \{ \psi_{m,n,p} [\partial_1 \hat{A}_1 + \partial_2 \hat{A}_2 + \partial_3 \hat{A}_3] \} d\mathbf{x} \\ - \int_{\mathbf{x} \in D} (\partial_k \psi_{m,n,p}) [\partial_1 \hat{A}_1 + \partial_2 \hat{A}_2 + \partial_3 \hat{A}_3] d\mathbf{x}. \end{aligned}$$

We rewrite the first integral on the right-hand side of Eq. (4.83) as

$$\begin{aligned} \int_{\mathbf{x} \in D} \partial_k \{ \psi_{m,n,p} [\partial_1 \hat{A}_1 + \partial_2 \hat{A}_2 + \partial_3 \hat{A}_3] \} d\mathbf{x} = & \quad (4.84) \\ \int_{\mathbf{x} \in \partial D} \nu_k \{ \psi_{m,n,p} [\partial_1 \hat{A}_1 + \partial_2 \hat{A}_2 + \partial_3 \hat{A}_3] \} d\mathbf{x} = 0, \end{aligned}$$

where ν_k is the unit vector normal to ∂D . The integral over ∂D in Eq. (4.84) reduces to an integral over the domain spanned by the expansion function $\psi_{m,n,p}$, which means that this integral is zero because the expansion function is zero on the boundary of its support. By employing integration by parts, we let one differential operator work on the weighting function and the other on the expansion function of the vector potential, which are both given by $\psi_{m,n,p}$. Consequently, we have only single differentiations acting on these functions and we can suffice by requiring $\psi_{m,n,p}$ to be piece-wise linear and continuous.

Using the expansions for the vector potentials as defined in Eqs. (4.73) – (4.74), in Eq. (4.83), we encounter the following types of integrals over the expansion functions

$$\begin{aligned} \int_{\mathbf{x} \in D} (\partial_1 \psi_{m,n,p}) (\partial_1 \psi_{q,r,s}) d\mathbf{x} = -\frac{\Delta x_2 \Delta x_3}{36 \Delta x_1} (\delta_{q,m-1} - 2\delta_{q,m} + \delta_{q,m+1}) \times \\ (\delta_{r,n-1} + 4\delta_{r,n} + \delta_{r,n+1}) (\delta_{s,p-1} + 4\delta_{s,p} + \delta_{s,p+1}), \end{aligned} \quad (4.85)$$

and

$$\begin{aligned} \int_{\mathbf{x} \in D} (\partial_1 \psi_{m,n,p}) (\partial_2 \psi_{q,r,s}) d\mathbf{x} = -\frac{\Delta x_3}{24} (\delta_{q,m+1} - \delta_{q,m-1}) \times \\ (\delta_{r,n+1} - \delta_{r,n-1}) (\delta_{s,p-1} + 4\delta_{s,p} + \delta_{s,p+1}). \end{aligned} \quad (4.86)$$

The other integrals over the expansion functions occurring in Eq. (4.83) are of the same type as those shown above. Furthermore, we have

$$\int_{\mathbf{x} \in D} \psi_{m,n,p}(\mathbf{x}) d\mathbf{x} = \Delta x_1 \Delta x_2 \Delta x_3. \quad (4.87)$$

Combining these results, we arrive at the following expression for the discretized form of $\hat{A}'_{k;m,n,p}$

$$\hat{A}'_{k;m,n,p} = \sum_{j=1}^3 \sum_{q=1}^M \sum_{r=1}^N \sum_{s=1}^P a_{m,n,p,q,r,s}^{(k,j)} \hat{A}_{j;q,r,s}, \quad (4.88)$$

where the difference operator $a_{m,n,p,q,r,s}^{(k,j)}$ is defined as

$$a_{m,n,p,q,r,s}^{(1,1)} = \frac{1}{36(\Delta x_1)^2} (\delta_{q,m-1} - 2\delta_{q,m} + \delta_{q,m+1}) \times (\delta_{r,n-1} + 4\delta_{r,n} + \delta_{r,n+1}) (\delta_{s,p-1} + 4\delta_{s,p} + \delta_{s,p+1}), \quad (4.89)$$

$$a_{m,n,p,q,r,s}^{(1,2)} = \frac{1}{24\Delta x_1 \Delta x_2} (\delta_{q,m-1} - \delta_{q,m+1}) (\delta_{r,n-1} - \delta_{r,n+1}) \times (\delta_{s,p-1} + 4\delta_{s,p} + \delta_{s,p+1}), \\ = a_{m,n,p,q,r,s}^{(2,1)}, \quad (4.90)$$

$$a_{m,n,p,q,r,s}^{(1,3)} = \frac{1}{24\Delta x_1 \Delta x_3} (\delta_{q,m-1} - \delta_{q,m+1}) (\delta_{r,n-1} + 4\delta_{r,n} + \delta_{r,n+1}) \times (\delta_{s,p-1} - \delta_{s,p+1}), \\ = a_{m,n,p,q,r,s}^{(3,1)}, \quad (4.91)$$

$$a_{m,n,p,q,r,s}^{(2,2)} = \frac{1}{36(\Delta x_2)^2} (\delta_{q,m-1} + 4\delta_{q,m} + \delta_{q,m+1}) (\delta_{r,n-1} - 2\delta_{r,n} + \delta_{r,n+1}) \times (\delta_{s,p-1} + 4\delta_{s,p} + \delta_{s,p+1}), \quad (4.92)$$

$$a_{m,n,p,q,r,s}^{(2,3)} = \frac{1}{24\Delta x_2 \Delta x_3} (\delta_{q,m-1} + 4\delta_{q,m} + \delta_{q,m+1}) \times (\delta_{r,n-1} - \delta_{r,n+1}) (\delta_{s,p-1} - \delta_{s,p+1}), \\ = a_{m,n,p,q,r,s}^{(3,2)}, \quad (4.93)$$

$$a_{m,n,p,q,r,s}^{(3,3)} = \frac{1}{36(\Delta x_3)^2} (\delta_{q,m-1} + 4\delta_{q,m} + \delta_{q,m+1}) (\delta_{r,n-1} + 4\delta_{r,n} + \delta_{r,n+1}) \times (\delta_{s,p-1} - 2\delta_{s,p} + \delta_{s,p+1}), \quad (4.94)$$

in which $\delta_{m,n}$ denotes the Kronecker delta function. It is noted that $a_{m,n,p,q,r,s}^{(k,j)}$ is symmetric. Substitution of Eqs. (4.89) – (4.94) into Eq. (4.88) gives the explicit expressions for $\hat{A}'_{k;m,n,p}$. We can write similar expressions for $\hat{F}'_{j;m,n,p}$, therefore

$$\hat{F}'_{j;m,n,p} = \sum_{k=1}^3 \sum_{q=1}^M \sum_{r=1}^N \sum_{s=1}^P f_{m,n,p,q,r,s}^{(j,k)} \hat{F}_{k;q,r,s}, \quad (4.95)$$

in which

$$f_{m,n,p,q,r,s}^{(j,k)} = a_{m,n,p,q,r,s}^{(j,k)}. \quad (4.96)$$

The discretized expression for $\hat{F}'_{j;m,n,p}$ has a form similar to that of $\hat{A}'_{k;m,n,p}$.

4.3.4 Weighted forms of $\hat{A}''_{k;m,n,p}$ and $\hat{F}''_{j;m,n,p}$

We recall \hat{A}''_k as

$$\hat{A}''_k = \epsilon_{k,m,r} \partial_m \hat{A}_r. \quad (4.97)$$

The weighted form is given by

$$\hat{A}''_{k;m,n,p} = \frac{\int_{\mathbf{x} \in D} \psi_{m,n,p}(\mathbf{x}) \epsilon_{k,v,w} \partial_v \sum_{q,r,s} \hat{A}_{w;q,r,s} \psi_{q,r,s}(\mathbf{x}) d\mathbf{x}}{\int_{\mathbf{x} \in D} \psi_{m,n,p}(\mathbf{x}) d\mathbf{x}}. \quad (4.98)$$

The integrals occurring in this expression are similar to those discussed in the previous section. Using those results, we write $\hat{A}''_{k;m,n,p}$ as

$$\hat{A}''_{k;m,n,p} = \sum_{j=1}^3 \sum_{q=1}^M \sum_{r=1}^M \sum_{s=1}^P a''_{m,n,p,q,r,s}{}^{(k,j)} \hat{A}_{j;q,r,s}, \quad (4.99)$$

in which the difference operator $a''_{m,n,p,q,r,s}{}^{(k,j)}$ is defined as

$$a''_{m,n,p,q,r,s}{}^{(1,1)} = 0, \quad (4.100)$$

$$a''_{m,n,p,q,r,s}{}^{(1,2)} = \frac{1}{72\Delta x_3} (\delta_{q,m-1} + 4\delta_{q,m} + \delta_{q,m+1}) (\delta_{r,n-1} + 4\delta_{r,n} + \delta_{r,n+1}) \times (\delta_{s,p-1} - \delta_{s,p+1}), \quad (4.101)$$

$$a''_{m,n,p,q,r,s}{}^{(1,3)} = -\frac{1}{72\Delta x_2} (\delta_{q,m-1} + 4\delta_{q,m} + \delta_{q,m+1}) (\delta_{r,n-1} - \delta_{r,n+1}) \times (\delta_{s,p-1} + 4\delta_{s,p} + \delta_{s,p+1}), \quad (4.102)$$

$$a''_{m,n,p,q,r,s}{}^{(2,1)} = -a''_{m,n,p,q,r,s}{}^{(1,2)}, \quad (4.103)$$

$$a''_{m,n,p,q,r,s}{}^{(2,2)} = 0, \quad (4.104)$$

$$a''_{m,n,p,q,r,s}{}^{(2,3)} = \frac{1}{72\Delta x_1} (\delta_{q,m-1} - \delta_{q,m+1}) (\delta_{r,n-1} + 4\delta_{r,n} + \delta_{r,n+1}) \times (\delta_{s,p-1} + 4\delta_{s,p} + \delta_{s,p+1}), \quad (4.105)$$

$$a''_{m,n,p,q,r,s}{}^{(3,1)} = -a''_{m,n,p,q,r,s}{}^{(1,3)}, \quad (4.106)$$

$$a''_{m,n,p,q,r,s}{}^{(3,2)} = -a''_{m,n,p,q,r,s}{}^{(2,3)}, \quad (4.107)$$

$$a''_{m,n,p,q,r,s}{}^{(3,3)} = 0. \quad (4.108)$$

It can be seen that $a''_{m,n,p,q,r,s}{}^{(k,j)}$ is antisymmetric. The expression for $\hat{F}''_{j;m,n,p}$ is obtained in a similar manner as

$$\hat{F}''_{j;m,n,p} = \sum_{k=1}^3 \sum_{q=1}^M \sum_{r=1}^M \sum_{s=1}^P f''_{m,n,p,q,r,s}{}^{(j,k)} \hat{F}_{k;q,r,s}, \quad (4.109)$$

in which the elements of the operator $f''_{m,n,p,q,r,s}{}^{(j,k)}$ are the same as those of $a''_{m,n,p,q,r,s}{}^{(j,k)}$.

4.3.5 Weighted forms of $\hat{A}_{k;m,n,p}$ and $\hat{F}_{j;m,n,p}$

The scalar Green's functions occurring in the electric and magnetic vector potentials contain a singularity at $\mathbf{x} = \mathbf{x}'$ which can be dealt with by taking the spherical mean

of the vector potentials. We integrate \hat{A}_k and \hat{F}_j over a spherical domain (in the Cartesian space) with the center point $(x_{1;m}, x_{2;n}, x_{3;p})$. The spherical domain has radius $\frac{1}{2}\Delta x = \frac{1}{2}\min(\Delta x_1, \Delta x_2, \Delta x_3)$. The result is then divided by the volume of the spherical domain. We may then write

$$\begin{aligned}\hat{A}_k(\mathbf{x}_{m,n,p}) &= \\ &= \frac{\int_{|\mathbf{x}''| < \frac{1}{2}\Delta x} \hat{A}_k(x_{1;m} + x''_1, x_{2;n} + x''_2, x_{3;p} + x''_3) dx''_1 dx''_2 dx''_3}{\int_{|\mathbf{x}''| < \frac{1}{2}\Delta x} dx''_1 dx''_2 dx''_3} \\ &= \int_{\mathbf{x}' \in D^S} \mathcal{G}(\mathbf{x}_{m,n,p} - \mathbf{x}') \chi^E(\mathbf{x}') \hat{E}_k(\mathbf{x}') d\mathbf{x}'.\end{aligned}$$

where we have changed the order of integration, such that

$$\begin{aligned}\mathcal{G}(x_1, x_2, x_3) &= \tag{4.110} \\ &= \frac{\int_{[(x''_1)^2 + (x''_2)^2 + (x''_3)^2]^{\frac{1}{2}} < \frac{1}{2}\Delta x} \hat{G}(x_1 + x''_1, x_2 + x''_2, x_3 + x''_3) dx''_1 dx''_2 dx''_3}{\int_{[(x''_1)^2 + (x''_2)^2 + (x''_3)^2]^{\frac{1}{2}} < \frac{1}{2}\Delta x} dx''_1 dx''_2 dx''_3}.\end{aligned}$$

The spherical mean $\mathcal{G}(\mathbf{x})$ is calculated as

$$\mathcal{G}(\mathbf{x}) = \begin{cases} \frac{\left[1 - \frac{1}{2}ik_b\Delta x\right] \exp\left(\frac{1}{2}ik_b\Delta x\right) - 1}{\frac{1}{6}\pi k_b^2(\Delta x)^3}, & \text{if } R(\mathbf{x}) = 0, \\ \frac{\exp(ik_b R(\mathbf{x})) \left[\frac{\sinh\left(\frac{1}{2}ik_b\Delta x\right)}{\frac{1}{2}ik_b\Delta x} - \cosh\left(\frac{1}{2}ik_b\Delta x\right) \right]}{\frac{1}{3}\pi(k_b\Delta x)^2 R(\mathbf{x})}, & \text{if } R(\mathbf{x}) > \frac{\Delta x}{2}, \end{cases} \tag{4.111}$$

in which the distance function $R(\mathbf{x})$ is given by

$$R(\mathbf{x}) = (x_1^2 + x_2^2 + x_3^2)^{\frac{1}{2}} = |\mathbf{x}|. \tag{4.112}$$

In the same way we arrive at the expression for the weak form of the magnetic vector potential as

$$\hat{F}_j(\mathbf{x}_{m,n,p}) = \int_{\mathbf{x}' \in D^S} \mathcal{G}(\mathbf{x}_{m,n,p} - \mathbf{x}') \chi^H(\mathbf{x}') \hat{H}_j(\mathbf{x}') d\mathbf{x}', \tag{4.113}$$

where the Green's function is again given by Eq. (4.111). Alternatively, we could also take only the spherical mean for the singular point of the Green's function and use Eq. (4.54) for all other points. Numerical experiments have shown that this does not make a significant difference.

After this weighting procedure, we can now write the integrals over the computational domain in Eqs. (4.62) and (4.63) in discrete form. In view of the functional properties of \hat{E}_k and \hat{H}_j , we approximate the integrals in Eqs. (4.62) and (4.63) using a midpoint rule. We then arrive at

$$\hat{A}_{k;m,n,p} = \Delta x_1 \Delta x_2 \Delta x_3 \sum_{m'=1}^M \sum_{n'=1}^N \sum_{p'=1}^P \mathcal{G}(\mathbf{x}_{m,n,p} - \mathbf{x}_{m',n',p'}) \chi_{m',n',p'}^E \hat{E}_{k;m',n',p'}, \quad (4.114)$$

and

$$\hat{F}_{j;m,n,p} = \Delta x_1 \Delta x_2 \Delta x_3 \sum_{m'=1}^M \sum_{n'=1}^N \sum_{p'=1}^P \mathcal{G}(\mathbf{x}_{m,n,p} - \mathbf{x}_{m',n',p'}) \chi_{m',n',p'}^H \hat{H}_{j;m',n',p'}. \quad (4.115)$$

The discrete convolutions appearing in Eqs. (4.114) and (4.115) can be efficiently computed using 3D FFT routines.

4.4 Operator formulation

Now that we have obtained the weak forms of the pertaining (discrete) integral equations, we can form a system of linear equations for the electric and magnetic field quantities, in which the known electric and magnetic contrasts occur. We then proceed to solve this system using a conjugate gradient (CG) scheme, which we will describe in the next section. To this end we introduce the operator form of the system of integral equations for $\hat{\mathbf{E}}$ and $\hat{\mathbf{H}}$ as

$$\begin{bmatrix} \hat{\mathbf{E}}^i \\ \hat{\mathbf{H}}^i \end{bmatrix} = (\mathbf{I} - \mathbf{K}^D \chi) \begin{bmatrix} \hat{\mathbf{E}} \\ \hat{\mathbf{H}} \end{bmatrix}, \quad (4.116)$$

in which

$$\mathbf{I} = \text{diag}(\mathcal{I}, \mathcal{I}), \quad (4.117)$$

$$\chi = \text{diag}(\chi^E, \chi^H), \quad (4.118)$$

where \mathcal{I} is the identity operator. The operator matrix \mathbf{K}^D is defined as

$$\mathbf{K}^D = \begin{bmatrix} \kappa^{D,EE} & \kappa^{D,EH} \\ \kappa^{D,HE} & \kappa^{D,HH} \end{bmatrix}, \quad (4.119)$$

where the superscript D denotes the direct part of the Green's function, corresponding to a configuration with a homogeneous background. The elements of the operator

matrix \mathbf{K}^D are defined as

$$\mathcal{K}^{D,EE} \chi^E \hat{\mathbf{E}} = k_b^2 \hat{\mathbf{A}} + \hat{\mathbf{A}}', \quad (4.120)$$

$$\mathcal{K}^{D,EH} \chi^H \hat{\mathbf{H}} = i\omega\mu_b \hat{\mathbf{F}}'', \quad (4.121)$$

$$\mathcal{K}^{D,HH} \chi^H \hat{\mathbf{H}} = k_b^2 \hat{\mathbf{F}} + \hat{\mathbf{F}}', \quad (4.122)$$

$$\mathcal{K}^{D,HE} \chi^E \hat{\mathbf{E}} = \sigma_b \hat{\mathbf{A}}''. \quad (4.123)$$

4.4.1 Inner product and norm

For the CG method we need to define an inner product over the computational domain. In the continuous case and for three-dimensional vectorial quantities, this is given by

$$\langle \hat{\mathbf{E}}, \hat{\mathbf{H}} \rangle_D = \int_D \hat{\mathbf{E}}(\mathbf{x}) \cdot \overline{\hat{\mathbf{H}}(\mathbf{x})} d\mathbf{x}. \quad (4.124)$$

in which the overbar symbol denotes the complex conjugate. The discrete version of the inner product is defined as

$$\langle \hat{\mathbf{E}}, \hat{\mathbf{H}} \rangle_D = \Delta x_1 \Delta x_2 \Delta x_3 \sum_{k=1}^3 \sum_{m=1}^M \sum_{n=1}^N \sum_{p=1}^P \hat{\mathbf{E}}_{k,m,n,p} \overline{\hat{\mathbf{H}}_{k,m,n,p}}. \quad (4.125)$$

We now define the norm on D to be

$$\|\hat{\mathbf{E}}\|_D = \sqrt{\langle \hat{\mathbf{E}}, \hat{\mathbf{E}} \rangle_D}. \quad (4.126)$$

4.5 Conjugate Gradient scheme

In the conjugate gradient method a system of equations is solved by iteratively reducing a cost functional, which in our case is defined as

$$\begin{aligned} F_{D,n} &= \eta_D^E \|\mathbf{r}_n^E\|_D^2 + \eta_D^H \|\mathbf{r}_n^H\|_D^2, \\ &= \eta_D^E \left\| \hat{\mathbf{E}}^i - (\mathbf{I} - \mathcal{K}^{D,EE} \chi^E) \hat{\mathbf{E}}_n + \mathcal{K}^{D,EH} \chi^H \hat{\mathbf{H}}_n \right\|_D^2 \\ &\quad + \eta_D^H \left\| \hat{\mathbf{H}}^i - (\mathbf{I} - \mathcal{K}^{D,HH} \chi^H) \hat{\mathbf{H}}_n + \mathcal{K}^{D,HE} \chi^E \hat{\mathbf{E}}_n \right\|_D^2, \end{aligned} \quad (4.127)$$

where the residuals for the field components at iteration n are given by

$$\begin{bmatrix} \mathbf{r}_n^E \\ \mathbf{r}_n^H \end{bmatrix} = \begin{bmatrix} \hat{\mathbf{E}}^i \\ \hat{\mathbf{H}}^i \end{bmatrix} - (\mathbf{I} - \mathbf{K}^D \chi) \begin{bmatrix} \hat{\mathbf{E}} \\ \hat{\mathbf{H}} \end{bmatrix}_n, \quad (4.128)$$

and the normalization coefficients η_D^E and η_D^H are defined as

$$\eta_D^E = \frac{1}{\|\hat{\mathbf{E}}^i\|_D^2}, \quad (4.129)$$

$$\eta_D^H = \frac{1}{\|\hat{\mathbf{H}}^i\|_D^2}. \quad (4.130)$$

Note that the residuals are normalized such that the cost functional is dimensionless. The CG algorithm constructs sequences for the field vectors $\hat{\mathbf{E}}$ and $\hat{\mathbf{H}}$, which iteratively reduce the value of the cost functional defined in Eq. (4.127). The field vectors are updated as follows

$$\begin{bmatrix} \hat{\mathbf{E}} \\ \hat{\mathbf{H}} \end{bmatrix}_n = \begin{bmatrix} \hat{\mathbf{E}} \\ \hat{\mathbf{H}} \end{bmatrix}_{n-1} + \alpha_n \begin{bmatrix} \hat{\mathbf{e}} \\ \hat{\mathbf{h}} \end{bmatrix}_n, \quad (4.131)$$

in which α_n is a constant (scalar) weighting parameter and the update directions $\hat{\mathbf{e}}_n$ and $\hat{\mathbf{h}}_n$ are functions of position. The residuals at the n^{th} iteration can be written as

$$\begin{bmatrix} \mathbf{r}^E \\ \mathbf{r}^H \end{bmatrix}_n = \begin{bmatrix} \mathbf{r}^E \\ \mathbf{r}^H \end{bmatrix}_{n-1} - \alpha_n (\mathbf{I} - \mathbf{K}^D \chi) \begin{bmatrix} \hat{\mathbf{e}} \\ \hat{\mathbf{h}} \end{bmatrix}_n, \quad (4.132)$$

and the error at iteration n is defined as

$$\text{ERR}_n^2 = \eta_D^E \|\mathbf{r}_n^E\|_D^2 + \eta_D^H \|\mathbf{r}_n^H\|_D^2. \quad (4.133)$$

The algorithm will be completely specified when the starting values, update directions and weighting parameter are known. For the starting values of the field quantities we can take either zero or the incident field values (Born approximation). Additionally, when we need to use the CG scheme for a large number of frequencies and for the same configuration, we can use an extrapolation of the previously calculated field values as the starting values. This method is described by Tjihuis and Peng [77] and is called the Marching-on-in-Frequency method. We will discuss this technique in Section 4.7.

4.5.1 Update directions

The update directions are given by

$$\begin{bmatrix} \hat{\mathbf{e}} \\ \hat{\mathbf{h}} \end{bmatrix}_n = \begin{bmatrix} \partial \hat{\mathbf{e}} \\ \partial \hat{\mathbf{h}} \end{bmatrix}_n + \gamma_n \begin{bmatrix} \hat{\mathbf{e}} \\ \hat{\mathbf{h}} \end{bmatrix}_{n-1}. \quad (4.134)$$

For the first iteration, the update directions are simply the gradients of the cost functional with respect to the field values, i.e.,

$$\begin{bmatrix} \hat{\mathbf{e}} \\ \hat{\mathbf{h}} \end{bmatrix}_{n=1} = \begin{bmatrix} \partial \hat{\mathbf{e}} \\ \partial \hat{\mathbf{h}} \end{bmatrix}_{n=1}, \quad (4.135)$$

where

$$\partial \hat{\mathbf{e}}_n = \frac{\partial}{\partial \hat{\mathbf{E}}} F_{D;n-1}, \quad (4.136)$$

$$\partial \hat{\mathbf{h}}_n = \frac{\partial}{\partial \hat{\mathbf{H}}} F_{D;n-1}. \quad (4.137)$$

These gradients are calculated by using the Fréchet derivative, which is given by

$$\frac{\partial}{\partial \hat{\mathbf{E}}} F_{D;n-1} = \lim_{\delta \rightarrow 0} \frac{F_D(\hat{\mathbf{E}}_{n-1} + \delta \hat{\mathbf{e}}_n) - F_D(\hat{\mathbf{E}}_{n-1})}{\delta}, \quad (4.138)$$

$$\frac{\partial}{\partial \hat{\mathbf{H}}} F_{D;n-1} = \lim_{\delta \rightarrow 0} \frac{F_D(\hat{\mathbf{H}}_{n-1} + \delta \hat{\mathbf{h}}_n) - F_D(\hat{\mathbf{H}}_{n-1})}{\delta}. \quad (4.139)$$

Using the definition of the inner product, the gradients are obtained as

$$\begin{bmatrix} \partial \hat{\mathbf{e}} \\ \partial \hat{\mathbf{h}} \end{bmatrix}_n = (\mathbf{I} - \bar{\chi} \mathbf{K}^{D*}) \Gamma \begin{bmatrix} \mathbf{r}^E \\ \mathbf{r}^H \end{bmatrix}_{n-1}, \quad (4.140)$$

where the * symbol denotes the adjoint of the operator, which is given by

$$\mathbf{K}^{D,*} = \begin{bmatrix} \kappa^{D,EE*} & \kappa^{D,HE*} \\ \kappa^{D,EH*} & \kappa^{D,HH*} \end{bmatrix}, \quad (4.141)$$

and

$$\bar{\chi} = \text{diag}(\overline{\chi^E}, \overline{\chi^H}), \quad (4.142)$$

in which the overbar symbol again denotes the complex conjugate. The normalization matrix Γ in Eq. (4.140) is defined as

$$\Gamma = \text{diag}(\eta_D^E, \eta_D^H). \quad (4.143)$$

The coefficient γ_n for the update directions is defined as

$$\gamma_n = \frac{\|\partial \hat{\mathbf{e}}_n\|_D^2 + \|\partial \hat{\mathbf{h}}_n\|_D^2}{\|\partial \hat{\mathbf{e}}_{n-1}\|_D^2 + \|\partial \hat{\mathbf{h}}_{n-1}\|_D^2}, \quad (4.144)$$

for Fletcher-Reeves update directions and

$$\gamma_n = \frac{(\partial \hat{\mathbf{e}}_n, \partial \hat{\mathbf{e}}_n - \partial \hat{\mathbf{e}}_{n-1})_D + \langle \partial \hat{\mathbf{h}}_n, \partial \hat{\mathbf{h}}_n - \partial \hat{\mathbf{h}}_{n-1} \rangle_D}{\|\partial \hat{\mathbf{e}}_{n-1}\|_D^2 + \|\partial \hat{\mathbf{h}}_{n-1}\|_D^2}, \quad (4.145)$$

for Polak-Ribière update directions.

4.5.2 Weighting parameters

The weighting parameter α_n determines the length of the step taken along the CG direction at iteration n of the minimization scheme. The value of α_n is determined by setting the derivative of the cost functional with respect to the weighting parameter to zero, and solving for α_n , i.e.,

$$\frac{\partial}{\partial \alpha_n} F_{D,n} = 0. \quad (4.146)$$

This leads to

$$\begin{aligned} \alpha_n = & \left[\eta_D^E \left\| (\mathcal{I} - \mathcal{K}^{D,EE} \chi^E) \hat{e}_n + \mathcal{K}^{D,EH} \chi^H \hat{h}_n \right\|_D^2 + \right. \\ & \left. \eta_D^H \left\| (\mathcal{I} - \mathcal{K}^{D,HH} \chi^H) \hat{h}_n + \mathcal{K}^{D,HE} \chi^E \hat{e}_n \right\|_D^2 \right]^{-1} \times \\ & \left[\langle \partial \hat{e}_n, \hat{e}_n \rangle_D + \langle \partial \hat{h}_n, \hat{h}_n \rangle_D \right]. \end{aligned} \quad (4.147)$$

It should be noted that it is also possible to calculate the field quantities by using a CG scheme where two separate update coefficients and update directions are used for the fields. Strictly speaking this would not be a CG scheme since orthogonality between the update sequences is lost and consequently convergence is not guaranteed. Furthermore, it was found that numerical convergence for this pseudo CG scheme is slower.

4.5.3 The object operator and adjoint object operator

We will now define the operators and adjoint operators as described in the previous section, using the expressions for the electric and magnetic vector potentials and their derivatives, as given in Section 4.3. We recall that

$$\hat{A}_{k;m,n,p} = \Delta x_1 \Delta x_2 \Delta x_3 \sum_{m'=1}^M \sum_{n'=1}^N \sum_{p'=1}^P \mathcal{G}(\mathbf{x}_{m,n,p} - \mathbf{x}_{m',n',p'}) \chi_{m',n',p'}^E \hat{E}_{k;m',n',p'}, \quad (4.148)$$

$$\hat{F}_{j;m,n,p} = \Delta x_1 \Delta x_2 \Delta x_3 \sum_{m'=1}^M \sum_{n'=1}^N \sum_{p'=1}^P \mathcal{G}(\mathbf{x}_{m,n,p} - \mathbf{x}_{m',n',p'}) \chi_{m',n',p'}^H \hat{H}_{j;m',n',p'}, \quad (4.149)$$

$$\hat{A}'_{k;m,n,p} = \sum_{j=1}^3 \sum_{q=1}^M \sum_{r=1}^N \sum_{s=1}^P a_{m,n,p,q,r,s}^{(k,j)} \hat{A}_{j;q,r,s} \quad (4.150)$$

$$\hat{F}'_{j;m,n,p} = \sum_{k=1}^3 \sum_{q=1}^M \sum_{r=1}^N \sum_{s=1}^P f_{m,n,p,q,r,s}^{(j,k)} \hat{F}_{k;q,r,s} \quad (4.151)$$

$$\hat{A}''_{k;m,n,p} = \sum_{j=1}^3 \sum_{q=1}^M \sum_{r=1}^N \sum_{s=1}^P a''_{m,n,p,q,r,s}^{(k,j)} \hat{A}_{j;q,r,s} \quad (4.152)$$

$$\hat{F}''_{j;m,n,p} = \sum_{k=1}^3 \sum_{q=1}^M \sum_{r=1}^N \sum_{s=1}^P f''_{m,n,p,q,r,s}^{(j,k)} \hat{F}_{k;q,r,s} \quad (4.153)$$

Using the definition of the inner product over D , we substitute Eq. (4.148) and Eq. (4.150) into Eq. (4.125) and interchange the various summations, which results in the expressions for the elements of the adjoint operator \mathbf{K}^{D*} pertaining to the integral equation of the electric type

$$(\mathcal{K}^{D,EE*} \eta_D^E \mathbf{r}^E)_{k;m,n,p} = \quad (4.154)$$

$$\Delta x_1 \Delta x_2 \Delta x_3 \eta_D^E \sum_{m'=0}^{M+1} \sum_{n'=0}^{N+1} \sum_{p'=0}^{P+1} \bar{\mathcal{G}}(\mathbf{x}_{m,n,p} - \mathbf{x}_{m',n',p'}) M_{k;m',n',p'}^{EE}$$

in which

$$M_{k;m,n,p}^{EE} = \bar{k}_b^2 r_{k;m,n,p}^E + \sum_{j=1}^3 \sum_{q=1}^M \sum_{r=1}^N \sum_{s=1}^P a_{m,n,p,q,r,s}^{(k,j)} r_{j;q,r,s}^E \quad (4.155)$$

For the $\mathcal{K}^{D,HE*}$ element of \mathbf{K}^{D*} we obtain

$$(\mathcal{K}^{D,HE*} \eta_D^H \mathbf{r}^H)_{k;m,n,p} = \quad (4.156)$$

$$\Delta x_1 \Delta x_2 \Delta x_3 \eta_D^H \sum_{m'=0}^{M+1} \sum_{n'=0}^{N+1} \sum_{p'=0}^{P+1} \bar{\mathcal{G}}(\mathbf{x}_{m,n,p} - \mathbf{x}_{m',n',p'}) M_{k;m',n',p'}^{HE}$$

in which

$$M_{k;m,n,p}^{HE} = (\sigma_b - i\omega\epsilon_0) \sum_{j=1}^3 \sum_{q=1}^M \sum_{r=1}^N \sum_{s=1}^P f''_{m,n,p,q,r,s}^{(k,j)} r_{j;q,r,s}^H \quad (4.157)$$

Note that the summations occurring in Eqs. (4.154) and (4.156) are discrete convolutions, which can be efficiently calculated using FFT routines. For the components of the adjoint operator pertaining to the integral equation of the magnetic type, $\mathcal{K}^{D,EH*}$ and $\mathcal{K}^{D,HH*}$, we follow a similar procedure, leading to

$$(\mathcal{K}^{D,EH*} \eta_D^E \mathbf{r}^E)_{j;m,n,p} = \quad (4.158)$$

$$\Delta x_1 \Delta x_2 \Delta x_3 \eta_D^E \sum_{m'=0}^{M+1} \sum_{n'=0}^{N+1} \sum_{p'=0}^{P+1} \bar{\mathcal{G}}(\mathbf{x}_{m,n,p} - \mathbf{x}_{m',n',p'}) M_{j;m',n',p'}^{EH}$$

where

$$M_{j;m,n,p}^{EH} = \overline{i\omega\mu_b} \sum_{k=1}^3 \sum_{q=1}^M \sum_{r=1}^N \sum_{s=1}^P a''^{(j,k)}_{m,n,p,q,r,s} r_{k;q,r,s}^E \quad (4.159)$$

For \mathcal{K}^{D,HH^*} element of \mathbf{K}^{D^*} we obtain

$$\left(\mathcal{K}^{D,HH^*} \eta_D^H \mathbf{r}^H \right)_{j;m,n,p} = \Delta x_1 \Delta x_2 \Delta x_3 \eta_D^H \sum_{m'=0}^{M+1} \sum_{n'=0}^{N+1} \sum_{p'=0}^{P+1} \bar{G}(\mathbf{x}_{m,n,p} - \mathbf{x}_{m',n',p'}) M_{j;m',n',p'}^{HH} \quad (4.160)$$

in which

$$M_{j;m,n,p}^{HH} = \overline{k_b^2} r_{j;m,n,p}^H + \sum_{k=1}^3 \sum_{q=1}^M \sum_{r=1}^N \sum_{s=1}^P f_{m,n,p,q,r,s}^{(j,k)} r_{k;q,r,s}^H \quad (4.161)$$

The discrete convolutions occurring in Eqs. (4.158) and (4.160) are again calculated using FFT routines. Since the summations in the expressions for the elements of the adjoint operator run from $m' = 0$ to $M + 1$, $n' = 0$ to $N + 1$ and $p' = 0$ to $P + 1$, we set

$$r_{k;m,n,p}^{E,H} = 0, \quad \text{for } m = -1, 0, M + 1, M + 2, \quad \forall n, p, \quad (4.162)$$

$$r_{k;m,n,p}^{E,H} = 0, \quad \text{for } n = -1, 0, N + 1, N + 2, \quad \forall m, p, \quad (4.163)$$

$$r_{k;m,n,p}^{E,H} = 0, \quad \text{for } p = -1, 0, P + 1, P + 2, \quad \forall m, n, \quad (4.164)$$

in Eqs. (4.155), (4.157), (4.159) and (4.161). In Figure 4.4, we illustrate the different areas in the computational domain where the vector potentials are defined and where the residuals are set to zero to obtain a boundary condition for the finite difference scheme. The contrasts are constrained to the shaded domain D_1 , which is defined by $m = 1, \dots, M$, $n = 1, \dots, N$ and $p = 1, \dots, P$. Because of the finite difference operators acting on the vector potentials, we calculate the vector potentials on domain D_2 , which is defined by $m = 0, \dots, M + 1$, $n = 0, \dots, N + 1$ and $p = 0, \dots, P + 1$. Note that if we had used a larger finite difference stencil, domain D_2 would have to be larger as well. Finally, the residuals need yet another extra layer of grid cells (again because of the finite difference operators), hence the residuals are defined on domain D_3 , which is given by $m = -1, \dots, M + 2$, $n = -1, \dots, N + 2$ and $p = -1, \dots, P + 2$. Note that the residuals are set to zero for the cells indicated in Eqs. (4.162) - (4.164).

4.5.4 The data operator and the adjoint data operator

The data operator maps the total fields $\hat{\mathbf{E}}$ and $\hat{\mathbf{H}}$ from the scattering domain D to the receiver domain S . It is assumed that the receiver domain and the computational

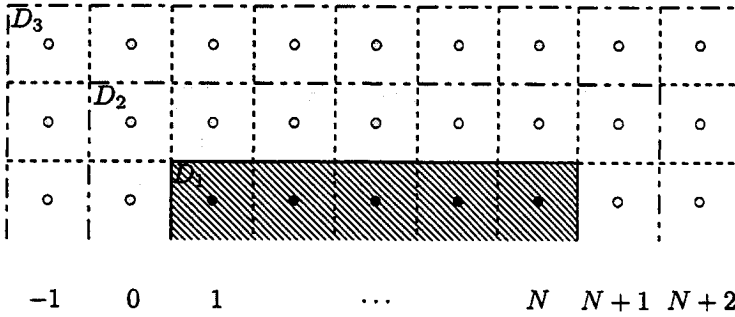


Figure 4.4: Slice of the discretized computational domain, with D_1 the domain where the contrasts are defined, D_2 the domain where the vector potentials are defined and D_3 the domain where the residuals are defined.

domain do not overlap, i.e., $D \cap S = 0$. The scattered electric and magnetic fields at the receiver locations are given by

$$\hat{\mathbf{E}}^S(\mathbf{x}) = \int_{\mathbf{x}' \in D^S} \left(\mathcal{G}^{EE}(\mathbf{x}, \mathbf{x}') \cdot \chi^E \hat{\mathbf{E}}(\mathbf{x}') + \mathcal{G}^{EH}(\mathbf{x}, \mathbf{x}') \cdot \chi^H \hat{\mathbf{H}}(\mathbf{x}') \right) d\mathbf{x}', \quad (4.165)$$

$$\hat{\mathbf{H}}^S(\mathbf{x}) = \int_{\mathbf{x}' \in D^S} \left(\mathcal{G}^{HH}(\mathbf{x}, \mathbf{x}') \cdot \chi^H \hat{\mathbf{H}}(\mathbf{x}') + \mathcal{G}^{HE}(\mathbf{x}, \mathbf{x}') \cdot \chi^E \hat{\mathbf{E}}(\mathbf{x}') \right) d\mathbf{x}'. \quad (4.166)$$

We can write this in operator form as

$$\begin{bmatrix} \hat{\mathbf{E}}^S \\ \hat{\mathbf{H}}^S \end{bmatrix} = \mathbf{K}^S \chi \begin{bmatrix} \hat{\mathbf{E}} \\ \hat{\mathbf{H}} \end{bmatrix}, \quad (4.167)$$

where the contrast matrix χ is defined in Eq. (4.118), and the data operator \mathbf{K}^S is given by

$$\mathbf{K}^S = \begin{bmatrix} \mathcal{K}^{S,EE} & \mathcal{K}^{S,EH} \\ \mathcal{K}^{S,HE} & \mathcal{K}^{S,HH} \end{bmatrix}. \quad (4.168)$$

The elements of the operator matrix \mathbf{K}^S are given by

$$\left(\mathcal{K}^{S,EE}\chi^E\hat{\mathbf{E}}\right)(\mathbf{x}) = \int_{\mathbf{x}'\in D} (k_b^2 + \nabla\nabla\cdot)\hat{G}(\mathbf{x}-\mathbf{x}')\chi^E(\mathbf{x}')\hat{\mathbf{E}}(\mathbf{x}')d\mathbf{x}', \quad (4.169)$$

$$\left(\mathcal{K}^{S,EH}\chi^H\hat{\mathbf{H}}\right)(\mathbf{x}) = i\omega\mu_b \int_{\mathbf{x}'\in D} \nabla \times \hat{G}(\mathbf{x}-\mathbf{x}')\chi^H(\mathbf{x}')\hat{\mathbf{H}}(\mathbf{x}')d\mathbf{x}', \quad (4.170)$$

$$\left(\mathcal{K}^{S,HH}\chi^H\hat{\mathbf{H}}\right)(\mathbf{x}) = \int_{\mathbf{x}'\in D} (k_b^2 + \nabla\nabla\cdot)\hat{G}(\mathbf{x}-\mathbf{x}')\chi^H(\mathbf{x}')\hat{\mathbf{H}}(\mathbf{x}')d\mathbf{x}', \quad (4.171)$$

$$\left(\mathcal{K}^{S,HE}\chi^E\hat{\mathbf{E}}\right)(\mathbf{x}) = (\sigma_b - i\omega\varepsilon_0) \int_{\mathbf{x}'\in D} \nabla \times \hat{G}(\mathbf{x}-\mathbf{x}')\chi^E(\mathbf{x}')\hat{\mathbf{E}}(\mathbf{x}')d\mathbf{x}'. \quad (4.172)$$

Note that the differentiations act on the scalar Green's function only. Since the two domains D and S do not overlap, we have no singularity in the Green's function and hence the differentiations occurring in Eqs. (4.169) – (4.172) can be performed analytically, which results in

$$\partial_k\hat{G}(\mathbf{x}) = \frac{\exp(ik_bR)}{4\pi R^3} (ik_bR - 1) x_k, \quad (4.173)$$

and

$$\begin{aligned} \partial_k\partial_j\hat{G}(\mathbf{x}) &= \frac{1}{4\pi} \left[\frac{1}{R^3} \left(\frac{3x_kx_j}{R^2} - \delta_{k,j} \right) - \frac{ik_b}{R^2} \left(\frac{3x_kx_j}{R^2} - \delta_{k,j} \right) \right. \\ &\quad \left. + \frac{(ik_b)^2}{R} \frac{x_kx_j}{R^2} \right] \exp(ik_bR), \end{aligned} \quad (4.174)$$

where the distance function $R(\mathbf{x})$ is defined by

$$R(\mathbf{x}) = (x_1^2 + x_2^2 + x_3^2)^{\frac{1}{2}} = |\mathbf{x}|. \quad (4.175)$$

Adjoint data operator

For the inverse problem, we will need the adjoint data operator. In order to be able to define the adjoint data operator, we first need to define an inner product and a norm on the receiver domain S . The inner product of a three-dimensional vector on S is defined as

$$\langle \hat{\mathbf{E}}^S, \hat{\mathbf{H}}^S \rangle_S = \sum_{\mathbf{x}\in S} \hat{\mathbf{E}}^S(\mathbf{x}) \cdot \overline{\hat{\mathbf{H}}^S(\mathbf{x})}, \quad (4.176)$$

where the superscript 'S' denotes a scattered field quantity at the receiver positions. The norm on the receiver domain S is given by

$$\|\hat{\mathbf{E}}^S\|_S^2 = \langle \hat{\mathbf{E}}^S, \hat{\mathbf{E}}^S \rangle_S. \quad (4.177)$$

Using the definition of the inner products on S and D , we can now define the adjoint data operator \mathbf{K}^{S*} as the complex conjugate transpose of \mathbf{K}^S , giving

$$\mathbf{K}^{S*} = \begin{bmatrix} \mathcal{K}^{S,EE*} & \mathcal{K}^{S,HE*} \\ \mathcal{K}^{S,EH*} & \mathcal{K}^{S,HH*} \end{bmatrix}. \quad (4.178)$$

Discretized data operator

Using the definitions of the various vector quantities and discretizing the integrals gives the discrete representation for the scattered electric and magnetic fields at the receiver positions.

$$\begin{aligned} \hat{E}_k^S(\mathbf{x}^S) &= k_b^2 \Delta x_1 \Delta x_2 \Delta x_3 \sum_{m=1}^M \sum_{n=1}^N \sum_{p=1}^P \hat{G}(\mathbf{x}^S - \mathbf{x}_{m,n,p}) \chi_{m,n,p}^E \hat{E}_{k;m,n,p} \\ &+ \Delta x_1 \Delta x_2 \Delta x_3 \sum_{m=1}^M \sum_{n=1}^N \sum_{p=1}^P \partial_k \partial_j \hat{G}(\mathbf{x}^S - \mathbf{x}_{m,n,p}) \chi_{m,n,p}^E \hat{E}_{j;m,n,p} \\ &+ i\omega \mu_b \Delta x_1 \Delta x_2 \Delta x_3 \sum_{m=1}^M \sum_{n=1}^N \sum_{p=1}^P \epsilon_{k,r,s} \partial_r \hat{G}(\mathbf{x}^S - \mathbf{x}_{m,n,p}) \chi_{m,n,p}^H \hat{H}_{s;m,n,p}. \end{aligned} \quad (4.179)$$

The magnetic field at the receiver points is given by

$$\begin{aligned} \hat{H}_j^S(\mathbf{x}^S) &= k_b^2 \Delta x_1 \Delta x_2 \Delta x_3 \sum_{m=1}^M \sum_{n=1}^N \sum_{p=1}^P \hat{G}(\mathbf{x}^S - \mathbf{x}_{m,n,p}) \chi_{m,n,p}^H \hat{H}_{j;m,n,p} \\ &+ \Delta x_1 \Delta x_2 \Delta x_3 \sum_{m=1}^M \sum_{n=1}^N \sum_{p=1}^P \partial_j \partial_k \hat{G}(\mathbf{x}^S - \mathbf{x}_{m,n,p}) \chi_{m,n,p}^H \hat{H}_{k;m,n,p} \\ &+ (\sigma_b - i\omega \epsilon_0) \Delta x_1 \Delta x_2 \Delta x_3 \sum_{m=1}^M \sum_{n=1}^N \sum_{p=1}^P \epsilon_{j,r,s} \partial_r \hat{G}(\mathbf{x}^S - \mathbf{x}_{m,n,p}) \chi_{m,n,p}^E \hat{E}_{s;m,n,p}. \end{aligned} \quad (4.180)$$

Note that we have used point-matching to calculate the scattered fields at the receiver positions.

Discretized adjoint data operator

The elements of the discrete adjoint data operator working on $\hat{\mathbf{E}}^S$ and $\hat{\mathbf{H}}^S$ are given by

$$\begin{aligned} \left(\overline{\chi^E} \mathcal{K}^{S,EE*} \hat{\mathbf{E}}^S \right)_{k;m,n,p} &= \overline{\chi_{m,n,p}^E} \sum_{\mathbf{x}^S \in S} \left[k_b^2 \overline{\hat{G}}(\mathbf{x}_{m,n,p} - \mathbf{x}^S) \hat{E}_k^S(\mathbf{x}^S) \right. \\ &\quad \left. + \partial_k \partial_j \overline{\hat{G}}(\mathbf{x}_{m,n,p} - \mathbf{x}^S) \hat{E}_j^S(\mathbf{x}^S) \right], \end{aligned} \quad (4.181)$$

$$\left(\overline{\chi^H} \mathcal{K}^{S,EH*} \hat{\mathbf{E}}^S \right)_{k;m,n,p} = \overline{i\omega\mu_b \chi_{m,n,p}^H} \sum_{\mathbf{x}^S \in S} \epsilon_{k,r,s} \partial_r \overline{\hat{G}}(\mathbf{x}_{m,n,p} - \mathbf{x}^S) \hat{E}_s^S, \quad (4.182)$$

$$\begin{aligned} \left(\overline{\chi^H} \mathcal{K}^{S,HH*} \hat{\mathbf{H}}^S \right)_{k;m,n,p} &= \overline{\chi_{m,n,p}^H} \sum_{\mathbf{x}^S \in S} \left[k_b^2 \overline{\hat{G}}(\mathbf{x}_{m,n,p} - \mathbf{x}^S) \hat{H}_k^S \right. \\ &\quad \left. + \partial_k \partial_j \overline{\hat{G}}(\mathbf{x}_{m,n,p} - \mathbf{x}^S) \hat{H}_j^S \right], \end{aligned} \quad (4.183)$$

$$\left(\overline{\chi^E} \mathcal{K}^{S,HE*} \hat{\mathbf{H}}^S \right)_{k;m,n,p} = (\sigma_b - \overline{i\omega\epsilon_0}) \overline{\chi_{m,n,p}^E} \sum_{\mathbf{x}^S \in S} \epsilon_{k,r,s} \partial_r \overline{\hat{G}}(\mathbf{x}_{m,n,p} - \mathbf{x}^S) \hat{H}_s^S. \quad (4.184)$$

4.6 Preconditioning operator

To accelerate the convergence of the CG scheme for configurations with high contrasts, we will now discuss a preconditioning operator for the CG scheme based on the extended Born approximation. The extended Born approximation was introduced by Habashy *et al.* [36] and [79], who have shown that this technique works very well for diffusive problems over a wide range of frequencies. We can write the preconditioned system of integral equations as

$$\mathbf{P} \begin{bmatrix} \hat{\mathbf{E}}^i \\ \hat{\mathbf{H}}^i \end{bmatrix} = \mathbf{P} (\mathbf{I} - \mathbf{K}^D \chi) \begin{bmatrix} \hat{\mathbf{E}} \\ \hat{\mathbf{H}} \end{bmatrix}, \quad (4.185)$$

in which \mathbf{P} is the preconditioning operator. Ideally, the preconditioning operator \mathbf{P} should be chosen such that the product $\mathbf{P} (\mathbf{I} - \mathbf{K}^D \chi)$ is the identity operator, in which case the system of equations would be solved. However, this is usually not possible, and therefore we must find an approximation to this 'ideal' preconditioning operator. In our case, we choose to use a preconditioning operator derived from the extended Born approximation.

Preconditioned gradients

Using the preconditioning operator, we obtain new expressions for the gradients with respect to the fields

$$\begin{bmatrix} \partial \hat{e} \\ \partial \hat{h} \end{bmatrix}_n^P = \mathbf{PP}^* \begin{bmatrix} \partial \hat{e} \\ \partial \hat{h} \end{bmatrix}, \quad (4.186)$$

$$= \mathbf{PP}^* (\mathbf{I} - \bar{\chi} \mathbf{K}^{D*}) \Gamma \begin{bmatrix} \mathbf{r}^E \\ \mathbf{r}^H \end{bmatrix}_{n-1}, \quad (4.187)$$

where the superscript P denotes the preconditioned gradients and the $*$ symbol denotes the adjoint of the operator. The preconditioning operator \mathbf{P} is calculated once at the start of the CG scheme for all points in the computational grid. Apart from the preconditioned gradients, the CG scheme is implemented as before.

Extended Born approximation

Following Abubakar [2], who used this technique for preconditioning of a CG scheme for integral equations of the electric type, we first write our system of integral equations (cf. Eq. (4.116)) as

$$\begin{bmatrix} \hat{\mathbf{E}} \\ \hat{\mathbf{H}} \end{bmatrix}(\mathbf{x}) = \begin{bmatrix} \hat{\mathbf{E}}^i \\ \hat{\mathbf{H}}^i \end{bmatrix}(\mathbf{x}) + \mathbf{K}^D(\mathbf{x}, \mathbf{x}') \begin{bmatrix} \hat{\mathbf{W}}^E \\ \hat{\mathbf{W}}^H \end{bmatrix}(\mathbf{x}'), \quad (4.188)$$

where we have explicitly indicated the spatial dependence of each quantity (note that the integral operator \mathbf{K}^D works on the primed coordinates). The contrast sources $\hat{\mathbf{W}}^E$ and $\hat{\mathbf{W}}^H$ in Eq. (4.188) are defined as

$$\begin{bmatrix} \hat{\mathbf{W}}^E \\ \hat{\mathbf{W}}^H \end{bmatrix}(\mathbf{x}') = \chi(\mathbf{x}') \begin{bmatrix} \hat{\mathbf{E}} \\ \hat{\mathbf{H}} \end{bmatrix}(\mathbf{x}'). \quad (4.189)$$

We now rewrite Eq. (4.188) as

$$\begin{bmatrix} \hat{\mathbf{E}} \\ \hat{\mathbf{H}} \end{bmatrix}(\mathbf{x}) = \begin{bmatrix} \hat{\mathbf{E}}^i \\ \hat{\mathbf{H}}^i \end{bmatrix}(\mathbf{x}) + \mathbf{K}^D(\mathbf{x}, \mathbf{x}') \left(\begin{bmatrix} \hat{\mathbf{W}}^E \\ \hat{\mathbf{W}}^H \end{bmatrix}(\mathbf{x}') - \begin{bmatrix} \hat{\mathbf{W}}^E \\ \hat{\mathbf{W}}^H \end{bmatrix}(\mathbf{x}) \right) + \mathbf{K}^D(\mathbf{x}, \mathbf{x}') \begin{bmatrix} \hat{\mathbf{W}}^E \\ \hat{\mathbf{W}}^H \end{bmatrix}(\mathbf{x}). \quad (4.190)$$

Note again that the integral operator matrix \mathbf{K}^D works on quantities with the primed coordinates. We now move the last term on the right-hand side of Eq. (4.190) to the left-hand side and rewrite the contrast sources occurring in this term in the form given in Eq. (4.189). The left-hand side of Eq. (4.190) is now given by

$(\mathbf{I} - \chi \mathbf{K}^D \mathbf{I}) \begin{bmatrix} \hat{\mathbf{E}} \\ \hat{\mathbf{H}} \end{bmatrix}$. Using these expressions, Eq. (4.190) can be rewritten as

$$\begin{bmatrix} \hat{\mathbf{E}} \\ \hat{\mathbf{H}} \end{bmatrix}(\mathbf{x}) = \left(\mathbf{I}(\mathbf{x}) - \chi(\mathbf{x}) \mathbf{K}^D(\mathbf{x}, \mathbf{x}') \mathbf{I}(\mathbf{x}') \right)^{-1} \times \quad (4.191) \\ \left(\begin{bmatrix} \hat{\mathbf{E}}^i \\ \hat{\mathbf{H}}^i \end{bmatrix}(\mathbf{x}) + \mathbf{K}^D(\mathbf{x}, \mathbf{x}') \left(\begin{bmatrix} \hat{\mathbf{W}}^E \\ \hat{\mathbf{W}}^H \end{bmatrix}(\mathbf{x}') - \begin{bmatrix} \hat{\mathbf{W}}^E \\ \hat{\mathbf{W}}^H \end{bmatrix}(\mathbf{x}) \right) \right).$$

Because of the singularity of the Green's function, we now assume that the main contribution to the convolution integrals in the operator \mathbf{K}^D comes from points around $\mathbf{x}' = \mathbf{x}$. In that case, we can neglect the terms containing the contrast sources in Eq. (4.191), since the term $\hat{\mathbf{W}}^{E,H}(\mathbf{x}') - \hat{\mathbf{W}}^{E,H}(\mathbf{x})$ is close to zero around $\mathbf{x}' = \mathbf{x}$. Therefore we can approximate the field quantities by writing

$$\begin{bmatrix} \hat{\mathbf{E}} \\ \hat{\mathbf{H}} \end{bmatrix}(\mathbf{x}) \approx \mathbf{P}(\mathbf{x}) \begin{bmatrix} \hat{\mathbf{E}}^i \\ \hat{\mathbf{H}}^i \end{bmatrix}(\mathbf{x}), \quad (4.192)$$

which is the extended Born approximation. This amounts to assuming that the field quantities within the scattering domain D^S can be accurately approximated by their first order Taylor expansion around the point $\mathbf{x}' = \mathbf{x}$ (i.e., we state that $\hat{\mathbf{W}}(\mathbf{x}') = \hat{\mathbf{W}}(\mathbf{x})$, which is referred to as the localized approximation). The operator $\mathbf{P}(\mathbf{x})$ is defined by

$$\mathbf{P}(\mathbf{x}) = \left(\mathbf{I} - \chi \mathbf{K}^D \mathbf{I} \right)^{-1}(\mathbf{x}), \quad (4.193)$$

or, explicitly

$$\mathbf{P}(\mathbf{x}) = \quad (4.194)$$

$$\begin{bmatrix} \mathbf{I} - \chi^E(\mathbf{x}) \int_{\mathbf{x}' \in D^S} \mathcal{G}^{EE}(\mathbf{x}, \mathbf{x}') \cdot \text{Id}\mathbf{x}' & -\chi^H(\mathbf{x}) \int_{\mathbf{x}' \in D^S} \mathcal{G}^{EH}(\mathbf{x}, \mathbf{x}') \cdot \text{Id}\mathbf{x}' \\ -\chi^E(\mathbf{x}) \int_{\mathbf{x}' \in D^S} \mathcal{G}^{HE}(\mathbf{x}, \mathbf{x}') \cdot \text{Id}\mathbf{x}' & \mathbf{I} - \chi^H(\mathbf{x}) \int_{\mathbf{x}' \in D^S} \mathcal{G}^{HH}(\mathbf{x}, \mathbf{x}') \cdot \text{Id}\mathbf{x}' \end{bmatrix}^{-1}.$$

Writing the preconditioning operator as

$$\mathbf{P} = \begin{bmatrix} \mathcal{P}^{EE} & \mathcal{P}^{EH} \\ \mathcal{P}^{HE} & \mathcal{P}^{HH} \end{bmatrix}^{-1}, \quad (4.195)$$

we can see that this is a 6 by 6 matrix for each discrete grid position. The submatrices \mathcal{P}^{EE} and \mathcal{P}^{HH} are symmetric, while the submatrices \mathcal{P}^{EH} and \mathcal{P}^{HE} are antisymmetric, with zeroes on the diagonal. It is possible to derive a simplified preconditioning operator by setting \mathcal{P}^{EH} and \mathcal{P}^{HE} to 0, creating a block-diagonal matrix for \mathbf{P} , which has an inverse that is simpler to implement and is computationally less costly. The preconditioning operator is calculated using the same numerical techniques that we use to calculate the integral operator matrix \mathbf{K}^D .

4.7 Marching-on-in-frequency

When performing the CG scheme for a series of values of the same parameter (such as stepping in frequency) while the rest of the configuration is invariant, one can use the previously obtained results to calculate an improved initial guess for the CG scheme (see Tijhuis and Peng [77], [64]). Since calculating the response of the PEC tool (i.e., solving the forward problem) involves calculating a time domain signal, we need to solve the previously described system of integral equations for a large number of frequencies, where the configuration is invariant. Therefore we use the marching-on-in-frequency scheme to solve the forward problem, calculating the field quantities in the scatterer for a number of frequencies $\omega_0 + k\Delta\omega$, $k = 1, \dots, K$, while implicitly assuming that the field solution does not change considerably over one frequency step. In that case it is advantageous not to start with a zero initial estimate for the fields at the start of the CG scheme, but instead we can extrapolate the previously calculated field quantities to obtain the initial guess. By using marching-on-in-frequency for the initial guess of the CG scheme, we are able to reduce the number of iterations significantly (see Section 5.3).

The marching-on-in-frequency method is based on the fact that when the frequency step is small, the successive field solutions will not differ significantly at each frequency step. If that is the case, we can write the initial guess for the field quantities at frequency ω_k as linear combination the previous results, i.e.,

$$\begin{bmatrix} \hat{\mathbf{E}} \\ \hat{\mathbf{H}} \end{bmatrix}_{n=0}(\omega_k) = \sum_{m=1}^M \xi_m \begin{bmatrix} \hat{\mathbf{E}} \\ \hat{\mathbf{H}} \end{bmatrix}(\omega_{k-m}), \quad (4.196)$$

where the ω symbol between brackets denotes the frequency dependence of the corresponding quantity and the quantity ξ_m denotes the (complex) extrapolation coefficients. Substituting this in Eq. (4.116) results in

$$\mathbf{L}(\omega_k) \left(\sum_{m=1}^M \xi_m \begin{bmatrix} \hat{\mathbf{E}} \\ \hat{\mathbf{H}} \end{bmatrix}(\omega_{k-m}) \right) = \begin{bmatrix} \hat{\mathbf{E}}^i \\ \hat{\mathbf{H}}^i \end{bmatrix}(\omega_k), \quad (4.197)$$

where the integral operator \mathbf{L} is given by

$$\mathbf{L}(\omega_k) = \mathbf{I} - \mathbf{K}^D(\omega_k)\chi. \quad (4.198)$$

Defining $\mathbf{L}_k = \mathbf{L}(\omega_k)$, $\mathbf{U}_k = [\hat{\mathbf{E}} \ \hat{\mathbf{H}}]^T(\omega_k)$ and $\mathbf{U}_k^i = [\hat{\mathbf{E}}^i \ \hat{\mathbf{H}}^i]^T(\omega_k)$, we now write Eq. (4.197) in matrix form as

$$[\mathbf{L}_k \mathbf{U}_{k-1} \ \mathbf{L}_k \mathbf{U}_{k-1} \ \cdots \ \mathbf{L}_k \mathbf{U}_{k-M}] \cdot \begin{bmatrix} \xi_1 \\ \xi_2 \\ \vdots \\ \xi_M \end{bmatrix} = \mathbf{U}_k^i. \quad (4.199)$$

Next, we choose the extrapolation coefficients such that Eq. (4.199) is satisfied in a least-squares sense, leading to

$$\begin{bmatrix} \mathbf{L}_k U_{k-1} \\ \mathbf{L}_k U_{k-2} \\ \vdots \\ \mathbf{L}_k U_{k-M} \end{bmatrix}^* [\mathbf{L}_k U_{k-1} \quad \mathbf{L}_k U_{k-1} \quad \cdots \quad \mathbf{L}_k U_{k-M}] \cdot \begin{bmatrix} \xi_1 \\ \xi_2 \\ \vdots \\ \xi_M \end{bmatrix} = \begin{bmatrix} \mathbf{L}_k U_{k-1} \\ \mathbf{L}_k U_{k-2} \\ \vdots \\ \mathbf{L}_k U_{k-M} \end{bmatrix}^* U_k^i \quad (4.200)$$

Using the definition of the inner product, we now obtain the following system of linear equations for the extrapolation coefficients ξ_m

$$\sum_{m'=1}^M \langle \mathbf{L}(\omega_k) \begin{bmatrix} \hat{\mathbf{E}} \\ \hat{\mathbf{H}} \end{bmatrix} (\omega_{k-m}), \mathbf{L}(\omega_k) \begin{bmatrix} \hat{\mathbf{E}} \\ \hat{\mathbf{H}} \end{bmatrix} (\omega_{k-m'}) \rangle_D \xi_{m'} = \langle \mathbf{L}(\omega_k) \begin{bmatrix} \hat{\mathbf{E}} \\ \hat{\mathbf{H}} \end{bmatrix} (\omega_{k-m}), \begin{bmatrix} \hat{\mathbf{E}}^i \\ \hat{\mathbf{H}}^i \end{bmatrix} (\omega_k) \rangle_D, \quad m = 1, \dots, M, \quad (4.201)$$

By taking this choice of extrapolation coefficients, the vector of incident fields $[\hat{\mathbf{E}}^i \hat{\mathbf{H}}^i]^T$ at frequency ω_k is projected onto the space spanned by the vectors $\{\mathbf{L}(\omega_k)[\hat{\mathbf{E}} \hat{\mathbf{H}}]^T(\omega_{k-m}), m = 1, \dots, M\}$. Consequently, the residual $[\mathbf{r}^E \mathbf{r}^H]_{n=0}^T(\omega_k)$ at first iteration of the CG scheme at frequency ω_k is orthogonal to that space and the CG scheme will search for update directions which are orthogonal to that space as well. The value of M determines the type of extrapolation, for example $M = 2$ gives linear extrapolation, whereas $M = 3$ gives quadratic extrapolation. For large values of M the previous field solutions will become almost linearly dependent, hence no further improvement can be obtained. Note that it is also possible to do 'marching-on-in-scatterer-size', where the frequency is kept constant and the only changing parameter is, for example, the size of the scatterer. Note that we have not used marching-on-in-frequency for the inverse problem, we only consider single-frequency inversion in this thesis.

4.8 Calculation of the incident fields

In this section we will calculate the incident fields corresponding to a magnetic dipole. The incident field of a circular loop source is obtained using the expressions derived in Appendix A. These sources are assumed to be located in a homogeneous space with conductivity σ_b , permeability μ_b and permittivity ϵ_0 .

4.8.1 Incident field of a magnetic dipole

In the case of a magnetic dipole oriented in the i_3 -direction, we have the following source terms for Maxwell's equations

$$\mathbf{j}^{ext}(\mathbf{x}) = \mathbf{0}, \quad (4.202)$$

$$\hat{\mathbf{K}}^{ext}(\mathbf{x}) = i\omega\mu_b\delta(\mathbf{x} - \mathbf{x}^S)\mathbf{i}_3, \quad (4.203)$$

where \mathbf{x}^S denotes the source position. The incident fields are then given by

$$\hat{\mathbf{E}}^{inc}(\mathbf{x}) = -\nabla \times \int_{\mathbf{x}' \in D^{ext}} \hat{G}(\mathbf{x} - \mathbf{x}') \hat{\mathbf{K}}^{ext}(\mathbf{x}') d\mathbf{x}', \quad (4.204)$$

$$\hat{\mathbf{H}}^{inc}(\mathbf{x}) = -\frac{1}{i\omega\mu_b} [k_b^2 + \nabla\nabla\cdot] \int_{\mathbf{x}' \in D^{ext}} \hat{G}(\mathbf{x} - \mathbf{x}') \hat{\mathbf{K}}^{ext}(\mathbf{x}') d\mathbf{x}', \quad (4.205)$$

in which $\hat{G}(\mathbf{x})$ is the scalar Green's function defined in Eq. (4.54). Substitution of the sources given in Eqs. (4.202) and (4.203) into these equations yields

$$\hat{\mathbf{E}}^{inc}(\mathbf{x}) = -i\omega\mu_b \nabla \times [\hat{G}(\mathbf{x} - \mathbf{x}')\mathbf{i}_3], \quad (4.206)$$

$$= -i\omega\mu_b [\partial_2 \hat{G}(\mathbf{x} - \mathbf{x}')\mathbf{i}_1 - \partial_1 \hat{G}(\mathbf{x} - \mathbf{x}')\mathbf{i}_2], \quad (4.207)$$

and

$$\hat{\mathbf{H}}^{inc}(\mathbf{x}) = -[k_b^2 + \nabla\nabla\cdot] (\hat{G}(\mathbf{x} - \mathbf{x}')\mathbf{i}_3), \quad (4.208)$$

$$= -[\partial_1 \partial_3 \hat{G}(\mathbf{x} - \mathbf{x}')\mathbf{i}_1 + \partial_2 \partial_3 \hat{G}(\mathbf{x} - \mathbf{x}')\mathbf{i}_2 + (\partial_3^2 + k_b^2) \hat{G}(\mathbf{x} - \mathbf{x}')\mathbf{i}_3]. \quad (4.209)$$

The differentiations occurring in these expressions can be calculated analytically (see Section 4.5.4), since we calculate the incident field at locations other than the source coordinates and hence the singularity in the Green's function causes no problems.

4.9 3D Stratified configuration

In this section, we will discuss the calculation of the forward problem in the case where the background medium is layered. Specifically, we will focus our attention on a single-layer configuration, i.e., the 3-media problem, where the scattering object is assumed to be located within the layer. For the Green's function we will have direct and reflected contributions from the source, as indicated in Figure 4.5. Since we are solving the full vectorial problem, we need to use the dyadic Green's functions for this **layered medium, which are discussed in Appendix B. Using the expressions derived in Appendix B, we calculate all components (EE, EH, HH and HE) of the reflected part of the Green's function directly in the Fourier-transform domain, hence there**

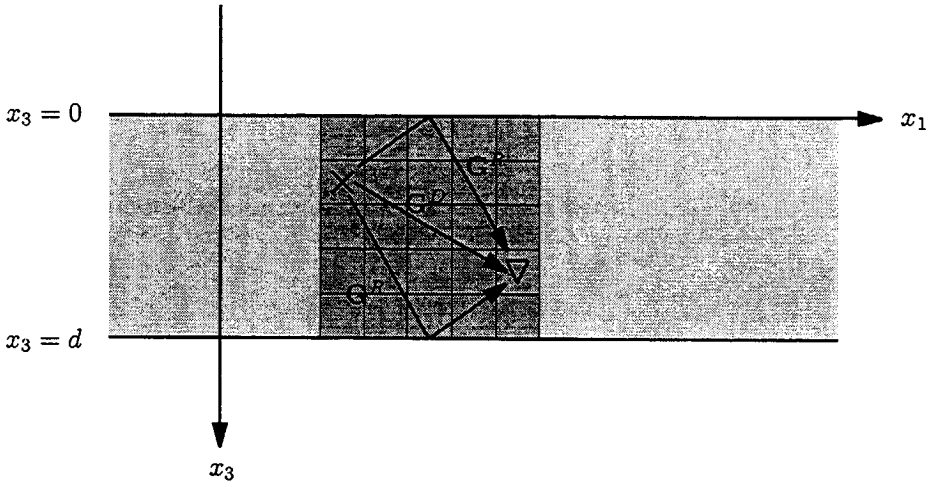


Figure 4.5: Direct (G^D) and reflected (G^R) contributions from a source located within a layer.

is no need to use expansion functions for the reflected part of the Green's function. We use FFTs to perform the inverse spatial Fourier transformation, which can be done very efficiently using a grid-reduction technique (see Appendix C).

The integral operator which was introduced in the previous sections is now modified to include the effects of the layered configuration. We start again from the integral representations for the electric and magnetic field quantities, which are given by Eqs. (4.44) and (4.45). The Green's functions are split into direct and reflected parts, which leads to

$$\begin{aligned} \hat{\mathbf{E}}(\mathbf{x}) &= \hat{\mathbf{E}}^i(\mathbf{x}) + \int_{\mathbf{x}' \in D} \left(\mathcal{G}^{EE,D} \cdot \chi^E \hat{\mathbf{E}} + \mathcal{G}^{EH,D} \cdot \chi^H \hat{\mathbf{H}} \right) d\mathbf{x}' \\ &+ \int_{\mathbf{x}' \in D} \left((\sigma_b - i\omega\epsilon_0) \hat{\mathbf{G}}^{EE,R} \cdot \chi^E \hat{\mathbf{E}} - i\omega\mu_b \hat{\mathbf{G}}^{EH,R} \cdot \chi^H \hat{\mathbf{H}} \right) d\mathbf{x}', \end{aligned} \quad (4.210)$$

and

$$\begin{aligned} \hat{\mathbf{H}}(\mathbf{x}) &= \hat{\mathbf{H}}^i(\mathbf{x}) + \int_{\mathbf{x}' \in D} \left(\mathcal{G}^{HH,D} \cdot \chi^H \hat{\mathbf{H}} + \mathcal{G}^{HE,D} \cdot \chi^E \hat{\mathbf{E}} \right) d\mathbf{x}' \\ &+ \int_{\mathbf{x}' \in D} \left((\sigma_b - i\omega\epsilon_0) \hat{\mathbf{G}}^{HE,R} \cdot \chi^E \hat{\mathbf{E}} - i\omega\mu_b \hat{\mathbf{G}}^{HH,R} \cdot \chi^H \hat{\mathbf{H}} \right) d\mathbf{x}'. \end{aligned} \quad (4.211)$$

Where the presence of the interfaces is taken into account by the reflected Green's

functions (see Figure 4.5). Written in (normalized) operator form, this becomes

$$\begin{bmatrix} \hat{\mathbf{E}}^i \\ \hat{\mathbf{H}}^i \end{bmatrix} = (\mathbf{I} - \mathbf{K}\chi) \begin{bmatrix} \hat{\mathbf{E}} \\ \hat{\mathbf{H}} \end{bmatrix}, \quad (4.212)$$

where the total operator $\mathbf{K} = (\mathbf{K}^D + \mathbf{K}^R)$ contains the direct and reflected contributions from the source. The direct part of the operator, \mathbf{K}^D , is given in Eq. (4.119), while the reflected part is written in similar form as

$$\mathbf{K}^R = \begin{bmatrix} \mathcal{K}^{EE,R} & \mathcal{K}^{EH,R} \\ \mathcal{K}^{HE,R} & \mathcal{K}^{HH,R} \end{bmatrix}, \quad (4.213)$$

where

$$(\mathcal{K}^{EE,R} \cdot \chi^E \hat{\mathbf{E}})(\mathbf{x}) = (\sigma_b - i\omega\epsilon_0) \int_{\mathbf{x}' \in D} \hat{\mathbf{G}}^{EE,R}(\mathbf{x}, \mathbf{x}') \cdot \chi^E(\mathbf{x}') \hat{\mathbf{E}}(\mathbf{x}') d\mathbf{x}', \quad (4.214)$$

$$(\mathcal{K}^{EH,R} \cdot \chi^H \hat{\mathbf{H}})(\mathbf{x}) = -i\omega\mu_b \int_{\mathbf{x}' \in D} \hat{\mathbf{G}}^{EH,R}(\mathbf{x}, \mathbf{x}') \cdot \chi^H(\mathbf{x}') \hat{\mathbf{H}}(\mathbf{x}') d\mathbf{x}', \quad (4.215)$$

$$(\mathcal{K}^{HH,R} \cdot \chi^H \hat{\mathbf{H}})(\mathbf{x}) = -i\omega\mu_b \int_{\mathbf{x}' \in D} \hat{\mathbf{G}}^{HH,R}(\mathbf{x}, \mathbf{x}') \cdot \chi^H(\mathbf{x}') \hat{\mathbf{H}}(\mathbf{x}') d\mathbf{x}', \quad (4.216)$$

$$(\mathcal{K}^{HE,R} \cdot \chi^E \hat{\mathbf{E}})(\mathbf{x}) = (\sigma_b - i\omega\epsilon_0) \int_{\mathbf{x}' \in D} \hat{\mathbf{G}}^{HE,R}(\mathbf{x}, \mathbf{x}') \cdot \chi^E(\mathbf{x}') \hat{\mathbf{E}}(\mathbf{x}') d\mathbf{x}', \quad (4.217)$$

where we have used the fact that $\mathcal{G}_{k,j}^{EH,R}(\mathbf{x}, \mathbf{x}') = -\mathcal{G}_{j,k}^{HE,R}(\mathbf{x}', \mathbf{x})$. Note that we calculate the gradient-divergence and curl terms for the reflected part of the Green's function in the Fourier-transform domain, making the need for dedicated expansion functions for this part of the Green's function superfluous.

To solve the forward problem for a layered configuration we use the CG scheme as defined in Section 4.5, where the operator \mathbf{K}^D is now replaced with the new operator \mathbf{K} . Next, we must define the components of the discrete operator \mathbf{K}^R and discrete adjoint operator \mathbf{K}^{R*} to complete the description of the CG scheme.

4.9.1 Discretized operators and adjoint operators

In order to define the components of the discretized operator and adjoint operator corresponding to the reflected part of the Green's function, we must first split **this reflected part of the Green's function into an even and an odd part to take into account the convolution and correlation structures that are present** (see Appendix B.3). We distinguish between even and odd parts by using the superscripts

'e' and 'o', respectively. The components of the operator are now given by

$$\begin{aligned} \left(\mathcal{K}^{EE,R} \cdot \chi^E \hat{\mathbf{E}} \right)_{k;m,n,p} &= (\sigma_b - i\omega\varepsilon_0) \Delta x_1 \Delta x_2 \Delta x_3 \\ &\times \left(\sum_{j=1}^3 \sum_{m'=1}^M \sum_{n'=1}^N \sum_{p'=1}^P \hat{\mathbf{G}}_{k,j}^{EE,R;e}(\mathbf{x}_{m,n,p} - \mathbf{x}_{m',n',p'}) \chi_{m',n',p'}^E \hat{\mathbf{E}}_{j;m',n',p'} \right. \\ &\left. + \sum_{j=1}^3 \sum_{m'=1}^M \sum_{n'=1}^N \sum_{p'=1}^P \hat{\mathbf{G}}_{k,j}^{EE,R;o}(\mathbf{x}_{m,n} - \mathbf{x}_{m',n'}; \mathcal{X}_{3;p} + \mathcal{X}_{3;p'}) \chi_{m',n',p'}^E \hat{\mathbf{E}}_{j;m',n',p'} \right) \end{aligned} \quad (4.218)$$

where we have used point-matching for the reflected part of the Green's function. Note that for the even part we have a convolution structure in the i_3 -direction, while for the odd part we have a correlation structure in the i_3 -direction. In the i_1 - and i_2 -directions, we have a convolution structure for both even and odd parts. For the other components of the operator \mathbf{K}^R we obtain

$$\begin{aligned} \left(\mathcal{K}^{EH,R} \cdot \chi^H \hat{\mathbf{H}} \right)_{k;m,n,p} &= -i\omega\mu_b \Delta x_1 \Delta x_2 \Delta x_3 \\ &\times \left(\sum_{j=1}^3 \sum_{m'=1}^M \sum_{n'=1}^N \sum_{p'=1}^P \hat{\mathbf{G}}_{k,j}^{EH,R;e}(\mathbf{x}_{m,n,p} - \mathbf{x}_{m',n',p'}) \chi_{m',n',p'}^H \hat{\mathbf{H}}_{j;m',n',p'} \right. \\ &\left. + \sum_{j=1}^3 \sum_{m'=1}^M \sum_{n'=1}^N \sum_{p'=1}^P \hat{\mathbf{G}}_{k,j}^{EH,R;o}(\mathbf{x}_{m,n} - \mathbf{x}_{m',n'}; \mathcal{X}_{3;p} + \mathcal{X}_{3;p'}) \chi_{m',n',p'}^H \hat{\mathbf{H}}_{j;m',n',p'} \right), \end{aligned} \quad (4.219)$$

$$\begin{aligned} \left(\mathcal{K}^{HH,R} \cdot \chi^H \hat{\mathbf{H}} \right)_{j;m,n,p} &= -i\omega\mu_b \Delta x_1 \Delta x_2 \Delta x_3 \\ &\times \left(\sum_{k=1}^3 \sum_{m'=1}^M \sum_{n'=1}^N \sum_{p'=1}^P \hat{\mathbf{G}}_{j,k}^{HH,R;e}(\mathbf{x}_{m,n,p} - \mathbf{x}_{m',n',p'}) \chi_{m',n',p'}^H \hat{\mathbf{H}}_{k;m',n',p'} \right. \\ &\left. + \sum_{k=1}^3 \sum_{m'=1}^M \sum_{n'=1}^N \sum_{p'=1}^P \hat{\mathbf{G}}_{j,k}^{HH,R;o}(\mathbf{x}_{m,n} - \mathbf{x}_{m',n'}; \mathcal{X}_{3;p} + \mathcal{X}_{3;p'}) \chi_{m',n',p'}^H \hat{\mathbf{H}}_{k;m',n',p'} \right), \end{aligned} \quad (4.220)$$

and

$$\begin{aligned} \left(\mathcal{K}^{HE,R} \cdot \chi^H \hat{\mathbf{H}} \right)_{j;m,n,p} &= (\sigma_b - i\omega\varepsilon_0) \Delta x_1 \Delta x_2 \Delta x_3 \\ &\times \left(\sum_{k=1}^3 \sum_{m'=1}^M \sum_{n'=1}^N \sum_{p'=1}^P \hat{\mathbf{G}}_{j,k}^{HE,R;e}(\mathbf{x}_{m,n,p} - \mathbf{x}_{m',n',p'}) \chi_{m',n',p'}^E \hat{\mathbf{E}}_{k;m',n',p'} \right. \\ &\left. + \sum_{k=1}^3 \sum_{m'=1}^M \sum_{n'=1}^N \sum_{p'=1}^P \hat{\mathbf{G}}_{j,k}^{HE,R;o}(\mathbf{x}_{m,n} - \mathbf{x}_{m',n'}; \mathcal{X}_{3;p} + \mathcal{X}_{3;p'}) \chi_{m',n',p'}^E \hat{\mathbf{E}}_{k;m',n',p'} \right). \end{aligned} \quad (4.221)$$

The adjoint operators are again obtained by using the inner product, which results in

$$\begin{aligned} \left(\overline{\chi^E} \mathcal{K}^{EE,R*} \eta_D^E \mathbf{r}^E \right)_{k;m,n,p} &= (\sigma_b - \overline{i\omega\varepsilon_0}) \overline{\chi^E}_{m,n,p} \eta_D^E \Delta x_1 \Delta x_2 \Delta x_3 \quad (4.222) \\ &\times \left(\sum_{j=1}^3 \sum_{m'=1}^M \sum_{n'=1}^N \sum_{p'=1}^P \overline{\hat{G}}_{k,j}^{EE,R;e} (\mathbf{x}_{m,n,p} - \mathbf{x}_{m',n',p'}) \Gamma_{j;m',n',p'}^E \right. \\ &\left. + \sum_{j=1}^3 \sum_{m'=1}^M \sum_{n'=1}^N \sum_{p'=1}^P \overline{\hat{G}}_{k,j}^{EE,R;o} (\mathbf{x}_{m,n} - \mathbf{x}_{m',n'}; \mathbf{x}_{3;p} + \mathbf{x}_{3;p'}) \Gamma_{j;m',n',p'}^E \right), \end{aligned}$$

$$\begin{aligned} \left(\overline{\chi^E} \mathcal{K}^{HE,R*} \eta_D^H \mathbf{r}^H \right)_{k;m,n,p} &= -(\sigma_b - \overline{i\omega\varepsilon_0}) \overline{\chi^E}_{m,n,p} \eta_D^H \Delta x_1 \Delta x_2 \Delta x_3 \quad (4.223) \\ &\times \left(\sum_{j=1}^3 \sum_{m'=1}^M \sum_{n'=1}^N \sum_{p'=1}^P \overline{\hat{G}}_{k,j}^{EH,R;e} (\mathbf{x}_{m,n,p} - \mathbf{x}_{m',n',p'}) \Gamma_{j;m',n',p'}^H \right. \\ &\left. + \sum_{j=1}^3 \sum_{m'=1}^M \sum_{n'=1}^N \sum_{p'=1}^P \overline{\hat{G}}_{k,j}^{EH,R;o} (\mathbf{x}_{m,n} - \mathbf{x}_{m',n'}; \mathbf{x}_{3;p} + \mathbf{x}_{3;p'}) \Gamma_{j;m',n',p'}^H \right), \end{aligned}$$

$$\begin{aligned} \left(\overline{\chi^H} \mathcal{K}^{HH,R*} \eta_D^H \mathbf{r}^H \right)_{j;m,n,p} &= \overline{i\omega\mu_b} \overline{\chi^H}_{m,n,p} \eta_D^H \Delta x_1 \Delta x_2 \Delta x_3 \quad (4.224) \\ &\times \left(\sum_{k=1}^3 \sum_{m'=1}^M \sum_{n'=1}^N \sum_{p'=1}^P \overline{\hat{G}}_{j,k}^{HH,R;e} (\mathbf{x}_{m,n,p} - \mathbf{x}_{m',n',p'}) \Gamma_{k;m',n',p'}^H \right. \\ &\left. + \sum_{k=1}^3 \sum_{m'=1}^M \sum_{n'=1}^N \sum_{p'=1}^P \overline{\hat{G}}_{j,k}^{HH,R;o} (\mathbf{x}_{m,n} - \mathbf{x}_{m',n'}; \mathbf{x}_{3;p} + \mathbf{x}_{3;p'}) \Gamma_{k;m',n',p'}^H \right), \end{aligned}$$

and

$$\begin{aligned} \left(\overline{\chi^H} \mathcal{K}^{EH,R*} \eta_D^E \mathbf{r}^E \right)_{j;m,n,p} &= -\overline{i\omega\mu_b} \overline{\chi^H}_{m,n,p} \eta_D^E \Delta x_1 \Delta x_2 \Delta x_3 \quad (4.225) \\ &\times \left(\sum_{k=1}^3 \sum_{m'=1}^M \sum_{n'=1}^N \sum_{p'=1}^P \overline{\hat{G}}_{j,k}^{HE,R;e} (\mathbf{x}_{m,n,p} - \mathbf{x}_{m',n',p'}) \Gamma_{k;m',n',p'}^E \right. \\ &\left. + \sum_{k=1}^3 \sum_{m'=1}^M \sum_{n'=1}^N \sum_{p'=1}^P \overline{\hat{G}}_{j,k}^{HE,R;o} (\mathbf{x}_{m,n} - \mathbf{x}_{m',n'}; \mathbf{x}_{3;p} + \mathbf{x}_{3;p'}) \Gamma_{k;m',n',p'}^E \right). \end{aligned}$$

Note that we have used point matching for the components of \mathbf{K}^R . Now that the operators and adjoint operators corresponding to the reflected part of the Green's

Table 4.2: Steps necessary to calculate the PEC signals for a configuration with a defect.

<i>I - Green's functions and incident fields</i>
<ul style="list-style-type: none"> • Loop over K frequencies <ul style="list-style-type: none"> • Create datafile with contrast data • Calculate domain Green's function • Calculate receiver Green's function • Calculate direct part of the domain Green's function • Calculate incident fields within the computational domain • Calculate incident fields at the receiver positions End loop over frequencies
<i>II - CGFFT scheme</i>
<ul style="list-style-type: none"> • Loop over K frequencies <ul style="list-style-type: none"> • Load data and calculate starting values • Iteratively reduce error to calculate fields in defect • Calculate scattered electric field at receiver positions End loop over frequencies
<i>III - Voltage in time domain</i>
<ul style="list-style-type: none"> • Load incident and scattered electric fields at receiver positions • Calculate the received voltage in the frequency domain • Use inverse FFT to calculate the voltage in the time domain • Filter and save data

function are defined we can use the CG scheme to calculate the fields within the scatterer. The derivation of the reflected part of the Green's function and its symmetry properties are discussed in Appendix B. Finally we note that for the PEC configuration, where the material parameters of the defect are $\sigma = 4 \text{ S/m}$ and $\mu = \mu_0$, the normalized contrasts are always negative, since the conductivity and permeability of a defect that is not filled with corrosion product will be lower than those of the layer.

4.9.2 Calculation of the PEC signals

In Table 4.2 we give a schematic description of the steps that are necessary to calculate the time domain PEC signal for a configuration where a defect is present. We start by calculating the Green's functions and the incident fields within the computational domain for each frequency. This data can be reused as long as the configuration parameters (such as thickness, medium parameters) remain unchanged. Next, we need the incident fields at the receiver positions. When we have a (loop) source above a layer with a defect, there are three contributions to the total field at

the receiver positions. First we have the direct contribution from source to receiver, which is neglected in our case, since this part of the signal does not contain any information about either the layer or the defect and can be filtered from the measured signals. Second, we have the part of the field caused by scattering from the undamaged layer, which we consider to be the incident field at the receiver positions, since the background configuration consists of an undamaged layer. This part of the field is calculated using the 2D formulation given in Appendix A. Finally, we have the part of the field which is caused by scattering from the defect, this is the part of the field that we calculate using the CGFFT scheme.

When the Green's functions and the incident fields within the scatterer are known, we can proceed to calculate the total electromagnetic fields within the defect by using the CGFFT scheme that was formulated in this chapter. This process is repeated for all frequencies. When the calculated fields satisfy the prescribed error criterion, we calculate the scattered electric field at the receiver positions. Combined with the incident electric field generated by scattering from an undamaged layer, this gives us the total electric field at the receiver positions, from which we are able to calculate the frequency domain voltage on the terminals of the receiving coils. Since convergence for the lower frequencies is very slow, we use a marching-up/marching-down scheme, whereby the starting values for the first two frequencies are zero. Due to the slow convergence, it would be prohibitive to iterate until the error criterion is reached, therefore the CG scheme is stopped after a predetermined number of iterations and the results are used in the marching-on-in-frequency method to calculate the starting values for the subsequent frequencies. When the fields have been calculated for all frequencies, we recalculate for those frequencies where convergence to the error criterion was not reached, using the results obtained for higher frequencies in a marching-down method to calculate the initial values.

In the third step of the scheme, we calculate the time domain voltage on the terminals of the receiving coils by calculating the contour integral of the electric field over the contour spanned by the receiving coils (Eq. (4.8)). Performing an inverse temporal Fourier transformation results in the desired time domain voltage.

Chapter 5

Numerical Results for the Forward Problem

In this chapter we present numerical results for the two- and three-dimensional forward problems. For the 2D forward problem we calculate the transient electric field within a metal layer using the theory from Section 4.2 and Appendix A. We can also use this configuration to calculate the response of the PEC tool for various medium and configuration parameters, these results are given in Chapter 3. Next, we test the 3D model for a homogeneous background by comparing it with previous results and the analytical solution for scattering by a conducting and permeable sphere. Subsequently, we validate the preconditioning operator described in Section 4.6. To calculate the influence of a defect on the PEC signals, we use the theory of Sections 4.3 and 4.9 to first calculate the field quantities with the defect, and subsequently the voltage on the receiving coil terminals.

5.1 2D Configuration

For the 2D configuration we have a coil configuration as shown in Figure 5.1, with two transmitting and two receiving coils, where the transmitting coils are circular with a radius of 25 mm and the receiving coils are square with dimensions 25×25 mm. A rectangular pulse current is generated in the transmitting coils, which is modelled using a switch-off time signature since we are only interested in the response to the switch-off part of the block pulse. To calculate the voltage on the terminals of the receiving coils we determine the electric field in the frequency

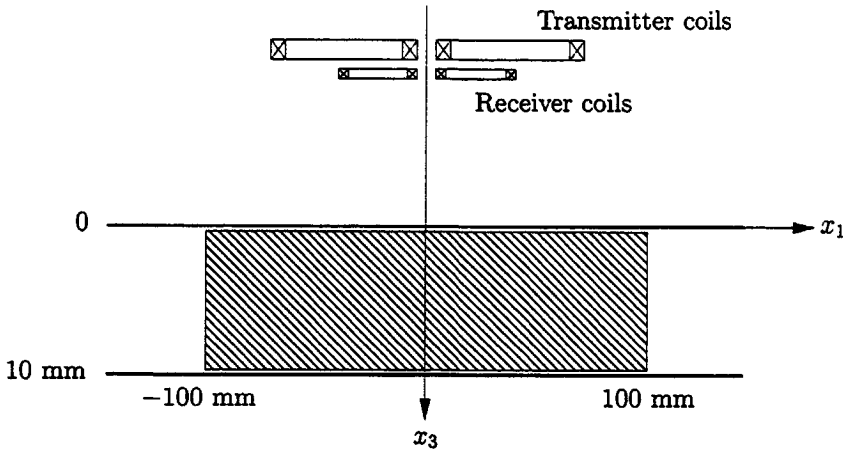


Figure 5.1: Configuration for the 2D model, computational domain is shaded. Medium parameters of the metal layer are $\sigma = 6.7 \times 10^6$ S/m and $\mu = 200\mu_0$, medium parameters for the halfspaces are $\sigma = 4$ S/m, $\mu = \mu_0$. Permittivity is ϵ_0 throughout the configuration.

domain on the contour spanned by the receiving coils (see Figures 5.9 and 5.10 for a view of the coil configuration in the x_1 - x_2 plane where the location and size of the receiving coils can be found), after which we perform an inverse temporal Fourier transformation to obtain the time domain signal. These voltages (PEC signals) as function of time for various configurations can be found in Chapter 3. In the figures in this section, we use a time-scale where $t = 0$ ms corresponds to the instant when the block-pulse in the transmitting coils is switched off. We also give a normalized time, where we have used the characteristic diffusion time of the metal layer as the normalization factor. This diffusion time is given by $\tau_m = \mu\sigma d^2$, where d is the thickness of the layer. For the reference configuration defined in Section 3.2.1, the value of the characteristic diffusion time is $\tau_m = 168.4$ ms. To visualize the electromagnetic diffusion of the field quantities within the layer, we calculate the electric field on a grid in the computational domain (indicated by the shaded area in Figure 5.1), after which we perform an inverse temporal Fourier transformation for each position. We calculated the frequency domain electric field at each position for 800 frequencies, evenly spaced from 0 Hz to 2 kHz, after which the time domain electric field was obtained using an FFT. The metal layer was taken to be 10 mm thick and the conductivity and permeability were taken to be 6.7×10^6 S/m and $200\mu_0$, respectively. The permittivity was taken to be ϵ_0 throughout the configuration. The computational domain is indicated by the shaded area in Figure 5.1, and ranges from 0 to 10 mm in the x_3 -direction and from -100 mm to 100 mm in the x_1 -direction. In Figure 5.2 we plot the electric field distribution

within the computational domain for various times. The focussing effect of the two transmitting coils can be clearly seen, as well as the diffusion of the electric field in the x_3 -direction. Since the induced current density is proportional to the electric field, Figure 5.2 also represents the current distribution within the layer. The conductivity of the halfspaces is taken to be 4 S/m to move poles and branch point off the integration axis (see Appendix A). These values of the medium parameters correspond to seawater, and this does not affect the calculated PEC signals and electric fields within the layer. This fact has been experimentally verified during underwater inspections of offshore platforms. It can be seen that the frequency domain reflection coefficient is very small due to the large difference in medium parameters between the halfspaces and the metal layer. This has consequences for the sensitivity with respect to a contrast within the layer and for the inversion, as can be seen from the results in Chapter 7.

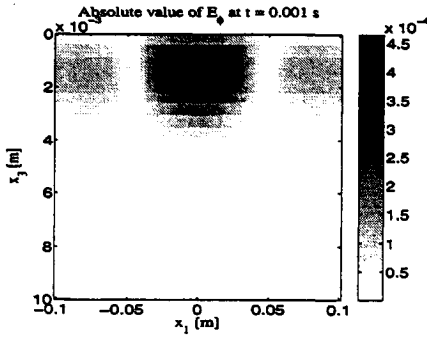
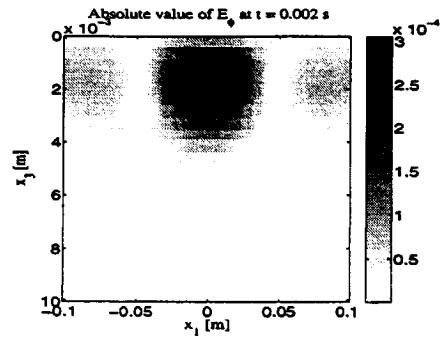
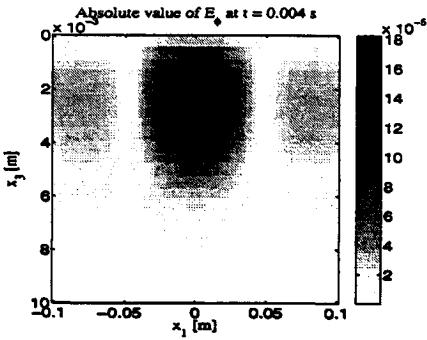
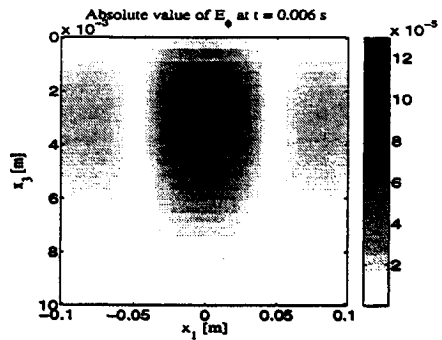
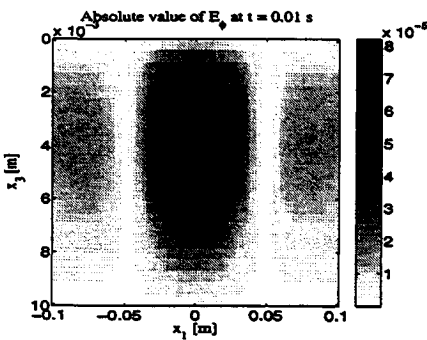
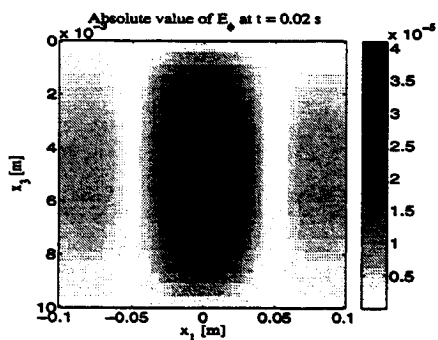
(a) $t = 1$ ms, $5.94 \times 10^{-3} \tau_m$ (b) $t = 2$ ms, $11.9 \times 10^{-3} \tau_m$ (c) $t = 4$ ms, $23.8 \times 10^{-3} \tau_m$ (d) $t = 6$ ms, $35.6 \times 10^{-3} \tau_m$ (e) $t = 10$ ms, $59.4 \times 10^{-3} \tau_m$ (f) $t = 20$ ms, $119 \times 10^{-3} \tau_m$

Figure 5.2: Absolute value of the electric field within the layer at $t = 1$ ms (a), $t = 2$ ms (b), $t = 4$ ms (c), $t = 6$ ms (d), $t = 10$ ms (e), $t = 20$ ms (f), x_1 - and x_3 -axes not to the same scale.

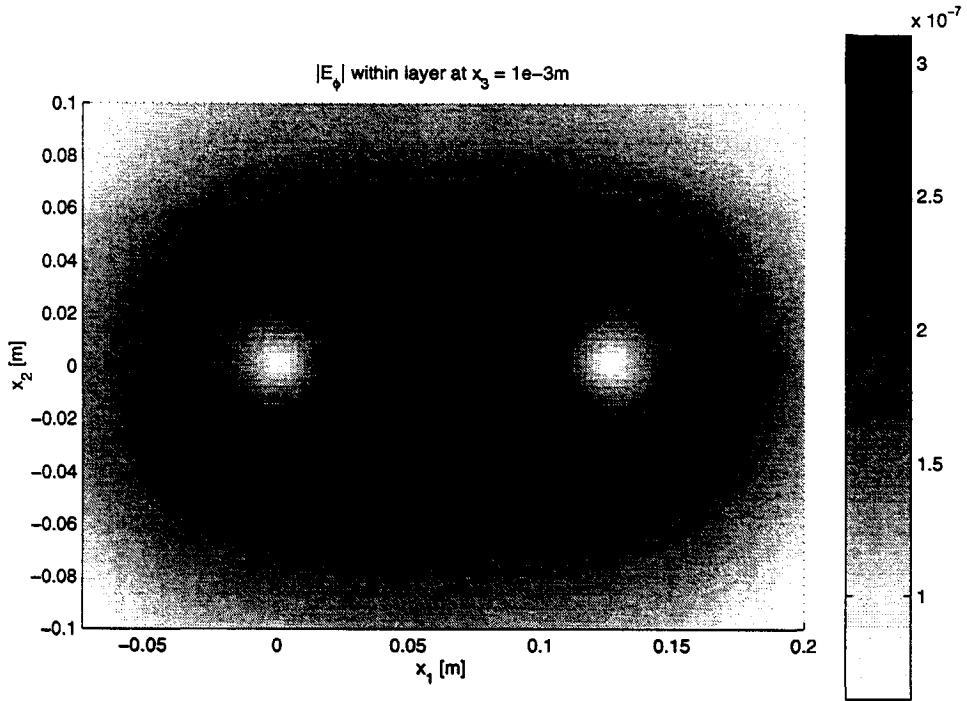


Figure 5.3: Absolute value of \hat{E}_ϕ in the x_1 - x_2 plane at $x_3 = 1$ mm, generated by two transmitting coils.

In the lateral directions (the x_1 - and x_2 -directions) the focussing of the electric field is also readily apparent when we plot the absolute value of the electric field in the x_1 - x_2 plane (Figure 5.3). The electric field was calculated at $x_3 = 1$ mm, i.e., just within the layer. Material and configuration parameters are those of the reference configuration defined in Section 3.2.1, the field was calculated for a single frequency only, in this case 50 Hz. The presence of the two transmitting coils can be deduced from the two minima that are present in Figure 5.3. At the location where the current density has a maximum (i.e., exactly halfway between the centers of the transmitting coils), the flow of the induced current is in the x_2 -direction.

5.2 3D Configuration with a homogeneous background

In this section we will present numerical results for the 3D model for configurations with a homogeneous background. We will compare the model to the scheme described by Abubakar [2], which takes electric contrasts into account (conductivity and permittivity) and we will also consider the problem of scattering by a conducting and permeable sphere, which can be solved analytically.

5.2.1 Conducting cube

First we compare the 3D model for a homogeneous background with the model by Abubakar [2], which uses a combination of piecewise constant and piecewise continuous expansion functions to solve the electric field integral equation when a contrast in conductivity or permittivity (in case of the wave problem) or only conductivity (in case of the diffusive problem) is present. Since we consider contrasts in conductivity and/or permeability only, we take a contrast in conductivity to compare both methods. The scatterer is a cube with sides of 20 m, centered at the origin, and the computational domain is discretized using $14 \times 14 \times 14$ grid points. The background medium parameters are $\sigma_b = 0.1$ S/m and $\mu_b = \mu_0$. The conductivity of the cube is taken to be $\sigma_{cube} = 1$ S/m, making the contrast $\chi^E = 9$. The source is a vertical magnetic dipole (i.e., oriented in the x_3 -direction) and at the receiver positions we calculate the x_3 component of the scattered magnetic field. There are 33 receiver positions, located on a circle around the cube in the $x_1 - x_2$ plane at a distance of 25 m from the origin (see Figure 5.4). The frequency used was 20 kHz. In Figure 5.5 we compare the real and imaginary parts of the x_3 -component of the scattered magnetic field at the receiver positions to the results obtained with Abubakar's model. It can be seen that there is good agreement between the two models, with some differences in the real part of H_3^{sc} for the receiver positions which are closest to the source. The expansion functions used in the two schemes are not equal, leading to different finite difference stencils in the operators. This explains the small differences that can be seen in Figure 5.5. The desired error criterion was set to 10^{-9} for both models, in Figure 5.6 we plot the normalized errors in both the integral equation of the electric type and the integral equation of the magnetic type, together with the combined error. It can be seen that the normalized error of either individual integral equation is not uniformly decreasing, but the total error is, which is conform the CG scheme. The computation time for Abubakar's method was 273 s, for the method presented here 629 s. This does not include the time needed to calculate the Green's functions and the incident fields. The difference in computation time between the methods lies in the fact that we solve both the integral equation of the electric type and of the magnetic type, which results in more FFTs that need to be calculated, as well as a larger finite difference stencil. Abubakar solves only the integral equation of the electric type, which is

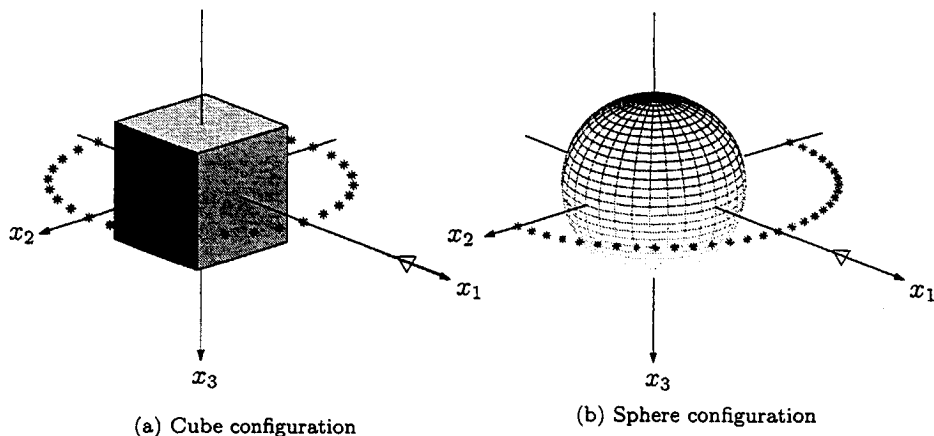


Figure 5.4: Configurations for scattering by a conducting cube and by a conducting and permeable sphere. Receivers are denoted by stars, the vertical magnetic dipole source is denoted by the triangle.

computationally less costly. The calculations were performed on a dual processor 600 MHz Pentium 3 computer with 1Gb memory.

5.2.2 Scattering by a conducting and permeable sphere

In order to test the model with a configuration for which an analytical solution exists, we consider a conducting and permeable sphere illuminated by a magnetic dipole source, as depicted in Figure 5.4. The scattered electromagnetic fields for such a configuration are given by Ward and Hohmann [90].

As can be seen from Figure 5.4, the receivers are placed in a semi-circle around the sphere. The source is a magnetic dipole located at $\mathbf{x} = (50, 0, 0)$ m and oriented in the x_3 -direction, while there are 31 receivers located 25 m from the center of the sphere, which is centered at the origin. The radius of the sphere is 11 m and it is located in a computational domain with size $35 \times 35 \times 35$ m³. A frequency of 20 kHz was used. In Figure 5.7, we plot the real and imaginary parts of the radial component of the scattered electric field at the receiver positions.

The availability of the analytical solution for the scattered fields enables us to investigate the effect of the grid sizing on the calculated fields. The grid sizes used are $6 \times 6 \times 6$, $14 \times 14 \times 14$, $28 \times 28 \times 28$ and $40 \times 40 \times 40$ grid points. It can be seen that the solution of our CGFFT method converges to the analytical solution as the discretization is refined. There is still some discrepancy between the analytical and

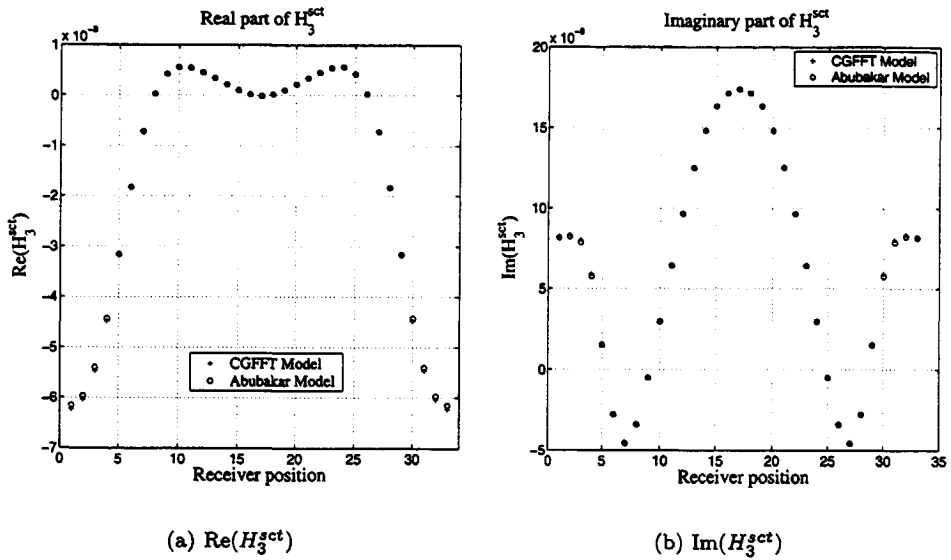


Figure 5.5: Real (a) and imaginary (b) parts of H_3^{sct} for the CGFFT model and Abubakar's model for the case of scattering by a conducting cube.

CGFFT solutions since the discretization of the sphere is such that a grid cell only has a contrast with respect to the background when it is located completely within the sphere.

5.2.3 Numerical results for the preconditioning operator

We compare the preconditioned CGFFT method to the normal method for the configuration of a conducting and permeable block with dimensions $30 \times 30 \times 30 \text{ m}^3$, located in a computational domain with size $35 \times 35 \times 35 \text{ m}^3$ that was discretized in $14 \times 14 \times 14$ points. We used one source and 5 receivers, a frequency of 20 kHz and the error criterion was set to 10^{-9} . We calculated the field quantities within the scatterer using the normal and preconditioned CG methods for the following values of the contrasts: $\{\chi^E, \chi^H\} = \{1, 1\}, \{5, 5\}, \{10, 10\}, \{20, 20\}$. In Figure 5.8 we plot the total error as function of the iteration number. The corresponding computation times are given in Table 5.2.3. We can see from Figure 5.8 and Table 5.2.3 that the preconditioning operator is more effective for higher contrast values.

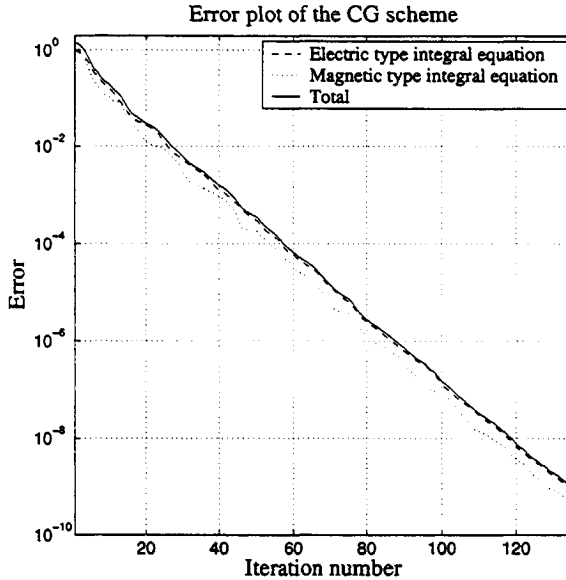


Figure 5.6: Error plot of the CG scheme, error of the electric type integral equation (dotted), error of the magnetic type integral equation (dashed) and total error (solid).

5.3 3D Stratified configuration

In this section we will discuss the numerical results for the 3D layered configuration, where we have a PEC probe above a metal layer containing a defect. The coil and defect configuration for this problem is given in Figures 5.9 and 5.10. We first consider a defect with an area of $56 \times 56 \text{ mm}^2$ and a depth of 2, 5 and 8 mm, discretized into $14 \times 14 \times 10$ points and located in a metal layer with medium and configuration parameters as given in Table 3.1. In Figure 5.9 we plot the PEC signal as function of time for these defect configurations and for a metal layer without defects. For the background (metal layer and halfspaces), we have the following medium parameters: the conductivity and permeability of the halfspaces was $\sigma = 4 \text{ S/m}$ and $\mu = \mu_0$, respectively, which corresponds to the electromagnetic properties of seawater. Note that the permittivity is set to ϵ_0 throughout the configuration. For the metal layer and the coil parameters we used the standard configuration defined in Chapter 3 (see Table 3.1). The desired error criterion for the CG scheme was set to 10^{-3} . This value was chosen comparatively large to reduce the computation times. Furthermore, since we perform filtering on the time domain signal as described below, it is not necessary to calculate the field quantities to a higher precision.

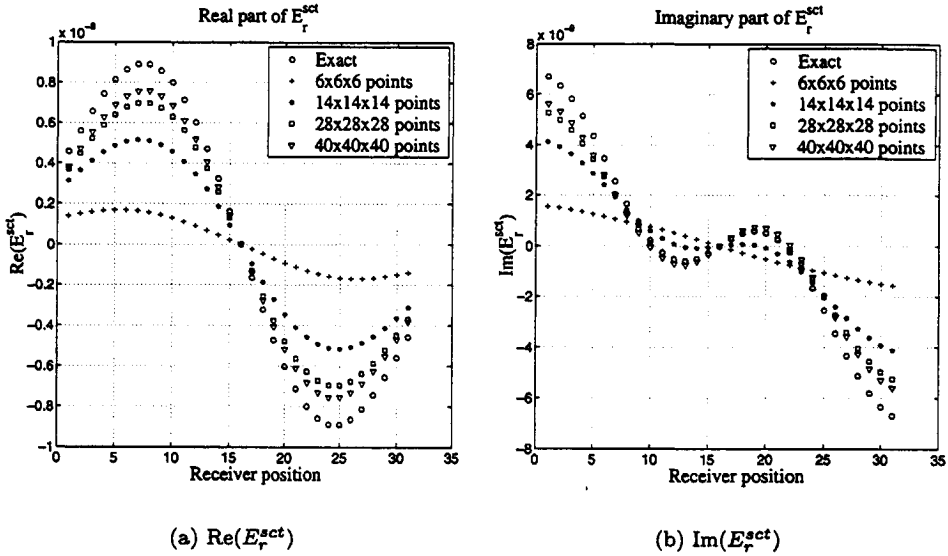


Figure 5.7: Real (c) and imaginary (d) parts of E_r^{sct} for the case of scattering by a conducting and permeable sphere.

The scattered electric field was calculated at 40 points located on the receiver coil contours (see also Figure 5.10), divided into 20 points per receiver coil. The voltage was then calculated by performing a numerical contour integral over the receiver coil contour. The scattered electric field and the corresponding voltages were calculated for 200 frequencies, evenly spaced from 0 to 2 kHz (0 Hz not included), after which an inverse temporal Fourier transformation was used to obtain the time domain voltage. Due to the small number of samples, filtering is needed to smoothen the time domain voltage, which was done using a moving-average filter.

From the calculated PEC signals in Figure 5.11, we see that the signal corresponding to a $56 \times 56 \times 5 \text{ mm}^3$ defect deviates from the no-defect-signal (corresponding to a layer where no defect is present) for times greater than 0.5 ms, while the signal for a $56 \times 56 \times 2 \text{ mm}^3$ defect deviates from the no-defect signal for times greater than 1.5 ms. After this, the presence of the defect causes a decrease in amplitude of the signals and a decrease in the τ_0 -parameter, which characterizes the thickness of the layer. In contrast to this, the signal for a $56 \times 56 \times 8 \text{ mm}^3$ defect is almost exactly equal to the no-defect-signal, indicating that very deep defects where **almost no material is left (where defect depth almost equal plate thickness)** cannot be detected using the PEC tool. In this case, the eddy currents flow around the defect, resulting in a signal that cannot readily be distinguished from the no-defect

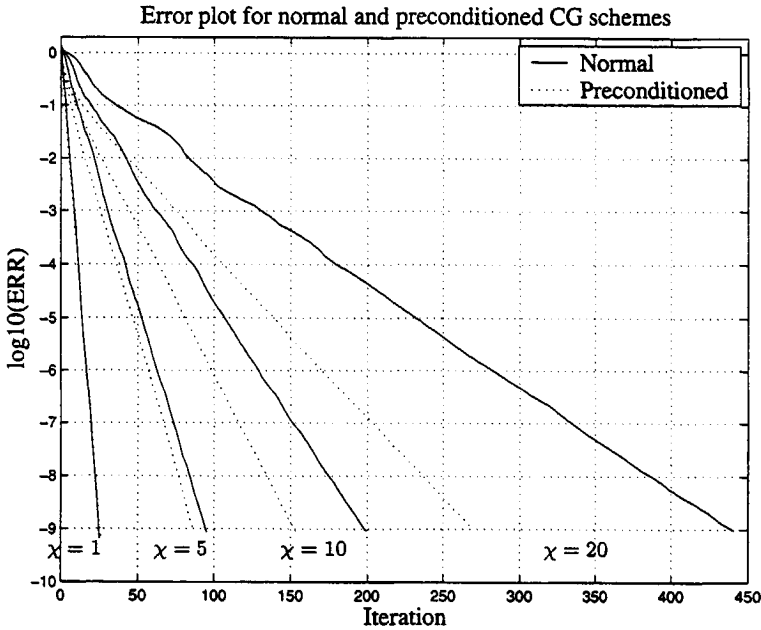


Figure 5.8: Error plot for the normal and preconditioned CG schemes

signal. This illustrates the fact that a PEC measurement is a volume measurement.

Since we calculate the fields in the same configuration for a number of frequencies, it was advantageous to use the Marching-on-in-frequency technique as described in Section 4.7. In Figure 5.12 we plot the number of iterations of the CG scheme as function of frequency. It can be seen that this technique results in a drastic reduction in the number of iterations that are needed to converge to the desired accuracy.

The computation times for the calculation of the PEC signal should be split in two parts, one for the Green's function, which needs to be calculated only once for each configuration, and one for the actual CG scheme to calculate the scattered fields. The domain Green's function for a single frequency and an FFT grid of 1024×1024 points takes approximately one hour of CPU time, after which the grid size is reduced to the 32×32 CGFFT grid. Using the grid reduction method described in Appendix C, the computation time for the domain Green's function can be reduced to approximately 5 minutes per frequency. For both cases the CGFFT grid is 32×32 points in the x_1 - and x_3 -directions. The accuracy of the Green's function obtained in this manner is same for both methods. The storage requirements for the domain Green's function is 8 Mb per frequency.

The receiver Green's function takes approximately 30 minutes per frequency

Table 5.1: Computation times for the normal and preconditioned CG schemes

<i>Contrast value</i>	<i>Normal CG</i>	<i>Preconditioned CG</i>
$\{\chi^E, \chi^H\} = \{1, 1\}$	81.1 s	109.6 s
$\{\chi^E, \chi^H\} = \{5, 5\}$	332.5 s	353.7 s
$\{\chi^E, \chi^H\} = \{10, 10\}$	933.9 s	560.8 s
$\{\chi^E, \chi^H\} = \{20, 20\}$	1549.5 s	1089.1 s

for a grid of $14 \times 14 \times 10$ points in the computational domain and 40 receiver points. The storage requirements for the receiver Green's function (22 Mb per frequency at present for a $14 \times 14 \times 10$ grid and 40 receiver points) can be alleviated by using the fact that only those components of the electric field that are tangential to the receiving coil contour are needed. Therefore, if the (square) receiving coils are oriented along the x_1 - and x_2 -axes, we need to store only some components of the Green's function. Calculations were performed on a dual processor 2 GHz P4 computer with 2 Gb of memory.

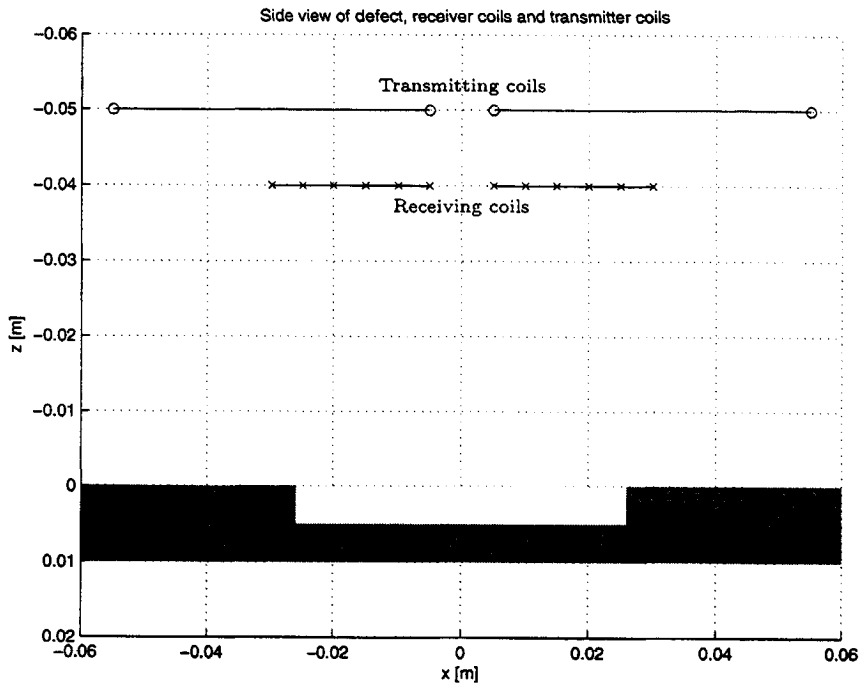


Figure 5.9: PEC coil configuration with 50% defect, side view.

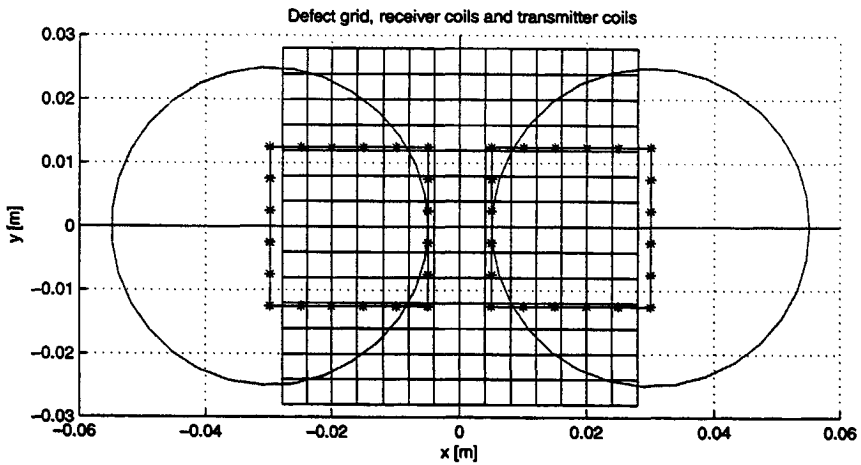


Figure 5.10: PEC coil configuration with 50% defect, top view, stars denote the points where the electric field is calculated (compare with Figure 5.9).

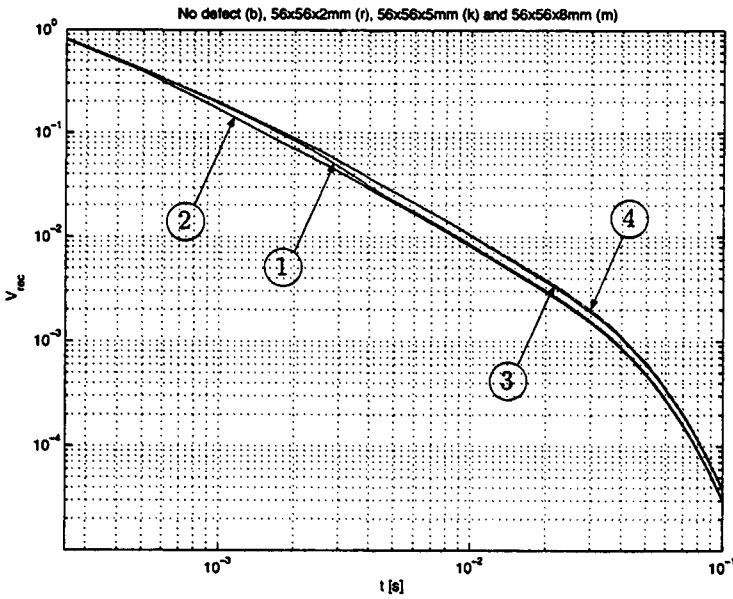


Figure 5.11: PEC signals for a $56 \times 56 \text{ mm}^2$ defect with a depth of 2 mm (1), 5 mm (2), 8 mm (3) and no-defect signal (4).

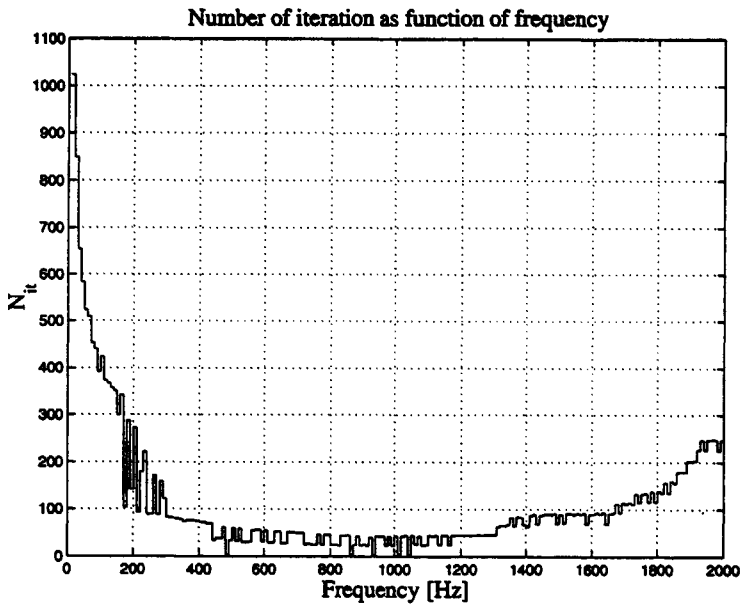


Figure 5.12: Number of iterations of the marching-on-in-frequency CG scheme per frequency for a typical PEC configuration.

Chapter 6

The Inverse Problem

Having defined a mathematical model to calculate the response of the PEC tool in the presence of a defect, we will now turn our attention to the inverse problem. This entails the reconstruction of the dimensions and medium parameters of a defect from measured signals when the rest of the configuration is known. For the inverse problem, the configuration is such that the source-receiver setup is known, as well as the dimensions and medium parameters of the metal layer, but the dimensions and medium parameters of the defect that is located within the layer are unknown. By means of the measurements taken at the receiver locations, we attempt to reconstruct the dimensions and medium parameters of the defect. While doing this, we assume that the medium parameters of the defect are equal to those of the halfspaces on either side of layer, i.e., the defect does not contain any corrosion products.

We will use the Extended Contrast Source Inversion (ECSI) method (see Van den Berg *et al.* [84]), which is based on the CSI method by Van den Berg and Kleinman [82]. We start by summarizing the ECSI method for contrasts located in a homogeneous background using the operators defined in the previous chapter. Next, we include the effects of the interfaces for a configuration consisting of a layer, where a contrast (i.e., a defect) can be located somewhere within that layer. Finally we describe a method for binary inversion, where the magnitude of the contrasts is assumed to be known, and we discuss the TV regularization method. Since the medium parameters of a defect in a PEC configuration are known, it is expected that a binary inversion method will yield better results than full inversion. Note that throughout this thesis we will be using single-frequency inversion methods.

6.1 3D Inversion for a homogeneous background

The operator equations pertaining to the inverse problem are the object equation

$$\begin{bmatrix} \hat{\mathbf{E}}^i \\ \hat{\mathbf{H}}^i \end{bmatrix}_k = (\mathbf{I} - \mathbf{K}^D \chi) \begin{bmatrix} \hat{\mathbf{E}} \\ \hat{\mathbf{H}} \end{bmatrix}_k, \quad (6.1)$$

which relates the contrast sources and the contrasts to the fields within the scattering domain, and the data equation,

$$\begin{bmatrix} \hat{\mathbf{E}}^S \\ \hat{\mathbf{H}}^S \end{bmatrix}_k = \mathbf{K}^S \chi \begin{bmatrix} \hat{\mathbf{E}} \\ \hat{\mathbf{H}} \end{bmatrix}_k, \quad (6.2)$$

which relates the (measured or synthetic) data to the contrasts and field quantities. The contrast matrix χ and the operators are defined in Chapter 4, while the subscript k denotes the source position. For multi-frequency inversion the operator will be frequency-dependent, however we will confine ourselves to single-frequency inversion in this thesis. The contrast sources can be recognized as

$$\begin{bmatrix} \hat{\mathbf{W}}^E \\ \hat{\mathbf{W}}^H \end{bmatrix}_k = \chi \begin{bmatrix} \hat{\mathbf{E}} \\ \hat{\mathbf{H}} \end{bmatrix}_k, \quad (6.3)$$

The ECSI scheme now aims to use a CG scheme to construct sequences for the contrast sources and contrasts, such that a cost functional is iteratively minimized. To this end we define the cost functional F_n at the n^{th} iteration of the scheme as

$$\begin{aligned} F_n(\hat{\mathbf{W}}_{k,n}^E, \hat{\mathbf{W}}_{k,n}^H, \chi_n^E, \chi_n^H) &= F_{S,n}(\hat{\mathbf{W}}_{k,n}^E, \hat{\mathbf{W}}_{k,n}^H) + F_{D,n}(\hat{\mathbf{W}}_{k,n}^E, \hat{\mathbf{W}}_{k,n}^H, \chi_n^E, \chi_n^H), \\ &= \eta_S^E \sum_k \|\rho_{k,n}^E\|_S^2 + \eta_S^H \sum_k \|\rho_{k,n}^H\|_S^2 \\ &\quad + \eta_D^E \sum_k \|x_{k,n}^E\|_D^2 + \eta_D^H \sum_k \|x_{k,n}^H\|_D^2. \end{aligned} \quad (6.4)$$

where the residuals in the data and object equations are defined as

$$\begin{bmatrix} \mathbf{r}^E \\ \mathbf{r}^H \end{bmatrix}_{k,n} = \chi_n \begin{bmatrix} \hat{\mathbf{E}}^i \\ \hat{\mathbf{H}}^i \end{bmatrix}_k - (\mathbf{I} - \chi_n \mathbf{K}^D) \begin{bmatrix} \hat{\mathbf{W}}^E \\ \hat{\mathbf{W}}^H \end{bmatrix}_{k,n}, \quad (6.5)$$

$$\begin{bmatrix} \rho^E \\ \rho^H \end{bmatrix}_{k,n} = \begin{bmatrix} \hat{\mathbf{E}}^S \\ \hat{\mathbf{H}}^S \end{bmatrix}_k - \mathbf{K}^S \begin{bmatrix} \hat{\mathbf{W}}^E \\ \hat{\mathbf{W}}^H \end{bmatrix}_{k,n}, \quad (6.6)$$

respectively. The normalization coefficients are given by

$$\eta_{D,n}^E = \frac{1}{\sum_k \left\| \chi_n^E \hat{\mathbf{E}}_k^i \right\|_D^2}, \quad (6.7)$$

$$\eta_{D,n}^H = \frac{1}{\sum_k \left\| \chi_n^H \hat{\mathbf{H}}_k^i \right\|_D^2}, \quad (6.8)$$

$$\eta_S^E = \frac{1}{\sum_k \left\| \hat{\mathbf{E}}_k^S \right\|_S^2}, \quad (6.9)$$

$$\eta_S^H = \frac{1}{\sum_k \left\| \hat{\mathbf{H}}_k^S \right\|_S^2}. \quad (6.10)$$

The components of the cost functional can be written explicitly in terms of the operators working on the contrast sources as

$$\begin{aligned} F_{S,n}(\hat{\mathbf{W}}_{k,n}^E, \hat{\mathbf{W}}_{k,n}^H) &= \quad (6.11) \\ &= F_{S,n}^E(\hat{\mathbf{W}}_{k,n}^E, \hat{\mathbf{W}}_{k,n}^H) + F_{S,n}^H(\hat{\mathbf{W}}_{k,n}^E, \hat{\mathbf{W}}_{k,n}^H) \\ &= \eta_S^E \sum_k \left\| \hat{\mathbf{E}}_k^S - \mathbf{K}^{S,EE} \hat{\mathbf{W}}_{k,n}^E - \mathbf{K}^{S,EH} \hat{\mathbf{W}}_{k,n}^H \right\|_S^2 \\ &\quad + \eta_S^H \sum_k \left\| \hat{\mathbf{H}}_k^S - \mathbf{K}^{S,HH} \hat{\mathbf{W}}_{k,n}^H - \mathbf{K}^{S,HE} \hat{\mathbf{W}}_{k,n}^E \right\|_S^2, \end{aligned}$$

and

$$\begin{aligned} F_{D,n}(\hat{\mathbf{W}}_{k,n}^E, \hat{\mathbf{W}}_{k,n}^H, \chi_n^E, \chi_n^H) &= \quad (6.12) \\ &= F_{D,n}^E(\hat{\mathbf{W}}_{k,n}^E, \hat{\mathbf{W}}_{k,n}^H, \chi_n^E) + F_{D,n}^H(\hat{\mathbf{W}}_{k,n}^E, \hat{\mathbf{W}}_{k,n}^H, \chi_n^H) \\ &= \eta_{D,n}^E \sum_k \left\| \chi_n^E \hat{\mathbf{E}}_k^i - \hat{\mathbf{W}}_{k,n}^E + \chi_n^E \mathbf{K}^{D,EE} \hat{\mathbf{W}}_{k,n}^E + \chi_n^E \mathbf{K}^{D,EH} \hat{\mathbf{W}}_{k,n}^H \right\|_D^2 \\ &\quad + \eta_{D,n}^H \sum_k \left\| \chi_n^H \hat{\mathbf{H}}_k^i - \hat{\mathbf{W}}_{k,n}^H + \chi_n^H \mathbf{K}^{D,HH} \hat{\mathbf{W}}_{k,n}^H + \chi_n^H \mathbf{K}^{D,HE} \hat{\mathbf{W}}_{k,n}^E \right\|_D^2. \end{aligned}$$

The ECSI scheme [84] now aims to iteratively minimize the cost functional F_n by constructing sequences for the contrast sources and the contrasts. The contrast sources and the contrasts are updated in separate steps, which enables us to use analytical expressions for the update coefficients, unlike for example the Modified Gradient method, where numerical (line) minimizations are necessary because in that method the fields and contrasts are updated simultaneously at each iteration.

6.1.1 Updating the contrast sources

Assuming that the contrast sources and the contrasts at the previous iteration are known, we write

$$\begin{bmatrix} \hat{\mathbf{W}}^E \\ \hat{\mathbf{W}}^H \end{bmatrix}_{k,n} = \begin{bmatrix} \hat{\mathbf{W}}^E \\ \hat{\mathbf{W}}^H \end{bmatrix}_{k,n-1} + \alpha_{k,n}^W \begin{bmatrix} \hat{\mathbf{w}}^E \\ \hat{\mathbf{w}}^H \end{bmatrix}_{k,n}, \quad (6.13)$$

where the update directions $\hat{\mathbf{w}}_{k,n}^E$ and $\hat{\mathbf{w}}_{k,n}^H$ are functions of position. The update directions are given by

$$\begin{bmatrix} \hat{\mathbf{w}}^E \\ \hat{\mathbf{w}}^H \end{bmatrix}_{k,0} = \mathbf{0}, \quad n = 0, \quad (6.14)$$

$$\begin{bmatrix} \hat{\mathbf{w}}^E \\ \hat{\mathbf{w}}^H \end{bmatrix}_{k,n} = \begin{bmatrix} \partial \hat{\mathbf{w}}^E \\ \partial \hat{\mathbf{w}}^H \end{bmatrix}_{k,n} + \gamma_{k,n}^W \begin{bmatrix} \hat{\mathbf{w}}^E \\ \hat{\mathbf{w}}^H \end{bmatrix}_{k,n-1}, \quad n \geq 1. \quad (6.15)$$

The coefficient $\gamma_{k,n}^W$ can be either the Fletcher-Reeves or the Polak-Ribière update coefficient, given by

$$\gamma_{k,n}^W = \frac{\|\partial \hat{\mathbf{w}}_{k,n}^E\|_D^2 + \|\partial \hat{\mathbf{w}}_{k,n}^H\|_D^2}{\|\partial \hat{\mathbf{w}}_{k,n-1}^E\|_D^2 + \|\partial \hat{\mathbf{w}}_{k,n-1}^H\|_D^2}, \quad (6.16)$$

or

$$\gamma_{k,n}^W = \frac{\text{Re} \langle \partial \hat{\mathbf{w}}_{k,n}^E, \partial \hat{\mathbf{w}}_{k,n}^E - \partial \hat{\mathbf{w}}_{k,n-1}^E \rangle_D + \text{Re} \langle \partial \hat{\mathbf{w}}_{k,n}^H, \partial \hat{\mathbf{w}}_{k,n}^H - \partial \hat{\mathbf{w}}_{k,n-1}^H \rangle_D}{\|\partial \hat{\mathbf{w}}_{k,n-1}^E\|_D^2 + \|\partial \hat{\mathbf{w}}_{k,n-1}^H\|_D^2}, \quad (6.17)$$

$$\frac{\text{Re} \langle \partial \hat{\mathbf{w}}_{k,n}^E, \partial \hat{\mathbf{w}}_{k,n}^E - \partial \hat{\mathbf{w}}_{k,n-1}^E \rangle_D + \text{Re} \langle \partial \hat{\mathbf{w}}_{k,n}^H, \partial \hat{\mathbf{w}}_{k,n}^H - \partial \hat{\mathbf{w}}_{k,n-1}^H \rangle_D}{\|\partial \hat{\mathbf{w}}_{k,n-1}^E\|_D^2 + \|\partial \hat{\mathbf{w}}_{k,n-1}^H\|_D^2},$$

respectively. The quantity $\partial \hat{\mathbf{w}}^{E,H}$ is the gradient of the cost functional $F_n(\hat{\mathbf{W}}_k, \chi)$ with respect to $\hat{\mathbf{W}}^E$ or $\hat{\mathbf{W}}^H$, evaluated at $\hat{\mathbf{W}}_{k,n-1}^E$, $\hat{\mathbf{W}}_{k,n-1}^H$ and χ_{n-1} . The gradients are derived using the Fréchet derivative, which results in

$$\begin{bmatrix} \partial \hat{\mathbf{w}}^E \\ \partial \hat{\mathbf{w}}^H \end{bmatrix}_{k,n} = -\mathbf{K}^{S,*} \Gamma_S \begin{bmatrix} \rho^E \\ \rho^H \end{bmatrix}_{k,n-1} - (\mathbf{I} - \mathbf{K}^{D,*} \bar{\chi}_{n-1}) \Gamma_{D,n-1} \begin{bmatrix} \mathbf{r}^E \\ \mathbf{r}^H \end{bmatrix}_{k,n-1}, \quad (6.18)$$

where the * symbol denotes the adjoint of the operator as defined in Chapter 4 and where the normalization matrices Γ_S and $\Gamma_{D,n}$ are defined as $\Gamma_S = \text{diag}(\eta_S^E, \eta_S^H)$ and $\Gamma_{D,n} = \text{diag}(\eta_{D,n}^E, \eta_{D,n}^H)$, respectively. The parameters $\alpha_{k,n}^W$ are determined by minimizing the cost functional with respect to $\alpha_{k,n}^W$. We write the cost functional

Eq. (6.4) as

$$\begin{aligned}
 F_n(\hat{\mathbf{W}}_{k,n}^E, \hat{\mathbf{W}}_{k,n}^H, \chi_{n-1}^E, \chi_{n-1}^H) = & \quad (6.19) \\
 & \eta_S^E \left\| \rho_{k,n-1}^E - \alpha_{k,n}^W (\mathbf{K}^{S,EE} \hat{\mathbf{w}}_{k,n}^E + \mathbf{K}^{S,EH} \hat{\mathbf{w}}_{k,n}^H) \right\|_S^2 \\
 & + \eta_S^H \left\| \rho_{k,n-1}^H - \alpha_{k,n}^W (\mathbf{K}^{S,HH} \hat{\mathbf{w}}_{k,n}^H + \mathbf{K}^{S,HE} \hat{\mathbf{w}}_{k,n}^E) \right\|_S^2 \\
 & + \eta_{D,n-1}^E \left\| \mathbf{r}_{k,n-1}^E - \alpha_{k,n}^W (\mathbf{I} - \chi_{n-1}^E \mathbf{K}^{D,EE}) \hat{\mathbf{w}}_{k,n}^E + \alpha_{k,n}^W \chi_{n-1}^E \mathbf{K}^{D,EH} \hat{\mathbf{w}}_{k,n}^H \right\|_D^2 \\
 & + \eta_{D,n-1}^H \left\| \mathbf{r}_{k,n-1}^H - \alpha_{k,n}^W (\mathbf{I} - \chi_{n-1}^H \mathbf{K}^{D,HH}) \hat{\mathbf{w}}_{k,n}^H + \alpha_{k,n}^W \chi_{n-1}^H \mathbf{K}^{D,HE} \hat{\mathbf{w}}_{k,n}^E \right\|_D^2,
 \end{aligned}$$

and then take

$$\frac{\partial F_n}{\partial \alpha_{k,n}^W} = 0. \quad (6.20)$$

This results in the following expression for the update coefficient of the contrast sources

$$\begin{aligned}
 \alpha_{k,n}^W = & \quad (6.21) \\
 & \left[\eta_S^E \left\| \mathbf{K}^{S,EE} \hat{\mathbf{w}}_{k,n}^E + \mathbf{K}^{S,EH} \hat{\mathbf{w}}_{k,n}^H \right\|_S^2 + \eta_S^H \left\| \mathbf{K}^{S,HH} \hat{\mathbf{w}}_{k,n}^H + \mathbf{K}^{S,HE} \hat{\mathbf{w}}_{k,n}^E \right\|_S^2 \right. \\
 & + \eta_{D,n-1}^E \left\| \hat{\mathbf{w}}_{k,n}^E - \chi_{n-1}^E \mathbf{K}^{D,EE} \hat{\mathbf{w}}_{k,n}^E - \chi_{n-1}^E \mathbf{K}^{D,EH} \hat{\mathbf{w}}_{k,n}^H \right\|_D^2 \\
 & \left. + \eta_{D,n-1}^H \left\| \hat{\mathbf{w}}_{k,n}^H - \chi_{n-1}^H \mathbf{K}^{D,HH} \hat{\mathbf{w}}_{k,n}^H - \chi_{n-1}^H \mathbf{K}^{D,HE} \hat{\mathbf{w}}_{k,n}^E \right\|_D^2 \right]^{-1} \\
 & \times \left[\langle \partial \hat{\mathbf{w}}_{k,n}^E, \hat{\mathbf{w}}_{k,n}^E \rangle_D + \langle \partial \hat{\mathbf{w}}_{k,n}^H, \hat{\mathbf{w}}_{k,n}^H \rangle_D \right]
 \end{aligned}$$

From numerical experiments it was found that the parameter $\alpha_{k,n}^W$ can be taken real without detrimental effects on convergence and results (see Abubakar [2]).

6.1.2 Updating the contrasts

The contrasts χ^E and χ^H are only present in the second term of the cost functional, which is the part relating to the error in the object equation. This part of the cost functional is given according to Eq. (6.12) as

$$\begin{aligned}
 F_{D,n}(\hat{\mathbf{W}}_{k,n}^E, \hat{\mathbf{W}}_{k,n}^H, \chi_n^E, \chi_n^H) = & \quad (6.22) \\
 & \eta_{D,n}^E \sum_k \left\| \chi_n^E \hat{\mathbf{E}}_{k,n} - \hat{\mathbf{W}}_{k,n}^E \right\|_D^2 + \eta_{D,n}^H \sum_k \left\| \chi_n^H \hat{\mathbf{H}}_{k,n} - \hat{\mathbf{W}}_{k,n}^H \right\|_D^2.
 \end{aligned}$$

We can update the contrasts in two different ways, by using either a non-CG or a CG update. The non-CG update was used by Kleinman and Van den Berg in the original version of the CSI method, but this does not ensure the reduction of $F_{D,n}$. However, from numerical experiments it was observed that after a few iterations this update for the contrasts does always reduce $F_{D,n}$. Using a CG update for the contrasts ensures the reduction of the quantity $F_{D,n}$, and enables us to use regularization methods. In the next two sections we will discuss these update methods for the contrasts.

Non-CG update of the contrasts

Taking the gradient of $F_{D,n}(\hat{\mathbf{W}}_{k,n}^E, \hat{\mathbf{W}}_{k,n}^H, \chi_{n-1}^E, \chi_{n-1}^H)$ with respect to χ_{n-1}^E and χ_{n-1}^H , we observe that the cost functional $F_{D,n}$ is minimized when

$$\chi_n^E = \frac{\sum_k \hat{\mathbf{W}}_{k,n}^E \cdot \bar{\hat{\mathbf{E}}}_{k,n}}{\sum_k |\hat{\mathbf{E}}_{k,n}|^2} = \chi_{n-1}^E - \frac{\sum_k \mathbf{r}_{k,n}^{E'} \cdot \bar{\hat{\mathbf{E}}}_{k,n}}{\sum_k |\hat{\mathbf{E}}_{k,n}|^2}, \quad (6.23)$$

and

$$\chi_n^H = \frac{\sum_k \hat{\mathbf{W}}_{k,n}^H \cdot \bar{\hat{\mathbf{H}}}_{k,n}}{\sum_k |\hat{\mathbf{H}}_{k,n}|^2} = \chi_{n-1}^H - \frac{\sum_k \mathbf{r}_{k,n}^{H'} \cdot \bar{\hat{\mathbf{H}}}_{k,n}}{\sum_k |\hat{\mathbf{H}}_{k,n}|^2}, \quad (6.24)$$

in which $\mathbf{r}_{k,n}^{E'}$ and $\mathbf{r}_{k,n}^{H'}$ are given by

$$\mathbf{r}_{k,n}^{E'} = \chi_{n-1}^E \hat{\mathbf{E}}_{k,n} - \hat{\mathbf{W}}_{k,n}^E, \quad (6.25)$$

$$\mathbf{r}_{k,n}^{H'} = \chi_{n-1}^H \hat{\mathbf{H}}_{k,n} - \hat{\mathbf{W}}_{k,n}^H. \quad (6.26)$$

CG update of the contrasts

For the CG update of the contrasts, we write

$$\chi_n = \chi_{n-1} + \alpha_n^X \mathbf{d}_n, \quad (6.27)$$

where

$$\begin{bmatrix} \chi_n^E & 0 \\ 0 & \chi_n^H \end{bmatrix} = \begin{bmatrix} \chi_{n-1}^E & 0 \\ 0 & \chi_{n-1}^H \end{bmatrix} + \begin{bmatrix} \alpha_n^{X,E} & 0 \\ 0 & \alpha_n^{X,H} \end{bmatrix} \begin{bmatrix} d^E \\ d^H \end{bmatrix}_n. \quad (6.28)$$

In recent work, Van den Berg *et al.* [85] take the non-CG update given in Eqs. (6.23) and (6.24) instead of χ_{n-1} for the CG update of the contrasts in Eq. (6.27), essentially taking two steps for the update of the contrasts. The quantities d_n^E and

d_n^H are the update directions for the contrasts, which are taken to be the Polak-Ribière conjugate gradient directions, given by

$$\begin{aligned} \begin{bmatrix} d^E \\ d^H \end{bmatrix}_0 &= \mathbf{0}, & n = 0, \quad (6.29) \\ \begin{bmatrix} d^E \\ d^H \end{bmatrix}_n &= \begin{bmatrix} g^{\chi,E} \\ g^{\chi,H} \end{bmatrix}_n + \begin{bmatrix} \gamma^{\chi,E} & 0 \\ 0 & \gamma^{\chi,H} \end{bmatrix}_n \begin{bmatrix} d^E \\ d^H \end{bmatrix}_{n-1}, & n \geq 1, \end{aligned}$$

where the coefficients $\gamma_n^{\chi,E}$ and $\gamma_n^{\chi,H}$ are defined as

$$\gamma_n^{\chi,E} = \frac{\text{Re} \langle g_n^{\chi,E}, g_n^{\chi,E} - g_{n-1}^{\chi,E} \rangle_D}{\|g_{n-1}^{\chi,E}\|_D^2}, \quad (6.30)$$

$$\gamma_n^{\chi,H} = \frac{\text{Re} \langle g_n^{\chi,H}, g_n^{\chi,H} - g_{n-1}^{\chi,H} \rangle_D}{\|g_{n-1}^{\chi,H}\|_D^2}. \quad (6.31)$$

The quantities $g_n^{\chi,E}$ and $g_n^{\chi,H}$ are the gradients of the numerator of the cost functional with respect to χ^E and χ^H , respectively. The gradients are calculated at χ_{n-1}^E and χ_{n-1}^H . We obtain

$$g_n^{\chi,E} = - \frac{\sum_k \mathbf{r}_{k,n}^{E'} \cdot \bar{\hat{\mathbf{E}}}_{k,n}}{\sum_k \left\| \chi_{n-1}^E \hat{\mathbf{E}}_k^i \right\|_D^2}, \quad (6.32)$$

$$g_n^{\chi,H} = - \frac{\sum_k \mathbf{r}_{k,n}^{H'} \cdot \bar{\hat{\mathbf{H}}}_{k,n}}{\sum_k \left\| \chi_{n-1}^H \hat{\mathbf{H}}_k^i \right\|_D^2}. \quad (6.33)$$

Where $\mathbf{r}_{k,n}^{E'}$ and $\mathbf{r}_{k,n}^{H'}$ are given in Eqs. (6.25) and (6.26). Numerical experiments have shown (see Van den Berg *et al.* [84]) that neglecting the influence of the denominator of the cost functional in the gradients has little effect. Furthermore, in the diffusive approximation, where the contrasts are real-valued, we can take the real parts of the gradients in Eqs. (6.32) and (6.33). Comparing Eqs. (6.23) - (6.24) with Eqs. (6.32) - (6.33), we can derive preconditioned gradients with respect to the contrasts as

$$g_n^{\chi,E} = - \frac{1}{\sum_k |\hat{\mathbf{E}}_{k,n}|^2} \frac{\sum_k \mathbf{r}_{k,n}^{E'} \cdot \bar{\hat{\mathbf{E}}}_{k,n}}{\sum_k \left\| \chi_{n-1}^E \hat{\mathbf{E}}_k^i \right\|_D^2}, \quad (6.34)$$

$$g_n^{\chi,H} = - \frac{1}{\sum_k |\hat{\mathbf{H}}_{k,n}|^2} \frac{\sum_k \mathbf{r}_{k,n}^{H'} \cdot \bar{\hat{\mathbf{H}}}_{k,n}}{\sum_k \left\| \chi_{n-1}^H \hat{\mathbf{H}}_k^i \right\|_D^2}. \quad (6.35)$$

Following Van den Berg *et al.* [84], we choose the update coefficients $\alpha_n^{\chi,E}$ and $\alpha_n^{\chi,H}$ to be real and write the cost functional $F_{D,n}$ in terms of the the update

coefficients. For the electric contrast, this gives

$$F_{D,n} = F_{D,n}^E + F_{D,n}^H \quad (6.36)$$

$$\begin{aligned} &= \frac{\sum_k \left\| (\chi_{n-1}^E + \alpha_n^{\chi,E} d_n^E) \hat{\mathbf{E}}_{k,n} - \hat{\mathbf{W}}_{k,n}^E \right\|_D^2}{\sum_k \left\| (\chi_{n-1}^E + \alpha_n^{\chi,E} d_n^E) \hat{\mathbf{E}}_k^i \right\|_D^2} + F_{D,n}^H, \\ &= \frac{A_1 (\alpha_n^{\chi,E})^2 + 2A_2 (\alpha_n^{\chi,E}) + A_3}{B_1 (\alpha_n^{\chi,E})^2 + 2B_2 (\alpha_n^{\chi,E}) + B_3} + F_{D,n}^H, \end{aligned} \quad (6.37)$$

in which

$$A_1 = \sum_k \left\| d_n^E \hat{\mathbf{E}}_{k,n} \right\|_D^2, \quad (6.38)$$

$$A_2 = \operatorname{Re} \sum_k \left\langle \mathbf{r}_{k,n}^{E'}, d_n^E \hat{\mathbf{E}}_{k,n} \right\rangle_D, \quad (6.39)$$

$$A_3 = \sum_k \left\| \mathbf{r}_{k,n}^{E'} \right\|_D^2, \quad (6.40)$$

$$B_1 = \sum_k \left\| d_n^E \hat{\mathbf{E}}_k^i \right\|_D^2, \quad (6.41)$$

$$B_2 = \operatorname{Re} \sum_k \left\langle \chi_{n-1}^E \hat{\mathbf{E}}_k^i, d_n^E \hat{\mathbf{E}}_k^i \right\rangle_D, \quad (6.42)$$

$$B_3 = \sum_k \left\| \chi_{n-1}^E \hat{\mathbf{E}}_k^i \right\|_D^2. \quad (6.43)$$

For the magnetic contrast we have

$$F_{D,n} = F_{D,n}^E + F_{D,n}^H \quad (6.44)$$

$$\begin{aligned} &= \frac{\sum_k \left\| (\chi_{n-1}^H + \alpha_n^{\chi,H} d_n^H) \hat{\mathbf{H}}_{k,n} - \hat{\mathbf{W}}_{k,n}^H \right\|_D^2}{\sum_k \left\| (\chi_{n-1}^H + \alpha_n^{\chi,H} d_n^H) \hat{\mathbf{H}}_k^i \right\|_D^2} + F_{D,n}^E, \\ &= \frac{C_1 (\alpha_n^{\chi,H})^2 + 2C_2 (\alpha_n^{\chi,H}) + C_3}{D_1 (\alpha_n^{\chi,H})^2 + 2D_2 (\alpha_n^{\chi,H}) + D_3} + F_{D,n}^E, \end{aligned} \quad (6.45)$$

where

$$C_1 = \sum_k \left\| d_n^H \hat{\mathbf{H}}_{k,n} \right\|_D^2, \quad (6.46)$$

$$C_2 = \operatorname{Re} \sum_k \left\langle \mathbf{r}_{k,n}^{H'}, B d_n^H \hat{\mathbf{H}}_{k,n} \right\rangle_D, \quad (6.47)$$

$$C_3 = \sum_k \left\| \mathbf{r}_{k,n}^{H'} \right\|_D^2, \quad (6.48)$$

$$D_1 = \sum_k \left\| d_n^H \hat{\mathbf{H}}_k^i \right\|_D^2, \quad (6.49)$$

$$D_2 = \operatorname{Re} \sum_k \left\langle \chi_{n-1}^H \hat{\mathbf{H}}_k^i, d_n^H \hat{\mathbf{H}}_k^i \right\rangle_D, \quad (6.50)$$

$$D_3 = \sum_k \left\| \chi_{n-1}^H \hat{\mathbf{H}}_k^i \right\|_D^2. \quad (6.51)$$

These cost functionals are minimized when

$$\frac{\partial}{\partial \alpha_n^{\chi,E}} F_{D,n} = 0, \quad \text{and} \quad \frac{\partial}{\partial \alpha_n^{\chi,H}} F_{D,n} = 0, \quad (6.52)$$

which results in the following expressions for the update coefficients in terms of A_i, B_i, C_i and D_i ($i = 1, 2, 3$)

$$\alpha_n^{\chi,E} = [2(A_1 B_2 - A_2 B_1)]^{-1} \times [-(A_1 B_3 - A_3 B_1) + (A_1 B_3 - A_3 B_1)^2 - 4(A_1 B_2 - A_2 B_1)(A_2 B_3 - A_3 B_2)]^{\frac{1}{2}}. \quad (6.53)$$

$$\alpha_n^{\chi,H} = [2(C_1 D_2 - C_2 D_1)]^{-1} \times [-(C_1 D_3 - C_3 D_1) + (C_1 D_3 - C_3 D_1)^2 - 4(C_1 D_2 - C_2 D_1)(C_2 D_3 - C_3 D_2)]^{\frac{1}{2}}. \quad (6.54)$$

6.1.3 Starting values

At the start of the ECSI scheme, we need initial values for the contrasts and the contrast sources. It is not possible to set the initial values to zero, since the cost functional is undefined for $\chi = 0$. Therefore we choose to take the backpropagation of the data as initial values. We let the starting values of the contrast sources minimize F_S only, giving

$$F_{S,0}(\hat{\mathbf{W}}_{k,0}^E, \hat{\mathbf{W}}_{k,0}^H) = \eta_S^E \sum_k \left\| \rho_{k,0}^E \right\|_S^2 + \eta_S^H \sum_k \left\| \rho_{k,0}^H \right\|_S^2. \quad (6.55)$$

We now write the contrast sources at iteration $n = 0$ as

$$\begin{bmatrix} \hat{\mathbf{W}}^E \\ \hat{\mathbf{W}}^H \end{bmatrix}_{k,0} = \alpha_{k,0}^W \begin{bmatrix} \partial \hat{\mathbf{w}}^E \\ \partial \hat{\mathbf{w}}^H \end{bmatrix}_{k,0}, \quad (6.56)$$

where the gradients of F_S with respect to the contrast sources are given by

$$\begin{bmatrix} \partial \hat{\mathbf{w}}^E \\ \partial \hat{\mathbf{w}}^H \end{bmatrix}_{k,0} = \mathbf{K}^{S,*} \Gamma_S \begin{bmatrix} \hat{\mathbf{E}}^S \\ \hat{\mathbf{H}}^S \end{bmatrix}_k, \quad (6.57)$$

in which the $*$ symbol denotes the adjoint operator. The coefficient $\alpha_{k,0}^W$ is found by minimizing F_S for variation of $\alpha_{k,0}^W$, leading to

$$\alpha_{k,0}^W = \frac{\left\| \partial \hat{\mathbf{w}}_{k,0}^E \right\|_D^2 + \left\| \partial \hat{\mathbf{w}}_{k,0}^H \right\|_D^2}{\left\| \mathbf{K}^{S,EE} \partial \hat{\mathbf{w}}_{k,0}^E + \mathbf{K}^{S,EH} \partial \hat{\mathbf{w}}_{k,0}^H \right\|_S^2 + \left\| \mathbf{K}^{S,HH} \partial \hat{\mathbf{w}}_{k,0}^H + \mathbf{K}^{S,HE} \partial \hat{\mathbf{w}}_{k,0}^E \right\|_S^2}. \quad (6.58)$$

The gradients represent the backprojection of the data on S onto D . The initial estimates for the fields are obtained from the contrast sources as

$$\begin{bmatrix} \hat{\mathbf{E}} \\ \hat{\mathbf{H}} \end{bmatrix}_{k,0} = \begin{bmatrix} \hat{\mathbf{E}}^i \\ \hat{\mathbf{H}}^i \end{bmatrix}_k + \mathbf{K}^D \begin{bmatrix} \hat{\mathbf{W}}^E \\ \hat{\mathbf{W}}^H \end{bmatrix}_{k,0}. \quad (6.59)$$

Finally, the initial estimates for the contrasts are given by

$$\chi_0^E = \frac{\sum_k \hat{\mathbf{W}}_{k,0}^E \cdot \bar{\hat{\mathbf{E}}}_{k,0}}{\sum_k |\hat{\mathbf{E}}_{k,0}|^2}, \quad (6.60)$$

$$\chi_0^H = \frac{\sum_k \hat{\mathbf{W}}_{k,0}^H \cdot \bar{\hat{\mathbf{H}}}_{k,0}}{\sum_k |\hat{\mathbf{H}}_{k,0}|^2}. \quad (6.61)$$

6.2 3D Inversion for a stratified configuration

We can use the inversion algorithm described in the previous section for the problem where the scattering object is located within a layer. To include the (multiple) reflection and transmission effects at the interfaces, we have to modify the Green's functions occurring in the expressions for the object operator and adjoint object operator, which are described in Section 4.9. We will now define the data operator for the stratified configuration. Starting from

$$\hat{\mathbf{E}}^s = \int_{\mathbf{x}' \in D} \left((\sigma_b - i\omega\epsilon_0) \hat{\mathbf{G}}^{S,EE} \cdot \chi^E \mathbf{E} - i\omega\mu_b \hat{\mathbf{G}}^{S,EH} \cdot \chi^H \mathbf{H} \right) d\mathbf{x}', \quad (6.62)$$

$$\hat{\mathbf{H}}^s = \int_{\mathbf{x}' \in D} \left((\sigma_b - i\omega\epsilon_0) \hat{\mathbf{G}}^{S,HE} \cdot \chi^E \mathbf{E} - i\omega\mu_b \hat{\mathbf{G}}^{S,HH} \cdot \chi^H \mathbf{H} \right) d\mathbf{x}', \quad (6.63)$$

where the superscript S denotes the Green's function from scattering domain to the receiver positions and ε_0 , σ_b and μ_b are the medium parameters corresponding to the layer. We then define the discrete data operator corresponding to the layered configuration as

$$\begin{bmatrix} \hat{\mathbf{E}}^S \\ \hat{\mathbf{H}}^S \end{bmatrix} = \mathbf{K}^{S,R} \chi \begin{bmatrix} \hat{\mathbf{E}} \\ \hat{\mathbf{H}} \end{bmatrix}, \quad (6.64)$$

where the operator matrix $\mathbf{K}^{S,R}$ is defined by

$$\mathbf{K}^{S,R} = \begin{bmatrix} \mathcal{K}^{S,EE,R} & \mathcal{K}^{S,EH,R} \\ \mathcal{K}^{S,HE,R} & \mathcal{K}^{S,HH,R} \end{bmatrix}. \quad (6.65)$$

The expressions for the scattered fields at the receiver positions \mathbf{x}^S in discrete form are given by

$$\begin{aligned} \hat{\mathbf{E}}_k^s(\mathbf{x}^S) = & \quad (6.66) \\ & (\sigma_b - i\omega\varepsilon_0)\Delta x_1\Delta x_2\Delta x_3 \sum_{j=1}^3 \sum_{m=1}^M \sum_{n=1}^N \sum_{p=1}^P \hat{\mathbf{G}}_{k,j}^{S,EE,R}(\mathbf{x}^S - \mathbf{x}_{m,n,p}) \chi_{m,n,p}^E \hat{\mathbf{E}}_{j;m,n,p} \\ & - i\omega\mu_b\Delta x_1\Delta x_2\Delta x_3 \sum_{j=1}^3 \sum_{m=1}^M \sum_{n=1}^N \sum_{p=1}^P \hat{\mathbf{G}}_{k,j}^{S,EH,R}(\mathbf{x}^S - \mathbf{x}_{m,n,p}) \chi_{m,n,p}^H \hat{\mathbf{H}}_{j;m,n,p}, \end{aligned}$$

and

$$\begin{aligned} \hat{\mathbf{H}}_k^s(\mathbf{x}^S) = & \quad (6.67) \\ & (\sigma_b - i\omega\varepsilon_0)\Delta x_1\Delta x_2\Delta x_3 \sum_{j=1}^3 \sum_{m=1}^M \sum_{n=1}^N \sum_{p=1}^P \hat{\mathbf{G}}_{k,j}^{S,HE,R}(\mathbf{x}^S - \mathbf{x}_{m,n,p}) \chi_{m,n,p}^E \hat{\mathbf{E}}_{j;m,n,p} \\ & - i\omega\mu_b\Delta x_1\Delta x_2\Delta x_3 \sum_{j=1}^3 \sum_{m=1}^M \sum_{n=1}^N \sum_{p=1}^P \hat{\mathbf{G}}_{k,j}^{S,HH,R}(\mathbf{x}^S - \mathbf{x}_{m,n,p}) \chi_{m,n,p}^H \hat{\mathbf{H}}_{j;m,n,p}, \end{aligned}$$

The adjoint data operator is again defined by using the inner product on S , leading to

$$\mathbf{K}^{S,R*} = \begin{bmatrix} \mathcal{K}^{S,EE,R*} & \mathcal{K}^{S,HE,R*} \\ \mathcal{K}^{S,EH,R*} & \mathcal{K}^{S,HH,R*} \end{bmatrix}. \quad (6.68)$$

For the elements of $\mathbf{K}^{S,R*}$ working on the residuals of the data equation, we obtain

$$\begin{aligned} (\mathcal{K}^{S,EE,R*} \rho_k^E)_{j;m,n,p} = & \quad (6.69) \\ & (\sigma_b - i\omega\varepsilon_0) \sum_{k=1}^3 \sum_{\mathbf{x}^S} \hat{\mathbf{G}}_{j,k}^{S,EE,R*}(\mathbf{x}_{m,n,p} - \mathbf{x}^S) \rho_k^E(\mathbf{x}^S), \end{aligned}$$

$$\begin{aligned} \left(\boldsymbol{\kappa}^{S,HE,R*} \rho_k^H \right)_{j;m,n,p} &= \\ (\sigma_b - \overline{i\omega\epsilon_0}) \sum_{k=1}^3 \sum_{\mathbf{x}^S} \hat{\mathbf{G}}_{j,k}^{S,HE,R*}(\mathbf{x}_{m,n,p} - \mathbf{x}^S) \rho_k^H(\mathbf{x}^S), \end{aligned} \quad (6.70)$$

$$\left(\boldsymbol{\kappa}^{S,EH,R*} \rho_k^E \right)_{j;m,n,p} = -\overline{i\omega\mu_b} \sum_{k=1}^3 \sum_{\mathbf{x}^S} \hat{\mathbf{G}}_{j,k}^{S,EH,R*}(\mathbf{x}_{m,n,p} - \mathbf{x}^S) \rho_k^E(\mathbf{x}^S), \quad (6.71)$$

$$\left(\boldsymbol{\kappa}^{S,HH,R*} \rho_k^H \right)_{j;m,n,p} = -\overline{i\omega\mu_b} \sum_{k=1}^3 \sum_{\mathbf{x}^S} \hat{\mathbf{G}}_{j,k}^{S,HH,R*}(\mathbf{x}_{m,n,p} - \mathbf{x}^S) \rho_k^H(\mathbf{x}^S). \quad (6.72)$$

6.3 Binary inversion

In this section we will discuss binary inversion, where the exact value of the contrast is known and constant, as is the case for the PEC configuration, where we have a defect in a metal layer. We know that the conductivity in the defect volume is equal to that of the halfspaces and that its relative permeability is one when the defect is not filled with rust. Essentially, for the binary inversion method we prescribe a value for the contrast and then proceed to recover the volume occupied by the scatterer.

For these configurations we can employ a number of techniques to improve the inversion results. First of all, it is possible to use a constraint in the normal ECSI algorithm by enforcing limits on the values of the contrasts at each iteration. For example, to ensure positivity, at each iteration we simply set the value of the contrast to zero when it is negative. This leads to better inversion results, however, changing the values of the contrasts at each iteration causes the cost functional to be no longer uniformly decreasing, which can lead to instability in the inversion algorithm.

A better option would be to use a nonlinear mapping function (for example an exponential constraint) for the contrasts. Using the ECSI algorithm, we calculate auxiliary functions at each iteration, from which we calculate the contrasts by using the mapping function. This mapping function ensures that the reconstructed values of the contrasts are within the range defined by the mapping function. This technique was used by Lambert and Lesselier [46] to reconstruct a buried cylindrical obstacle from magnetic field data and by Dos Reis *et al.* [29] to reconstruct conductivity contrasts in metal layers. We have modified this technique to be used for contrasts in both conductivity and permeability. Another technique to improve the reconstruction results is the TV regularization, which is described in the next section.

For the inversion scheme with exponential constraint, we write the contrast

functions as

$$\chi^E(\mathbf{x}) = \chi_s^E \psi(\tau^E(\mathbf{x})), \quad (6.73)$$

$$\chi^H(\mathbf{x}) = \chi_s^H \psi(\tau^H(\mathbf{x})), \quad (6.74)$$

where the quantities χ_s^E and χ_s^H denote the 'set' value of the contrast, i.e., the maximum allowed value. The mapping function ψ is given by

$$\psi(\tau(\mathbf{x})) = \frac{1}{1 + \exp(-\tau(\mathbf{x}))}. \quad (6.75)$$

This function has the property that

$$\psi \rightarrow 0, \quad \tau \rightarrow -\infty, \quad (6.76)$$

$$\psi \rightarrow 1, \quad \tau \rightarrow +\infty. \quad (6.77)$$

Lambert and Lesselier [46] take $1/(1 + \exp(-\tau/a))$ as mapping function, where a is an adjustable parameter to control the slope of the mapping function. However, adjusting the value of this parameter gives rise to jumps in the residual. We have chosen to take $a = 1$ in our scheme, since adjusting the parameter during the inversion process could cause instability and choosing the correct value of a is an empirical process. We now construct sequences for τ^E and τ^H by writing

$$\tau_n^E = \tau_{n-1}^E + \beta_n^E d_n^E, \quad (6.78)$$

$$\tau_n^H = \tau_{n-1}^H + \beta_n^H d_n^H, \quad (6.79)$$

where we take d_n^E and d_n^H to be the Polak-Ribière update directions

$$d_0^E = 0, \quad n = 0, \quad (6.80)$$

$$d_n^E = g_n^{\tau,E} + \gamma_n^{\tau,E} d_{n-1}^E, \quad n \geq 1, \quad (6.81)$$

and

$$d_0^H = 0, \quad n = 0, \quad (6.82)$$

$$d_n^H = g_n^{\tau,H} + \gamma_n^{\tau,H} d_{n-1}^H, \quad n \geq 1. \quad (6.83)$$

The update coefficients $\gamma_n^{\tau,E}$ and $\gamma_n^{\tau,H}$ are defined by

$$\gamma_n^{\tau,E} = \frac{\operatorname{Re} \langle g_n^{\tau,E}, g_n^{\tau,E} - g_{n-1}^{\tau,E} \rangle_D}{\|g_{n-1}^{\tau,E}\|_D^2}, \quad (6.84)$$

$$\gamma_n^{\tau,H} = \frac{\operatorname{Re} \langle g_n^{\tau,H}, g_n^{\tau,H} - g_{n-1}^{\tau,H} \rangle_D}{\|g_{n-1}^{\tau,H}\|_D^2}. \quad (6.85)$$

The gradients $g_n^{\tau,E}$ and $g_n^{\tau,H}$ are the gradients of the cost functional $F_{D,n}$ with respect to τ^E and τ^H , respectively, evaluated at τ_{n-1}^E and τ_{n-1}^H . These gradients can be written in terms of the gradients derived in Section 6.1.2 by taking into account that

$$g_n^\tau = \left. \frac{\partial F_{D,n}}{\partial \tau} \right|_{n-1} = \frac{\partial \chi}{\partial \tau} \frac{\partial F_{D,n}}{\partial \chi} \Big|_{n-1} = \frac{\partial \chi}{\partial \tau} g^\chi \Big|_{n-1}. \quad (6.86)$$

Using this result, we obtain the following expression for the gradients with respect to $\tau_n^{E/H}$

$$g_n^{\tau,E} = \chi_s^E \frac{\exp(-\tau_{n-1}^E)}{[1 + \exp(-\tau_{n-1}^E)]^2} g_n^{\chi,E}, \quad (6.87)$$

$$g_n^{\tau,H} = \chi_s^H \frac{\exp(-\tau_{n-1}^H)}{[1 + \exp(-\tau_{n-1}^H)]^2} g_n^{\chi,H}, \quad (6.88)$$

in which χ_s^E and χ_s^H are the 'set' values of the contrasts. We can now write the cost functional in terms of the update coefficients $\beta_n^{E,H}$ as (taking $F_{D,n}^E$ as an example)

$$F_{D,n}^E(\beta_n^E) = \frac{\sum_k \left\| \chi_s^E [1 + \exp(-\tau_{n-1}^E - \beta_n^E d_n^E)]^{-1} \hat{\mathbf{E}}_{k,n} - \hat{\mathbf{W}}_{k,n}^E \right\|_D^2}{\sum_k \left\| [1 + \exp(-\tau_{n-1}^E - \beta_n^E d_n^E)]^{-1} \hat{\mathbf{E}}_k \right\|_D^2}. \quad (6.89)$$

The values of the update coefficients β_n^E and β_n^H are found by minimizing the derivative of $F_{D,n}$ with respect to β_n^E and β_n^H for variation of these coefficients. Due to the nonlinearity of the mapping, this minimization cannot be done analytically, hence we employ a numerical line minimization routine from Numerical Recipes [67]. Following Section 6.1.2, we minimize only for variation in the nominator of the cost functional.

For the derivative of the nominator of the cost functional with respect to the update coefficient β_n^E we write (again taking $F_{D,n}^E$ as an example)

$$\frac{\partial}{\partial \beta_n^E} F_{D,n}^E(\beta_n^E) = \frac{\sum_k \left\langle \frac{\partial}{\partial \beta_n^E} \chi^E(\beta_n^E) \hat{\mathbf{E}}_{k,n}, \chi^E(\beta_n^E) \hat{\mathbf{E}}_{k,n} - \hat{\mathbf{W}}_{k,n}^E \right\rangle_D}{\sum_k \left\| \chi_{n-1} \hat{\mathbf{E}}_k \right\|_D^2}, \quad (6.90)$$

in which

$$\frac{\partial}{\partial \beta_n^E} \chi^E(\beta_n^E) = \chi_s^E \frac{d_n^E \exp(-\tau_{n-1}^E - \beta_n^E d_n^E)}{[1 + \exp(-\tau_{n-1}^E - \beta_n^E d_n^E)]^2}. \quad (6.91)$$

For the line minimization algorithm we need a starting value for β_n^E , which we obtain by using a Taylor expansion of the contrast in terms of β_n^E . Taking the first two

terms of the expansion linearizes the cost functional and we are able to obtain the following starting value for β_n^E by minimizing the nominator of the linearized cost functional for variation of β_n^E

$$\beta_{initial}^E = - \frac{\text{Re} \left\langle \chi^E(\beta^E = 0) \hat{\mathbf{E}}_{k,n} - \hat{\mathbf{W}}_{k,n}, \chi^{E'}(\beta^E = 0) \hat{\mathbf{E}}_{k,n} \right\rangle_D}{\left\| \chi^{E'}(\beta^E = 0) \hat{\mathbf{E}}_{k,n} \right\|_D^2}, \quad (6.92)$$

where $\chi^{E'}(\beta^E = 0)$ is defined as

$$\chi^{E'}(\beta^E = 0) = \left. \frac{\partial \chi^E(\beta^E)}{\partial \beta^E} \right|_{\beta^E=0} = \chi_s^E \frac{d_n^E \exp(-\tau_{n-1}^E)}{[1 + \exp(-\tau_{n-1}^E)]^2}. \quad (6.93)$$

The expression for β_n^H has a similar form. From numerical experiments we have seen that the starting values of β_n^E and β_n^H are already very close to the final values obtained by using the line minimization.

6.4 Total variation regularization

In this section we discuss the use of Total Variation (TV) as a regularization term for the inverse problem. Van den Berg *et al.* [85] have obtained good results with this type of regularization, and since the problem of reconstructing a defect in a PEC configuration is rather ill-posed due to the negative contrasts and the one-sided illumination, the inclusion of a regularization term in the inversion scheme is expected to yield better results.

Taking the regularization into account as a multiplicative constraint, we write the new cost functional as

$$F_n = \left[F_{S,n}^E(\hat{\mathbf{W}}_{k,n}^E, \hat{\mathbf{W}}_{k,n}^H) + F_{D,n}^E(\hat{\mathbf{W}}_{k,n}^E, \hat{\mathbf{W}}_{k,n}^H, \chi_n^E) \right] F_{TV,n}^E(\chi^E) \quad (6.94) \\ + \left[F_{S,n}^H(\hat{\mathbf{W}}_{k,n}^E, \hat{\mathbf{W}}_{k,n}^H) + F_{D,n}^H(\hat{\mathbf{W}}_{k,n}^E, \hat{\mathbf{W}}_{k,n}^H, \chi_n^H) \right] F_{TV,n}^H(\chi^H),$$

where we have used a separate TV functional for the electric and magnetic parts of the cost functional. The TV-factors are taken to be the weighted L^2 norm on the domain D , i.e.,

$$F_{TV,n}^E = \frac{1}{V} \int_D \frac{|\nabla \chi_n^E|^2 + \delta_{n-1}^2}{|\nabla \chi_{n-1}^E|^2 + \delta_{n-1}^2} dV, \quad (6.95)$$

$$F_{TV,n}^H = \frac{1}{V} \int_D \frac{|\nabla \chi_n^H|^2 + \delta_{n-1}^2}{|\nabla \chi_{n-1}^H|^2 + \delta_{n-1}^2} dV. \quad (6.96)$$

It can be seen that both $F_{TV,n-1}^E = 1$ and $F_{TV,n-1}^H = 1$. Note that these TV-factors have to be changed for binary inversion, see Abubakar and Van den Berg [4]. At

the start of each iteration, the TV-terms are equal to one, therefore the update for the contrast sources does not change. For the contrasts we again use a CG update, which is different from the update used in the ECSI scheme due to the dependence of the TV-terms on the contrasts. In the subsequent analysis, we shall take the electric contrast as an example; the relations for the magnetic contrast have a similar form. The total gradient of the cost functional with respect to the electric contrast is given by

$$g_n^E = F_{TV} g_n^{\chi, E} + (F_{S, n-1} + F_{D, n-1}^E) g_n^{TV, E}, \quad (6.97)$$

where $g_n^{\chi, E}$ is the gradient with respect to χ^E as defined in Eqs. (6.32) or (6.34) and $g_n^{TV, E}$ is the gradient of the TV-term with respect to χ^E . The gradient $g_n^{TV, E}$ is derived as

$$\begin{aligned} \frac{\partial}{\partial \chi^E} F_{TV}^E &= \lim_{\epsilon \rightarrow 0} \frac{1}{\epsilon} \left\{ \frac{1}{V} \int_D \frac{|\nabla(\chi_{n-1}^E + \epsilon d_n^E)|^2 + \delta_{n-1}^2}{|\nabla \chi_{n-1}^E|^2 + \delta_{n-1}^2} dV - F_{TV, n-1}^E \right\} \\ &= \frac{2}{V} \int_D \frac{\nabla \chi_{n-1}^E \cdot \nabla d_n^E}{|\nabla \chi_{n-1}^E|^2 + \delta_{n-1}^2} dV \\ &= \frac{2}{V} \left[\int_D \nabla \cdot \left(d_n^E \frac{\nabla \chi_{n-1}^E}{|\nabla \chi_{n-1}^E|^2 + \delta_{n-1}^2} \right) dV - \int_D \frac{(\nabla \cdot \nabla \chi_{n-1}^E) d_n^E}{|\nabla \chi_{n-1}^E|^2 + \delta_{n-1}^2} dV \right]. \end{aligned} \quad (6.98)$$

The first integral on the last line of Eq. (6.98) is zero because of the expansion functions that we use. Recognizing the second integral as an inner product over D , we obtain the gradient of the TV-term of the cost functional with respect to the contrast as

$$g_n^{TV} = \frac{\nabla \cdot \nabla \chi_{n-1}^E}{V(|\nabla \chi_{n-1}^E|^2 + \delta_{n-1}^2)}. \quad (6.99)$$

The expression for $g_n^{TV, H}$ obtained in a similar manner.

Now that we have determined the new gradients we only need to calculate the new update coefficients $\alpha_n^{\chi, E}$ and $\alpha_n^{\chi, H}$, which we take to be real. To this end, we write the part of the cost functional corresponding to the electric field as

$$\begin{aligned} F_n^E &= [F_{S, n}^E + F_{D, n}^E (\chi_{n-1}^E + \alpha_n^{\chi, E} d_n^E)] F_{TV, n}^E (\chi_{n-1}^E + \alpha_n^{\chi, E} d_n^E), \\ &= \left(F_{S, n}^E + \frac{\sum_k \|(\chi_{n-1}^E + \alpha_n^{\chi, E} d_n^E) \hat{\mathbf{E}}_{k, n} - \hat{\mathbf{W}}_{k, n}^E\|_D^2}{\sum_k \|\chi_{n-1}^E \hat{\mathbf{E}}_k^i\|_D^2} \right) \times \\ &\quad \frac{1}{V} \int_D \frac{|\nabla(\chi_{n-1}^E + \alpha_n^{\chi, E} d_n^E)|^2 + \delta_{n-1}^2}{|\nabla \chi_{n-1}^E|^2 + \delta_{n-1}^2} dV. \end{aligned} \quad (6.100)$$

Note that we have only considered the nominator of $F_{D, n}^E$, the denominator was kept fixed at χ_{n-1}^E . Doing this enables us to calculate the update coefficient analytically,

and numerical experiments (Abubakar *et al.*) have shown that this method leads to good results. We now write Eq. (6.100) in terms of $\alpha_n^{\chi,E}$, giving

$$F_n^E(\alpha_n^{\chi,E}) = (A_1(\alpha_n^{\chi,E})^2 + 2A_2\alpha_n^{\chi,E} + A_3) \times (B_1(\alpha_n^{\chi,E})^2 + 2B_2\alpha_n^{\chi,E} + B_3), \quad (6.101)$$

where the coefficients $A_{1,2,3}$ and $B_{1,2,3}$ are given by

$$A_1 = \eta_{D,n-1}^E \sum_k \|d_n^E \hat{\mathbf{E}}_{k,n}\|_D^2, \quad (6.102)$$

$$A_2 = \eta_{D,n-1}^E \operatorname{Re} \sum_k \langle d_n^E \hat{\mathbf{E}}_{k,n}, \chi_{n-1}^E \hat{\mathbf{E}}_{k,n} - \hat{\mathbf{W}}_{k,n}^E \rangle_D, \quad (6.103)$$

$$A_3 = F_S^E(\hat{\mathbf{W}}_{k,n}^E) + F_D^E(\hat{\mathbf{W}}_{k,n}^E, \chi_{n-1}^E), \quad (6.104)$$

$$B_1 = \|b_{n-1} \nabla d_n^E\|_D^2, \quad (6.105)$$

$$B_2 = \operatorname{Re} \langle b_{n-1} \nabla \chi_{n-1}^E, b_{n-1} \nabla d_n^E \rangle_D, \quad (6.106)$$

$$B_3 = 1, \quad (6.107)$$

and b_{n-1} is defined as

$$b_{n-1} = \left(\frac{1}{V} \frac{1}{|\nabla \chi_{n-1}^E|^2 + \delta_{n-1}^2} \right)^{\frac{1}{2}}. \quad (6.108)$$

Taking the derivative with respect to $\alpha_n^{\chi,E}$ and setting this to zero results in a 3rd order polynomial with one real root and a pair of complex conjugate roots, where the real root is the desired update coefficient. Finally, we remark that the expression for the update coefficient $\alpha_n^{\chi,H}$ is found in a similar manner.

We have chosen to use separate TV terms for the electric and magnetic parts of the cost functional as defined in Eqs. (6.94) - (6.96), since the regularization terms then act on those parts of the cost functional where the respective contrasts (electric and magnetic) occur.

Since the contrast values are known for the case of a PEC configuration (a defect in a metal layer), we can also use a binary inversion scheme using TV regularization (Abubakar and Van den Berg [4]), however, this has not been implemented here.

Chapter 7

Numerical Results for the Inverse Problem

In this chapter we present numerical results for the inverse problem. We first test our algorithms by reconstructing contrasts in conductivity and permeability in a homogeneous background, after which we give results for the inverse problem in a layered configuration. For the configuration where the background is homogeneous, we will first take a single scatterer with a contrast in both conductivity and permeability, after which we will use a configuration consisting of two separate scatterers, with a contrast in either conductivity or permeability. This second configuration will be used to investigate the mutual influence between the medium parameters in the inversion. For the layered configuration we start with a geophysical setup where a contrast is located within a layer. For this configuration the contrasts are small and positive, and a high frequency is used. Finally, we investigate the inversion for a PEC configuration, where a scatterer (defect) is located within a metal layer. Note that in all our inversion experiments we use only a single frequency.

7.1 Inversion for a homogeneous background

In this section we present numerical results for the inversion algorithms described in Chapter 6. To test the inversion schemes we first consider configurations with a homogeneous background, since this presents a much simpler problem compared to the situation where the background medium is inhomogeneous. Note that we have used the diffusion approximation for configurations with a homogeneous background. In the subsequent results we take a geophysical problem, where the computational domain is surrounded by four boreholes, in which the transmitters and receivers are

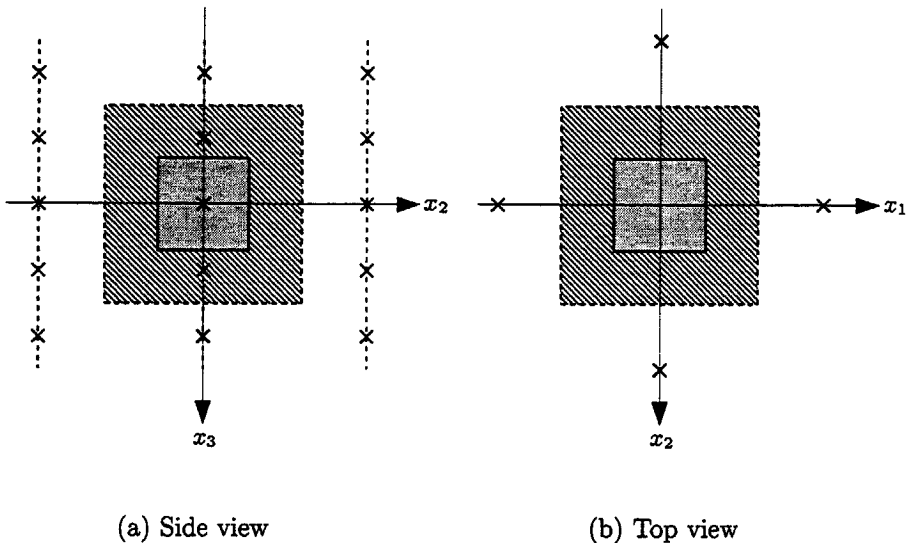


Figure 7.1: Configuration for the inverse problem in a homogeneous background, side view (a) and top view (b). The computational domain is indicated by the shaded area, the scattering block is located at its center. The transmitters/receivers (denoted by crosses) are located on 4 lines (boreholes) on either side of the computational domain.

located. We use vertical magnetic dipole (VMD) sources and use both the electric and magnetic field components as synthetic data in the inversion scheme. The configuration is given in Figures 7.1 and 7.2.

In our inversion experiments, we use all components of the scattered electric and magnetic fields as data. It can be expected that if we use only some components or only one field type as data, our inversion results will be worse. The boreholes were located at $(x_1, x_2) = (-25, 0), (25, 0), (0, -25)$ and $(0, 25)$, where the dimensions are in meters. The dimensions of the computational domain were $35 \times 35 \times 35 \text{ m}^3$ and a single frequency of 20 kHz was used. We used 8 sources in total, 2 in each borehole, located at $z = -10 \text{ m}$ and $z = 10 \text{ m}$. Each source successively radiated while all receivers recorded data. There were 20 receivers in total, with 5 in each borehole, located at $z = -20, -10, 0, 10, 20 \text{ m}$.

7.1.1 Single scatterer with contrast in μ and σ

For the configuration of a single cube with a contrast in both conductivity and permeability, the original contrasts are given in Figure 7.3. The scatterer was a cube

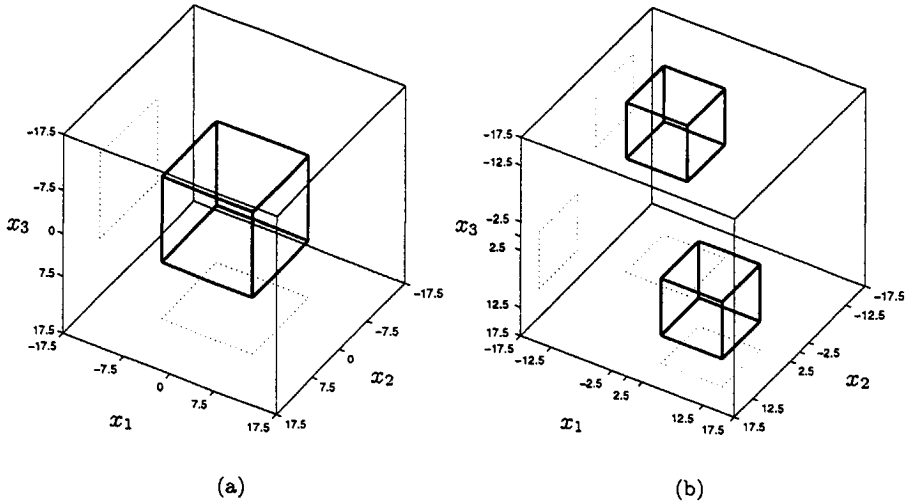


Figure 7.2: Configurations for the single and separate scatterers.

with dimensions of $15 \times 15 \times 15 \text{ m}^3$, a conductivity of $\sigma = 0.3 \text{ S/m}$ and a relative permeability $\mu_r = 2$. The homogeneous background had a conductivity of $\sigma_b = 0.1 \text{ S/m}$ and relative permeability $\mu_r = 1$, giving an electric contrast $\chi^E = 2$ and a magnetic contrast $\chi^H = 1$. The cube was centered in the computational domain. The reconstructed contrast profiles after 1024 iterations of the ECSI method with CG update for the contrasts are given in Figure 7.4, no regularization was used. It can be seen that the edges of the scatterer are smoothed because of the diffusive nature of the fields and lack of regularization. The maximum value of the contrasts is overshoot by almost a factor of 2 in both cases.

7.1.2 Separate scatterers

To investigate the mutual influence between σ and μ in the reconstruction, we consider the configuration given in Figure 7.2b. The scattering objects are cubes of $10 \times 10 \times 10 \text{ m}^3$, located at opposite corners of the computational domain. We use the same transmitter/receiver combination, background medium parameters and frequency as for the single scatterer. The contrast values are now $\chi^E = 1, \chi^H = 0$ for the scatterer located near \mathbf{x}_{min} and $\chi^E = 0, \chi^H = 1$ for the scatterer located near \mathbf{x}_{max} , where $\mathbf{x}_{min} = (-17.5, -17.5, -17.5) \text{ m}$ and $\mathbf{x}_{max} = (17.5, 17.5, 17.5) \text{ m}$. The exact profiles are give in Figure 7.5.

The reconstructed contrast profiles after 1024 iterations of the ECSI method

with CG update for the contrasts are given in Figure 7.6. Again, no regularization was used. We can see that there is very little mutual influence between the two medium parameters in the reconstruction. As with the configuration for a single scatterer, the edges of the contrasts are not reconstructed very well.

7.1.3 Binary inversion

When the exact value of the scatterer is known, we can employ binary inversion (see Section 6.3). Assuming a contrast which has a value of either 0 or χ_{max} , a simple algorithm would be to check the minimum and maximum values of the reconstructed contrast at each iteration and set these to either 0 or χ_{max} , respectively. A more sophisticated method using a non-linear mapping function was described in Section 6.3, and we will now present the results for this method. The transmitter/receiver configuration used was the same as in the previous sections, and we will consider configuration with both single and multiple scatterers. The reconstructed profiles of the single scatterer after 1024 iterations of the ECSI scheme with exponential constraint is given in Figure 7.7.

It can be seen that the edges of the scatterer are now reconstructed fairly well. For the configuration with the two separate scatterers, the reconstructed profiles are given in Figure 7.8. As with the single scatterer, the edges are now reconstructed much better when compared to the inversion scheme without constraint. The amount of mutual influence between σ and μ in the reconstructions is negligible.

7.1.4 One-sided illumination

Since we have only one-sided illumination for the case of a PEC configuration, it is advisable to investigate the effect of one-sided illumination in the case of a homogeneous background configuration. Again, we take the background and frequency parameters the same as those used in the previous sections and we change the transmitter/receiver configuration such that all transmitters and receivers are located on one side of the scatterer. For the scatterer we take the single block described in the previous section. We used 16 transmitters and 25 receivers, located at $z = -22.5$ m. The transmitters were evenly spaced in the x_1 - x_2 plane, at $(x_1, x_2) = (-25, -10, 10, 25)$ m, while the receivers were located at $(x_1, x_2) = (-25, -12.5, 0, 12.5, 25)$ m. The exact contrast profiles are given in Figure 7.3, while the reconstructed profiles after 1024 iterations of the ECSI scheme are given in Figure 7.9. No regularization or constraints were used.

From Figure 7.9 we see that the top of the contrast, near the transmitters and receivers, is reconstructed reasonably well. However, the bottom of the scatterer is reconstructed poorly, especially for the contrast in conductivity. This effect is much less pronounced in the case of the contrast in permeability.

7.1.5 Negative contrasts

Since the contrasts for the PEC configuration will be negative, we first test our inverse scheme with negative contrasts located in a homogeneous background. We again have a single block scatterer with a contrast in conductivity and permeability, but in this case the scatterer is located in a homogeneous background configuration with medium parameters $\sigma_b = 1$ S/m and $\mu_b = 2\mu_0$. The medium parameters of the scatterer are given by $\sigma = 0.1$ S/m and $\mu = \mu_0$, leading to contrast values of $\chi^E = -0.9$ and $\chi^H = -0.5$, respectively. We used a frequency of 20 kHz, while the receiver and transmitter configuration is the same as that given in Figure 7.1. It can be seen that the reconstruction is much worse than for the positive contrasts and that the contrast in conductivity is reconstructed better than the contrast in permeability. It must be noted that when the contrast values are smaller, $\chi^E = -0.5$ and $\chi^H = -0.1$, the reconstruction results are much better (all other parameters begin equal). This indicates that it will be difficult to reconstruct a defect in a PEC configuration.

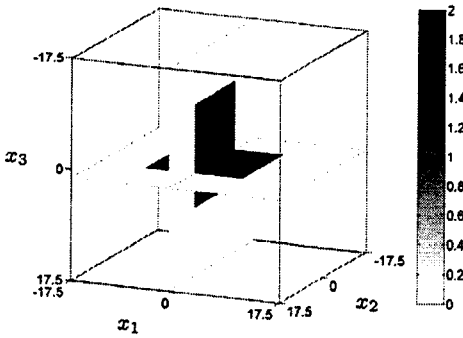
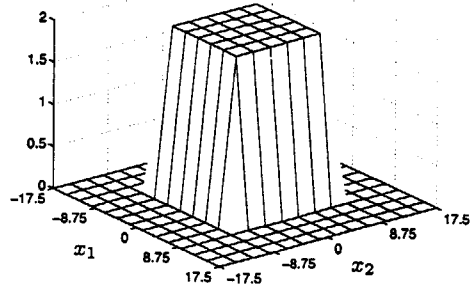
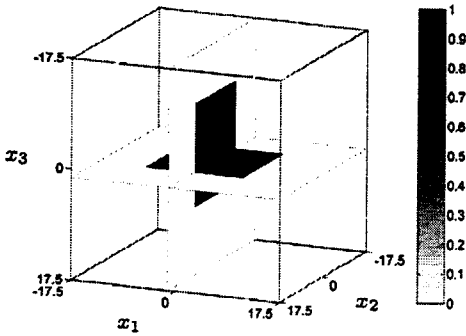
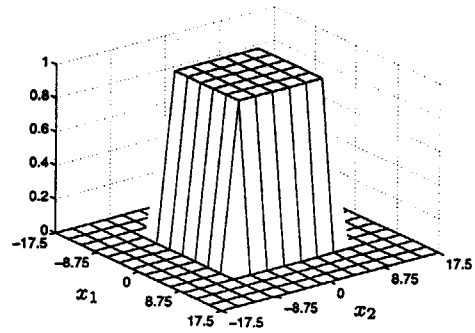
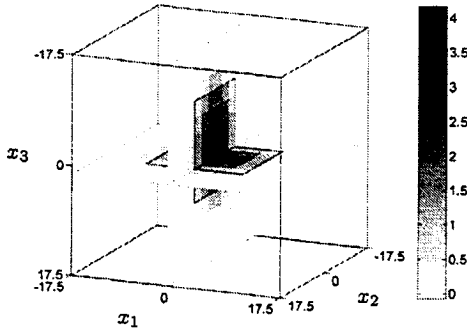
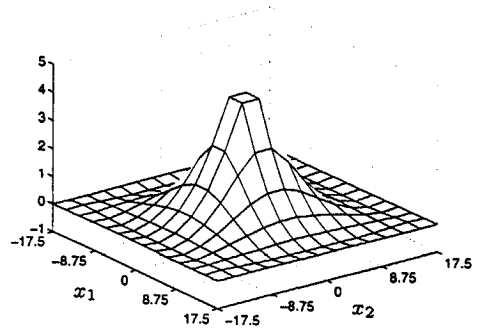
(a) Exact contrast in conductivity χ^E (b) Exact contrast in conductivity χ^E at $x_3 = 0$ (c) Exact contrast in permeability χ^H (d) Exact contrast in permeability χ^H at $x_3 = 0$

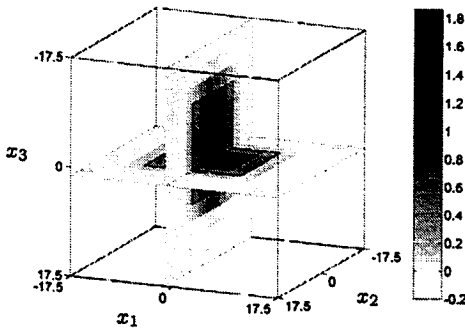
Figure 7.3: Exact contrasts for the single scatterer configuration.



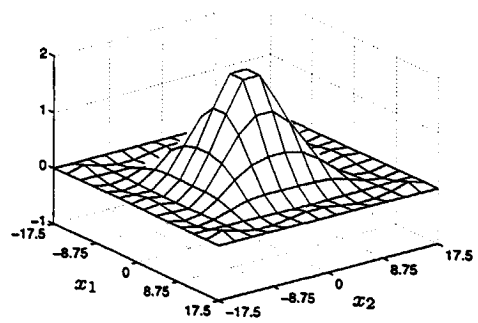
(a) Reconstructed contrast in conductivity χ^E



(b) Reconstructed contrast in conductivity χ^E at $x_3 = 0$



(c) Reconstructed contrast in permeability χ^H



(d) Reconstructed contrast in permeability χ^H at $x_3 = 0$

Figure 7.4: Reconstructed contrasts for the single scatterer configuration after 1024 iterations of the ECSI scheme, black lines in Figures (a) and (c) denote the edge of the scatterer.

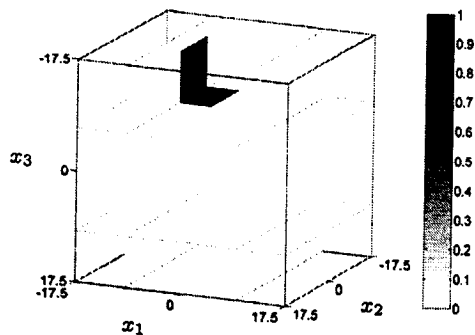
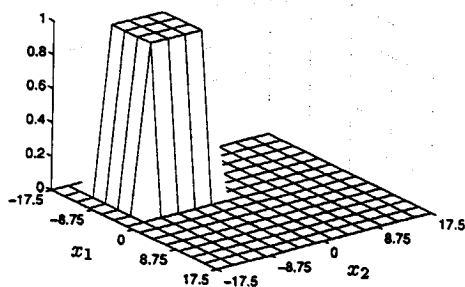
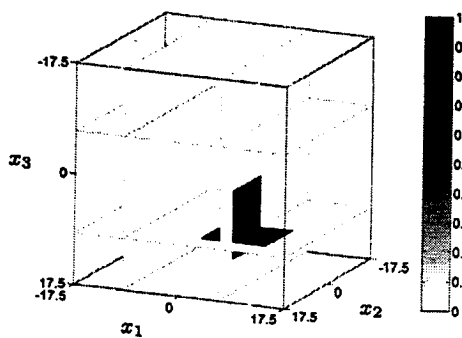
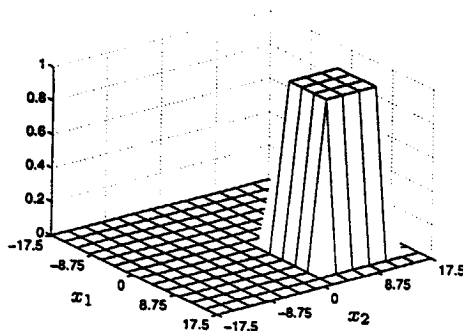
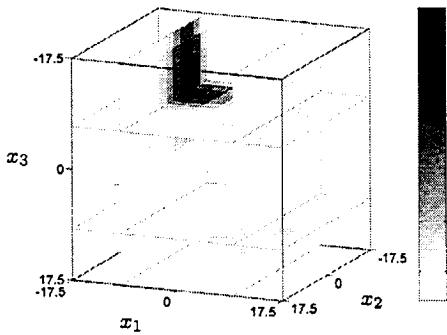
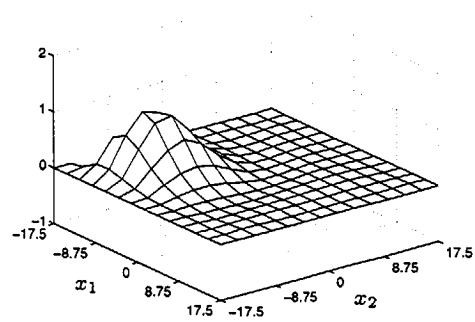
(a) Exact contrast in conductivity χ^E (b) Exact contrast in conductivity χ^E at $x_3 = -8.75$ m(c) Exact contrast in permeability χ^H (d) Exact contrast in permeability χ^H at $x_3 = 8.75$ m

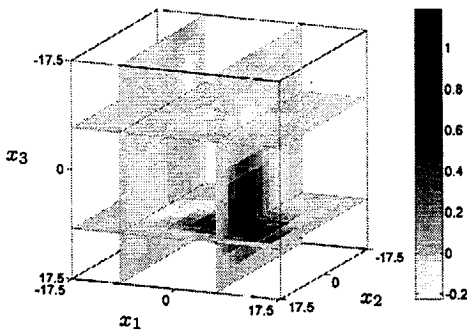
Figure 7.5: Exact contrasts for the separate scatterer configuration.



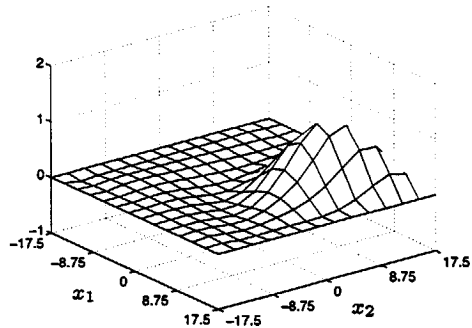
(a) Reconstructed contrast in conductivity χ^E



(b) Reconstructed contrast in conductivity χ^E at $x_3 = -8.75$ m

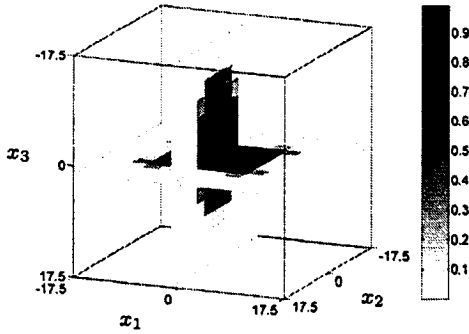


(c) Reconstructed contrast in permeability χ^H

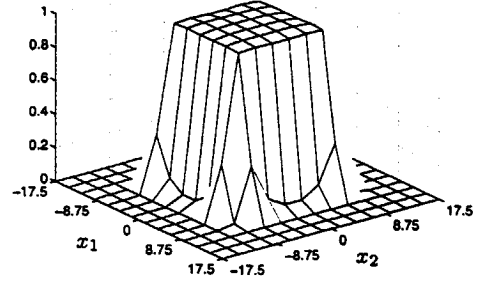


(d) Reconstructed contrast in permeability χ^H at $x_3 = 8.75$ m

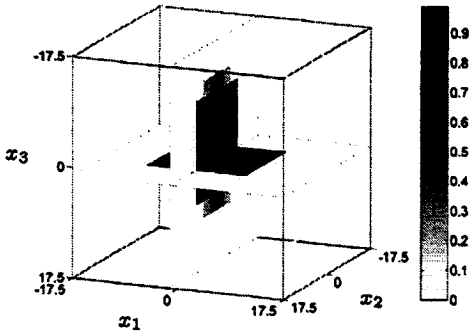
Figure 7.6: Reconstructed contrasts for the separate scatterer configuration after 1024 iterations of the ECSI scheme, black lines in Figures (a) and (c) denote the edge of the scatterer.



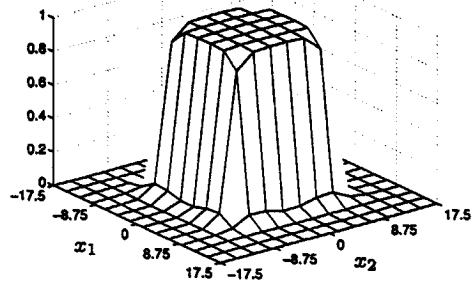
(a) Reconstructed contrast in conductivity χ^E



(b) Reconstructed contrast in conductivity χ^E at $x_3 = 0$

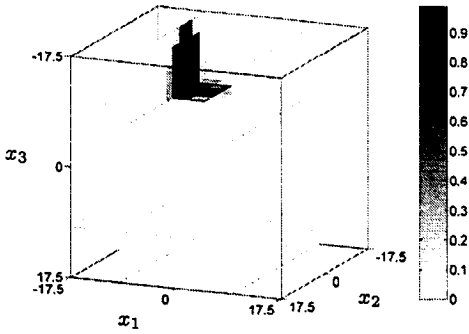


(c) Reconstructed contrast in permeability χ^H

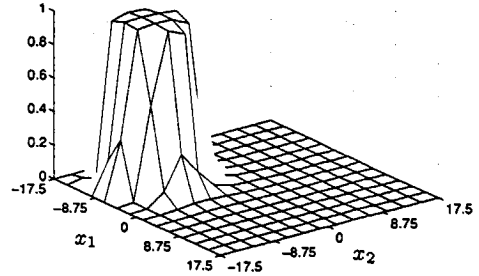


(d) Reconstructed contrast in permeability χ^H at $x_3 = 0$

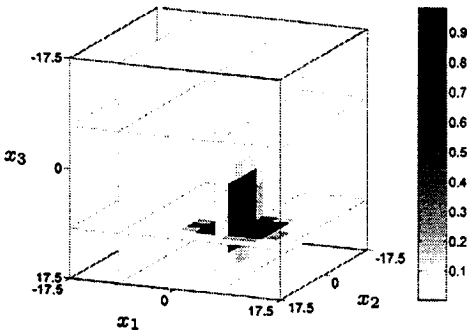
Figure 7.7: Reconstructed contrasts for the single scatterer configuration with exponential constraint after 1024 iterations, black lines in Figures (a) and (c) denote the edge of the scatterer.



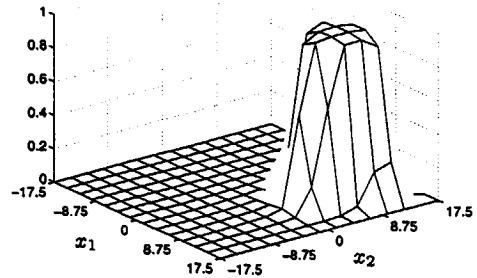
(a) Reconstructed contrast in conductivity χ^E



(b) Reconstructed contrast in conductivity χ^E at $x_3 = -8.75$ m

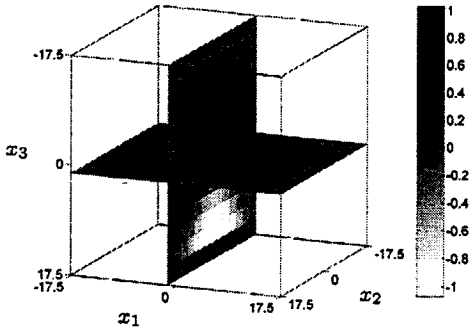


(c) Reconstructed contrast in permeability χ^H

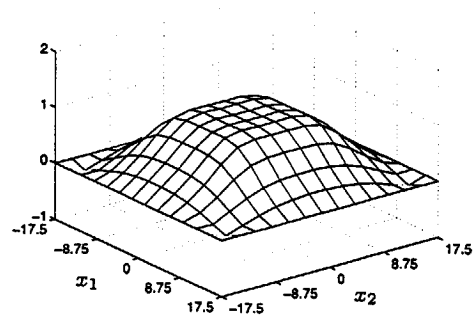


(d) Reconstructed contrast in permeability χ^H at $x_3 = 8.75$ m

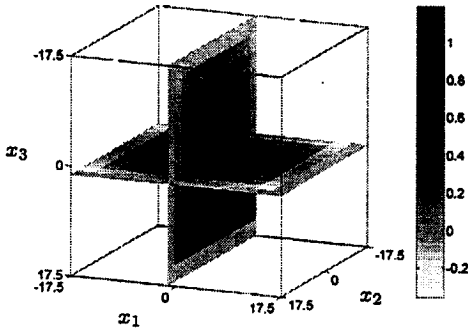
Figure 7.8: Reconstructed contrasts for the separate scatterer configuration with exponential constraint after 1024 iterations, black lines in Figures (a) and (c) denote the edge of the scatterer.



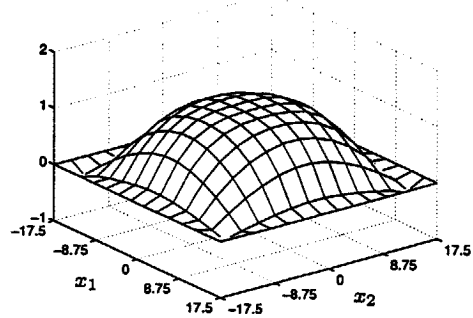
(a) Reconstructed contrast in conductivity χ^E



(b) Reconstructed contrast in conductivity χ^E at $x_3 = 0$



(c) Reconstructed contrast in permeability χ^H



(d) Reconstructed contrast in permeability χ^H at $x_3 = 0$

Figure 7.9: Reconstructed contrasts for the single scatterer configuration with one-sided illumination after 1024 iterations of the ECSI scheme, black lines in Figures (a) and (c) denote the edge of the scatterer. No constraint was used.

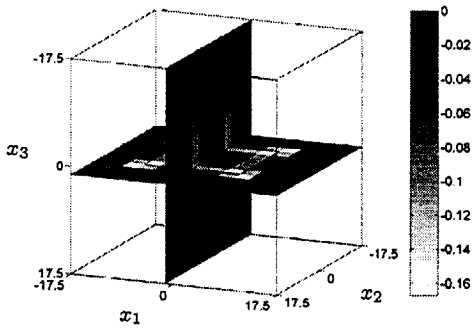
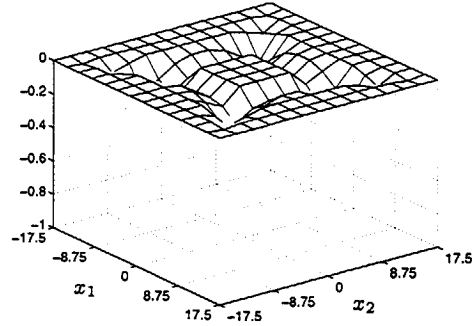
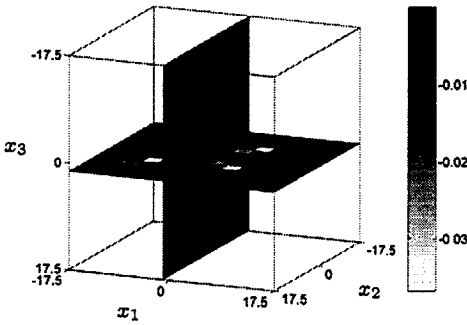
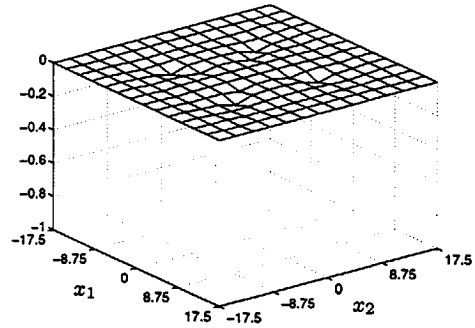
(a) Reconstructed contrast in conductivity χ^E (b) Reconstructed contrast in conductivity χ^E at $x_3 = 0$ (c) Reconstructed contrast in permeability χ^H (d) Reconstructed contrast in permeability χ^H at $x_3 = 0$

Figure 7.10: Reconstructed contrasts for the single scatterer configuration with a negative contrast after 1024 iterations of the ECSI scheme, black lines in Figures (a) and (c) denote the edge of the scatterer. Exact contrast values are $\chi^E = -0.9$ and $\chi^H = -0.5$.

7.2 Inversion for a stratified configuration

In this section we will discuss the numerical results for the Extended Contrast Source Inversion scheme for a stratified configuration. For these configurations, the scatterer is located within a layer, while the sources and receivers are located above the layer. Again, to test the inversion schemes, we first consider a geophysical configuration which is similar in size to the configurations used in Section 7.1. Subsequently we apply the inversion schemes to a configuration of a metal layer containing a defect. Note that we use single-frequency inversion and that we have one-sided illumination for the stratified configurations. We take the permittivity to be $\epsilon = \epsilon_0$ for all the configurations that we consider.

7.2.1 Sensitivity

Whether or not it is possible to reconstruct the dimensions and medium parameters of a scatterer in a certain configuration depends on the sensitivity of the scattered fields with respect to the medium parameters of the scatterer. In this section we present the results for the sensitivity function with respect to conductivity as defined in Section 4.2.2. The configuration is taken to be stratified, consisting of three layers where the sources are located above the top layer (see also Figure 4.1). We calculate the partial derivative of the electric field with respect to the conductivity of the center layer, and we do this for both a geophysical configuration and a configuration compatible to the PEC tool (note that we use a 2D configuration for the sensitivity functions).

For the geophysical configuration all layers have a thickness of 10 m, while the medium parameters were $\sigma = 0.1$ S/m and $\mu = \mu_0$ for the outer layers and $\sigma = 0.11$ S/m and $\mu = 1.1\mu_0$ for the halfspaces. The medium parameters of the center layer are given by $\sigma = 2.2$ S/m and $\mu = 2.2\mu_0$. A vertical magnetic dipole source was used and the field quantities were calculated with the same numerical code that we employed for the 2D configuration. We calculate the sensitivity function $\partial_\sigma \hat{E}$ with respect to the conductivity of the center layer as function of frequency, the result of which is given in Figure 7.11.

The PEC configuration consisted of three metal layers above which a horizontal loop source was located (see Figure 4.1). The medium parameters of the layers were $\sigma = 6.7 \times 10^6$ S/m and $\mu = 200\mu_0$, while the medium parameters of the halfspaces on either side were $\sigma = 4$ S/m and $\mu = \mu_0$. The metal layers had a thickness of 3 mm each. We calculate the sensitivity function $\partial_\sigma \hat{E}$ with respect to the conductivity of the center layer as function of frequency, the result of which is given in Figure 7.12.

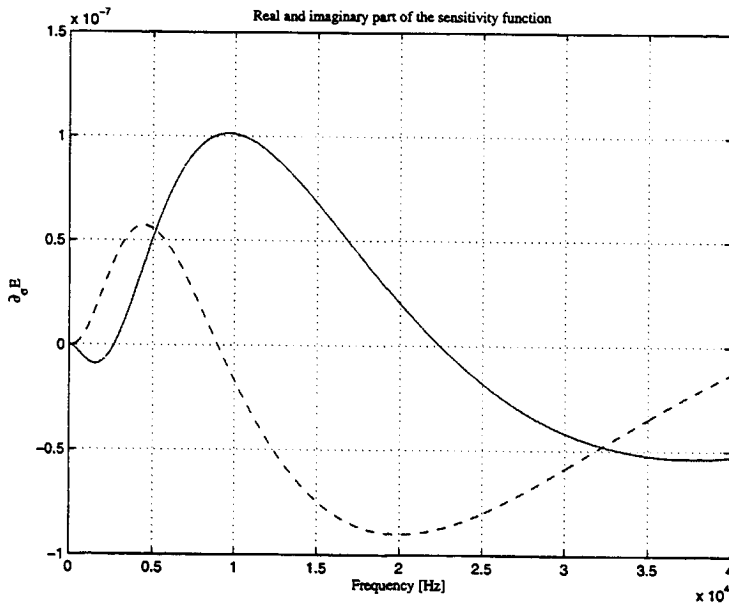


Figure 7.11: Sensitivity function $\partial_{\sigma} \hat{E}$ as function of frequency for a geophysical layered configuration. Solid line denotes real part, dashed line denotes imaginary part.

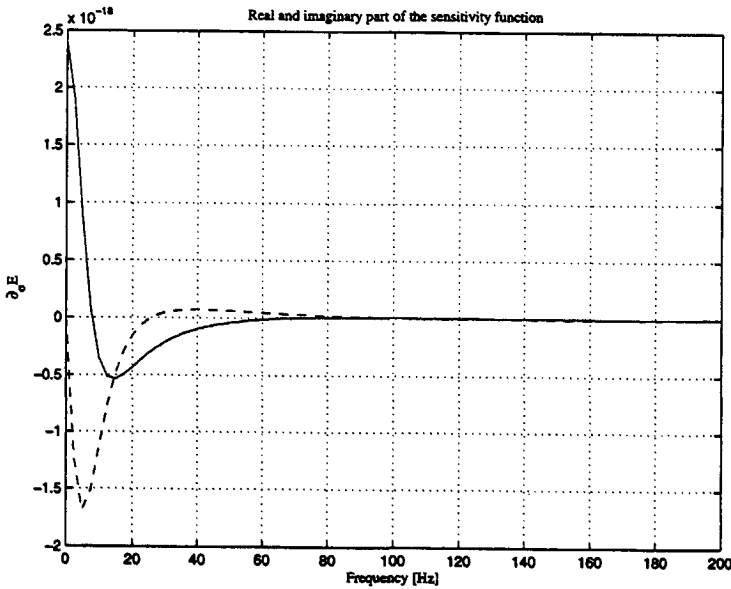


Figure 7.12: Sensitivity function $\partial_{\sigma} \hat{E}$ as function of frequency for a PEC configuration. Solid line denotes real part, dashed line denotes imaginary part.

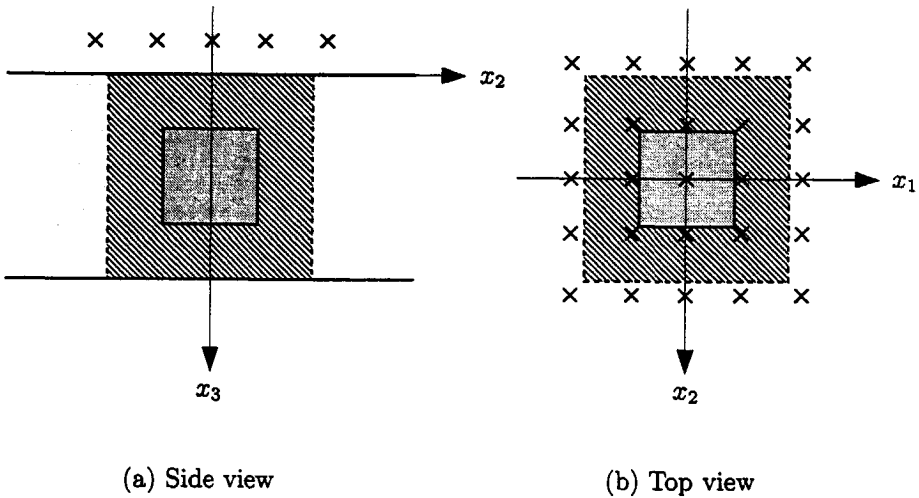


Figure 7.13: Configuration for the inversion of a buried scatterer in a stratified geophysical setting, with sources and receivers on one side of the layer, side view (a) and top view (b). Crosses denote transmitters/receivers, the computational domain is indicated by the shaded area with the scatterer at its center.

It can be seen that the sensitivity of the PEC configuration is much lower than that of the geophysical configuration. This is due to the very high values of the medium parameters of the layers in the PEC configuration. Due to the skin effect, the amplitude of the electromagnetic fields with the layers is much smaller, which has direct consequences for the sensitivity function and hence for the inversion results. Given the sensitivity function of the PEC configuration as given in Figure 7.12, it is evident that a very low frequency should be used for the inversion experiments, which leads to loss of resolution. In addition, the amplitude of the sensitivity function is such that good inversion results cannot be expected. In contrast, the sensitivity function for the geophysical configuration shows that higher frequencies (in the kHz range) can be used. Consequently, we may expect better inversion results for this configuration.

7.2.2 Geophysical configuration

To test the inversion scheme for a layered configuration we first consider a **geophysical configuration with a low contrast in conductivity and permeability**. The configuration, given in Figure 7.13, is that of a scatterer located within a layer, where the sources and receivers are located above the layer. For the sources we take

vertical magnetic dipoles and we measure the scattered electromagnetic fields (i.e., all components of $\hat{\mathbf{E}}^{sct}$ and $\hat{\mathbf{H}}^{sct}$) at the receiver locations. The layer thickness was taken to be 35 m, while the computational domain was taken to be $35 \times 35 \times 35 \text{ m}^3$, subdivided into $14 \times 14 \times 14$ grid cells. The scatterer itself was a cube, centered in the x_3 -direction, with dimensions $20 \times 20 \times 20 \text{ m}^3$. We used 25 sources and receivers at 20 kHz, where the scattered fields were calculated at all 25 source/receiver positions for each source in turn. The sources and receivers were located 5 m from the top of the layer, and at $(-25, -12.5, 0, 12.5, 25)$ m in the x_1 - and x_2 -directions (see Figure 7.13). The medium parameters of the configuration were $\{\sigma = 0.1 \text{ S/m}, \mu = \mu_0\}$ for the halfspaces on either side of the layer, and $\{\sigma = 0.11 \text{ S/m}, \mu = 1.1\mu_0\}$ for the layer. The medium parameters for the scatterer were $\{\sigma = 0.22 \text{ S/m}, \mu = 2.2\mu_0\}$, leading to the contrast values $\chi^E = 1$ and $\chi^H = 1$, respectively. Note that the permittivity is set to ϵ_0 throughout the configuration.

In Figure 7.14 we give the exact and reconstructed contrasts in conductivity and permeability in the $x_2 - x_3$ plane at $x_1 = 0$ after 1536 iterations of the inversion scheme. Positivity was enforced at each iteration by setting the negative parts of the contrast to zero. It can be seen that the part of the scatterer that was located closest to the sources and receivers is reconstructed reasonably well, however, the underside of the scatterer is not reconstructed well due to the lack of sources and receivers on that side.

To investigate effects of a surface-breaking scatterer, we use the configuration given in Figure 7.13, where the same scatterer is now located against the top of the layer at the side of the transmitters and receivers. The dimensions, frequency and medium parameters remain the same. In Figure 7.15, we give the exact and reconstructed contrasts in conductivity and permeability in the $x_2 - x_3$ plane at $x_1 = 0$ after 1024 iterations of the inversion scheme. Positivity was enforced at each iteration by setting the negative parts of the contrasts to zero, while the magnitude was limited to the known maximum values. It can be seen that both contrast are reconstructed reasonably well in the $x_1 - x_2$ plane at the surface of the layer, but the lack of resolution in the x_3 -direction is apparent. This would be better if multi-frequency and/or full illumination were to be used.

When the medium parameters of the layer have higher values, we are forced to use a lower frequency to compensate for the skin-effect. In Figure 7.16, we give the exact and reconstructed contrasts in conductivity and permeability in the $x_2 - x_3$ plane at $x_1 = 0$ for a configuration where the medium parameters of the layer are $\{\sigma = 0.1 \text{ S/m}, \mu = \mu_0\}$ for the halfspaces and $\{\sigma = 0.2 \text{ S/m}, \mu = 2\mu_0\}$ for the layer. The medium parameters of the scatterer were $\{\sigma = 0.4 \text{ S/m}, \mu = 3\mu_0\}$, leading to the contrast values $\chi^E = 1$ and $\chi^H = 0.5$, respectively. A frequency of 2 kHz was used while the transmitter/receiver configuration and the dimensions were the same as those given in Figure 7.13, with the exception that the scatterer was surface-breaking, as in the previous configuration. It can be seen that the lower frequency leads to a loss of resolution, which is most apparent in the reconstruction of the permeability. This is to be expected, since the sensitivity with respect to

permeability is proportional to frequency (see Section 4.2.2).

7.2.3 PEC configuration

For the inversion with Pulsed Eddy Current data we take a configuration of a void in a metal layer (i.e., an inclusion-type defect). The transmitter-receiver configuration is not the same as that of the PEC tool, since for the inversion we use 25 point sources and receivers located similarly to those used in the geophysical configuration (see Figure 7.13). The transmitters and receivers were located at 5 mm above the top surface of the metal layer and at $(-14, -7, 0, 7, 14)$ mm in the x_1 - and x_2 -directions. The medium parameters of the configuration were $\{\sigma = 4 \text{ S/m}, \mu = \mu_0\}$ for the halfspaces on either side of the layer (which corresponds to seawater), and $\{\sigma = 6.7 \times 10^6 \text{ S/m}, \mu = 200\mu_0\}$ for the metal layer. The medium parameters for the scatterer were $\{\sigma = 4 \text{ S/m}, \mu = \mu_0\}$, leading to the contrast values $\chi^E = -1$ and $\chi^H = -0.995$, respectively. Note that the permittivity is set to ϵ_0 throughout the configuration. Because of the high values of the conductivity and permeability within the layer, a frequency of 10 Hz was used. The forward scheme described in Chapter 4 was used to generate synthetic data. Note that we use point sources and receivers instead of the coils that are present in the actual PEC probe. The defect itself was located within the computational domain that consisted of $14 \times 14 \times 10$ grid cells.

In Figure 7.17 we give the exact and reconstructed contrasts in conductivity and permeability in the x_2 - x_3 plane at $x_1 = 0$ after 1920 iterations of the inversion scheme. Negativity was enforced at each iteration by setting the contrasts to zero if the reconstructed value was positive and to -1 when the reconstructed value was smaller than -1 for contrast in conductivity. For the contrast in permeability, the lower limit was set to -0.995 . It can be seen that only the reconstruction of the contrast in conductivity yields reasonable results, considering the fact that no regularization was used apart from the aforementioned constraint. The contrast in permeability however, is not reconstructed at all, the values being effectively zero. This is due to the low frequency that is used: this same effect was observed for inversion experiments using a frequency of 10 Hz for the configuration given in Figure 7.1. Even though this configuration provides illumination from all sides and the contrasts were low ($\chi^E = 1$ and $\chi^H = 1$), it was not possible to reconstruct the permeability at all at a frequency of 10 Hz. Since the sensitivity function with respect to permeability (see Section 4.2.2) is proportional to frequency, it is to be expected that it is very difficult to reconstruct contrasts in permeability at low frequencies.

To improve the reconstruction results, multi-frequency inversion can be used, which would also help to alleviate resolution problems and the problem of one-sided illumination since more independent data would be generated. Because of the low sensitivity for scatterers when these are located in a layer with such high values of the medium parameters, it would also be advantageous to use a binary inversion scheme, where only the edges of the scatterer are located.

It is noted that Dos Reis *et al.* [29] obtained significantly better results for the inversion of defects in thin metal plates, however, the PEC configuration makes inversion much more difficult. The configuration used by Dos Reis consisted of a non-magnetic layer, where very small coils were used to measure the scattered magnetic field at a frequency of either 150kHz or 300kHz. Furthermore, much more transmitter/receiver positions were used and the computational domain consisted of $52 \times 52 \times 20$ grid cells. The low frequency, relatively coarse spatial grid, probe size and the presence of magnetic materials in the configuration makes the inversion for the PEC configuration much more difficult.

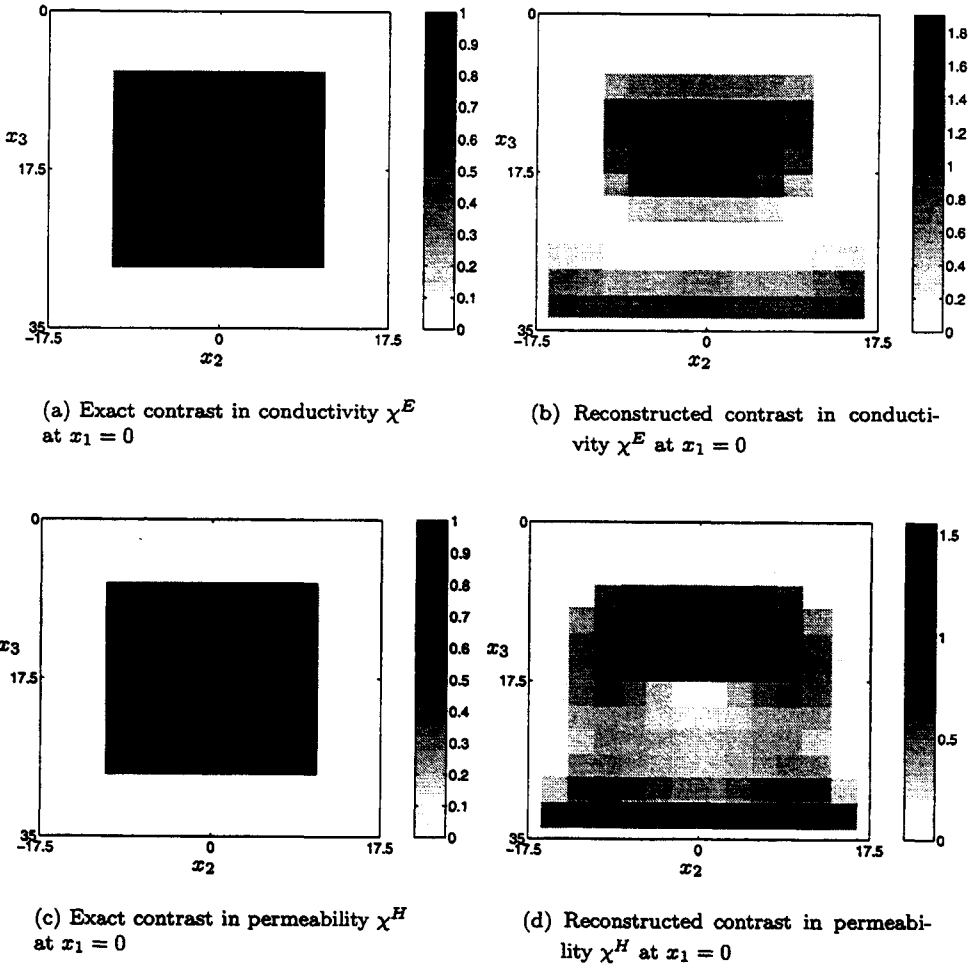


Figure 7.14: Exact and reconstructed contrasts for a layered geophysical configuration with embedded scatterer after 1536 iterations, frequency is 20 kHz. Exact (a) and reconstructed (b) contrast in conductivity at $x_1 = 0$ and exact (c) and reconstructed (d) contrast in permeability at $x_1 = 0$. Dimensions are in meters.

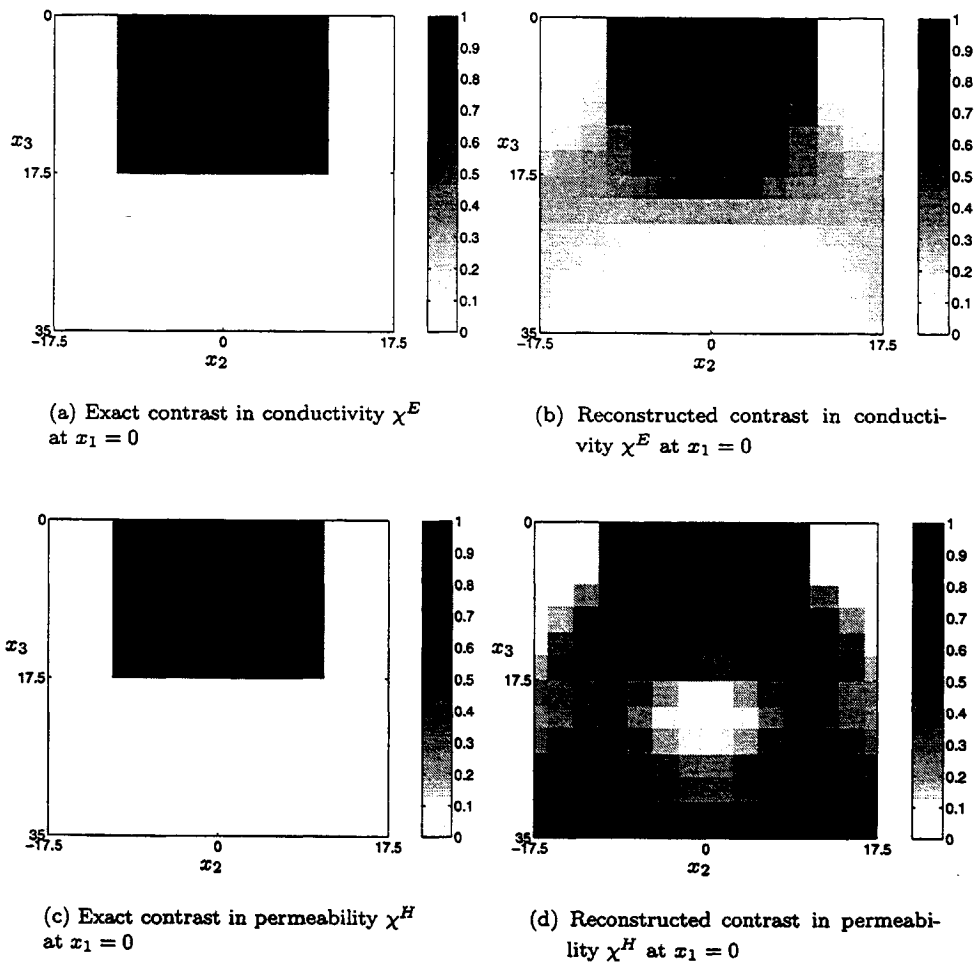


Figure 7.15: Exact and reconstructed contrasts for a layered geophysical configuration with a surface-breaking scatterer after 1024 iterations, frequency is 20 kHz. Exact (a) and reconstructed (b) contrast in conductivity at $x_1 = 0$ and exact (c) and reconstructed (d) contrast in permeability at $x_1 = 0$. Dimensions are in meters.

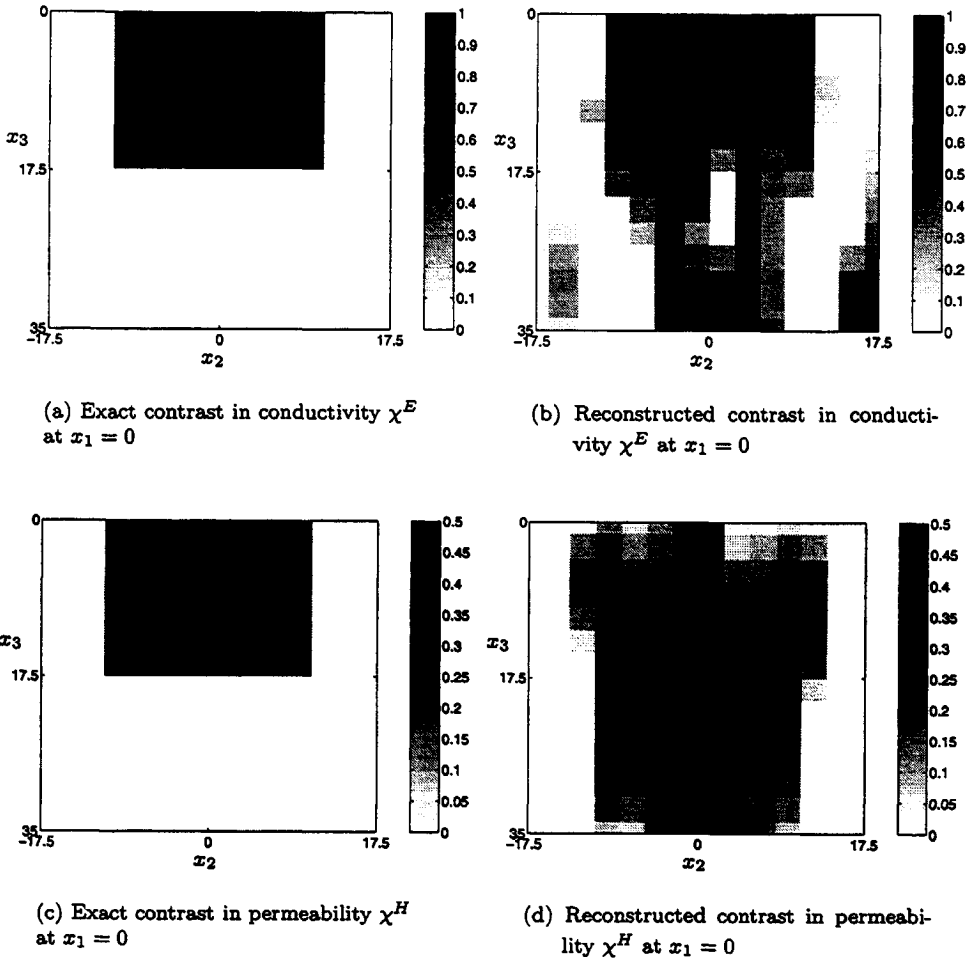


Figure 7.16: Exact and reconstructed contrasts for a layered geophysical configuration with a surface-breaking scatterer after 1024 iterations, frequency is 2 kHz. Exact (a) and reconstructed (b) contrast in conductivity at $x_1 = 0$ and exact (c) and reconstructed (d) contrast in permeability at $x_1 = 0$. Dimensions are in meters.

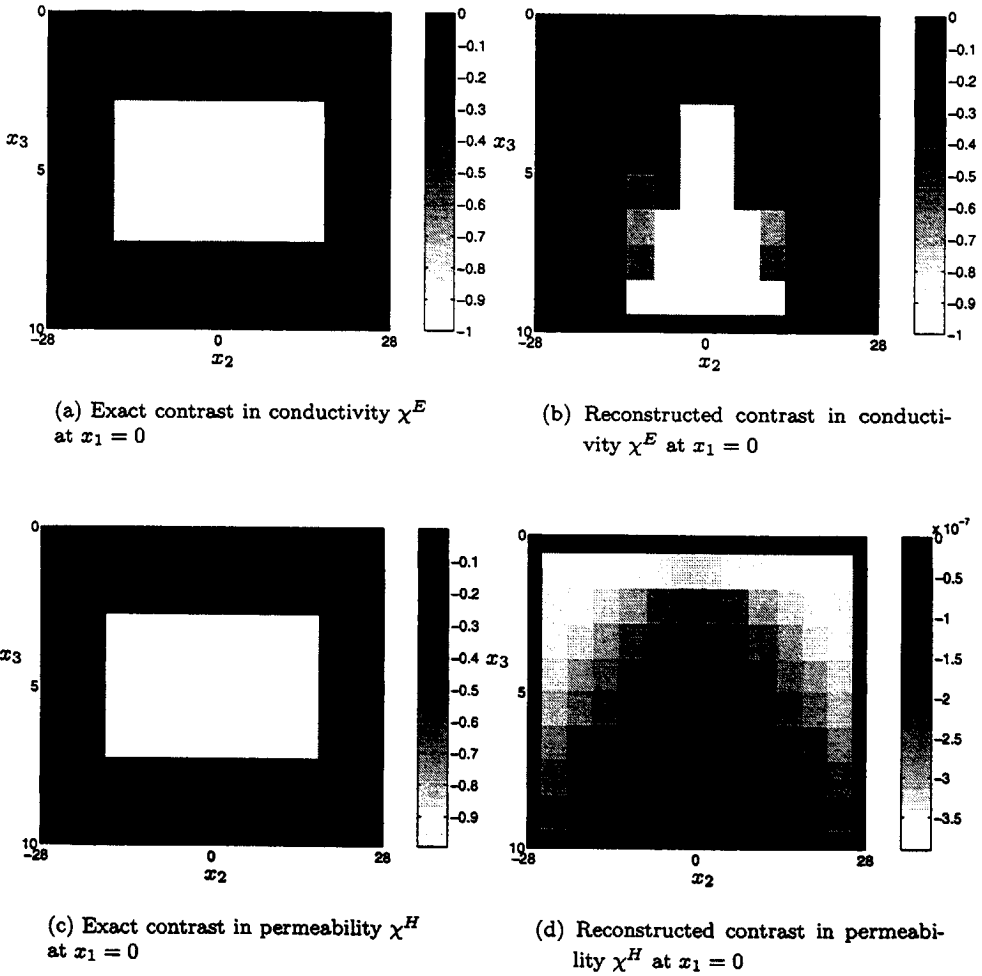


Figure 7.17: Exact and reconstructed contrasts for layered PEC configuration after 1920 iterations. Exact (a) and reconstructed (b) contrast in conductivity at $x_1 = 0$ and exact (c) and reconstructed (d) contrast in permeability at $x_1 = 0$. Dimensions are in millimeters.

Chapter 8

Discussion and Conclusions

In this thesis we have described the modelling and inversion of Pulsed Eddy Current data. We have presented several methods to calculate the response of the PEC tool: first of all we introduced a simple, physical model based on discrete current filaments, which leads to a system of coupled differential equations for the currents in each current filament. Based on the eigenvalues and eigenvectors of the system matrix, we describe the electromagnetic diffusion of the induced currents within the layer.

To solve the problem of a circular loop source above a conducting and permeable layer, we used the symmetry of the configuration to derive a scalar differential equation for the electric field within and above the layer. Applying a Hankel transformation leads to expressions for the pertaining electric and magnetic field quantities, after which numerical integration and a Fast Fourier Transform are used to obtain the field quantities in the frequency and time domain, respectively. Using this model, we have calculated the response of the PEC tool for various configurations, as well as the induced current density within the layer as function of time.

If a defect is present within the layer, the configuration is no longer symmetric with respect to the axis of the transmitting coil, hence the need to solve the full three-dimensional problem. We derived the integral equations for the electric and magnetic field quantities for the case where both electric (conductivity) and magnetic (permeability) contrasts are present. The Green's function is split into direct and reflected parts, which are treated separately.

For the direct part of the Green's function, we have a configuration where the scatterer is located in a homogeneous background. We extended the work of Kooij

and Van den Berg [44], and expressed the coupled integral equations for the field quantities in terms of the vector potentials. Subsequently, we used piecewise linear expansion functions for the vector potentials which leads to the finite-difference approximation for the differential operators acting on the vector potentials. The resulting system of equations is then solved using a Conjugate Gradient scheme employing FFTs for the convolutions. We compare the method with the one used by Abubakar [2] and we test the method with the analytical solution of scattering by a conductive and permeable sphere, finding good agreement in the results.

For the layered configuration, the reflected part of the Green's function is derived by taking a spatial Fourier transformation with respect to the i_1 - and i_2 -coordinates and solving the resulting problem in the Fourier-transform domain. We use an FFT for the inverse transformation, combined with a grid reduction technique, which allows us to calculate the inverse transformation with an FFT grid that is equal to the (much smaller) grid used in the subsequent CG scheme. This method offers a considerable reduction in computation time while conserving accuracy. To be able to use FFT routines in the CG scheme, the reflected part of the Green's function is split into even and odd parts, with a convolution and a correlation structure, respectively. Since the CG scheme we use to solve the forward problem needs to be calculated for a large number of frequencies, we have implemented the marching-on-in-frequency method to accelerate the convergence of the CG scheme.

For negative contrasts, the convergence of the CG scheme was quite slow, especially for low frequencies. Therefore, we used a combination of marching-up-and marching-down-in-frequency to find good initial estimates for the CG scheme. This slow convergence was also apparent in the inversion for a PEC configuration, where a large number of iterations were necessary.

For the inverse problem, we distinguish again between the configurations with a homogeneous and a layered background. We modified the Extended Contrast Source Inversion scheme by Van den Berg *et al.* [84] to include both the electric and magnetic field quantities and contrasts, using single-frequency inversion throughout. For the PEC configuration, the contrast values are known, therefore we also used the nonlinear mapping for the contrasts as described by Lambert and Lesselier [46] for binary inversion. Furthermore, we implemented Total Variation, which Abubakar and Van den Berg used to great effect, as a regularization method.

The inversion scheme for configurations with a homogeneous background was tested for various scatterers. When the scattering domain was illuminated from all sides, the reconstruction results were generally good, it was found that the presence of a magnetic contrast did not influence the reconstruction of the electric contrast and vice versa. The application of regularization methods such as Total Variation or the nonlinear mapping method resulted in vast improvements in the reconstructed contrasts. Reconstruction results for negative contrasts were poor, even for configurations with a homogeneous background.

Inversion for a layered configuration, where a scatterer was located within a layer, was first performed for a geophysical configuration (where the contrasts are positive). Since one-sided illumination was used, we were only able to reconstruct that part of the scatterer closest to the sources and receivers. The use of multi-frequency and regularization methods will lead to improvements in the reconstructed contrasts, but this was not validated. For inversion with the PEC configuration, we chose a scatterer that was located completely within the layer, modelling an inclusion-type defect. This was done in order to facilitate comparisons with the results of the geophysical configuration and results obtained by Dos Reis *et al.* [29].

A very low frequency (10 Hz) was used for inversion experiments with PEC configurations because of the skin effect. From the results of the sensitivity analysis in Chapter 7 we can see that it will be very difficult to reconstruct defect parameters. Because of the low frequency, it is impossible to reconstruct the contrast in permeability, while the reconstruction results for the conductivity contrast are poor. When we compare our results to the work of Dos Reis *et al.* we can conclude that the fact that the layer has a magnetic permeability greater than μ_0 , combined with the low frequency that was used, makes our problem significantly more difficult. To make optimal use of the single-frequency data set, binary and/or parametric inversion methods should be used, but multiple frequency inversion is recommended. For inversion using measured data, there is the added difficulty that the scattered field will be averaged over an area due to the finite dimensions of the receiving coils. This means that many measurements are necessary to construct a workable data set. Furthermore, noise will be present on the measured data, making it necessary to use multi-frequency inversion.

We would like to make the following recommendations for further research

- Development of an efficient preconditioning operator for use in the CGFFT method for layered configurations. This would be especially useful for configuration with negative contrasts, where convergence is very slow.
- The implementation of an FFT routine that can handle branch points and/or poles on the integration axis. The current implementation is limited to lossy configurations, while it could be advantageous to use the grid reduction technique for non-lossy configurations, especially for the case of stratified configurations with more than one interface. Furthermore, the use of fast FFT methods, such as the FFTW (see www.fftw.org) routines, should be considered.
- The use of binary and parametric inversion (see Section 1.4.3), combined with the use of multiple frequencies. By doing this, the number of unknowns is greatly reduced and more independent data is obtained. Furthermore, the fact that the contrast values are known is taken into account. In this way it may be possible to compensate for the one-sided illumination and limited number of data measurement points. Alternatively, effective inversion can be used, where the inversion results are added in the x_3 -direction to increase sensitivity.

- The use of the fact that for our specific configuration the contrasts share a common boundary. This could be incorporated as a penalty term in the cost functional, hopefully leading to more accurate reconstruction of the boundaries of the scatterer.
- Inversion by means of a lookup table (directly in the time domain), where measured data is compared to a library of signals which are obtained either by numerical calculations using the forward model described in this thesis or by measurements from controlled experiments (or a combination of these methods). The measured signal could then be matched to a signal from the library by means of some minimization procedure.

Finally, it should be noted that for a configuration where the defects are located at the surface of the layer and where the source can be placed in close contact to the defect, it would be advantageous to use a high frequency (in the order of several hundred kHz) and make reflection measurements, where the pipe wall is taken to be perfectly conducting. In this manner the problem of the high contrasts of the layer with respect to the halfspaces can be avoided, while high resolution can be obtained.

Appendix A

Scalar Green's Functions

In this appendix we will discuss the derivation of the Green's function for a stratified configuration consisting of one and three layers, respectively. Assuming a loop current source, we see that the configuration is axially symmetric around the transmitting coil axis and therefore we can use a scalar Green's function (see also Looijer [51]).

A.1 Single layer configuration

The configuration, given in Figure A.1, is that of a circular transmitting coil located above a single layer and we have taken the permittivity into account. Because of the symmetry properties of the configuration it is advantageous to introduce cylindrical coordinates, as defined in Section 4.2. We start from the differential equation for the scalar Green's function which is given in Eq. (4.10) and is repeated here in slightly different form

$$\frac{-1}{i\omega\mu_n} \left[\partial_3^2 \hat{G} + \partial_r \frac{1}{r} \partial_r (r\hat{G}) + i\omega\mu_n(\sigma_n - i\omega\epsilon_0)\hat{G} \right] = \hat{j}_\phi^{ext}, \quad (\text{A.1})$$

where the subscript n denotes the domain D_n , $n = 1, 2, 3$ (note that we take $\epsilon = \epsilon_0$ throughout the configuration). The source term \hat{j}_ϕ^{ext} is given by

$$\hat{j}_\phi^{ext} = \frac{\delta(r - r')\delta(x_3 - x'_3)}{2\pi r}. \quad (\text{A.2})$$

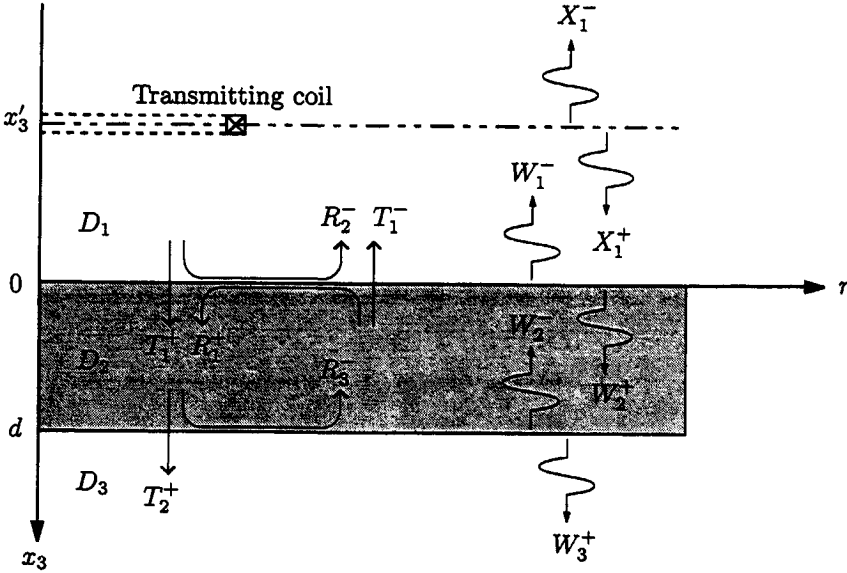


Figure A.1: Single-layer configuration for the scalar Green's function.

Using the Hankel transformation with respect to r , Eq. (A.1) can be rewritten as

$$\frac{-1}{i\omega\mu_n} [\partial_3^2 - (k_r^2 - k_n^2)] \tilde{G}(k_r, x_3; r', x'_3; \omega) = \frac{1}{2\pi} J_1(k_r r') \delta(x_3 - x'_3) \quad (\text{A.3})$$

which represents a one-dimensional wave equation. The quantity J_1 is the Bessel function of the first kind and order one. The wave number k_n is defined as

$$k_n^2 = [\omega^2 \epsilon_0 \mu_n + i\omega \mu_n \sigma_n], \quad n = 1, 2, 3. \quad (\text{A.4})$$

We have the following boundary conditions

$$\lim_{x_3 \downarrow \{0, d\}} \tilde{G}(k_r, x_3; r', x'_3; \omega) - \lim_{x_3 \uparrow \{0, d\}} \tilde{G}(k_r, x_3; r', x'_3; \omega) = 0, \quad (\text{A.5})$$

$$\lim_{x_3 \downarrow \{0, d\}} \partial_3 \tilde{G}(k_r, x_3; r', x'_3; \omega) - \lim_{x_3 \uparrow \{0, d\}} \partial_3 \tilde{G}(k_r, x_3; r', x'_3; \omega) = 0, \quad (\text{A.6})$$

at $x_3 = 0$ and $x_3 = d$, and the excitation conditions

$$\lim_{x_3 \downarrow x'_3} \tilde{G}(k_r, x_3; r', x'_3; \omega) - \lim_{x_3 \uparrow x'_3} \tilde{G}(k_r, x_3; r', x'_3; \omega) = 0, \quad (\text{A.7})$$

$$\lim_{x_3 \downarrow x'_3} \partial_3 \tilde{G}(k_r, x_3; r', x'_3; \omega) - \lim_{x_3 \uparrow x'_3} \partial_3 \tilde{G}(k_r, x_3; r', x'_3; \omega) = \frac{-i\omega\mu_1}{2\pi} J_1(k_r r'), \quad (\text{A.8})$$

at the source interface $x_3 = x'_3$. The one-dimensional scalar differential equation for $\tilde{G}(k_r, x_3; r', x'_3; \omega)$ admits solutions of the type

$$\tilde{G}_n(k_r, x_3; r', x'_3; \omega) = W_n^+ \exp(-\gamma_n x_3) + W_n^- \exp(\gamma_n x_3), \quad (\text{A.9})$$

which represent up- and downgoing waves in subdomain D_n . The propagation coefficient γ_n is given by

$$\gamma_n = [k_r^2 - k_n^2]^{\frac{1}{2}}, \quad \text{Re}(\gamma_n) \geq 0, \quad (\text{A.10})$$

in which k_n is the wave number corresponding to subdomain D_n . The amplitude of the source terms is denoted by X_0^\pm . Substituting the solutions for the up- and downgoing waves in each subdomain into the boundary conditions results in a system of linear equations which can be solved for the amplitude coefficients W_n^\pm . We first introduce the impedance Z_n of subdomain D_n as

$$Z_n = \frac{-i\omega\mu_n}{\gamma_n}, \quad (\text{A.11})$$

and the reflection and transmission coefficients R_2^-, T_1^+, R_1^- and T_0^+ as

$$R_3^- = \frac{\gamma_3 - \gamma_2}{\gamma_3 + \gamma_2}, \quad (\text{A.12})$$

$$T_2^+ = \frac{2\gamma_3}{\gamma_3 + \gamma_2}, \quad (\text{A.13})$$

$$R_2^- = \frac{(1 + R_C)\gamma_2 - (1 - R_C)\gamma_1}{(1 + R_C)\gamma_2 + (1 - R_C)\gamma_1}, \quad (\text{A.14})$$

$$T_1^+ = \frac{2\gamma_2}{(1 + R_C)\gamma_2 + (1 - R_C)\gamma_1}, \quad (\text{A.15})$$

where the constant R_C is defined by

$$R_C = R_2^- \exp(-2\gamma_2 d). \quad (\text{A.16})$$

We can then write the following expression for the Green's function for the configuration where the source is located above the layer

$$\tilde{G}(k_r, x_3; r', x'_3; \omega) = \quad (\text{A.17})$$

$$\begin{cases} G_1 [\exp(-\gamma_1 |x_3 - x'_3|) + R_2^- \exp(\gamma_1 (x_3 + x'_3))], & x_3 < 0, \\ G_1 T_1^+ \exp(\gamma_1 x'_3) [\exp(-\gamma_2 x_3) + R_3^- \exp(-\gamma_2 (2d - x_3))], & 0 \leq x_3 < d, \\ G_1 T_1^+ \exp(\gamma_1 x'_3) T_2^+ \exp(-\gamma_2 d) \exp(-\gamma_3 (x_3 - d)), & x_3 > d, \end{cases}$$

in which the amplitude factor G_1 is given by

$$G_1 = \frac{1}{4\pi} Z_1 J_1(k_r r'). \quad (\text{A.18})$$

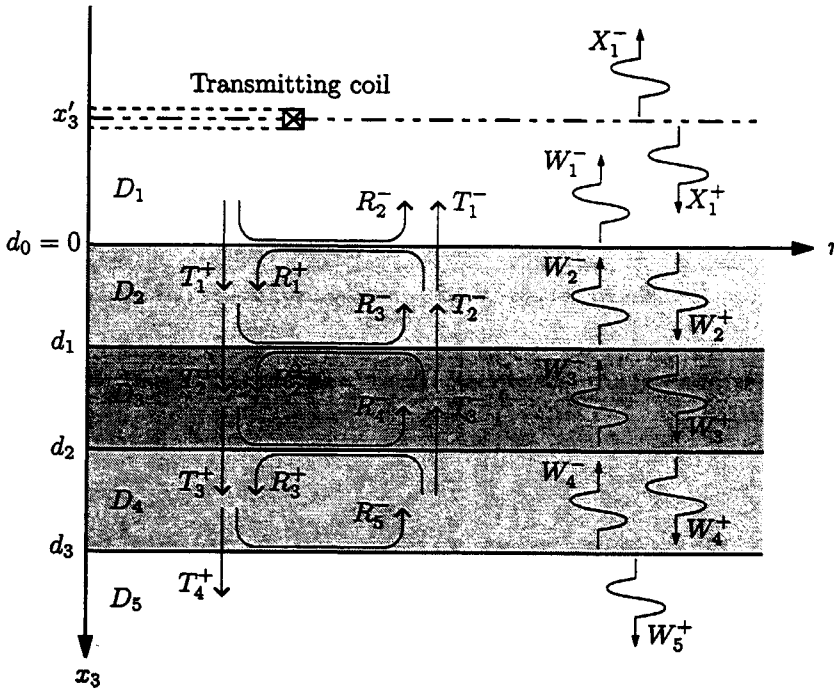


Figure A.2: Three-layer configuration for the scalar Green's function.

Note that in this formulation we have $x'_3 < 0$. The first exponential function in the expression for the Green's function for $x_3 < 0$ is the direct contribution from source to receiver. This part is neglected when we use this Green's function to calculate the PEC signals, since it does not contain any information on the medium parameters or the thickness of the layer (subdomain D_2). The influence of the medium parameters and thickness d of the layer are contained within the reflection coefficient R_2^- . In the measurement setup, the direct part of the signal is removed by starting the measurement at a time in the order of $t \approx 0.1$ ms, at which time the direct contribution of the source can be considered close to zero.

A.2 Three-layer configuration

We will now discuss the configuration where a circular transmitting coil is located above three layers (denoted by domains D_2 , D_3 and D_4 , respectively), as depicted in Figure A.2. The wave equation in the Hankel-transform domain is given in Eq. (A.3). The boundary conditions of Eqs. (A.5) and (A.6) are valid for interfaces

$x_3 = \{d_0 = 0, d_1, d_2, d_3\}$ and we have again the excitation conditions given in Eqs. (A.7) and (A.8) at the source interface $x_3 = x'_3$. The one-dimensional scalar wave equation for $\bar{G}(k_r, x_3; r', x'_3; \omega)$ admits solutions of the type given in Eq. (A.9). Substitution of the solutions for the up- and downgoing waves in each subdomain into the boundary equations results in a system of linear equations for the amplitude coefficients W_n^\pm . The reflection and transmission coefficients for the configuration with three layers are given by

$$R_5^- = \frac{\gamma_5 - \gamma_4}{\gamma_5 + \gamma_4}, \tag{A.19}$$

$$T_4^+ = \frac{2\gamma_5}{\gamma_5 + \gamma_4}, \tag{A.20}$$

at interface $x_3 = d_3$, while the reflection and transmission coefficients at the other interfaces are given by the recursion formula

$$R_n^- = \frac{(1 + R_{C,n})\gamma_n - (1 - R_{C,n})\gamma_{n-1}}{(1 + R_{C,n})\gamma_n + (1 - R_{C,n})\gamma_{n-1}}, \tag{A.21}$$

$$T_{n-1}^+ = \frac{2\gamma_n}{(1 + R_{C,n})\gamma_n + (1 - R_{C,n})\gamma_{n-1}}, \tag{A.22}$$

$$R_{C,n} = R_{n+1}^- \exp(-2\gamma_n(d_{n-1} - d_{n-2})), \tag{A.23}$$

for $n \in \{2, 3, 4\}$ (note that $d_0 = 0$) and where γ_n is given in the previous section. We can now write the following expression for the Green's function for a configuration where a loop source is located above three layers

$$\bar{G}(k_r, x_3; r', x'_3; \omega) = \tag{A.24}$$

$$\left\{ \begin{array}{ll} G_1 [\exp(-\gamma_1|x_3 - x'_3|) + R_2^- \exp(\gamma_1(x_3 + x'_3))], & x_3 < 0, \\ G_1 T_1^+ \exp(\gamma_1 x'_3) [\exp(-\gamma_2 x_3) + R_3^- \exp(-\gamma_2(2d_1 - x_3))], & 0 \leq x_3 < d_1, \\ G_1 T_1^+ \exp(\gamma_1 x'_3) T_2^+ \exp(-\gamma_2 d_1) [\exp(-\gamma_3(x_3 - d_1)) \\ + R_4^- \exp(-\gamma_3(2(d_2 - d_1) - x_3))], & d_1 \leq x_3 < d_2 \\ G_1 T_1^+ \exp(\gamma_1 x'_3) T_2^+ \exp(-\gamma_2 d_1) T_3^+ \exp(-\gamma_3(d_2 - d_1)) \times \\ [\exp(-\gamma_4(x_3 - d_2)) + R_5^- \exp(-\gamma_4(2(d_3 - d_2) - x_3))], & d_2 \leq x_3 < d_3 \\ G_1 T_1^+ \exp(\gamma_1 x'_3) T_2^+ \exp(-\gamma_2 d_1) T_3^+ \exp(-\gamma_3(d_2 - d_1)) \times \\ T_4^+ \exp(-\gamma_4(d_3 - d_2)) \exp(-\gamma_5(x_3 - d_3)), & x_3 > d_3 \end{array} \right.$$

in which the amplitude factor G_1 is given by

$$G_1 = \frac{1}{4\pi} Z_1 J_1(k_r r'). \tag{A.25}$$

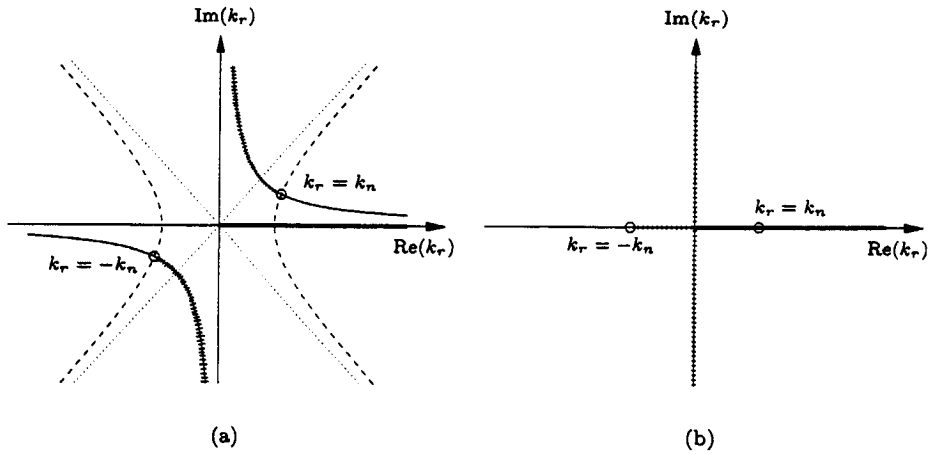


Figure A.3: Branch cuts, branch points and integration contours for a configuration with lossy (a) and lossless (b) halfspaces.

As with the Green's function for the single-layer configuration, we will neglect the direct contribution from source to receiver (which is included here for completeness' sake).

A.3 Branch points and poles

To obtain the Green's function in the frequency domain, we need to calculate the inverse Hankel transformation of Eq. (A.17). Since a closed-form expression for Eq. (A.17) does not exist, we employ a numerical integration routine using a trapezoidal rule. Care must be taken for the step size of the integration, since this depends strongly on the medium parameters and the dimensions of the configuration. Furthermore, branch points and poles will be present in the complex k_r plane and these could be located on the integration contour, depending on the medium parameters of the halfspaces. It can be shown (see Chew [22]) that the reflection coefficient R_1^- is not a double-valued function of γ_2 (or γ_j , $j = 2, 3, 4$, in case of the 3-layer configuration) and therefore the branch points are associated with the halfspaces on either side of the layer(s). For the case where the halfspaces are lossy, the branch points and branch cuts in the complex k_r plane are given in Figure A.3. The branch points are located at $k_r = \pm k_n$, where $n \in \{1, 3\}$ for the single-layer configuration and $n \in \{1, 5\}$ for the three-layer configuration. The integration contour is from $k_r = 0$ to $k_r \rightarrow \infty$, which means that we have to stop the numerical integration at some 'large' value of $k_r = k_{r,max}$, where the contribution to the integral for values larger than $k_{r,max}$ is below the predefined error criterion. It can be seen that for the

case of lossy halfspaces the branch points are not located on the integration contour. Likewise, if there are poles in the complex k_r plane, these will be located off the real k_r axis as well. We can see from Eq. (A.14) that the integrand is not singular at the branch point and from the properties of the Bessel function we know that the integrand goes to zero when $k_r \rightarrow 0$.

Note that when the halfspaces on either side of the layer have the same medium parameters as air, the branch points are located at $k_r = \pm\omega^2\varepsilon_0\mu_0$. For the numerical implementation, where we calculate the integral for frequencies up to several kHz, the branch point has a value of $k_r = O(10^{-5})$, which is much smaller than the integration step. Therefore, the first function evaluation in the numerical integration routine is done for a value of k_r that is already much larger than the value at which the branch point occurs and consequently we have no problems with the branch point, even though it is located on the integration axis in the case where the halfspaces are lossless. When we take the the halfspaces on either side of the layer to be lossy, the branch points and poles will move off the integration axis and hence we will encounter no singularities while performing the inverse Hankel transformation, since the integrand is otherwise well-behaved.

Appendix B

Dyadic Green's Functions

In this appendix we will discuss the derivation of the dyadic Green's functions for a piece-wise homogeneous stratified medium. We discern four cases of the dyadic Green's function, i.e., we have Electric-Electric, Electric-Magnetic, Magnetic-Electric and Magnetic-Magnetic components. Each of these quantities can be considered to be a 3x3 matrix, working on a field vector. For the unbounded media, the dyadic Green's function can easily be derived from the scalar 3D Green's function by letting the grad-div and curl operators act on it. For a stratified medium however, this operation is not so easily performed due to the complicated nature of the Green's function, which now includes reflections from the interfaces. In this case, we can take advantage of the invariance of the configuration in the i_1 - and i_2 -directions by performing a spatial Fourier transformation with respect to these coordinates. We then solve Maxwell's equations in the spatial Fourier-transform domain and calculate the inverse transformation numerically. The two-dimensional Fourier integral can either be simplified by introducing cylindrical coordinates (see for example Chew [22]), after which a numerical integration scheme is applied, or we can use an FFT to calculate the inverse transformation. Since we need to calculate the Green's function for a large number of points within the layer, we have chosen to use FFTs for the inverse transformation, combined with the use of a grid reduction technique (see Appendix C) to increase the computational efficiency. More information on the subject of fields in layered media can be found in Wait [87] and Chew [22]. In Section B.1 we discuss the formalism of the electromagnetic fields in a general stratified configuration, after which we will derive the Green's function for a 3-media configuration (a single layer between two half-spaces). We will consider sources located either within or above the layer (Sections B.2.1 and B.2.2,

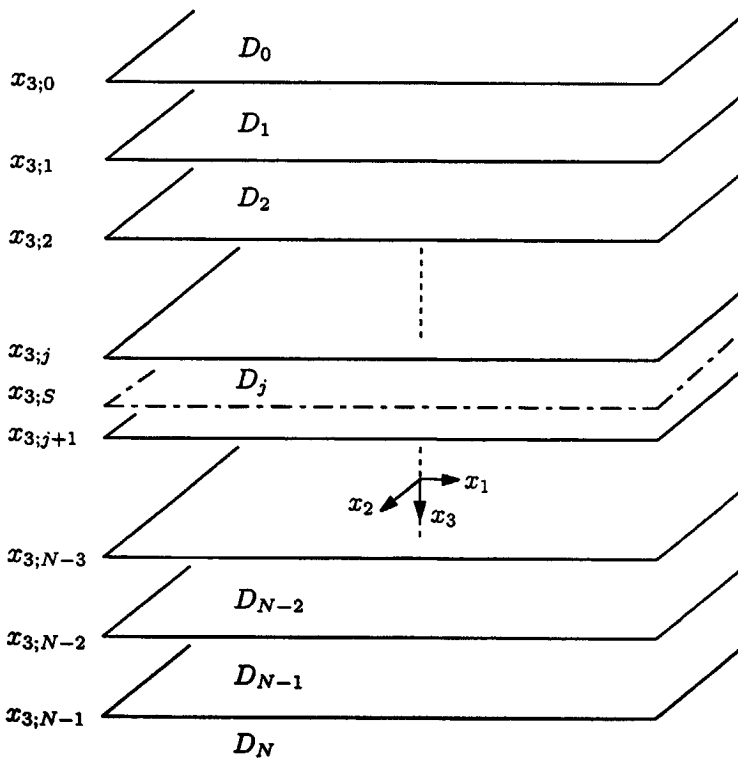


Figure B.1: Piecewise homogeneous stratified medium, the sources are located at interface $x_{3,S}$.

respectively). Subsequently we will discuss the symmetry properties of the Green's function in Section B.3 and the numerical implementation in Section B.4.

B.1 The Green's function for a stratified medium

The medium under consideration is assumed to be a piecewise homogeneous, stratified medium (see Figure B.1). The medium is discontinuous in the x_3 -direction, where the x_3 -axis is taken to be oriented downward. There are N interfaces, labelled 0 to $N-1$, separating the $N+1$ domains. Sources can be present in any of the domains and are denoted by the primed coordinates. When the sources are not located on an interface, we introduce an artificial source layer $x_{3,S} = x'_3$. The

domains between the interfaces are defined as

$$D_0 = \{(x_1, x_2) \in \mathbb{R}^2, -\infty < x_3 < x_{3;0}\}, \tag{B.1}$$

$$D_k = \{(x_1, x_2) \in \mathbb{R}^2, x_{3;k-1} < x_3 < x_{3;k}\}, \tag{B.2}$$

where $k = 1, \dots, N - 1,$

$$D_N = \{(x_1, x_2) \in \mathbb{R}^2, x_{3;N-1} < x_3 < \infty\}. \tag{B.3}$$

In each domain, the medium parameters are denoted by σ_j, ϵ_j and μ_j . For generality we have included the permittivity in the derivation of the Green's function, although we use $\epsilon = \epsilon_0$ for our calculations.

B.1.1 Maxwell's equations in the Fourier transform domain

Following Kooij [43], we start from the electromagnetic field equations given in Eqs. (2.16) and (2.17). First, we introduce the quantities η and ζ as

$$\eta = \sigma - i\omega\epsilon, \tag{B.4}$$

$$\zeta = -i\omega\mu. \tag{B.5}$$

Since the medium is shift-invariant in the x_1 - and x_2 -directions, it is advantageous to employ a spatial Fourier transformation as defined in Section 2.5. Using the fact that under this transformation $\partial_1 \rightarrow -jk_1$ and $\partial_2 \rightarrow -jk_2$, Maxwell's equations can be written as

$$-\epsilon_{k,3,p} \partial_3 \bar{H}_p + jk_\lambda \epsilon_{k,\lambda,p} \bar{H}_p + \eta \bar{E}_k = -\bar{J}_k^{ext}, \tag{B.6}$$

$$\epsilon_{j,3,r} \partial_3 \bar{E}_r - jk_\kappa \epsilon_{j,\kappa,r} \bar{E}_r + \zeta \bar{H}_j = -\bar{K}_j^{ext}. \tag{B.7}$$

For the source terms we will take point sources, therefore \bar{J}_k^{ext} and \bar{K}_j^{ext} are given by

$$\bar{J}_k^{ext} = \bar{J}'_k \delta(x_3 - x'_3), \tag{B.8}$$

$$\bar{K}_j^{ext} = \bar{K}'_j \delta(x_3 - x'_3), \tag{B.9}$$

where

$$\bar{J}'_k = \exp(i(k_1 x'_1 + k_2 x'_2)) \mathbf{i}_k, \tag{B.10}$$

$$\bar{K}'_j = \exp(i(k_1 x'_1 + k_2 x'_2)) \mathbf{i}_j. \tag{B.11}$$

Next, we express \bar{E}_3 and \bar{H}_3 , which are discontinuous across an interface, in terms of the source quantities and those field components that are continuous across an interface. This yields

$$\bar{E}_3 = \frac{1}{\eta} \left(-\bar{J}_3^{ext} - jk_1 \bar{H}_2 + jk_2 \bar{H}_1 \right), \tag{B.12}$$

$$\bar{H}_3 = \frac{1}{\zeta} \left(-\bar{K}_3^{ext} + jk_1 \bar{E}_2 - jk_2 \bar{E}_1 \right). \tag{B.13}$$

After eliminating the x_3 -components from the electromagnetic field equations, we end up with a 4×4 system of coupled differential equations. This system can be solved by decoupling and application of the boundary conditions to the resulting up- and downgoing waves. Introducing the state vector as

$$\mathbf{F} = \begin{bmatrix} \tilde{E}_1 \\ \tilde{E}_2 \\ -\tilde{H}_2 \\ \tilde{H}_1 \end{bmatrix}, \quad (\text{B.14})$$

we write the following system of differential equations for each layer

$$\partial_3 \mathbf{F} + j\mathbf{A}\mathbf{F} = 0, \quad (\text{B.15})$$

in which the 4×4 system matrix \mathbf{A} is given by

$$\mathbf{A} = \begin{bmatrix} 0 & \mathbf{A}^{EH} \\ \mathbf{A}^{HE} & 0 \end{bmatrix}. \quad (\text{B.16})$$

Using the definitions in Eqs. (B.12) and (B.13), we can write the submatrices \mathbf{A}^{EH} and \mathbf{A}^{HE} as

$$\mathbf{A}^{EH} = \begin{bmatrix} \frac{jk_1^2}{\eta} + j\zeta & \frac{jk_1 k_2}{\eta} \\ \frac{jk_1 k_2}{\eta} & \frac{jk_2^2}{\eta} + j\zeta \end{bmatrix}, \quad (\text{B.17})$$

$$\mathbf{A}^{HE} = \begin{bmatrix} \frac{jk_2^2}{\zeta} + j\eta & \frac{-jk_1 k_2}{\zeta} \\ \frac{-jk_1 k_2}{\zeta} & \frac{jk_1^2}{\zeta} + j\eta \end{bmatrix}. \quad (\text{B.18})$$

At the source level we have

$$\lim_{x_3 \downarrow x'_3} \mathbf{F} - \lim_{x_3 \uparrow x'_3} \mathbf{F} = \mathbf{Q}, \quad (\text{B.19})$$

where \mathbf{Q} is the source vector corresponding to the source at $x_{3,S} = x'_3$. This source vector is given by

$$\mathbf{Q} = \begin{bmatrix} -\tilde{K}'_2 + \frac{jk_1 \tilde{J}'_3}{\eta} \\ \tilde{K}'_1 + \frac{jk_2 \tilde{J}'_3}{\eta} \\ \tilde{J}'_1 - \frac{jk_2 \tilde{K}'_3}{\zeta} \\ \tilde{J}'_2 + \frac{jk_1 \tilde{K}'_3}{\zeta} \end{bmatrix}. \quad (\text{B.20})$$

B.1.2 Electromagnetic fields in a homogeneous subdomain

We first solve Eq. (B.15) in a source-free subdomain to obtain a homogeneous solution to Eq. (B.15). Performing a linear transformation on the state vector \mathbf{F} gives

$$\mathbf{F} = \mathbf{L}\mathbf{W}, \tag{B.21}$$

where \mathbf{L} is taken to be non-singular and independent of x_3 . Here, \mathbf{W} is the transformed wave vector. Using this in Eq. (B.15) and premultiplying by \mathbf{L}^{-1} yields the decoupled system of differential equations

$$\partial_3 \mathbf{W} + j\mathbf{L}^{-1}\mathbf{A}\mathbf{L}\mathbf{W} = 0, \tag{B.22}$$

in which $\mathbf{L}^{-1}\mathbf{A}\mathbf{L} = \mathbf{\Gamma}$ is a diagonal matrix, the elements of which are the eigenvalues of \mathbf{A} . The matrix \mathbf{L} has the eigenvectors of \mathbf{A} as its columns. Since $\mathbf{\Gamma}$ is a diagonal matrix, the system of equations in Eq. (B.22) is now decoupled. We define the propagation coefficient as

$$\gamma = (k^2 - k_1^2 - k_2^2)^{\frac{1}{2}}, \quad \text{Im}(\gamma) \leq 0 \tag{B.23}$$

where k is given by

$$k^2 = (\omega^2 \epsilon \mu + i\omega \mu \sigma). \tag{B.24}$$

With this definition, the diagonal matrix $\mathbf{\Gamma}$ is given by

$$\mathbf{\Gamma} = \text{diag}(-\gamma, -\gamma, \gamma, \gamma). \tag{B.25}$$

The solution to this system of uncoupled differential equations is the wave vector \mathbf{W} , which represents the up- and downgoing waves within each subdomain (see Figure B.2)

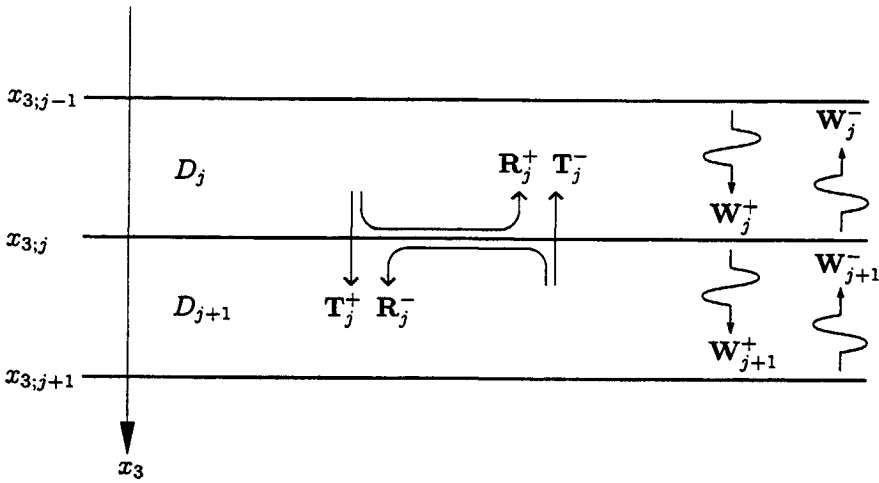
$$\mathbf{W} = \begin{bmatrix} \mathbf{W}^- \exp[j\gamma(x_3 - x_{3,J})] \\ \mathbf{W}^+ \exp[-j\gamma(x_3 - x_{3,J-1})] \end{bmatrix}. \tag{B.26}$$

The constants \mathbf{W}^- and \mathbf{W}^+ represent the amplitudes for the down- (negative x_3 -direction) and upgoing (positive x_3 -direction) waves, respectively. Since the total field vector \mathbf{F} has length 4, the amplitudes \mathbf{W}^- and \mathbf{W}^+ are each vectors of length 2. The amplitude factor \mathbf{W}^- represents the downgoing TM and TE modes, while the amplitude factor \mathbf{W}^+ represents the upgoing TM and TE modes within the layer. The matrices \mathbf{L} and \mathbf{L}^{-1} are given explicitly as

$$\mathbf{L} = \frac{1}{\sqrt{2(k_1^2 + k_2^2)}} \begin{bmatrix} k_1 & -k_2 & k_1 & -k_2 \\ k_2 & k_1 & k_2 & k_1 \\ Y_i k_1 & -\bar{Y}_i k_2 & -Y_i k_1 & \bar{Y}_i k_2 \\ Y_i k_2 & \bar{Y}_i k_1 & -Y_i k_2 & -\bar{Y}_i k_1 \end{bmatrix}, \tag{B.27}$$

and

$$\mathbf{L}^{-1} = \frac{1}{\sqrt{2(k_1^2 + k_2^2)}} \begin{bmatrix} k_1 & k_2 & Z_i k_1 & Z_i k_2 \\ -k_2 & k_1 & -\bar{Z}_i k_2 & \bar{Z}_i k_1 \\ k_1 & k_2 & -Z_i k_1 & -Z_i k_2 \\ -k_2 & k_1 & \bar{Z}_i k_2 & -\bar{Z}_i k_1 \end{bmatrix}, \tag{B.28}$$

Figure B.2: Scattering formalism at interface $x_{3,j}$.

where the admittances Y_i and \bar{Y}_i are given by

$$Y_i = \frac{\sigma_i - i\omega\epsilon_i}{j\gamma_i} = \frac{\eta_i}{j\gamma_i}, \quad (\text{B.29})$$

$$\bar{Y}_i = \frac{j\gamma_i}{-i\omega\mu_i} = \frac{j\gamma_i}{\zeta_i}, \quad (\text{B.30})$$

and the impedances Z_i and \bar{Z}_i by

$$Z_i = Y_i^{-1}, \quad (\text{B.31})$$

$$\bar{Z}_i = \bar{Y}_i^{-1}. \quad (\text{B.32})$$

Using this formulation, we have made a decomposition into TE and TM modi within the layer.

B.1.3 Scattering formalism at an interface

At an interface between two regions with different medium parameters and where no sources are present on the interface, the field vector \mathbf{F} is continuous, since it is composed of those field components that are tangential to the interface. The situation at the interface between subdomains D_j and D_{j+1} is given in Figure B.2. The up- and downgoing waves in each subdomain are related through the boundary conditions at the interface. The scattering formalism at interface $x_{3,j}$ is defined as

$$\begin{bmatrix} \mathbf{W}_j^- \\ \mathbf{W}_{j+1}^- \end{bmatrix} = \mathbf{S}_j \begin{bmatrix} \mathbf{W}_j^+ \\ \mathbf{W}_{j+1}^+ \end{bmatrix} + \begin{bmatrix} \mathbf{X}_j^- \\ \mathbf{X}_{j+1}^- \end{bmatrix}. \quad (\text{B.33})$$

Here, the vector on the left-hand side of Eq. (B.33) represents the waves propagating away from the interface $x_{3,j}$, while the wave vector on the right-hand side represents the wave components propagating towards the interface. The source vector \mathbf{X}_j represents the sources that are present at the interface, while the scattering matrix \mathbf{S}_j is a 4×4 matrix whose elements are the reflection and transmission coefficients at the interface. The scattering matrix relates the outgoing waves at the interface to the incoming waves and the sources at that interface.

$$\mathbf{S}_j = \begin{bmatrix} \mathbf{R}_j^+ & \mathbf{T}_j^- \\ \mathbf{T}_j^+ & \mathbf{R}_j^- \end{bmatrix}, \quad (\text{B.34})$$

where the reflection and transmission matrices are given by

$$\mathbf{R}_j^+ = \begin{bmatrix} \frac{Y_j - Y_{j+1}}{Y_j + Y_{j+1}} & 0 \\ 0 & \frac{\bar{Y}_j - \bar{Y}_{j+1}}{Y_j + Y_{j+1}} \end{bmatrix} \exp[-j\gamma_j(x_{3,j} - x_{3,j-1})], \quad (\text{B.35})$$

$$\mathbf{R}_j^- = \begin{bmatrix} \frac{Y_{j+1} - Y_j}{Y_{j+1} + Y_j} & 0 \\ 0 & \frac{\bar{Y}_{j+1} - \bar{Y}_j}{Y_{j+1} + Y_j} \end{bmatrix} \exp[-j\gamma_{j+1}(x_{3,j+1} - x_{3,j})], \quad (\text{B.36})$$

$$\mathbf{T}_j^+ = \begin{bmatrix} \frac{2Y_j}{Y_j + Y_{j+1}} & 0 \\ 0 & \frac{2\bar{Y}_j}{Y_j + Y_{j+1}} \end{bmatrix} \exp[-j\gamma_j(x_{3,j} - x_{3,j-1})], \quad (\text{B.37})$$

and

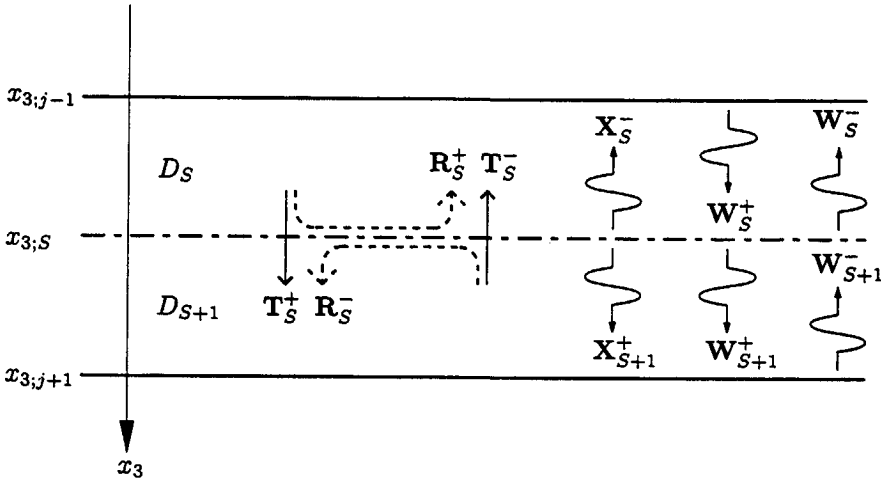
$$\mathbf{T}_j^- = \begin{bmatrix} \frac{2Y_{j+1}}{Y_{j+1} + Y_j} & 0 \\ 0 & \frac{2\bar{Y}_{j+1}}{Y_{j+1} + Y_j} \end{bmatrix} \exp[-j\gamma_{j+1}(x_{3,j+1} - x_{3,j})]. \quad (\text{B.38})$$

It can be seen that when the medium parameters in subdomains D_j and D_{j+1} are equal (i.e., the source is located in a homogeneous subdomain), the reflection coefficients are zero. For the transmission factors we then only have the exponential functions, which represent the propagation of the wave components within D_j and D_{j+1} .

B.1.4 Scattering formalism at the source interface

We take the sources to be located completely within a subdomain, i.e., there can be no sources present on an interface. Under this assumption, we introduce an artificial layer, the source layer $x_{3,S}$, where the sources are located (Figure B.3).

We now have the same configuration as in the previous section, with the exception that the source term in Eq. (B.33) now has some finite value. Furthermore,

Figure B.3: The artificial source level $x_{3,S}$.

we can immediately write down the reflection and transmission matrices, since the artificial source level is located in a homogeneous subdomain. To relate the up- and downgoing wave components emanating from the source level to the source components, we use the boundary condition at $x_{3,S}$, which is given by

$$\lim_{x_3 \downarrow x_{3,S}} \mathbf{F}_{S+1} - \lim_{x_3 \uparrow x_{3,S}} \mathbf{F}_S = \mathbf{Q}. \quad (\text{B.39})$$

The vector of corresponding wave amplitudes is related to the field vector by the linear transformation

$$\mathbf{F}_S = \mathbf{L}_S \mathbf{W}_S. \quad (\text{B.40})$$

The scattering formalism at the source interface is given by

$$\begin{bmatrix} \mathbf{W}_S^- \\ \mathbf{W}_{S+1}^+ \end{bmatrix} = \begin{bmatrix} \mathbf{R}_S^+ & \mathbf{T}_S^- \\ \mathbf{T}_S^+ & \mathbf{R}_S^- \end{bmatrix} \begin{bmatrix} \mathbf{W}_S^+ \\ \mathbf{W}_{S+1}^- \end{bmatrix} + \begin{bmatrix} \mathbf{X}_S^- \\ \mathbf{X}_{S+1}^+ \end{bmatrix}. \quad (\text{B.41})$$

Here, \mathbf{X}_S^- is the source term radiating in the negative x_3 -direction in D_S , away from the interface, while \mathbf{X}_{S+1}^+ is the source term radiating in the positive x_3 -direction in D_{S+1} , again away from the interface. In case the subdomains D_S and D_{S+1} have the same medium parameters, we have

$$\mathbf{R}_S^\pm = \mathbf{0}, \quad (\text{B.42})$$

$$\mathbf{T}_S^- = \mathbf{I} \exp(-j\gamma_S(x_{3,S} - x_{3,j-1})), \quad (\text{B.43})$$

$$\mathbf{T}_S^+ = \mathbf{I} \exp(-j\gamma_S(x_{3,j+1} - x_{3,S})), \quad (\text{B.44})$$

where \mathbf{I} is the 2x2 identity matrix. The source vector can be written as

$$\begin{bmatrix} \mathbf{X}_S^- \\ \mathbf{X}_{S+1}^+ \end{bmatrix} = \mathbf{N}\mathbf{L}^{-1}\mathbf{Q}, \quad (\text{B.45})$$

in which $\mathbf{N} = \text{diag}(-1, -1, 1, 1)$ and \mathbf{L}^{-1} and \mathbf{Q} have been given in the previous section. Eq. (B.45) can be written explicitly as

$$\begin{bmatrix} \mathbf{X}_S^- \\ \mathbf{X}_{S+1}^+ \end{bmatrix} = \frac{1}{\sqrt{2(k_1^2 + k_2^2)}} \begin{bmatrix} -k_1 Q_1 - k_2 Q_2 - k_1 Y_S^{-1} Q_3 - k_2 Y_S^{-1} Q_4 \\ k_2 Q_1 - k_1 Q_2 + k_2 \bar{Y}_S^{-1} Q_3 - k_1 \bar{Y}_S^{-1} Q_4 \\ k_1 Q_1 + k_2 Q_2 - k_1 Y_S^{-1} Q_3 - k_2 Y_S^{-1} Q_4 \\ -k_2 Q_1 + k_1 Q_2 + k_2 \bar{Y}_S^{-1} Q_3 - k_1 \bar{Y}_S^{-1} Q_4 \end{bmatrix}. \quad (\text{B.46})$$

The expression for the up- and downgoing wave components can now be obtained by substituting Eqs. (B.42) – (B.44) and (B.46) into Eq. (B.41). At the observation level $x_{3,obs}$, the electromagnetic state vector is obtained from the wave components by using Eq. (B.21). The discontinuous field components \bar{E}_3 and \bar{H}_3 are then obtained by using Eqs. (B.12) and (B.13), after which all field components are known in the Fourier-transform domain. Note that when the medium parameters on either side of the source interface are different, the expression for the source vector is more complicated (see Kooij [43]).

B.2 The Green's function for a 3-media configuration

In this section we will discuss the derivation of the dyadic Green's function for a 3-media configuration (i.e., a layer) where the sources are located either within or above the layer. We will use the theory for the electromagnetic fields in a stratified configuration from the previous sections to obtain expressions for the field quantities in the spatial Fourier-transform domain. Due to the presence of the Fourier-transform parameters in the reflection and transmission coefficients it is not possible to derive closed-form expressions for the field quantities and hence the inverse transformation must be calculated numerically, which is discussed in Section B.4. To facilitate the numerical implementation we take the halfspaces on either side of the layer to have the same medium parameters.

B.2.1 Sources located within the layer

The configuration where the source level is located within the layer is given in Figure B.4. Since the medium parameters in D_1 and D_2 are the same, we can

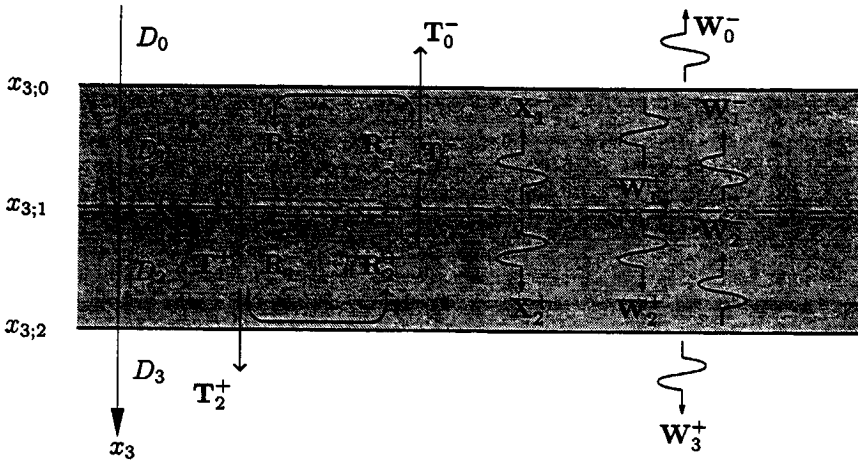


Figure B.4: The 3-media configuration, source located within the layer.

immediately see that (cf. Eqs. (B.42) - (B.44))

$$\mathbf{R}_1^\pm = \mathbf{0}, \quad (\text{B.47})$$

$$\mathbf{T}_1^- = \mathbf{I} \exp(-j\gamma_2(x_{3,2} - x_{3,1})), \quad (\text{B.48})$$

$$\mathbf{T}_1^+ = \mathbf{I} \exp(-j\gamma_1(x_{3,1} - x_{3,0})). \quad (\text{B.49})$$

The source vector at the interface $x_{3,S} = x_{3,1}$ is given by

$$\mathbf{X} = \begin{bmatrix} \mathbf{X}_0^- \\ \mathbf{X}_1^+ \end{bmatrix}. \quad (\text{B.50})$$

All the other source components are zero. We now obtain a coupled system of equations for the wave components in each layer

$$\text{interface } x_{3,0} \quad \begin{bmatrix} \mathbf{W}_0^- \\ \mathbf{W}_1^+ \end{bmatrix} = \mathbf{S}_0 \begin{bmatrix} \mathbf{0} \\ \mathbf{W}_1^- \end{bmatrix}, \quad (\text{B.51})$$

$$\text{interface } x_{3,1} \quad \begin{bmatrix} \mathbf{W}_1^- \\ \mathbf{W}_2^+ \end{bmatrix} = \mathbf{S}_1 \begin{bmatrix} \mathbf{W}_1^+ \\ \mathbf{W}_2^- \end{bmatrix} + \begin{bmatrix} \mathbf{X}_1^- \\ \mathbf{X}_2^+ \end{bmatrix}, \quad (\text{B.52})$$

$$\text{interface } x_{3,2} \quad \begin{bmatrix} \mathbf{W}_2^- \\ \mathbf{W}_3^+ \end{bmatrix} = \mathbf{S}_2 \begin{bmatrix} \mathbf{W}_2^+ \\ \mathbf{0} \end{bmatrix}. \quad (\text{B.53})$$

Note that the scattering matrix \mathbf{S}_1 is given by

$$\mathbf{S}_1 = \begin{bmatrix} \mathbf{0} & \mathbf{T}_1^- \\ \mathbf{T}_1^+ & \mathbf{0} \end{bmatrix}. \quad (\text{B.54})$$

Next, we express each up- and downgoing wave constituent in terms of the source vector and the reflection and transmission matrices, which results in the following expressions for W_j^\pm

$$\begin{bmatrix} W_0^- \\ W_0^+ \end{bmatrix} = M_0^R \begin{bmatrix} X_1^- \\ X_2^+ \end{bmatrix}, \quad (\text{B.55})$$

$$\begin{bmatrix} W_1^- \\ W_1^+ \end{bmatrix} = (M_1^R + M_1^D) \begin{bmatrix} X_1^- \\ X_2^+ \end{bmatrix}, \quad (\text{B.56})$$

$$\begin{bmatrix} W_2^- \\ W_2^+ \end{bmatrix} = (M_2^R + M_2^D) \begin{bmatrix} X_1^- \\ X_2^+ \end{bmatrix}, \quad (\text{B.57})$$

$$\begin{bmatrix} W_3^- \\ W_3^+ \end{bmatrix} = M_3^R \begin{bmatrix} X_1^- \\ X_2^+ \end{bmatrix}, \quad (\text{B.58})$$

where the matrices relating W_j^\pm to the source terms are defined as

$$M_0^R = \begin{bmatrix} DT_0^- & DT_0^- R_2^+ T_1^- \\ 0 & 0 \end{bmatrix}, \quad (\text{B.59})$$

$$M_1^R = \begin{bmatrix} DR_0^- R_2^+ T_1^- T_1^+ & DR_2^+ T_1^- \\ DR_0^- & DR_0^- R_2^+ T_1^- \end{bmatrix}, \quad (\text{B.60})$$

$$M_1^D = \begin{bmatrix} I & 0 \\ 0 & 0 \end{bmatrix}, \quad (\text{B.61})$$

$$M_2^R = \begin{bmatrix} DR_0^- R_2^+ T_1^+ & DR_2^+ \\ DR_0^- T_1^+ & DR_0^- R_2^+ T_1^- T_1^+ \end{bmatrix}, \quad (\text{B.62})$$

$$M_2^D = \begin{bmatrix} 0 & 0 \\ 0 & I \end{bmatrix}, \quad (\text{B.63})$$

$$M_3^R = \begin{bmatrix} 0 & 0 \\ DT_2^+ R_0^- T_1^+ & DT_2^+ \end{bmatrix}, \quad (\text{B.64})$$

in which the matrix D is defined as

$$D = (I - R_0^- R_2^+ T_1^- T_1^+)^{-1}. \quad (\text{B.65})$$

Note that R_j^\pm and T_j^\pm are all 2×2 diagonal matrices. The matrices M_1^D and M_2^D represent the direct contributions from the sources, while M_1^R and M_2^R represent the (multiple) reflections from the interfaces $x_{3,0}$ and $x_{3,2}$.

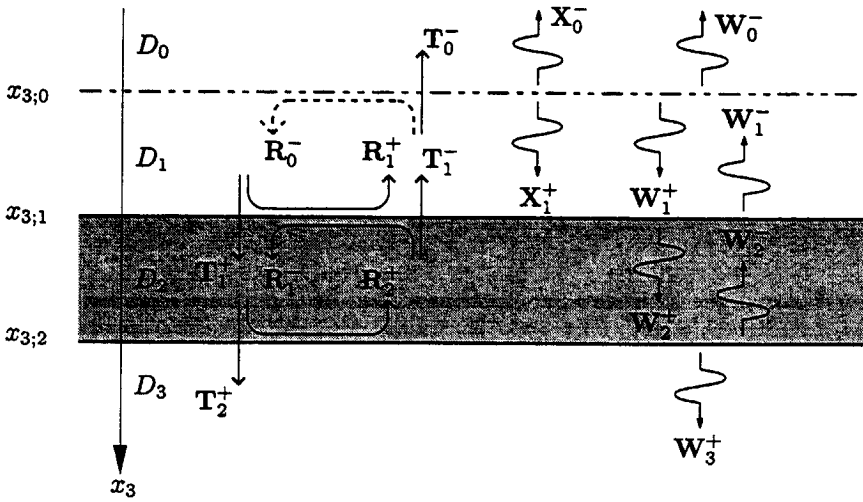


Figure B.5: The 3-media configuration, sources located above the layer.

B.2.2 Sources located above the layer

For the configuration where the source level is located above the layer, the is given in Figure B.5. Since the medium parameters in \$D_0\$ and \$D_1\$ are the same, we can immediately see that (cf. Eqs. (B.42) - (B.44))

$$R_0^\pm = 0, \tag{B.66}$$

$$T_0^- = \mathbf{I} \exp(-j\gamma_1(x_{3,1} - x_{3,0})), \tag{B.67}$$

$$T_0^+ = 0. \tag{B.68}$$

The source vector at the interface \$x_{3,S} = x_{3,0}\$ is given by

$$\mathbf{X} = \begin{bmatrix} \mathbf{X}_0^- \\ \mathbf{X}_1^+ \end{bmatrix}, \tag{B.69}$$

all other source components are zero. We now get a coupled system of equations for the wave components in each layer, consisting of

$$\text{interface } x_{3,0} \begin{bmatrix} \mathbf{W}_0^- \\ \mathbf{W}_1^+ \end{bmatrix} = \mathbf{S}_0 \begin{bmatrix} \mathbf{0} \\ \mathbf{W}_1^- \end{bmatrix} + \begin{bmatrix} \mathbf{X}_1^- \\ \mathbf{X}_2^+ \end{bmatrix}, \tag{B.70}$$

$$\text{interface } x_{3,1} \begin{bmatrix} \mathbf{W}_1^- \\ \mathbf{W}_2^+ \end{bmatrix} = \mathbf{S}_1 \begin{bmatrix} \mathbf{W}_1^+ \\ \mathbf{W}_2^- \end{bmatrix}, \tag{B.71}$$

$$\text{interface } x_{3,0} \begin{bmatrix} \mathbf{W}_2^- \\ \mathbf{W}_3^+ \end{bmatrix} = \mathbf{S}_2 \begin{bmatrix} \mathbf{W}_2^+ \\ \mathbf{0} \end{bmatrix}. \tag{B.72}$$

Note that the scattering matrix S_0 is given by

$$S_0 = \begin{bmatrix} 0 & T_0^- \\ 0 & 0 \end{bmatrix}. \quad (B.73)$$

Next, we express each up- and downgoing wave constituent in terms of the source vector and the reflection and transmission matrices, which results in the following expressions

$$\begin{bmatrix} W_0^- \\ W_0^+ \end{bmatrix} = (M_0^R + M_0^D) \begin{bmatrix} X_0^- \\ X_1^+ \end{bmatrix}, \quad (B.74)$$

$$\begin{bmatrix} W_1^- \\ W_1^+ \end{bmatrix} = (M_1^R + M_1^D) \begin{bmatrix} X_0^- \\ X_1^+ \end{bmatrix}, \quad (B.75)$$

$$\begin{bmatrix} W_2^- \\ W_2^+ \end{bmatrix} = M_2^R \begin{bmatrix} X_0^- \\ X_1^+ \end{bmatrix}, \quad (B.76)$$

$$\begin{bmatrix} W_3^- \\ W_3^+ \end{bmatrix} = M_3^R \begin{bmatrix} X_0^- \\ X_1^+ \end{bmatrix}, \quad (B.77)$$

where the matrices M_0, \dots, M_3 are defined as

$$M_0^R = \begin{bmatrix} 0 & T_0^- (R_1^+ + DT_1^+ R_2^+ T_1^-) \\ 0 & 0 \end{bmatrix}, \quad (B.78)$$

$$M_0^D = \begin{bmatrix} I & 0 \\ 0 & 0 \end{bmatrix}, \quad (B.79)$$

$$M_1^R = \begin{bmatrix} 0 & R_1^+ + DT_1^+ R_2^+ T_1^- \\ 0 & 0 \end{bmatrix}, \quad (B.80)$$

$$M_1^D = \begin{bmatrix} 0 & 0 \\ 0 & I \end{bmatrix}, \quad (B.81)$$

$$M_2^R = \begin{bmatrix} 0 & DT_1^+ R_2^+ \\ 0 & DT_1^+ \end{bmatrix}, \quad (B.82)$$

$$M_3^R = \begin{bmatrix} 0 & 0 \\ 0 & DT_1^+ T_2^+ \end{bmatrix}, \quad (B.83)$$

in which the matrix D is defined as

$$D = (I - R_1^- R_2^+)^{-1}. \quad (B.84)$$

Note that R_j^\pm and T_j^\pm are all 2×2 diagonal matrices. The matrices M_0^D and M_1^D represent the direct contributions from the sources, while M_0^R and M_1^R represent the (multiple) reflections from the interfaces $x_{3,1}$ and $x_{3,2}$.

B.2.3 Calculating the field quantities

The field quantities defined in the electromagnetic state vector can be derived from the up- and downgoing wave constituents by applying Eq. (B.21). To obtain the components of the electric-electric and magnetic-electric dyadic Green's function, we set

$$\hat{J}_k^{ext}(\mathbf{x}) = \delta(\mathbf{x} - \mathbf{x}')\mathbf{i}_k, \quad (\text{B.85})$$

$$\hat{K}_j^{ext}(\mathbf{x}) = 0, \quad (\text{B.86})$$

after which we obtain the components of the Green's function from the electromagnetic state vector as

$$\mathbf{F} = \mathbf{F}^R + \mathbf{F}^D = \begin{bmatrix} \tilde{\mathcal{G}}_{1,k}^{EE,R} \\ \tilde{\mathcal{G}}_{2,k}^{EE,R} \\ -\tilde{\mathcal{G}}_{2,k}^{HE,R} \\ \tilde{\mathcal{G}}_{1,k}^{HE,R} \end{bmatrix} + \begin{bmatrix} \tilde{\mathcal{G}}_{1,k}^{EE,D} \\ \tilde{\mathcal{G}}_{2,k}^{EE,D} \\ -\tilde{\mathcal{G}}_{2,k}^{HE,D} \\ \tilde{\mathcal{G}}_{1,k}^{HE,D} \end{bmatrix}, \quad (\text{B.87})$$

where we have split the Green's function into a direct and a reflected part. Note that we calculate only the reflected part of the Green's function using this formulation. For the calculation of the direct part we use expansion functions to derive expressions for the gradient-divergence and curl operators working on the vector potentials, while for the reflected part of the Green's function the effect of these differentiation operators is calculated in the k -domain. For the x_3 -components of the reflected part we write

$$\tilde{\mathcal{G}}_{3,k}^{EE,R} = \frac{1}{\eta} \left(-\bar{J}_3^{ext} - jk_1 \tilde{\mathcal{G}}_{2,k}^{HE,R} + jk_2 \tilde{\mathcal{G}}_{1,k}^{HE,R} \right), \quad (\text{B.88})$$

$$\tilde{\mathcal{G}}_{3,k}^{HE,R} = \frac{1}{\zeta} \left(-\bar{K}_3^{ext} + jk_1 \tilde{\mathcal{G}}_{2,k}^{EE,R} - jk_2 \tilde{\mathcal{G}}_{1,k}^{EE,R} \right). \quad (\text{B.89})$$

For the magnetic-magnetic and the electric-magnetic parts of the Green's functions we set

$$\hat{J}_k^{ext}(\mathbf{x}) = 0, \quad (\text{B.90})$$

$$\hat{K}_j^{ext}(\mathbf{x}) = \delta(\mathbf{x} - \mathbf{x}')\mathbf{i}_j, \quad (\text{B.91})$$

after which we obtain the components of the Green's function from the electromagnetic state vector as

$$\mathbf{F} = \mathbf{F}^R + \mathbf{F}^D = \begin{bmatrix} \tilde{\mathcal{G}}_{1,k}^{EH,R} \\ \tilde{\mathcal{G}}_{2,k}^{EH,R} \\ -\tilde{\mathcal{G}}_{2,k}^{HH,R} \\ \tilde{\mathcal{G}}_{1,k}^{HH,R} \end{bmatrix} + \begin{bmatrix} \tilde{\mathcal{G}}_{1,k}^{EH,D} \\ \tilde{\mathcal{G}}_{2,k}^{EH,D} \\ -\tilde{\mathcal{G}}_{2,k}^{HH,D} \\ \tilde{\mathcal{G}}_{1,k}^{HH,D} \end{bmatrix}, \quad (\text{B.92})$$

where we have again split the Green's function into a direct and a reflected part. For the x_3 -components of the reflected part we write

$$\tilde{\mathcal{G}}_{3,k}^{EH,R} = \frac{1}{\eta} \left(-\tilde{J}_3^{ext} - jk_1 \tilde{\mathcal{G}}_{2,k}^{HH,R} + jk_2 \tilde{\mathcal{G}}_{1,k}^{HH,R} \right), \quad (\text{B.93})$$

$$\tilde{\mathcal{G}}_{3,k}^{HH,R} = \frac{1}{\zeta} \left(-\tilde{K}_3^{ext} + jk_1 \tilde{\mathcal{G}}_{2,k}^{EH,R} - jk_2 \tilde{\mathcal{G}}_{1,k}^{EH,R} \right). \quad (\text{B.94})$$

The direct part of the Green's function can be calculated analytically from the scalar Green's function as

$$\mathcal{G}^{EE}(\mathbf{x}, \mathbf{x}') = (k^2 + \nabla \nabla \cdot) \hat{G}(\mathbf{x}, \mathbf{x}') \mathbf{I}, \quad (\text{B.95})$$

$$\mathcal{G}^{EH}(\mathbf{x}, \mathbf{x}') = i\omega\mu \nabla \times \hat{G}(\mathbf{x}, \mathbf{x}') \mathbf{I}, \quad (\text{B.96})$$

$$\mathcal{G}^{HE}(\mathbf{x}, \mathbf{x}') = (\sigma - i\omega\varepsilon) \nabla \times \hat{G}(\mathbf{x}, \mathbf{x}') \mathbf{I}, \quad (\text{B.97})$$

$$\mathcal{G}^{HH}(\mathbf{x}, \mathbf{x}') = (k^2 + \nabla \nabla \cdot) \hat{G}(\mathbf{x}, \mathbf{x}') \mathbf{I}, \quad (\text{B.98})$$

where k is the wave number as defined in Eq. (B.24).

B.3 Symmetry properties of the Green's function

In calculating the Green's function, we can take advantage of its symmetry properties. First of all, in the Fourier-transform domain, the state vector is symmetric or antisymmetric for a change in the sign of $k_{1,2}$. This reduces the number of function evaluations in the transform domain to $\frac{1}{4}N_k^2$, where N_k is the number of FFT grid points in one direction. Second, since the medium is isotropic and invariant in the x_1 - and x_2 -directions, the fields generated by sources in those directions are equivalent. This means that only 4 source types, J_1, J_3, K_1 and K_3 , have to be considered. Furthermore, the symmetry properties of the configuration in the x_3 -direction can be exploited, since we assume the halfspaces on either side of the layer to have the same medium parameters.

For a configuration with a homogeneous background, the integral relations for the field quantities contain convolution integrals of the Green's functions and the product of the contrasts and the fields (the contrast sources). In this case, it can be easily seen that the contribution of a certain point in the scatterer to the integral is solely dependent on the path length from that point to the receiver location, which gives rise to the convolution structure. For a 2-media configuration where both source and receiver are located on the same side, the Green's function can be split into a direct and a reflected part. The integral over direct part is still of the convolution type, but now the integral over the reflected part is of the correlation type.

In case of a configuration consisting of a layer where the source and receiver are both located within the layer, the situation is still more complicated. We again split the Green's function into a direct and a reflected part, but now it is also necessary

to split the reflected part further, giving a part corresponding to an odd number of reflections and another part corresponding to an even number of reflections. We can write

$$\tilde{\mathcal{G}} = \tilde{\mathcal{G}}^D + \tilde{\mathcal{G}}_{odd}^R + \tilde{\mathcal{G}}_{even}^R. \quad (\text{B.99})$$

Now the odd reflected part has a correlation structure while the even part has a convolution structure, which can be seen by considering the path length between transmitting and receiving positions. Therefore, when calculating the integral over the scattering domain of the Green's functions and the contrast sources, we need to calculate a correlation type integral and a convolution type integral, both of which can be efficiently calculated using FFTs. If our CG grid is $M \times N \times P$ points, we will need to calculate the Green's function on $2M \times 2N \times 2P$ points to be able to calculate the convolutions and correlations using FFTs. Because of the symmetry properties of the configuration, it suffices to calculate the fields at all grid positions in the x_3 -direction for only a single source position. The Green's function corresponding to other source positions can be obtained by using the symmetry of the configuration around the plane $(x_{3,2} - x_{3,0})/2$ and by using the fact that since the reflection factors \mathbf{R}_0^- and \mathbf{R}_2^+ are equal, only the path length from source to receiver determines the field values.

In order to split the reflected part of the Green's function into even and odd parts, we rewrite the denominator of the elements of the matrix \mathbf{M}_j^R in Eqs. (B.59) - (B.64) as

$$\begin{aligned} [\mathbf{I} - \mathbf{R}_0^- \mathbf{R}_2^+ \mathbf{T}_1^- \mathbf{T}_1^+]^{-1} = & \quad (\text{B.100}) \\ & [\mathbf{I} - (\mathbf{R}_0^- \mathbf{R}_2^+ \mathbf{T}_1^- \mathbf{T}_1^+)^2]^{-1} + [\mathbf{I} - (\mathbf{R}_0^- \mathbf{R}_2^+ \mathbf{T}_1^- \mathbf{T}_1^+)^2]^{-1} \mathbf{R}_0^- \mathbf{R}_2^+ \mathbf{T}_1^- \mathbf{T}_1^+, \end{aligned}$$

where the first term on the right-hand side represents the part corresponding to the even number of reflections and the second term represents the part corresponding to the odd number of reflections. These parts are calculated separately, which doubles the number of FFTs when calculating the Green's function. We calculate the convolutions and correlations using the same routine, the different operators being implemented by ordering the arrays containing the Green's functions in the appropriate manner.

Note that the medium parameters in halfspaces on either side of the layer must be equal for this reasoning to apply. If this is not the case, the reflection coefficients at the upper and lower interfaces would not be equal and the reflections from the upper and lower interfaces would have to be treated separately.

B.4 Numerical implementation of the Green's functions

In this section we will discuss the numerical implementation of the inverse spatial Fourier transformation occurring in the Green's functions. In the previous sections, we have derived expressions for the field vector in the Fourier-transform domain, and due to the complicated nature of these expressions it is not possible to find a closed-form solution for the field vector in the spatial domain, hence the need for a numerical inverse spatial Fourier transformation. In this section we discuss the method of integration, the integration path and the branch points and poles that are present in the complex k -plane. We have chosen to use FFTs for the inverse transformation since this allows us to calculate the Green's function in the x_1 - x_2 plane with a single FFT. Combined with the grid reduction technique discussed in Appendix C and the fact that introducing small losses in the halfspaces does not significantly influence the PEC signal, the use of FFTs leads to an efficient computational scheme.

B.4.1 Branch points and poles

In a layered configuration, the upper- and lowermost layers (i.e., the halfspaces) give rise to branch points in the complex k_1 and k_2 planes (see Chew [22]). When the halfspaces are lossless, the branch points and the associated branch cuts are located on the real and imaginary k_1 and k_2 axes and hence on the integration contour for the inverse Fourier transformation. In this case, it can be advantageous to use numerical integration routines to calculate the Green's function in the spatial domain, since this enables us to deform the integration contour around the branch points and poles. Furthermore, a steepest descent method can be used to evaluate the resulting integrals, which leads to an efficient scheme (see Cui [25], [26]). Since we have taken the halfspaces to be lossy, the branch points and associated branch cuts are located away from the real k_1 and k_2 axes (see Figure B.6). It can be seen that there are no branch points on the integration contour (the real k_1 and k_2 axes). If the halfspaces are taken to be lossless, the branch points and branch cuts move onto the real and imaginary k_1 and k_2 axes, as was the case for the 2D configuration (Figure A.3).

The presence of poles is caused by the zeros of the denominators of Eqs. (B.59) - (B.64) and Eqs. (B.78) - (B.83). Since we assume the halfspaces on either side of the layer to be lossy, the poles will be located off the real k_1 and k_2 axes and therefore we encounter no problems when performing the inverse Fourier transformation by integrating over the real k_1 and real k_2 axes. Should we have a configuration where the halfspaces are lossless, poles could be located on the integration contour and care must then be taken to deform the contour or to take the pole contributions into account.

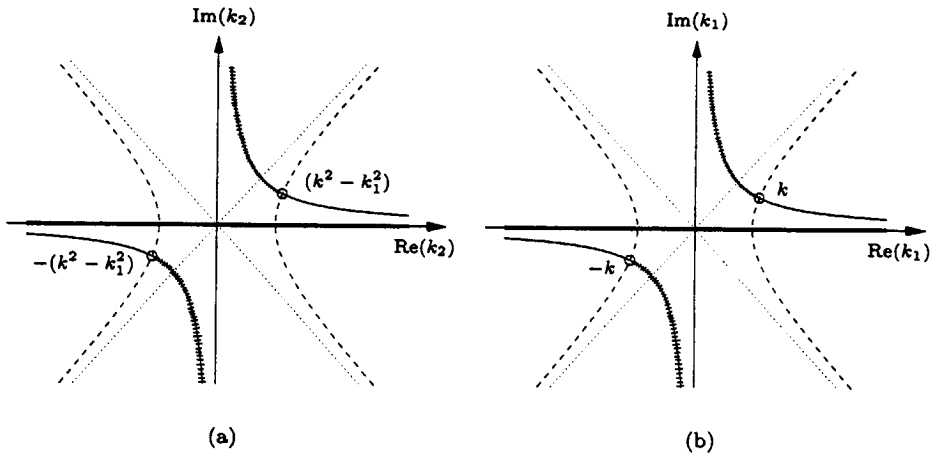


Figure B.6: Branch cuts, branch points and integration contours in the complex k_2 plane (a) and the complex k_1 plane (b) for a 3-media configuration with lossy halfspaces.

B.4.2 Using the FFT for the inverse transformation

In using the Fast Fourier Transform for the inverse transformation to the frequency domain, care must be taken to avoid errors caused by insufficient sampling etc. These errors are aliasing errors, caused by using an insufficient number of spatial frequencies, thereby violating the sampling theorem. Energy of the signal outside the sampling interval is then 'folded' into the resulting signal. When either branch points or poles are on or close to the integration axis, the integrand will be either singular or oscillating at or near these points, which makes a very large number of points in the Fourier-transform domain necessary. Another type of error that can occur are leakage errors, which are caused by using an insufficiently large sampling window. For the inverse transformation, it is assumed that the signal is zero outside the sampling window. If this is not the case, leakage errors will occur. In the next subsections, we describe the use of periodicity to decrease the size of the FFT grid and the accuracy of the FFT in calculating the reflected part of the Green's function.

Accuracy of the FFT

We have tested the accuracy of the Green's function obtained with the inverse FFT by taking the grid twice as fine and comparing the result with that obtained by performing the FFT over a coarser grid. We recommend that this procedure always be followed when calculating a Green's function with FFTs. This procedure also

ensures that aliasing and leakage are small enough not to affect accuracy. The same procedure should be followed when calculating the Green's function for grid points close to the interface. In order to determine the influence of the branch points and poles, we have taken several values for the conductivity of the halfspaces and compared the resulting Green's functions. It was found that a value of 4 S/m caused the branch points to be far enough away from the integration axes. This value for the conductivity of the halfspaces corresponds to seawater, which is realistic since the PEC tool has been operated under water without noticeable effect on the measured signals. The effect of the extent of the grid in the Fourier-transform domain was also investigated by taking several values of k_{max} and subsequently checking whether the variation in the Green's functions was small enough.

In order to compare the different Green's functions, we define the squared relative error of a quantity over the FFT grid at a fixed value of x_3 as

$$\text{ERR} = \frac{\sum_{m=1}^M \sum_{n=1}^N \left(\hat{G}_f(x_{m,n}) - \hat{G}(x_{m,n}) \right) \left(\hat{G}_f(x_{m,n}) - \hat{G}(x_{m,n}) \right)^*}{\sum_{m=1}^M \sum_{n=1}^N \hat{G}(x_{m,n}) \hat{G}^*(x_{m,n})} \quad (\text{B.101})$$

where the grid has M by N points and where \hat{G} is a component of the Green's function. The subscript f denotes the Green's function obtained with the finer sampled grid. Using this formulation, the relative error in the reflected parts of the Green's function used in Chapters 4 and 5 was about 2%. Note that we can increase the relative accuracy of the Green's function with only a small increase in computational cost by using the grid reduction technique described in Appendix C.

Appendix C

Grid reduction for FFTs

In this chapter we will discuss a method to reduce the grid size of the FFTs that are used to calculate the Green's function. In order to obtain sufficient accuracy, we need a large number of grid points to calculate the inverse spatial Fourier transformation using an FFT. However, having calculated the FFT, we only need the Green's function on a subset of these points, since the grid that is used for the CG scheme is much smaller than the grid used for the FFT. In this chapter we propose a method whereby the number of grid points is reduced before application of the FFT algorithm, leading to a considerable reduction in computation time.

C.1 Using periodicity to reduce the number of grid points

We will first discuss the effect of the periodicity of a function on its Fourier coefficients. A periodic function $f(t)$ has the Fourier transformation

$$F(j\omega) = \int_{-T_0/2}^{T_0/2} f(t) \exp(-j\omega t) dt, \quad (\text{C.1})$$

where T_0 is the period of $f(t)$. When the function is aperiodic ($T_0 \rightarrow \infty$), the integration limits are $-\infty$ and ∞ . The periodic function $f(t)$ can be written in terms of its Fourier components as

$$f(t) = \sum_{k=-\infty}^{\infty} c_k \exp(jk\omega_0 t), \quad (\text{C.2})$$

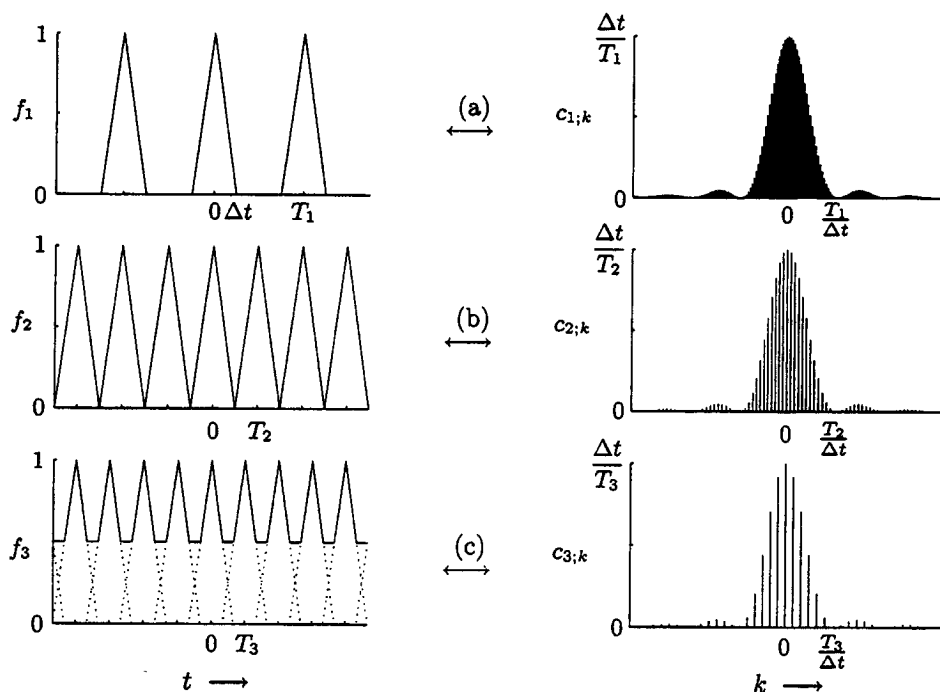


Figure C.1: Periodic hat functions and corresponding Fourier coefficients (normalized to T_i , $i = 1, 2, 3$)

where the Fourier coefficients c_k are given by

$$c_k = \frac{1}{T_0} \int_{-T_0/2}^{T_0/2} f(t) \exp(-jk\omega_0 t) dt, \quad (\text{C.3})$$

and $\omega_0 = 2\pi/T_0$. From Eqs. (C.3) and (C.1) it follows that

$$c_k = \frac{1}{T_0} F(j\omega) \Big|_{\omega=k\omega_0}, \quad (\text{C.4})$$

i.e., the coefficients c_k are the values of $F(j\omega)$ sampled at $\omega = k\omega_0$, $k \in \mathbb{Z}$. Consequently, the continuous frequency domain function $F(j\omega)$ is the envelope of the discrete Fourier coefficients c_k (see Figure C.1).

For now, we consider the hat function as an example to illustrate the effect on the Fourier coefficients of varying the period of a function. The aperiodic hat function is defined as

$$f(t) = \begin{cases} 1 - \frac{|t|}{\Delta t}, & |t| \leq \Delta t, \\ 0, & \text{elsewhere,} \end{cases} \quad (\text{C.5})$$

while its Fourier transformation is given by

$$F(j\omega) = \Delta t \operatorname{sinc}^2(\omega \Delta t / 2). \quad (\text{C.6})$$

When we convolve the function $f(t)$ with a time sampler $\sum_{m=-\infty}^{\infty} \delta(t - mT_i)$, we obtain a periodic function with period T_i and we can then calculate its Fourier coefficients by applying Eq. (C.3) (see Figure C.1a). For a function with period T_i the normalized coefficients $T_i c_{k,i}$ are found as

$$c_{k,i} = \frac{\Delta t}{T_i} \operatorname{sinc}^2\left(\frac{k\omega_i \Delta t}{2}\right), \quad (\text{C.7})$$

where $\omega_i = 2\pi/T_i$. Decreasing the period T_i results in less Fourier coefficients (compare Figures C.1a and C.1b). Specifically, if we halve the period, all odd-numbered Fourier coefficients will become zero, while the even numbered coefficients will be twice as large (note that all coefficients in Figure C.1 are normalized to T_i). We can continue to decrease the period until we arrive at the situation depicted in Figure C.1b, where we are sampling at exactly the Nyquist rate.

We now decrease the period even further, such that we are aliasing the function in the time domain. In the frequency domain, this results in even less Fourier coefficients, but those coefficients that remain nonzero still have the same values as before (scaled by the period T_i). Of course, the limiting case is where the period T tends to zero, and we then end up with a continuous and constant function which has a Dirac delta function as its transformation.

We can conclude that when we are interested in the exact function value on a small number of points in the transform-domain, we can reduce the period of the function to the point where we are deliberately aliasing. Then for that particular period of the function, we end up with exactly those points in the transform-domain that we were interested in. Note that this method also works for the inverse transformation because of the duality property of the Fourier transformation.

C.2 Application to the FFT algorithm

We will now apply the idea of deliberately aliasing to a discrete FFT. Given the discrete inverse Fourier transformation (see Press *et al.* [67])

$$f_k = \sum_{n=0}^{N-1} F_n \exp\left(-\frac{2\pi i k n}{N}\right), \quad (\text{C.8})$$

we now reduce the period of the function in the transform-domain by a factor of two (see Figure C.2). The length of the FFT changes from N to $N/2$ points, which leads to

$$f_{2k} = \sum_{n=0}^{N/2-1} F_n \exp\left(-\frac{2\pi i k n}{N/2}\right). \quad (\text{C.9})$$

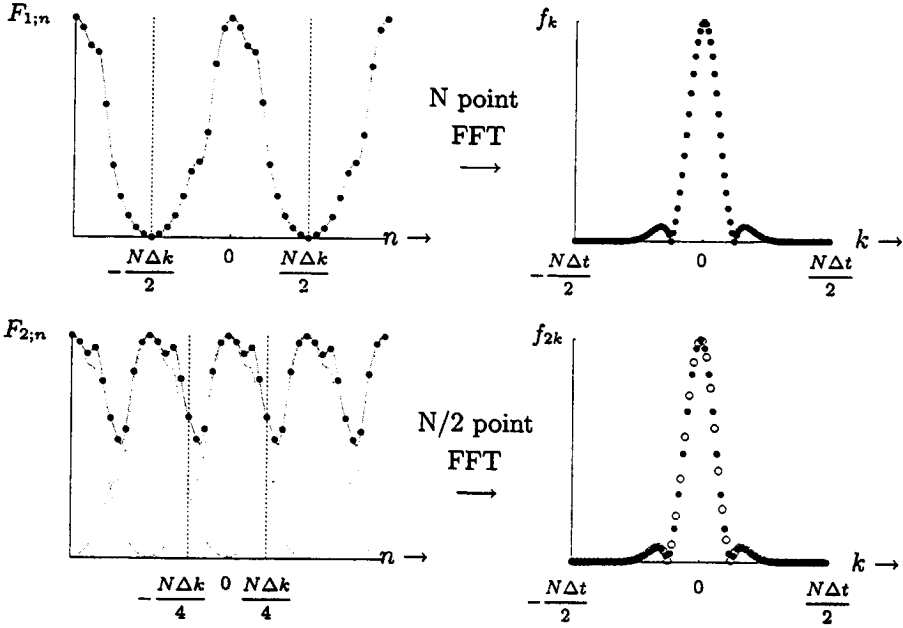


Figure C.2: Decreasing the period of the function by a factor of 2, open dots in lower left-hand figure correspond to the 'superfluous' points that are obtained using the large FFT.

Next we split the summation into three parts, one from $n = 0$ to $n = N/4 - 1$ over $N/4$ points, one from $n = N/4$ to $n = 3N/4 - 1$ over $N/2$ points and one from $n = 3N/4$ to $n = N - 1$, again over $N/4$ points. The summations over $N/4$ points can be rewritten as

$$\sum_{n=0}^{N/4-1} F_n \exp\left(-\frac{2\pi i k n}{N/2}\right) = \quad (C.10)$$

$$\sum_{n'=N/2}^{3N/4-1} F_{n'-N/2} \exp\left(-\frac{2\pi i k n'}{N/2}\right)$$

and

$$\sum_{n=3N/4}^{N-1} F_n \exp\left(-\frac{2\pi i k n}{N/2}\right) = \quad (C.11)$$

$$\sum_{n''=N/4}^{N/2-1} F_{n''+N/2} \exp\left(-\frac{2\pi i k n''}{N/2}\right)$$

where $n' = n + N/2$ and $n'' = n - N/2$. Combining these summations leads to the following inverse FFT over $N/2$ points

$$f_{2k} = \sum_{n=N/4}^{N/2-1} (F_n + F_{n+N/2}) \exp\left(-\frac{2\pi i k n}{N/2}\right) + \sum_{n=N/2}^{3N/4-1} (F_n + F_{n-N/2}) \exp\left(-\frac{2\pi i k n}{N/2}\right). \quad (\text{C.12})$$

Using the original transformation with N points, the function h in the spatial domain is obtained at the points $k\Delta x$, $k = 0, \dots, N - 1$. Taking the FFT over $N/2$ points as described in Eq. (C.12) yields the function h in the spatial domain at the points $2k\Delta x$, $k = 0, \dots, N/2 - 1$.

On these points, the reduced FFT yields exactly the same values as the original FFT, i.e., this corresponds to discarding all odd numbered grid points from the result of the original FFT. This doubling of the periodicity of the function can be done recursively, leading to $h_{2^p k}$, where p is number of times the periodicity has been doubled. The procedure described above is given graphically in Figure C.2, where the periodicity is increased by a factor of 2. The open dots in the lower left-hand figure are those points that are effectively neglected, i.e., the odd-numbered points (compare to Figures C.1a-b). Note that the grid reduction procedure described above can also be implemented for multi-dimensional FFTs, where we must successively fold along each direction before performing the FFT.

Note that we must divide by $1/2^p$ to obtain the correct amplitude for the inverse transformation. In effect, all normalizations that are done (division by N and division by Δx) for the inverse transformation must also be done for the folded inverse transformation. The reduction in N is exactly compensated for by the extra division by $1/2^p$, resulting in no net change in amplitude.

In the procedure described above, we start from the fact that we need the transformed function on only a small, specific number of points. Depending on the number of folding steps, we are interested in the points f_{nk} , $n = 2, 4, \dots$ of the original sequence that arises from the N -point FFT. This procedure is similar to using a decimation-in-frequency FFT (the Sande-Tukey algorithm), where only parts of the output and algorithm are used. In Figure C.3 we describe schematically the first step of the decimation-in-frequency algorithm working on a discrete function of length 8. In the decimation-in-frequency algorithm, the output sequence f_k is divided into smaller subsequences, as opposed to the decimation-in-time (Cooley-Tukey) algorithm, where the input sequence is divided into subsequences. From Figure C.3 we see that the N -point DFT is divided into two $N/2$ -point DFTs and performing this step recursively leads to the (decimation-in-frequency) FFT algorithm. If we now choose to omit the DFT for that part of the output sequence f_k where k is odd, we end up with the subsequence f_k , where k is even (i.e., we discard all odd-numbered samples). Note that it is not possible to use the decimation-in-time (Cooley-Tukey)

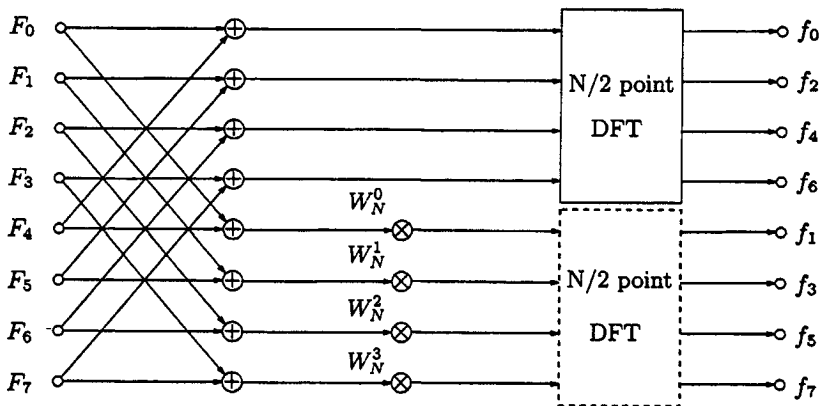


Figure C.3: Schematic description of the first step of the decimation-in-frequency FFT algorithm. Calculating only the DFT for f_n , n even, corresponds to decreasing the period of the function with a factor of 2. The factor W_N^k is defined as $\exp(-j2\pi k/N)$.

algorithm to this end, since in that algorithm the additions are at the end of the algorithm instead of the at the start.

This means that we only have to calculate an $N/2$ -point DFT in order to obtain f_k where k is even. Therefore, omitting one of the $N/2$ -point DFTs in Figure C.3 corresponds to decreasing the periodicity of the input sequence F_n with a factor of 2, as described previously. We can conclude that the reduction in grid size accomplished by the grid reduction technique corresponds to the decimation-in-frequency FFT algorithm, where only a part of the algorithm is used. Recursive application of the principle given in Figure C.3 enables us to reduce the size of the output sequence even further, which corresponds to taking more grid reduction steps.

Finally, we note that the grid reduction procedure described in this appendix can also be used for transformations of time domain signals to the frequency domain and vice versa. Causality is guaranteed, since the resulting discrete signal is merely a subset of the signal that would have been obtained using the larger FFT.

Bibliography

- [1] Abramowitz, M., and Stegun, I.A., *Handbook of Mathematical Functions*, 9th ed., Dover Publications, New York, 1970.
- [2] Abubakar, A., *Three-dimensional nonlinear inversion of electrical conductivity*, Ph.D. Thesis, Delft University Press, Delft, The Netherlands, 2000.
- [3] Abubakar, A. and P.M. van den Berg, Total variation as a multiplicative constraint for solving inverse problems, *IEEE Transactions on Image Processing*, 10, pp. 1384-1387, 2000.
- [4] Abubakar, A. and P.M. van den Berg, The contrast source inversion method for location and shape reconstructions, *Inverse Problems*, 18, pp. 495-510, 2002.
- [5] Albanese, R., G. Rubinacci and F. Villone, An Integral Computational Model for Crack Simulation and Detection via Eddy Currents, *Journal of Computational Physics*, 152, pp. 736-755, 1999.
- [6] Badics, Z., Y. Masumoto, K. Aoki, F. Nakayasu, M. Uesaka and K. Miya, An Effective 3-D Finite Element Scheme for Computing Electromagnetic Field Distortions due to Defects in Eddy-Current Nondestructive Evaluation, *IEEE Transactions on Magnetics*, 32, No. 2, pp. 1012-1020, 1997.
- [7] Badics, Z., H. Komatsu, Y. Matsumoto and K. Aoki, Inversion Scheme Based on Optimization for 3-D Eddy Current Flaw Reconstruction Problems, *Journal of Nondestructive Evaluation*, 17, No. 2, pp. 67-78, 1998.
- [8] Beissner, R.E., and M.J. Sablik, Theory of eddy currents induced by a nonsymmetric coil above a conducting half-space, *Journal of Applied Physics*, 56, No. 2, pp. 448-454, 1984.
- [9] Beissner, R.E., and J.L. Fisher, A model of pulsed eddy current crack detection, *Review of Progress in Quantitative Nondestructive Evaluation*, 5, pp. 189-197, 1986.

- [10] Bloemenkamp, R.F., *Time-Domain Nonlinear Profile Inversion of Subsurface Configurations*, Ph.D. Thesis, Delft University Press, Delft, The Netherlands, 2002.
- [11] Blok, H., and M.L. Oristaglio, *Wavefield imaging and inversion in electromagnetics and acoustics*, Report number Et/EM 1995-21, TU Delft, The Netherlands, 1995.
- [12] Bowler, J.R., Eddy current calculations using half-space Green's functions, *Journal of Applied Physics*, **61**, No. 3, pp. 833-839, 1986.
- [13] Bowler, J.R., A Theoretical and Computational Model for Eddy Current Probes Incorporating Volume Integral and Conjugate Gradient Methods, *IEEE Transactions on Magnetics*, **25**, No. 3, pp. 2650-2664, 1989.
- [14] Bowler, J.R., Eddy-current interaction with an ideal crack. I. The forward problem, *Journal of Applied Physics*, **75**, No. 12, pp. 8128-8137, 1994.
- [15] Bowler, J.R., Eddy-current interaction with an ideal crack. II. The inverse problem, *Journal of Applied Physics*, **75**, No. 12, pp. 8137-8144, 1994.
- [16] Bowler, J.R., S.A. Jenkins, L.D. Sabbagh and H.A. Sabbagh, Eddy-current probe impedance due to a volumetric flaw, *Journal of Applied Physics*, **70**, No. 3, pp. 1107-1114, 1991.
- [17] Bowler, J.R. and M. Johnson, Pulsed Eddy-Current Response to a Conducting Half-Space, *IEEE Transactions on Magnetics*, **33**, No. 3, pp. 2258-2264, 1997.
- [18] Bowler, J.R., and N. Harfield, Evaluation of Probe Impedance Due to Thin-Skin Eddy-Current Interaction with Surface Cracks, *IEEE Transactions on Magnetics*, **34**, No. 2, pp. 515-523, 1998.
- [19] Burrows, M., *A Theory of Eddy-Current Flaw Detection*, Ph.D. Thesis, University of Michigan, University Microfilms Inc., Ann Arbor, Michigan, 1964.
- [20] Cheesman, S.J., R.N. Edwards and A.D. Chave, 1987, On the theory of sea-floor conductivity mapping using transient electromagnetic systems, *Geophysics*, **52**, No. 2, pp. 204-217, 1987.
- [21] Cheng, C.C., C.V. Dodd and W.E. Deeds, General Analysis of Probe Coils near Stratified Conductors, *International Journal of Nondestructive Testing*, **3**, pp. 109-129, 1971.
- [22] Chew, W.C., *Waves and fields in inhomogeneous media*, IEEE Press, New York, 1995.
- [23] Clark, W.G., Multiple-Element Eddy Current Probes For Enhanced Inspection, *Materials Evaluation*, July 1993, pp. 794-802, 1993.
- [24] Creek, E.A. and R.E. Beissner, Eddy current exam simulation using coupled FEM/Volume integral or FEM/BEM method, *Review of Progress in Quantitative Nondestructive Evaluation*, **16**, pp. 225-232, 1997.

-
- [25] Cui, T.J. and W.C. Chew, Fast Evaluation of Sommerfeld Integrals for EM Scattering and Radiation by Three-Dimensional Buried Objects, *IEEE Transactions on Geoscience and Remote Sensing*, **37**, No. 2, pp. 887-899, 1999.
- [26] Cui, T.J. and W.C. Chew, Fast Algorithm for Electromagnetic Scattering by Buried 3-D Dielectric Objects of Large Size, *IEEE Transactions on Geoscience and Remote Sensing*, **37**, No. 5, pp. 2597-2608, 1999.
- [27] Dai, X-W., R. Ludwig, Numerical Simulation of Eddy-Current Nondestructive Testing Phenomena, *IEEE Transactions on Magnetics*, **26**, No. 6, pp. 3089-3096, 1990.
- [28] Dodd, C.V. and W.E. Deeds, Analytical Solutions to Eddy-Current Probe-Coil Problems, *Journal of Applied Physics*, **39**, No. 6, pp. 2829-2838, 1968.
- [29] Dos Reis, D., M. Lambert and D. Lesselier, Eddy-current evaluation of 3-D defects in a metal plate, to appear in *Inverse Problems*, December 2002.
- [30] Dunbar, W.S., The Volume Integral Method of Eddy-Current Modeling: Verification, *Journal of Nondestructive Evaluation*, **7**, Nos. 1/2, pp. 43-54, 1988.
- [31] Farquharson, C.G. and D.W. Oldenburg, Inversion of time-domain electromagnetic data for a horizontally layered Earth, *Geophys. J. Int.*, **114**, pp. 433-442, 1993.
- [32] Fukutomi, H., H. Huang, T. Takagi and J. Tani, Identification of Crack Depths from Eddy Current Testing Signal, *IEEE Transactions on Magnetics*, **34**, No. 5, pp. 2893-2896, 1998.
- [33] Fullagar, P.K. and D.W. Oldenburg, Inversion of horizontal loop electromagnetic frequency soundings, *Geophysics*, **49**, No. 2, pp. 150-164, 1984.
- [34] Goldman, M.M. and C.H. Stoyer, Finite-difference calculations of the transient field of an axially symmetric earth for vertical magnetic dipole excitation, *Geophysics*, **48**, No. 7, pp. 953-963, 1983.
- [35] Haak, K.F.I., *Multi-frequency nonlinear profile inversion methods*, Ph.D. Thesis, Delft University Press, Delft, The Netherlands, 1999.
- [36] Habashy, T.M., R.W. Groom and B. Spies, Beyond the Born and Rytov approximations: A nonlinear approach to electromagnetic scattering, *Journal of Geophysical Research*, **98**, pp. 1759-1775, 1987.
- [37] Haywood, N.C., *Eddy-Current Imaging of Cracks by Inverting Field Data*, Ph.D. Thesis, University of Surrey, The British Library Document Supply Centre, UK, 1990.
- [38] Hower, G.L., D. Philipp, A. Abtahi and R.W. Rupe, Some Computational Considerations in Eddy-Current NDE, *Journal of Nondestructive Evaluation*, **4**, No. 1, pp. 39-42, 1984.
- [39] Jenkins, S.A., *Theoretical Models of Eddy Current Interaction with Defects*, Ph.D. Thesis, University of Surrey, The British Library Document Supply Centre, UK, 1991.

- [40] Johnk, C.T.A., *Engineering Electromagnetic Fields & Waves*, John Wiley & Sons, 1975.
- [41] Juillard, J., G. Pichenot and A. Masia, Semianalytical Method for Calculating the Impedance Variation of an Arbitrary Eddy-Current Probe, *IEEE Transactions on Magnetics*, **38**, No. 5, pp. 3448-3453, 2002.
- [42] Idemen, M. and I. Akduman, Two-dimensional inverse scattering problems connected with bodies buried in a slab, *Inverse Problems*, **6**, pp. 749-766, 1990.
- [43] Kooij, B.J., *Analysis of Transient Electromagnetic Fields in an Electrical Utility Substation Environment*, Ph.D. Thesis, Delft University Press, Delft, The Netherlands, 1994.
- [44] Kooij, B.J., and P.M. van den Berg, Nonlinear inversion in TE scattering, *IEEE Transactions on Microwave Theory and Techniques*, **46**, No. 11, November 1998.
- [45] Kriezis, E.E., T.D. Tsiboukis, S.M. Panas and J.A. Tegopoulos, Eddy Currents: Theory and Applications, *Proceedings of the IEEE*, **80**, No. 10, pp. 1559-1585, 1992.
- [46] Lambert, M. and D. Lesselier, Binary-constrained inversion of a buried cylindrical obstacle from complete and phaseless magnetic fields, *Inverse Problems*, **16**, pp. 563-576, 2000.
- [47] Lebrun, B., Y. Jayet and J.C. Baboux, Pulsed Eddy Current Application to the Detection of Deep Cracks, *Materials Evaluation*, November 1995, pp. 1296-1300, 1995.
- [48] Lee, T. and R. Lewis, Transient EM response of a large loop on a layered ground, *Geophysical Prospecting*, **22**, pp. 430-444, 1974.
- [49] Lepelaars, E.S.A.M. *Transient Electromagnetic Excitation of Biological Media by Circular Loop Antennas*, Ph.D. Thesis, Universiteitsdrukkerij TUE, Eindhoven, The Netherlands, 1997.
- [50] Litman, A. and D. Lesselier, On attenuation-matched inversion methods of diffusive wavefields, *Inverse problems*, **15**, pp. 99-111, 1999.
- [51] Looijer, M.T., *Analysis of eddy-current inspection of cracks and corrosion in a simple configuration*, Report number Et/EM 1995-20, Delft University of Technology, The Netherlands, 1995.
- [52] Ludwig, R. and X. Dai, Numerical and analytical modeling of pulsed eddy currents in a conducting halfspace, *IEEE Transactions on Magnetics*, **26**, No. 1, pp. 299-307, 1990.
- [53] Luong, B. and F. Santosa, Quantitative imaging of corrosion in plates by eddy current methods, *Journal of Applied Mathematics*, **58**, No. 5, pp. 1509-1531, 1998.
- [54] McIntire, P. (editor), *Nondestructive Testing Handbook*, Volume 4, American Society for Nondestructive Testing, 1986.

- [55] Morsink, B.J., *Optimization of the pulsed eddy-current technique for non-intrusive inspection of corrosion under insulation*, Report number Et/EM 1997-14, Delft University of Technology, The Netherlands, 1997.
- [56] Nabighian, M.N., Quasi-static transient response of a conducting half-space - An approximate representation, *Geophysics*, **44**, No. 10, pp. 1700-1705, 1979.
- [57] Nair, S.M. and J.H. Rose, Reconstruction of three-dimensional conductivity variations from eddy current (electromagnetic induction) data, *Inverse Problems*, **6**, pp. 1007-1030, 1990.
- [58] Norton, S.J. and J.R. Bowler, Theory of eddy current inversion, *Journal of Applied Physics*, **73**, No. 2, pp. 501-512, 1993.
- [59] Oristaglio, M.L. and G.W. Hohmann, Diffusion of electromagnetic fields into a two-dimensional earth: A finite-difference approach, *Geophysics*, **49**, No. 7, pp. 870-894, 1984.
- [60] Oristaglio, M.L. and T.M. Habashy, Some uses (and abuses) of reciprocity in wavefield inversion, *Wavefields and Reciprocity*, Proceedings of a Symposium held in the honour of Professor dr. A.T. de Hoop, Delft University Press, pp. 1-22, 1996.
- [61] Pavlov, D.A. and M.S. Zhdanov, Analysis and interpretation of anomalous conductivity and magnetic permeability effects in time domain electromagnetic data. Part I: Numerical modeling, *Journal of Applied Geophysics*, **46**, pp. 217-233, 2001.
- [61] Pavlov, D.A. and M.S. Zhdanov, Analysis and interpretation of anomalous conductivity and magnetic permeability effects in time domain electromagnetic data. Part II: $S\mu$ -inversion, *Journal of Applied Geophysics*, **46**, pp. 235-248, 2001.
- [63] Pávó, J. Numerical Calculation Method for Pulsed Eddy-Current Testing, *IEEE Transactions on Magnetics*, **38**, No. 2, pp. 1169-1172, 2002.
- [64] Peng, Z.Q. and A.G. Tijhuis, Transient Scattering by a Lossy Dielectric Cylinder: Marching-on-in-Frequency Approach, *Journal of Electromagnetic Waves and Applications*, **7**, No. 5, pp. 739-763, 1993.
- [65] Placko, D. and I. Dufour, A Focused-Field Eddy Current Sensor for Nondestructive Testing, *IEEE Transactions on Magnetics*, **29**, No. 6, pp. 3192-3194, 1993.
- [66] Preda, G., B. Cranganu-Cretu, O. Mihalache, F.I. Hantila, Z. Chen and K. Miya, Nonlinear FEM-BEM Formulation and Model-Free Inversion Procedure for Reconstruction of Cracks using Pulse Eddy-Currents, *Proceedings of the 13th COMPUMAG conference, July 2001*, 2001.
- [67] Press, W.H., S.A. Teukolsky, W.T. Vetterling and B.P. Flanery, *Numerical Recipes*, Cambridge University Press, Cambridge, UK, 1992.

- [68] Rose, J.H., and E. Uzal, Calculated time-domain current-voltage response of ferrite-core probes : application to lap-splice corrosion, *Review of Progress in Quantitative Nondestructive Evaluation*, **13**, pp. 311-317, 1994.
- [69] Sabbagh, H.A., A Model of Eddy-Current Probes with Ferrite Cores, *IEEE Transactions on Magnetics*, **MAG-23**, No. 2, pp. 1888-1904, 1987.
- [70] Sabbagh, H.A., and R.G. Lautzenheiser, Inverse problems in electromagnetic nondestructive evaluation, *International Journal of Applied Electromagnetics*, **3**, pp. 253-261, 1993.
- [71] Sabbagh, H.A., J.C. Treece, R.K. Murphy and L.W. Woo, Computer modelling of Eddy Current Nondestructive Testing, *Materials Evaluation*, November 1993, pp. 1252-1257, 1993.
- [72] Sabbagh, H.A., and S.N. Vernon, Ferrite Core Eddy Current Probe Model : Description and Verification, *Materials Evaluation*, No. 43, pp. 184-187, 1984.
- [73] Sepulveda, N.G., I.M. Thomas and J.P. Wikswo, Magnetic Susceptibility Tomography for Three-Dimensional Imaging of Diamagnetic and Paramagnetic Objects, *IEEE Transactions on Magnetics*, **30**, No. 6, pp. 5062-5069, 1994.
- [74] Sethuraman, A. and J.H. Rose, Rapid Inversion of Eddy Current Data for Conductivity and Thickness of Metal Coatings, *Journal of Nondestructive Evaluation*, **14**, No. 1, pp. 39-46, 1995.
- [75] Shao, C.D.K.R., Z.X. Ren and J.D. Lavers, A Very Fast Numerical Analysis of Benchmark Models of Eddy Current Testing for Steam Generator Tube, *Proceedings of the 19th COMPUMAG conference, July 2001*, 2001.
- [76] Tai, C-C., J.H. Rose and J.C. Moulder, Thickness and conductivity of metallic layers from pulsed eddy-current measurements, *Review of Scientific Instruments*, **67**, Issue 11, pp. 3965, 1996.
- [77] Tijhuis, A.G. and Z.Q. Peng, Marching-on-in-frequency method for solving integral equations in transient electromagnetic scattering, *IEEE Transactions-H*, **138**, No. 4, pp. 347-355, 1991.
- [78] Tsuchida, Y., K. Shibao and M. Enokizono, Inverse Analysis for ECT Models Formulated by Laplace Transform BEM with Singular Value Decomposition and Fuzzy Inference, *IEEE Transactions on Magnetics*, **34**, No. 5, pp. 2916-2919, 1998.
- [79] Torres-Verdín, C. and T.M. Habashy, A Two-Step Linear Inversion of Two-Dimensional Electrical Conductivity, *IEEE Transactions on Antennas and Propagation*, **43**, No. 4, pp. 405-415, 1995.
- [80] Upda, L. and S.S. Upda, Solution of Inverse Problems in Eddy-Current Non-destructive Evaluation (NDE), *Journal of Nondestructive Evaluation*, **7**, Nos. 1/2, pp. 111-120, 1988.
- [81] Van den Berg, P.M., *Reconstruction of media posed as an optimization problem*, Report number Et/EM 1998-26, TU Delft, The Netherlands, 1998.

-
- [82] Van den Berg, P.M., and R.E. Kleinman, A contrast source inversion method, *Inverse Problems*, **13**, pp. 1607-1620, 1997.
- [83] Van den Berg, P.M., and M. van der Horst, Nonlinear inversion in induction logging using the modified gradient method, *Radio Science*, **30**, No. 5, pp. 1355-1369, 1995.
- [84] Van den Berg, P.M., A.L. van Broekhoven and A. Abubakar, Extended contrast source inversion, *Inverse Problems*, **15**, pp. 1325-1344.
- [85] Van den Berg, P.M., A. Abubakar and J.T. Fokkema, Multiplicative regularization for contrast profile inversion, *Radio Science*, **38**, No. 2, 2003.
- [86] Van der Kruk, J., *Three-dimensional imaging of multi-component ground penetrating radar data*, Ph.D. Thesis, Delft University Press, Delft, The Netherlands, 2001.
- [87] Wait, J.R., *Electromagnetic radiation from cylindrical structures*, IEE Electromagnetic Wave Series, **27**, 1988.
- [88] Wait, J.R. and D.A. Hill, Transient electromagnetic fields of a finite circular loop in the presence of a conducting half-space, *Journal of Applied Physics*, **43**, No. 11, pp. 4532-4534, 1971.
- [89] Wang, T., M. Oristaglio, A. Tripp and G. Hohmann, Inversion of diffusive transient electromagnetic data by a conjugate-gradient method, *Radio Science*, **29**, No. 4, pp. 1143-1156, 1994.
- [90] Ward, S.H. and G.W. Hohmann, Electromagnetic Theory for Geophysical Applications, *Investigations in Geophysics*, **1**, pp. 131-311, 1987.
- [91] Yan, M., S. Upda, S. Mandayam, Y. Sun, P. Sacks and W. Lord, Solution of Inverse Problems in Electromagnetic NDE Using Finite Element Methods, *IEEE Transactions on Magnetics*, **34**, No. 5, pp. 2924-2927, 1998.
- [92] Yang, H-C. and C-C. Tai, Pulsed eddy-current measurements of a conducting coating on a magnetic metal plate, *Meas. Sci. Technology*, **13**, pp. 1259-1265, 2002.
- [93] Zaman, A.J.M., S.A. Long and C.G. Gardner, The Impedance of a Single-Turn Coil Near a Conducting Half Space, *Journal of Nondestructive Evaluation*, **1**, No. 3, pp. 183-189, 1980.
- [94] Zhang, Z., and D.W. Oldenburg, Recovering magnetic susceptibility from electromagnetic data over a one-dimensional earth, *Geophys. J. Int.*, **130**, p. 422-434, 1997.
- [95] Zhang, Z., and D.W. Oldenburg, Simultaneous reconstruction of 1-D susceptibility and conductivity from electromagnetic data, *Geophysics*, **64**, No. 1, p. 33-47, 1999.
- [96] Zhorgati, R., B. Duchene, D. Lesselier and F. Pons, Eddy Current Testing of Anomalies in Conductive Materials, Part I : Qualitative Imaging via Diffraction Tomography Techniques, *IEEE Transactions on Magnetics*, **27**, No. 6, p. 4416-4437, 1991.

- [97] Zhorgati, R., B. Duchene, D. Lesselier and F. Pons, Eddy Current Testing of Anomalies in Conductive Materials, Part II : Quantitative Imaging via Deterministic and Stochastic Inversion Techniques, *IEEE Transactions on Magnetics*, 28, No. 3, p. 1850-1861, 1992.

Samenvatting

Dit proefschrift behandelt de modellering en inversie van Pulsed Eddy Current data voor Niet-Destructief Testen. De Pulsed Eddy Current (PEC) techniek is een relatief nieuwe elektromagnetische techniek op het gebied van Niet-Destructief Testen. Bij het Niet-Destructief Testen van een object wordt met behulp van een zender (een of meerdere spoelen in het geval van eddy current testen) een akoestisch of elektromagnetisch veld gegenereerd in het object. De invloed van het object op het aanwezige veld wordt met ontvangers (weer een of meerdere spoelen in het geval van eddy current NDT) gemeten. In het geval dat het object een defect (b.v. een gat, scheur of delaminatie) bevat, zal dit een verandering in het ontvangen signaal tot gevolg hebben, waardoor de aanwezigheid, plaats en grootte van het defect bepaald kunnen worden. In tegenstelling tot de normale eddy current techniek, waarbij met behulp van een zendspoel een elektromagnetisch veld met een vaste frequentie wordt opgewekt en vervolgens impedantieveranderingen in de ontvangstspoel ten gevolge van eventuele defecten worden gemeten, gebruikt men bij de PEC techniek een gepulste stroom in de zendspoel. Bij de meting wordt een DC-stroom in de zendspoel abrupt afgeschakeld, waardoor in het (metalen) object wervelstromen (eddy currents) worden gegenereerd. Deze wervelstromen genereren vervolgens een in de tijd variërend elektromagnetisch veld, dat met behulp van de ontvangstspoelen gemeten kan worden. Het gemeten voltage bevat informatie over onder andere de dikte en de mediumparameters van het metalen object.

Deze Pulsed Eddy Current NDT techniek is bij het Shell Research and Technology Centre in Amsterdam ontwikkeld om metingen te doen aan geïsoleerde pijpleidingen en drukvaten. Deze leidingen bestaan uit een stalen pijp, met daar omheen een laag isolatiemateriaal (steenwol) en een laagje aluminium ter bescherming van de isolatie. De aanwezigheid van de isolatie bemoeilijkt de periodieke inspectie en maakt het noodzakelijk om op gezette tijden de isolatie te verwijderen. De ontwikkeling van de PEC techniek maakt het mogelijk metingen aan de stalen pijp uit te voeren zonder dat daarvoor de isolatie verwijderd hoeft te worden, wat een

aanzienlijke reductie in de inspectiekosten met zich meebrengt.

Om deze techniek te modelleren zijn twee verschillende configuraties gebruikt: een waarbij het object uit een metalen laag bestaat zonder defecten, en een configuratie waarbij in deze laag een defect (put of holte) aanwezig kan zijn. De elektromagnetische parameters die van belang zijn voor het modelleren zijn: de elektrische geleidbaarheid σ en de magnetische permeabiliteit μ , in tegenstelling tot gangbare elektromagnetische toepassingen, waar meestal met de geleidbaarheid en de permittiviteit gerekend wordt. Het proefschrift valt globaal in twee delen uiteen: we beginnen met het oplossen van het voorwaartse probleem, waarbij voor een gegeven configuratie (zendspoel, metalen laag, al dan niet een defect) het elektromagnetisch veld bij de ontvangstspoel wordt berekend. Als tweede volgt het inverse probleem, dit behelst de reconstructie van de afmetingen en/of medium parameters van een verstrooiend object of defect als de rest van de configuratie en het gemeten veld bekend zijn. We presenteren numerieke resultaten van de methodes die ontwikkeld zijn om het voorwaartse en inverse probleem op te lossen.

In Hoofdstuk 1 van dit proefschrift bespreken we de motivatie voor het onderzoek en geven we tevens een korte en beknopte inleiding op het gebied van Niet-Destructief Testen. Vervolgens worden in Hoofdstuk 2 de Maxwell vergelijkingen voor het elektromagnetische veld gedefinieerd, alsmede de elektromagnetische randvoorwaarden en de integraaltransformaties die nodig zijn om de veldvergelijkingen in de hiervoor beschreven configuraties op te lossen.

In Hoofdstuk 3 gaan we dieper in op het bij SRTCA ontwikkelde meetapparaat en de werking ervan. Met behulp van een numeriek model dat wordt beschreven in Hoofdstuk 4 bepalen we de invloed van verschillende medium- en configuratieparameters op het PEC signaal. Uit de berekeningen blijkt dat de wervelstromen in het metaal een diffusieproces ondergaan, waarbij de verdeling van de stromen binnen het metaal vooral in de diepterichting varieert als functie van tijd. Aan de hand van dit gegeven beschrijven we een eenvoudig model, waarbij de wervelstromen als discrete stroomfilamenten gemodelleerd worden. Voor ieder stroomfilament definiëren we een weerstand, een coefficient van zelfinductie en een coefficient van mutuele inductie, waarmee het energietransport (en dus de elektromagnetische diffusie) beschreven wordt. Dit resulteert in een systeem van gekoppelde differentiaalvergelijkingen voor de stromen in de filamenten, waarbij de eigenwaarden en eigenvectoren van de systeemmatrix inzicht geven in het verloop van het diffusieproces.

Om het gedrag van de elektromagnetische velden in een defect te kunnen modelleren is het noodzakelijk om de volledige Maxwell-vergelijkingen op te lossen. In Hoofdstuk 4 beginnen we met de configuratie die bestaat uit een cirkelvormige zendspoel boven een metalen laag, zonder defect. In dit geval kunnen we gebruik maken van de symmetrie van de configuratie, wat leidt tot een scalaire differentiaalvergelijking voor het elektrisch veld in en boven de laag. Met behulp van een numerieke inverse Hankel-transformatie kunnen we het elektrisch en magnetisch veld uitrekenen in het frequentie-domein, waaruit het tijd-domein signaal volgt door gebruik te

maken van een Fast Fourier Transform.

Voor de configuratie van een cirkelvormige zendspoel boven een metalen laag met een defect is het niet langer mogelijk gebruik te maken van een scalaire vergelijking, derhale zijn we genooddaakt het volledige drie-dimensionale vectoriële probleem op te lossen. Met behulp van de reciprociteitsstelling leiden we de gekoppelde integraalvergelijkingen voor het elektrisch en magnetisch veld in het defect af, waarbij we voor de Green's functie onderscheid maken tussen de directe bijdrage van de bron en de reflecties van de randen van de laag. Voor het directe deel van het probleem schrijven we de integraalvergelijking in termen van de vectorpotentials die we vervolgens expanderen met behulp van stuksgewijs lineaire expansiefuncties. Door weging over het rekengebied benaderen we de differentiaaloperatoren die werken op de expansiefuncties met de eindige-differentie benadering. Het resulterende systeem van vergelijkingen voor de elektrische en magnetische veldgrootheden lossen we op met een Conjugate Gradient schema, waarbij de convolutie-operaties efficiënt worden opgelost met behulp van een FFT routine.

Voor de berekening van het gereflecteerde deel van de Green's functie gebruiken we een ruimtelijke Fourier-transformatie naar de i_1 - en i_2 -richtingen. Dit resulteert in uitdrukkingen voor de veldgrootheden in het ruimtelijk Fourier-domein, waarna de inverse transformatie met behulp van een FFT wordt uitgevoerd. Het is hierbij noodzakelijk om het gereflecteerde deel van de Green's functie te splitsen in een even en oneven deel. In het CG schema leidt dit tot een convolutiestructuur voor het even deel en een correlatiestructuur voor het oneven deel van de gereflecteerde Green's functie. Door het toepassen van grid reductie van de functie in het Fourier-domein kunnen we de Green's functie uitrekenen met een FFT waarvan de grootte van het grid gelijk is aan het CG grid, hetgeen een aanzienlijke tijdsbesparing oplevert. In Hoofdstuk 5 geven we de numerieke resultaten die zijn verkregen met behulp van de hiervoor beschreven rekenmodellen.

Nadat we in Hoofdstuk 4 het voorwaartse probleem hebben beschreven, richten we in Hoofdstuk 6 onze aandacht op het inverse probleem. Als eerste beschouwen we een configuratie van een verstrooiend object in een homogene achtergrond. We breiden de contrastbron inversiemethode, zoals beschreven door Van den Berg en Kleinman [82], uit voor de gecombineerde integraalvergelijkingen, waarbij zowel het elektrisch als het magnetisch veld opgelost wordt. Voor het geval van de PEC techniek, waarbij het te reconstrueren object een gat in de metalen achtergrond is, weten we de waarde van het contrast en zijn we vooral geïnteresseerd in de reconstructie van de afmetingen van het defect. In dat geval kunnen we gebruik maken van binaire inversie, waarbij we een niet-lineaire mapping introduceren voor het elektrisch en magnetisch contrast. Dit geeft een aanzienlijke verbetering in de reconstructies, maar heeft het nadeel dat een numerieke lijnminimalisatie nodig is in iedere iteratie van het inversieschema. Voor de inversie met een PEC configuratie, waarbij een laag aanwezig is definiëren we de extra operatoren die het gereflecteerde deel van de Green's functie in rekening brengen.

In Hoofdstuk 7 geven we de numerieke resultaten voor het inverse probleem

die zijn verkregen met behulp van de methoden die in de voorgaande hoofdstukken zijn gepresenteerd. Uiteindelijk geven we in Hoofdstuk 8 onze conclusies en enkele aanbevelingen voor verder onderzoek.

Curriculum Vitae

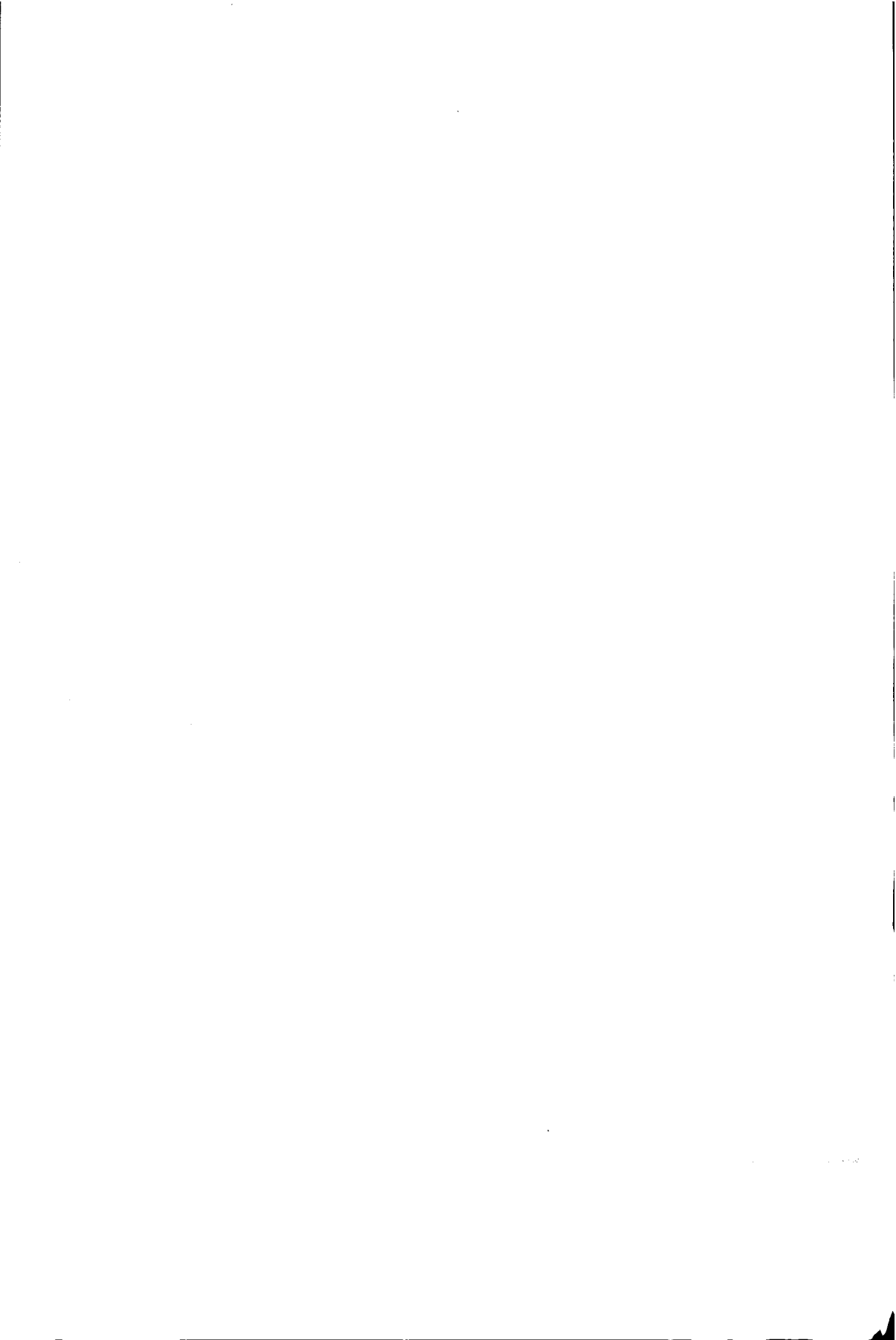
Simon Martijn van den Berg was born on December 30, 1973, in Brielle. He received his VWO-diploma in 1992 and in the same year started his study in electrical engineering at the Delft University of Technology. For his master's thesis he carried out research on the forward modelling of the Pulsed Eddy Current tool. The research was carried out at Shell Research and Technology Centre in Amsterdam and at the Laboratory of Electromagnetic Research under the supervision of Prof. dr. ir. H. Blok. In 1998 he received the M.Sc. degree and subsequently started as Ph.D. student at the Laboratory of Electromagnetic Research where he carried out research on the modelling and inversion of Pulsed Eddy Current data, which resulted in this thesis. The work reported on in this thesis was presented at several international conferences.

Acknowledgements

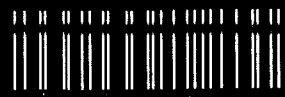
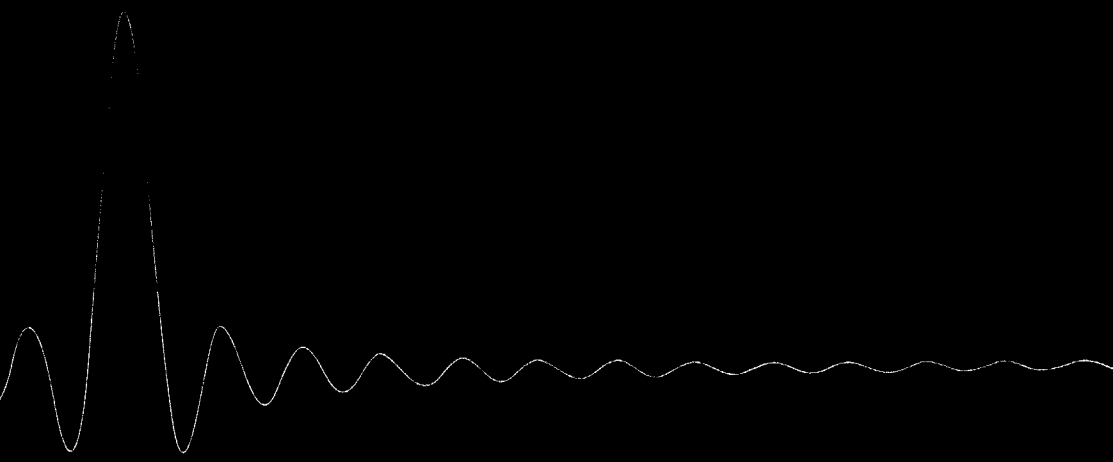
In concluding this thesis I would like to thank all those people who contributed to make this thesis possible. First of all I would like to thank the PEC-team at the Shell Research and Technology Centre, Amsterdam, for making this Ph.D. project possible. Paul Crouzen, Mark Looijer, Hans van der Steen, Sicco Jager, Ian Munns, Dave Badoux and all other people at the Inspection and Materials Engineering section at SRTCA.

I would like to thank Prof. Dr. Ir. Hans Blok and Prof. Dr. Ir. Peter van den Berg for giving me the opportunity to become a Ph.D. student at the Laboratory of Electromagnetic Research, especially Hans Blok for being my promotor. Dr. Ir. Bert Jan Kooij for reading the thesis, all his advice and being my co-promotor. Aria, for the discussions and help with the inversion schemes. And of course all the staff and AIOs at the EM lab for the pleasant environment (especially Martin, Pieter and Richard for the many and varied discussions over dinner).

Finally, I would like to express my gratitude to my parents, for their continued support over the years.







Delft University Press

